Understanding the Impacts of Mesosphere and Lower Thermosphere on Thermospheric Dynamics and Composition

by

Garima Malhotra

A dissertation submitted in partial fulfillment
of the requirements for the degree of
Doctor of Philosophy
(Climate and Space Sciences and Engineering)
in the University of Michigan
2021

Doctoral Committee:

Professor Aaron J. Ridley, Chair
Professor Dennis S. Bernstein
Research Professor Stephen W. Bougher
Associate Professor Shasha Zou

Garima Malhotra
garimam@umich.edu
ORCID iD: 0000-0003-4179-628X

To my family.

ACKNOWLEDGEMENTS

I am deeply grateful to my advisor Dr. Aaron Ridley for supporting me, guiding me and always being willing to help. Last year was an unprecedented year for the whole world and you have always responded to my chats and emails within hours. You are the hardest working person I know and your passion for your work is extremely inspiring. I aspire to be a rockstar scientist like you someday. I would also like to acknowledge my advisors and mentors from Virginia Tech, Dr. Joseph Baker and Dr. Michael Ruohoniemi, who gave me the opportunity to work in Space@VT and for being the most humble people I know. I would also like to offer my special thanks to the I.T. department of CLASP for being so swift in their responses and for making the transition during the pandemic much easier.

I want to express my deepest gratitude to my family for their unwavering support, encouragement, and belief in me. You are my true north, the kindest human beings, and no matter what challenges I face, your love helps me persist and persevere. Thank you Aarav and Samayra for lighting up my life with your beautiful smiles and being such bundles of joy. I hope you will read this someday and know how you have helped me reach this point in my career. To my aunts and grandparents who are no longer with me today, your love and encouragement throughout my childhood has made me into a very strong and ambitious person, Thank you ! Thanks to all my teachers, IGDTUW, and friends who have encouraged me and been with me in this journey.

Anyone who knows me well, would also know of my love for Ann Arbor and the University of Michigan. My time in this town and in this university is full of great memories that I will carry forth for the rest of my life. This place has been extremely nurturing and I have no hesitation in calling it my second home. This university has extended so many opportunities to me. I have met so many new people, attended inspiring seminars, and led and been a part of many student organizations (Thanks GRIN and MESWN!). I started out as a dreamy-eyed first-year graduate student, and I leave this place with the same dreams, more humility, knowledge, love for science, and even higher ambition. Thanks for making the last few years of my life so vibrant. Go Blue !

This thesis would be incomplete without mentioning my childhood idol, Dr. Kalpana Chawla. Thanks for igniting this spark in me. I will keep putting my best foot forward

as I move ahead in my scientific journey because - 'Sitaron Se Agay Jahan Aur Bhi Hain' (Translated as 'There are other worlds beyond the stars' - by Allama Iqbal).

TABLE OF CONTENTS

LIST OF FIGURES

Figure

LIST OF TABLES

Table

ABSTRACT

The Earth's Ionosphere and Thermosphere (IT) is a highly dynamic system persistently driven by variable forcings both from above (Solar EUV and the magnetosphere) and the lower atmosphere. The forcing from below accounts for the majority of the variability at low- and mid-latitude IT region during geomagnetic quiet times. The IT region is particularly sensitive to the composition, winds, and temperature of the Mesosphere and Lower Thermosphere (MLT) state. The goal of this dissertation is to help understand how the MLT region controls the upper atmosphere. This is achieved by using the IT model, Global Ionosphere Thermosphere Model (GITM) and altering its lower boundary (which is in the MLT) to allow a more accurate representation of the lower atmospheric physics within the model.

At the beginning of this thesis, it is identified that recent solstitial observations of MLT atomic oxygen (O) from the Sounding of the Atmosphere using Broadband Emission Radiometry (SABER) instrument show larger densities in the summer hemisphere than in the winter hemisphere. This is opposite to what has been previously known and specified in the IT models, and its cause is still under investigation. The first study focuses on understanding the influence of this latitudinal distribution by using a more realistic specification of MLT [O] from the Whole Atmosphere Community Climate Model with thermosphere and ionosphere extension (WACCM-X), in GITM. This study shows that despite being a minor species throughout the lower thermosphere, reversing the [O] distribution affects the pressure gradients, winds, temperature, and N_2 in the lower thermosphere. These changes then map to higher altitudes through diffusive equilibrium, improving the agreement between GITM O/N_2 and Global Ultraviolet Imager (GUVI) measurements.

Secondly, the importance of MLT variations on the thermospheric and ionospheric semiannual variation (T-I SAO) is investigated. This is done by analyzing the sensitivity of T-I SAO in GITM to different lower boundary assumptions. This study reveals that the primary driver of T-I SAO is the thermospheric spoon mechanism, as a significant T-I SAO is reproduced in GITM without an SAO variation in the MLT. However, using a more realistic MLT [O] from WACCM-X produces an oppositely-phased T-I SAO, maximizing at solstices, disagreeing with the observations. Since

the MLT [O] distribution is correct in WACCM-X, the results hint at incomplete specification/physics for lower thermospheric dynamics in GITM that can drive the transition of the SAO to its correct phase. These mechanisms warrant further investigation and may include stronger winter-to-summer winds, and lower thermospheric residual circulation.

The goal of the last study is to examine the effects of spatially non-uniform turbulent mixing in the MLT on the IT system. This is achieved by introducing latitudinal variation in the eddy diffusion parameter (K_{zz}) in GITM. The results reveal larger spatial variability in O/N_2 and TEC. However, the net effect is small (within 2-4%) on the globally averaged quantities and depends on the area of the turbulent patch. The results also show a different response between the summer and the winter IT region, with winter exhibiting larger changes.

Overall, this thesis has highlighted some of the outstanding questions in the domain of lower atmosphere-IT coupling and have answered them through exhaustive comparisons of GITM simulations with different satellite observations, and extensive term analyses of the GITM equations, while laying out a framework for coupling of GITM with WACCM-X.

CHAPTER I

Introduction

The Earth's atmosphere has been a subject of wonder and speculation since the beginning of civilization and has influenced the course of art, history, religion and folklore. In fact, the earliest known depiction of colorful display of aurora can be found in a Cro-Magnon cave painting, 'Macaronis' dating back to 30,000 BC. Different civilizations (including ancient Greece, Indian, Persian, and Chinese) have suggested that air is one of the five classical elements (with earth, water, fire, aether) that everything is made up of. These elements remained the cornerstone of philosophy and science for centuries.

However, only in the last 500 years, has this philosophical perspective towards the atmosphere gradually transitioned towards that of scientific doubt and inquiry. During the scientific revolution (mid- 17th century), after the barometer was invented, many experiments were conducted to measure air pressure and temperature at greater heights. This entailed endeavors to reach higher elevations by climbing mountains such as those by Florin Perier and Blaise Pascal. By the 18th century, hot air balloons were invented. One of the most famous hot air balloon missions was by Henry Coxwell and James Glaisher who flew in 1862 to reach up to a record height of 29000 feet (8.8 km). Astronomy and cosmology flourished during this time with the new heliocentric model by Nicolaus Copernicus in the 16th century, Johannes Kepler's law of planetary motions, and the use of telescopes to observe the Universe by Galileo Galilei in the 17th century.

However, space weather as a scientific discipline hasn't historically received much attention from the public and scientific community and has only come into common usage in the mid-late 20th century. Space weather emphasizes the study of varying conditions in the near-space environment of the Earth. In 1852, Edward Sabine realized that the magnetic field variations on Earth coincided with the 11-year sunspot cycle of the Sun. However, it was not until the powerful geomagnetic storm of 1859,

also referred to as the Carrington Event, that the relevance of Earth's upper atmosphere to the terrestrial life was recognized. It is still the most extreme storm to be documented, as the aurora was observed as far as the Caribbean and the telegraph machines shocked the operators and caused small fires around the world. In fact, the cause of this event was not linked to the Sun for many years. In 1882, Balfour Stewart theorized that there must be overhead currents in the Earth's atmosphere that lead to regular deflection of magnetic needle from the magnetic north. During the cold war era, as the space race unfolded and humans orbited the planet for the first time, the interest in understanding the near-space environment increased. In the 21st century, large corporations such as SpaceX and Blue Origin have dramatically increased our presence in this region. In fact, SpaceX recently announced the first all-civilian mission to space, Inspiration4, aboard its capsule Crew Dragon. Blue Origin and Virgin Galactic have also joined in this new era of space tourism with their recent missions onboard the New Shepard spacecraft and VSS Unity spaceplane, respectively. Our burgeoning dependence on satellites for navigation, communication and weather forecasting has also led to rapid commercialization of this region. Strong space weather events can damage the electronics on the satellites and pose risk of radiation to astronauts on the international space station (ISS), and passengers on trans-polar flights, thus requiring constant monitoring of space weather.

Even though the density of the atmosphere falls off exponentially with height, at about 500 km, which is a typical altitude for a Low Earth Orbit (LEO) satellite, the atmospheric drag is high enough to impact its orbit. Unless a satellite's propulsion system compensates for the changes in the drag, the orbit will decay over time, eventually re-entering the atmosphere. The density can also contribute to torques on the spacecraft which should be adjusted by the attitude control system. The uncertainty in densities can propagate through orbit propagators and affect our ability to accurately track the location of the satellites. The atmospheric density at LEO altitudes depends on the space weather events, such as coronal mass ejection, solar flares, and lower atmospheric perturbations, while exhibiting shorter and longer term variations due to Sun's 27-day rotation period and its 11-year cycle. The Sun goes through roughly an 11-year cycle, which is measured in terms of the variation in the number of sunspots on the solar surface. The probability of stronger space weather events is much higher during a solar maximum, i.e., when larger number of sunspots are observed. Thus, a large number of data-based and physics-based models of the upper atmosphere of the Earth have been created to accurately forecast space weather.

From a global perspective, the Earth's atmosphere is complex system that is

comprised of myriad different components interacting with each other non-linearly. These interacting components and processes span varying spatial and temporal scales. As a result, the outcome and total variability of an observable will be far from what could be generated by a simple linear additive superposition principle (Demaeyer & Vannitsem, 2018; X. Liu & Ridley, 2015; Nicolis & Nicolis, 1981). Sydney Chapman was the first to categorize the atmosphere into different regions depending on the temperature gradient and the inflection points. We will start with a brief introduction of the layers of the Earth's atmosphere.

1.1 Layers of the Earth's Atmosphere

The Earth's atmosphere is an extremely thin sheet of gas with a thickness of approximately 100 km. In comparison, the radius of the Earth is ∼6371 km. It is primarily composed of 78% N_2, and 21% O_2 and the density decreases exponentially with height. Most of the Earth's atmosphere is confined near the surface because of gravity. This is the reason why breathing is difficult at higher elevations and why airplanes are pressurized. The temperature structure is determined by the equilibrium between the heating mechanisms (solar UV absorption, chemical heating) and the cooling processes (conduction, radiative cooling). Along with the neutral gases, the upper atmosphere also has ions and electrons. This weakly ionized part of the atmosphere is called the ionosphere. The left illustration in Figure 1.1 shows the approximate location and temperature (in Kelvin) of each atmospheric layer. The illustration on the right shows the electron density in the ionosphere.

- The region closest to the surface of the Earth, in which we live, is called the troposphere. It extends till about 10-12 km above sea level, with temperature decreasing with altitude and is marked by turbulent weather phenomena and cloud formations. The surface of the Earth absorbs shortwave radiation from the Sun and radiates back longwave IR radiation. For perspective, the top of Mount Everest is at ∼9 km.

- The region extending from ∼12-50 km is called the stratosphere. The temperature in this region increases with height. It is marked by the presence of ozone which plays an important role in increasing its temperature, as it absorbs (and is heated by) the Sun's ultraviolet radiation. The famous ozone hole in Antarctica was a result of increased human-generated chlorofluorocarbons that caused depletion of ozone layer in this region. Commercial airplanes fly in this

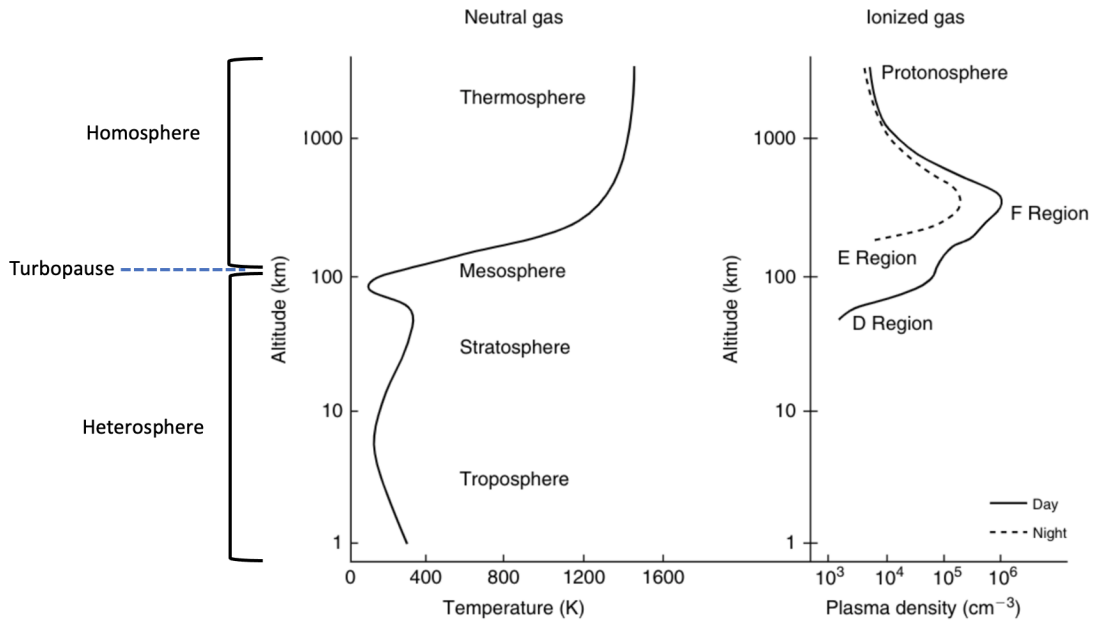

Figure 1.1: Typical profiles of neutral atmosphere temperature and ionospheric plasma density with the various layers designated. From Kelley (2009).

region because of lower turbulence and drag as compared to the troposphere. This region is studied primarily using weather balloons and aircrafts.

- The region from ∼50-100 km is called the mesosphere. Here, the air temperature decreases with height, reaching a minimum at the summer mesopause (down to ∼-90°C), making it the coldest region in the terrestrial atmosphere. It is marked by the formation of noctilucent or polar mesospheric clouds and the vaporization of meteors. This is a difficult region to study because the density is too low for normal aircrafts and weather balloons to reach and too high for satellites to orbit. Sounding rockets and ground/space-based remote sensing are the most common techniques to study this region. The air pressure at the bottom of mesosphere is below 1% of the pressure at sea level. The stratosphere and mesosphere together are usually referred to as the middle atmosphere.

- The region between 100-600 km is called the thermosphere. It is warmest region in the Earth's atmosphere because of the absorption of high energy X-rays and EUV radiation from the Sun, accompanied by relatively inefficient cooling mechanisms. This is the primary region that this thesis focuses on. Because of its low density, it is the region where the low earth orbiting satellites and

the international space station (∼400 km altitude) orbit. The region between 60-100 km is usually collectively referred to as the Mesosphere and the Lower Thermosphere (MLT) and is an important region for understanding the coupling of the lower atmosphere with the thermosphere. The region below 100 km is well mixed via turbulence and is referred to as the homosphere. The region above this altitude is called the heterosphere, as different neutral gases separate according to their mass. The transition region is called the turbopause and it marks the beginning of space.

- Embedded within the thermosphere is the ionosphere which is the weakly ionized part of the Earth's atmosphere. Solar EUV radiation with wavelength less than ∼100 nm has enough energy to free the electrons from atomic and molecular oxygen and nitrogen resulting in ionization. The ions and electrons react to the electric and magnetic fields while also interacting with the neutral gases of the thermosphere, making the dynamics of this region quite complex. The temperature of the thermosphere is also determined by the exchange of energy between ions and neutrals. Both thermosphere and ionosphere are strongly influenced by variations in solar EUV radiation and the Sun's magnetic activity, along with the perturbations in densities, temperature, and winds propagating up from the lower atmosphere. The ionosphere and thermosphere (IT) are usually referred to as the upper atmosphere.

- Above 600 km is the exosphere, in which neutral particles can escape the Earth's gravitational field. This is because collisions are rare (increasing the mean free path) and the atoms and molecules move in ballistic trajectories, no longer behaving as a continuum fluid. Because of low collisions, individual particles gain energy from the absorption of solar EUV photons. The main constituents at these heights are hydrogen and helium. Neutral hydrogen scatters the far ultraviolet radiation from the Sun resulting in a faint glow in this region, which is usually referred to as the geocorona and can be imaged from space-based detectors. The exosphere is typically considered the top of the neutral atmosphere and eventually leads into the outer space.

These layers do not exist in isolation, but interact vertically with each other via various non-linear mechanisms. One example of such an interaction is the cooling of the Earth's upper atmosphere due to the increase in carbon dioxide in the lower atmosphere over the past several decades (J. T. Emmert et al., 2012; Keating et al., 2000; Rishbeth & Roble, 1992; R. G. Roble & Dickinson, 1989).

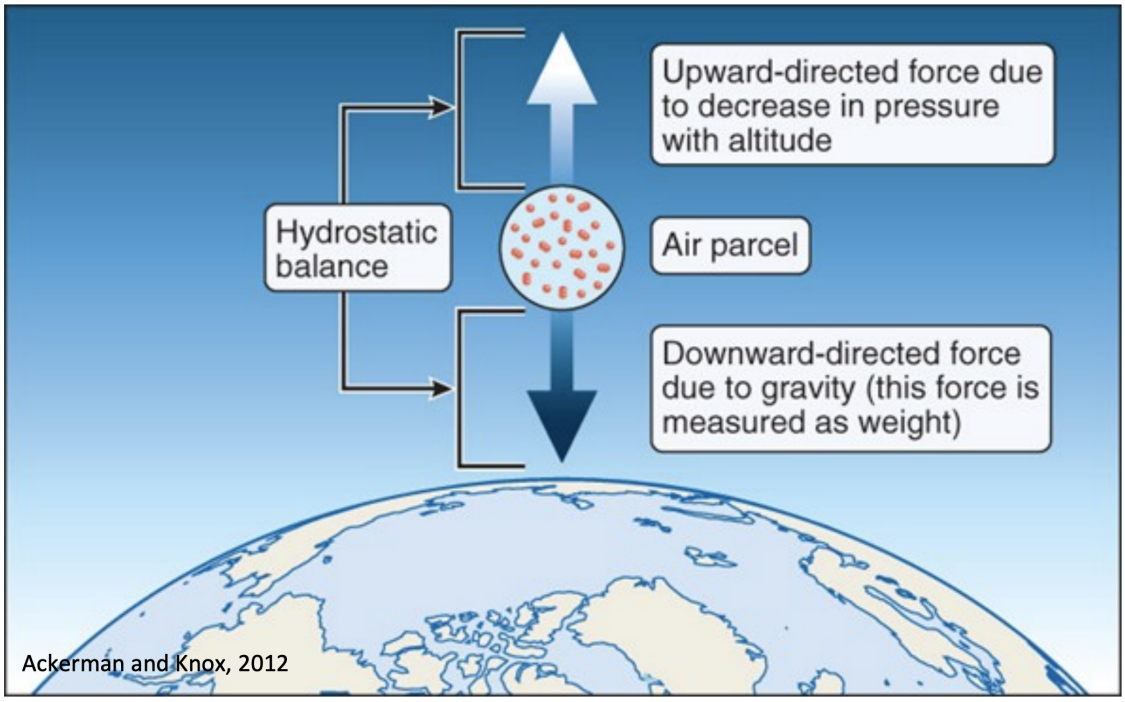

Figure 1.2: Illustration of hydrostatic equilibrium in the atmosphere.

1.2 Hydrostatic Equilibrium

The Earth's atmosphere is a fluid and, similar to oceans, the pressure at the bottom of the fluid column is larger than the pressure near the top of the column, leading to an upward pressure gradient force which is balanced by the downward gravitational force. This is called as the hydrostatic equilibrium and is responsible for the horizontally stratified atmospheres, such as of the planets and the Sun. Mathematically, it can be described as follows :

$$\nabla p + \rho g = 0 \tag{1.1}$$

where p is the pressure of the atmosphere, ρ is the total neutral mass density and g is the acceleration due to gravity, which points vertically downwards (-z). As a result, the equation becomes,

$$\frac{\partial p}{\partial z} = -\rho g \tag{1.2}$$

This force balance is also illustrated in Figure 1.2. Using the ideal gas law, we know, $p = \rho RT$. Here, R is the gas constant and T is the neutral temperature.

$$\frac{\partial p}{\partial z} = -\frac{g}{RT} p \tag{1.3}$$

This equation can be integrated as follows

$$p(z) = p_0 exp\left[-\int_{z_0}^{z} \frac{g(z')dz'}{RT(z')}\right] \tag{1.4}$$

where z_0 is the reference height. As a result, pressure for any altitude, z can be written as where

$$p(z) = p_0 exp\left[-\int_{z_0}^{z} \frac{dz'}{H(z')}\right] \tag{1.5}$$

Therefore, for an isothermal atmosphere with constant T and g, this hydrostatic equation can be written as

$$p(z) = p_0 e^{-(z-z_0)/H} \tag{1.6}$$

where

$$H(z) = \frac{RT}{g} = \frac{k_B T}{mg} \tag{1.7}$$

where k_B is the Boltzmann constant, and m is the mass of the neutral gas. Here, H is referred to as the scale height of the atmosphere and is defined as the vertical distance over which the density of a neutral gas drops by exp^{-1} or $\sim 1/2.7$. In the lower thermosphere, H is approximately 10 km, and it rises to $\sim$50 km in the upper thermosphere due to higher temperature and lower mean mass and gravity.

1.3 Periodic Variations in the Earth's Atmosphere

The atmosphere of the Earth exhibits variability in its physical properties (density, temperature, pressure) that span large spatial and temporal scales. These variations are ubiquitous and are both turbulent and periodic in nature. An example of a long term periodic oscillation would be periodic variation in the heating of stratosphere due to changes in UV radiation due to the 11-year solar cycle. The primary forces in the lower atmosphere of the Earth are the Coriolis force, (which arises from the rotation of the planet), centrifugal force, pressure gradient force, and gravity. At higher altitudes, in the thermosphere, ion-neutral frictional force also become significant at high latitudes. Any imbalance in these forces can lead to periodic oscillations that can propagate in space and time.

Atmospheric tides are oscillations of much shorter period as compared to the periodic variation due to the solar cycle. These can be understood to be similar to the ocean tides that have a repeating nature because of the gravitational force between

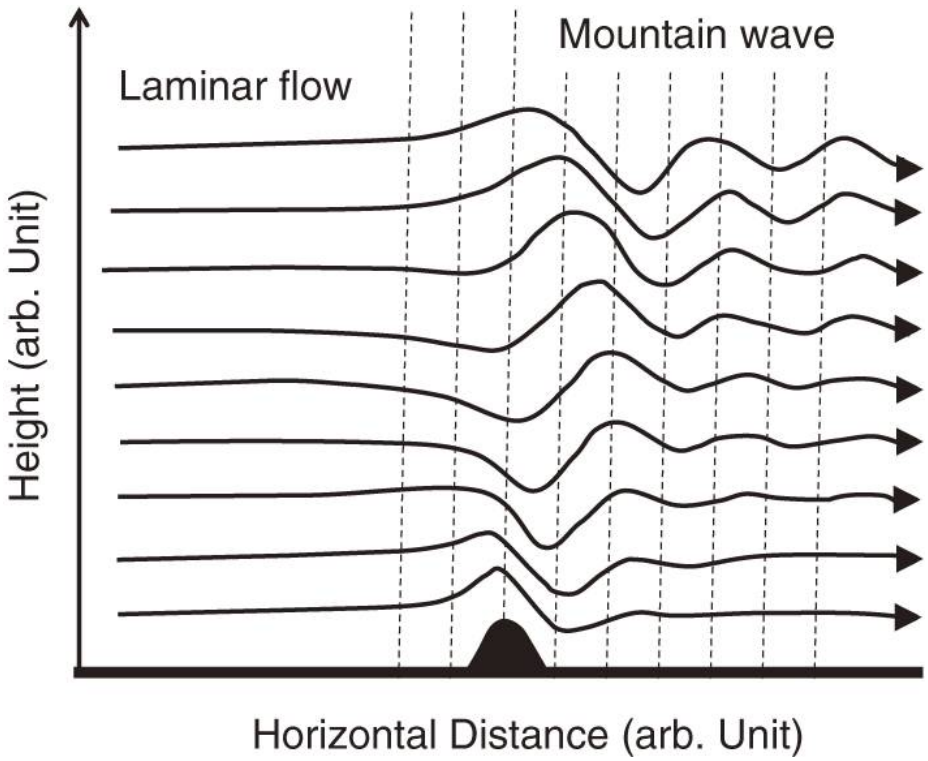

Figure 1.3: Generation of mountain (orographic) waves by the interaction of stably stratified air flow with topography. From Tsuda (2014)

the moon and the Earth. The atmospheric tides with the largest amplitude are the thermal tides (lunar tides have smaller amplitude) that are generated because of solar heating. These include diurnal tides with a period of 24 hours and its harmonics (12, 8, 6, etc. hours). They are generated in both the lower and upper atmosphere of the Earth when the neutral gases absorb the periodically varying heat from the Sun. These are called migrating tides as they appear to move westward to an observer on the ground, synchronizing with the motion of the Sun. Similar to a mechanical oscillator, these waves can be understood to be generated from a time varying thermal source oscillating with a regular period (Fritts & Alexander, 2003).

The non-migrating tides on the other hand are generated because of topography of the Earth, land-sea contrast, or latent heat release due to deep convection in the tropics. Another type of atmospheric waves are the global scale planetary waves which have periods that can range from a few days to a few weeks and are generated by the imbalance between temperature gradient (between equator and poles) and the Coriolis force. In addition, stationary planetary waves are generated by topography of the Earth, e.g., the land-sea contrast, large scale features such as the Rockies and Himalayas. These waves are known for breaking winter stratospheric polar vortex,

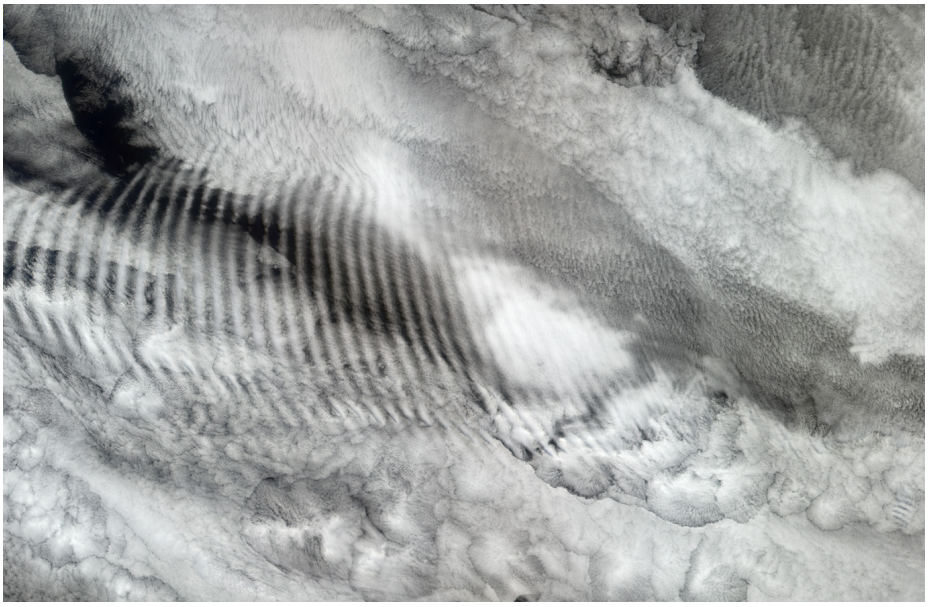

Figure 1.4: A natural-color image from the Multi-angle Imaging SpectroRadiometer (MISR), centered over the Indian Ocean, and acquired on October 29, 2003. Image courtesy NASA/GSFC/LaRC/JPL, MISR Team.

and thus bringing periods of extreme cold weather over the continental USA. Both tides and planetary waves propagate away from their source regions horizontally and vertically, thus playing an important role in the coupling of different layers of the Earth's atmosphere. They can be a significant source of day-to-day variability in the IT system during geomagnetic quiet times.

Gravity waves are waves in the Earth's atmosphere with gravity as the restoring force (also observed in oceans). They have horizontal wavelengths ranging between few tens and few thousands of kilometers and a vertical wavelength of several kilometers (Tsuda, 2014). Their period varies from several minutes to about one day. They are generated via various mechanisms such as topology, convective activity, and thunderstorms in the troposphere and stratosphere. The generation of gravity waves can be understood via air parcel model. In a static equilibrium in the Earth's atmosphere, an air parcel has gravity and buoyancy of the air acting on it in the downward and upward direction, respectively. If an external force is applied to an air parcel in static equilibrium, it will accelerate in the direction of perturbation. If the parcel propagates up to regions of lower density, the buoyancy around it decreases. This causes the parcel to eventually decelerate due to the opposing force of gravity until it stops and starts to move downward again. As the parcel moves downward, the buoyancy around it slowly increases. The parcel will overshoot its initial position eventually

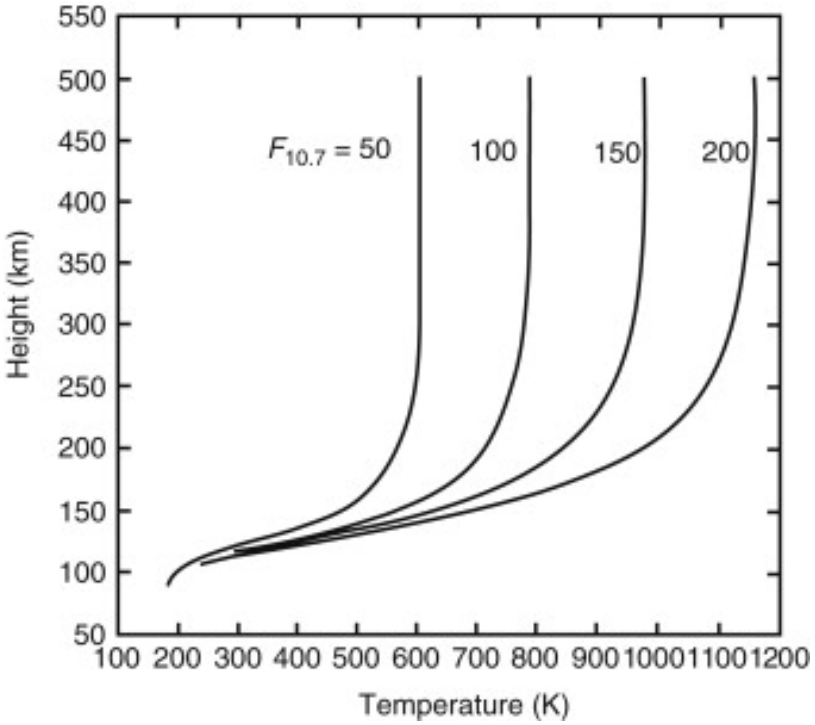

Figure 1.5: Global mean neutral gas temperature vertical profiles as a function of the solar decimeter radio emission at 10.7 cm wavelength (F10.7). The solar decimeter radio emission F10.7 (in units of 10^{-22} Wm^{-2} Hz^{-1}) is an indicator of the solar EUV radiative output. From Solomon & Roble (2015).

reversing its direction again when buoyancy exceeds gravity. Thus, a vertical oscillation is generated that can propagate away from the source region, generating a wave. Figure 1.3 shows an illustration of generation of gravity waves over mountains. When the air encounters a mountain range, it is lifted over the mountain and oscillations are generated on the leeward side of the mountain (Gossard & Hooke, 1975; Tsuda, 2014). Figure 1.4 shows an image of gravity waves in stratocumulus cellular clouds and can be visualized to be similar to ripples that occur when a stone is thrown into a water body. Both tides and gravity waves play an important role in vertically coupling the lower atmosphere with the IT region.

1.4 Thermosphere and Ionosphere

1.4.1 Thermal Structure and Composition

The temperature of the thermosphere is highly variable and depends on a number of physical and chemical processes. The primary heating mechanisms are absorption of the UV radiation by O_2, chemical heating by ion-neutral and neutral-neutral re-

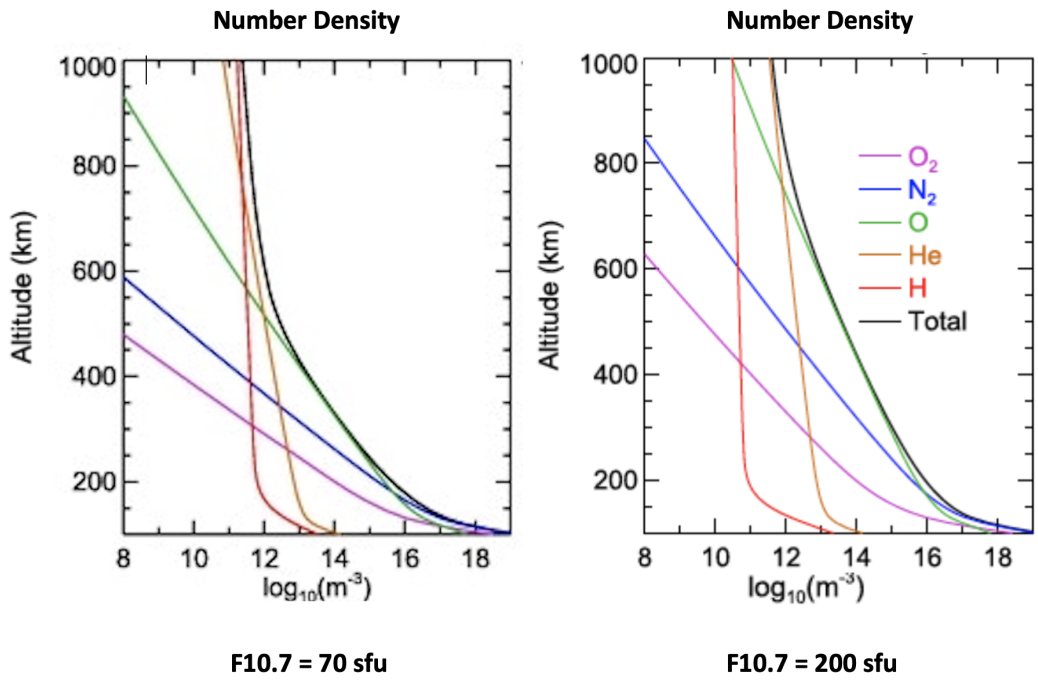

Figure 1.6: Global average number density profiles at solar min (F10.7=70 sfu) and solar max (F10.7=200 sfu) conditions from NRLMSISE-00 empirical model. From J. Emmert (2015).

actions, quenching of metastable species, recombination of atomic oxygen (O), Joule heating by dissipation of ionospheric currents, heating by photoelectrons and auroral electrons, exchange of heat with ions and electrons via elastic and inelastic collisions, and dissipation of tides and gravity waves from the lower atmosphere. The cooling mechanisms include infrared radiations from NO via 5.3μm, CO_2 via 15μm, and O via 63μm (R. G. Roble, 1995; Mlynczak et al., 2010). Other major cooling mechanisms include downward heat conduction via molecular conduction and turbulent (eddy) conduction into the lower layers of the atmosphere. The time rate of change of temperature is determined by the dynamic balance between these mechanisms. Figure 1.5 shows the variation of global mean temperature of the thermosphere as a function of solar activity. The temperature almost doubles between solar minimum (F10.7=50 sfu) and maximum (F10.7=200 sfu) conditions. Apart from this longer-term variation, shorter-term variability due to space weather events is also observed.

The thermospheric composition is governed by chemical sources and sinks, dynamics, and by molecular and eddy diffusion. The energy for solar UV radiation between 130-175 nm is sufficient to dissociate molecular species such as O_2 and N_2 into atomic species of O and atomic nitrogen (N), respectively. Figure 1.6 shows the

globally averaged composition of the thermosphere with height for solar minimum and maximum conditions. Above 100 km, due to the lack of turbulent mixing, the constituent species stratify according to their mass and follow individual hydrostatic profiles. Because of its larger mass, N_2 decreases much faster with altitude (smaller scale height, see equation 1.7) as compared to other species. Similar to the lower atmosphere, N_2 continues to be the major species in the lower thermosphere until 200 km. Between 200 and 500-800 km, depending on F10.7, O becomes the dominant species, above which He and H dominate. During solar maximum, the temperature of the thermosphere increases which increases the scale height of the constituent species, resulting in slower decrease with height. This results in overall upwelling of the thermospheric and ionospheric densities, leading to high drag on the satellites in the upper thermosphere. The total density at any height in the thermosphere is thus dependent on both the underlying composition and temperature.

Since O is the major species above 200 km, any changes in the lower thermospheric O density persist to higher altitudes via diffusive equilibrium. Figure 1.7 shows the lifetime of O as a function of altitude. Below about 100 km, O is chemically active and has a shorter lifetime. Above this altitude, the lifetime of O increases to several months, making it susceptible to the transport by winds in the thermosphere. This is discussed in detail in the next section.

1.4.2 Thermospheric Circulation

The atmosphere of the Earth responds to different forces via movement of constituent species, resulting in winds. Similar to the winds in the lower atmosphere and troposphere, the pressure gradient force and Coriolis force affects the motion of neutral gases in the upper thermosphere. However, there are additional forces that are added to the equation of motion in the upper atmosphere. These include viscosity and ion drag. Kinematic viscosity increases exponentially with altitude because of decreasing density and plays an important role in smoothing out vertical gradients in wind velocity. The viscosity in the thermosphere is large enough such that any turbulent structures in the neutral atmosphere are effectively dissipated. Ion Drag is a frictional force because of the collisions between the neutrals and ions and is proportional to the difference in their velocity. At high latitudes, the ions tend to work to speed up the neutrals, while at middle and lower latitudes, the ions are tied to relatively stationary magnetic field lines, and the neutrals are slowed down.

During quiet times, the primary heating source in the thermosphere is the solar UV and EUV radiation which causes variations in temperature with local time and

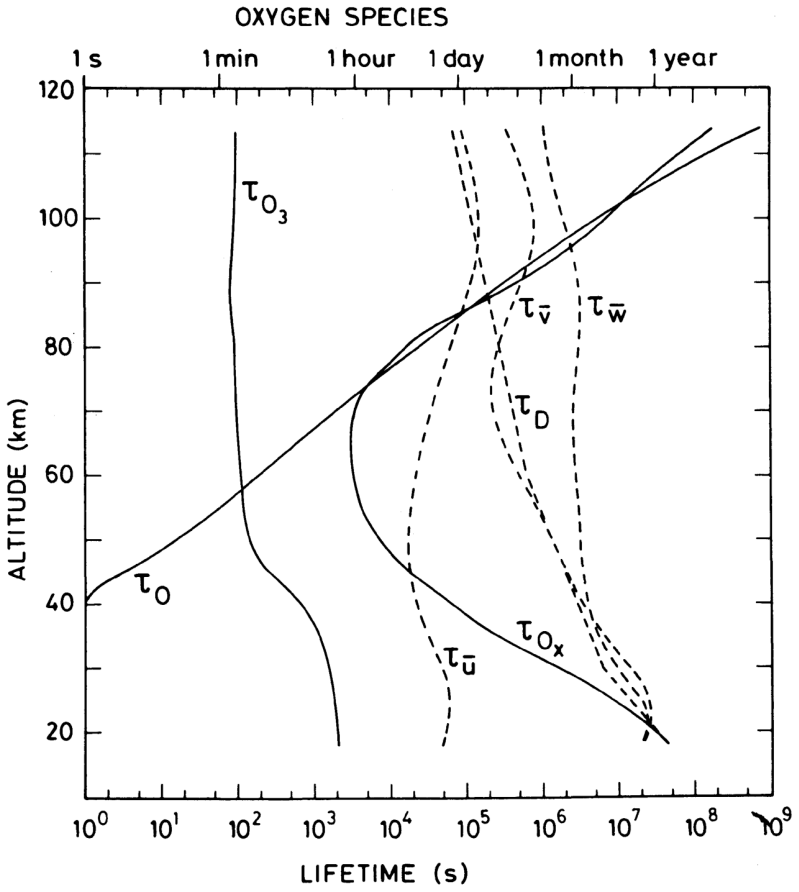

Figure 1.7: Photochemical lifetimes of O_3, O, O_x (odd oxygen family), and characteristic transport lifetimes. τ_D represents the one-dimensional vertical diffusive lifetime, assuming a vertical scale height of 5 km. $\tau_{\overline{u}}$, $\tau_{\overline{v}}$, $\tau_{\overline{w}}$ represent the time constants for transports by the zonal, meridional, and vertical winds at middle latitudes, assuming characteristic scales of 1000, 1000, and 5 km, respectively. From Brasseur & Solomon (1984).

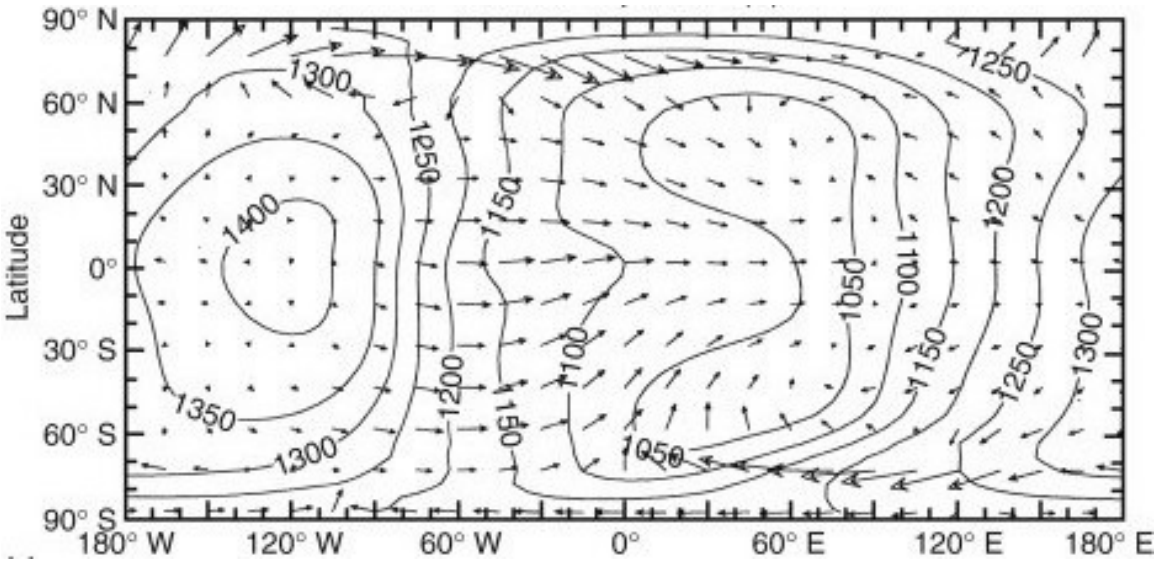

Figure 1.8: A calculation of temperature in degrees Kelvin (contours) and wind vectors (arrows) in the upper thermosphere near 300 km altitude, for solar medium conditions (F10.7 = 150). The temperature and wind structure are shown for 0 UTC. The length of the maximum wind vectors represents 450 m/s. From Solomon & Roble (2015).

latitude. The first order of heating rate difference is between dayside and nightside, also called as the thermospheric diurnal tide (24 hour period). As a result, large temperatures are observed at lower latitudes and on the dayside. This causes the dayside thermosphere to expand, creating day-night pressure gradients. At low- to mid-latitudes in the upper thermosphere, the ion-drag and viscous forces balance the pressure gradient forces, resulting in winds that blow from dayside to nightside. This is illustrated in Figure 1.8. In the lower thermosphere, the ion drag is larger and the neutral density is significantly larger, resulting in a much more complicated wind circulation pattern, that is also driven by the lower atmospheric tides and perturbations.

Similarly, the thermosphere has gradients in temperature that occur on much larger temporal and spatial scales; temperatures are larger in the summer hemisphere as compared to the winter hemisphere during both December and June solstice. This causes a large pressure gradient, which subsequently drives meridional circulation from summer to winter, as illustrated in Figure 1.9. This horizontal wind circulation is accompanied by upwelling (vertically up) in summer and downwelling (vertically down) in the winter thermosphere. The upwelling in summer results in N_2 rich air blowing up, increasing the concentration of N_2 in the thermosphere in the summer hemisphere, while the opposite happens in the winter hemisphere, where [O] rich air

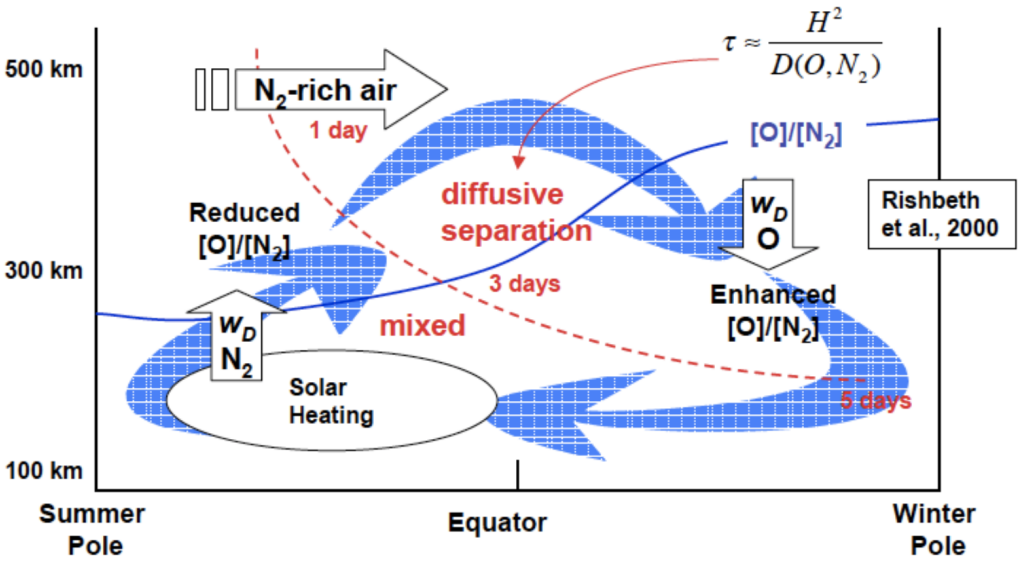

Figure 1.9: Meridional and Vertical circulation in the thermosphere.

from higher altitudes blows to lower altitudes, increasing its concentration in lower-middle thermosphere. The summer to winter winds also lead to meridional transport of [O] from summer to the winter hemisphere. As a result, between 140-300 km, larger [O] is observed in the winter hemisphere causing the winter ionosphere to have a larger F-region density than the summer hemisphere as explained below. A similar trend is also observed for other light species, such as Helium. Hence, during solstices, the thermospheric circulation is driven by atmospheric thermodynamics, i.e., the circulation moves energy and therefore mass from the summer pole to the winter pole (Jones Jr., Emmert, et al., 2018). This is accompanied by weak return flow in the MLT from the winter pole to the summer pole between the altitudes of 90-110 km (Qian et al., 2017).

The integrated O/N_2 is an important geophysical quantity that is used in the space science community to interpret the composition of the thermosphere. It is defined as the ratio of integrated O to N_2 column densities, from the top of the atmosphere downward until the altitude where the N_2 column integrated density reaches 10^{21} m^{-2} (Strickland et al., 1995). It represents the ratio of the sources ([O]) to losses ([N_2]) for the F-region in the ionospheric chemistry. When this ratio is low, the ionospheric density will decrease, while when it is high, the density will increase. Because of the above mentioned meridional circulation, larger O/N_2 is observed in the winter hemisphere (between 140-300 km).

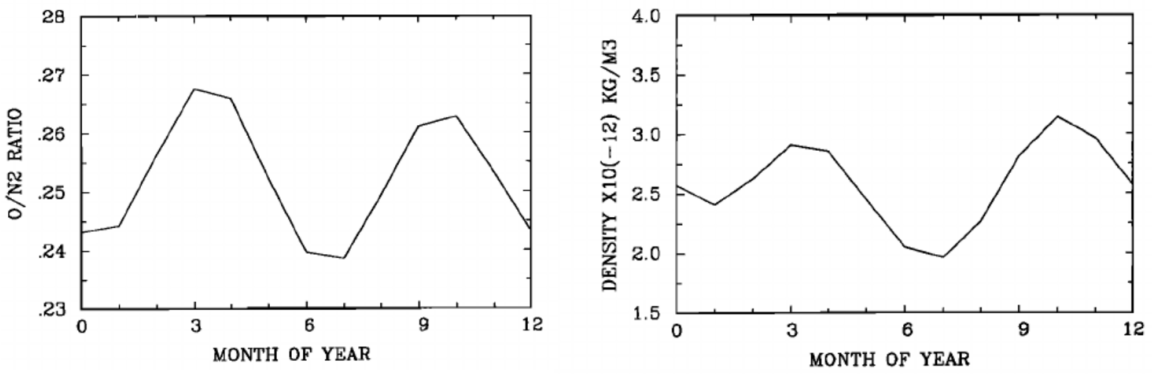

Figure 1.10: Globally averaged O/N_2 (left panel) and neutral mass density at 400 km, from the empirical model, MSIS (Hedin, 1987), at a fixed Ap of 5 and F10.7 of 125. From T. J. Fuller-Rowell (1998).

1.4.3 Thermospheric Intra-Annual Variations Semiannual Oscillation

The thermospheric and ionospheric semiannual oscillation (T-I SAO) is a variation with a period of 6 months that was first observed in the global neutral mass density of the thermosphere from satellite drag data (Paetzold & Zschörner, 1961) and has since been observed in the lower-middle thermosphere in global composition and temperature. The T-I SAO is characterized by maxima during equinoxes (March and September) and minima during solstices (June and December), and is illustrated in Figure 1.10. This variation has an amplitude of $\sim$15% in mass density at 400 km (Jones Jr., Emmert, et al., 2018). Similar variations were observed in the ionospheric electron density because the thermospheric neutral composition balances the chemical sources and losses for the ionospheric electron density (Rishbeth et al., 2000). Since the solar UV and EUV radiation is the primary source of large-scale T-I variations, the semiannual variation in the geomagnetic activity was initially believed to be the primary source of the T-I SAO (Paetzold & Zschörner, 1961; C. T. Russell & McPherron, 1973; Walterscheid, 1982). However, the variation in global temperature due to geomagnetic activity was too weak to explain the amplitude of T-I SAO (G. Cook & Scott, 1966; G. Cook, 1967). Another mechanism was later proposed to explain this variation via internal thermospheric circulation discussed in the previous section. The large-scale vertical (upwelling in summer and downwelling in winter) and meridional (summer-to-winter) wind circulation, causes the thermosphere to be well mixed during solstices. It acts as a global-scale 'turbulent eddy' that causes the molecular species to have a net upward flux into the thermosphere and atomic species to have a net downward flux (Mayr & Volland, 1972; Mayr et al., 1978; T. J. Fuller-Rowell,

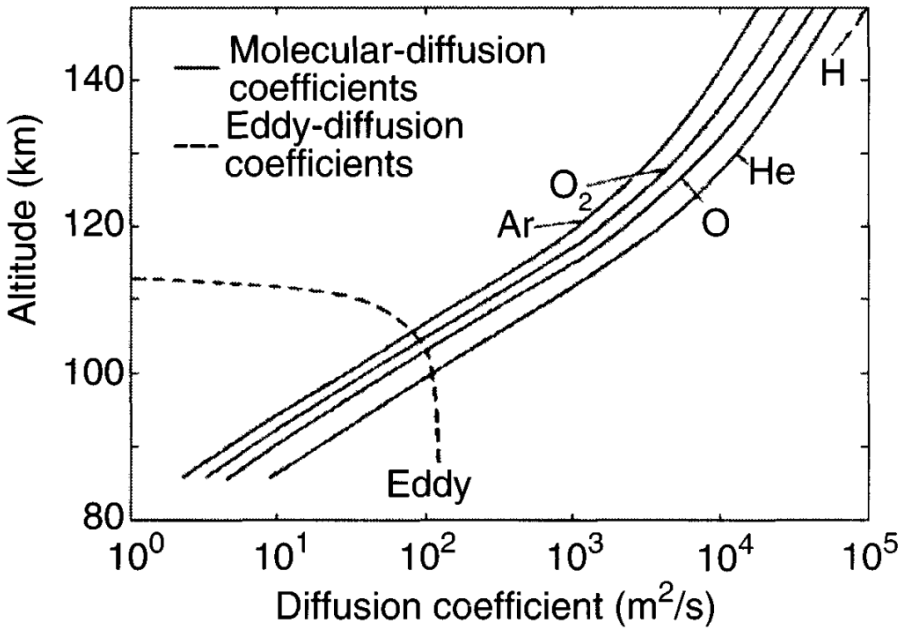

Figure 1.11: Estimated eddy diffusion coefficient along with molecular diffusion coefficient for some selected species. From Gombosi (1998) and Richmond (1983)

1998). This causes the mean molecular mass of the thermosphere to increase (N_2 has mass of 28 amu and O has mass of 16 amu). According to Equation 1.7, this results in lowering of density scale height, thereby forcing an SAO with minima during solstices relative to equinoxes. This circulation is also usually referred to as the thermospheric spoon mechanism (T. J. Fuller-Rowell, 1998).

1.4.4 Vertical coupling of Thermosphere and Ionosphere

As discussed previously, the temperature structure of the Earth's atmosphere depends greatly on the incoming radiation from the Sun. Apart from the radiation, the solar wind, which is a plasma of primarily energetic protons, electrons and alpha particles embedded with a magnetic field from the Sun, constantly bombard the Earth's magnetosphere. The wind interacts with the magnetic field of the Earth resulting in the deposition (precipitation) of energetic electrons and protons into the high latitude IT region. These particles collide with the thermospheric neutrals to cause ionization, dissociation and heating, which can be observed as airglow and the aurora. In addition, the precipitation is accompanied by strong ion drifts, driving collisions between the ions and neutrals. This results in heating of the thermosphere at high latitudes, and thus the upwelling of the neutral gas (scale height increases, see equation 1.7).

Figure 1.12: Photograph of a sodium vapor trail released from a sounding rocket showing the transition from a turbulent to a diffusive region. From Gombosi (1998)

Apart from the driving from above (i.e., the magnetosphere and solar EUV), the IT region is also driven by the perturbations from the lower atmosphere (e.g., Hagan & Forbes, 2002; Immel et al., 2006; Malhotra et al., 2016). The coupling of the IT region with the lower atmosphere is most significant below ∼150 km. However, changes in the lower thermosphere affect higher altitudes because of diffusion. As discussed above, tides and gravity waves propagate vertically and horizontally away from their source regions. As they propagate up, their amplitude increases exponentially due to decreasing atmospheric density (conservation of energy), such that the waves that start with amplitudes of few centimeters per second in the troposphere attain amplitudes of up to tens of meters per second at heights of 70 km and above. This can lead to instabilities resulting in the loss of energy and momentum, referred to as wave breaking. As they break, they deposit their momentum and energy into the background atmosphere. One of the most prominent examples of gravity wave effects is the cold summer mesopause which is the coldest region in the Earth's atmosphere. The gravity wave breaking in the mesosphere reverses the zonal winds, which under the Coriolis force, induces an interhemispheric summer-to-winter circulation. This is accompanied by upwelling and cooling (via adiabatic expansion) in the summer and warming (via adiabatic compression) in the winter. The breaking altitude is commonly in the MLT region and is dependent on the background wind and temperature conditions. These instabilities by a spectrum of waves can cause turbulence.

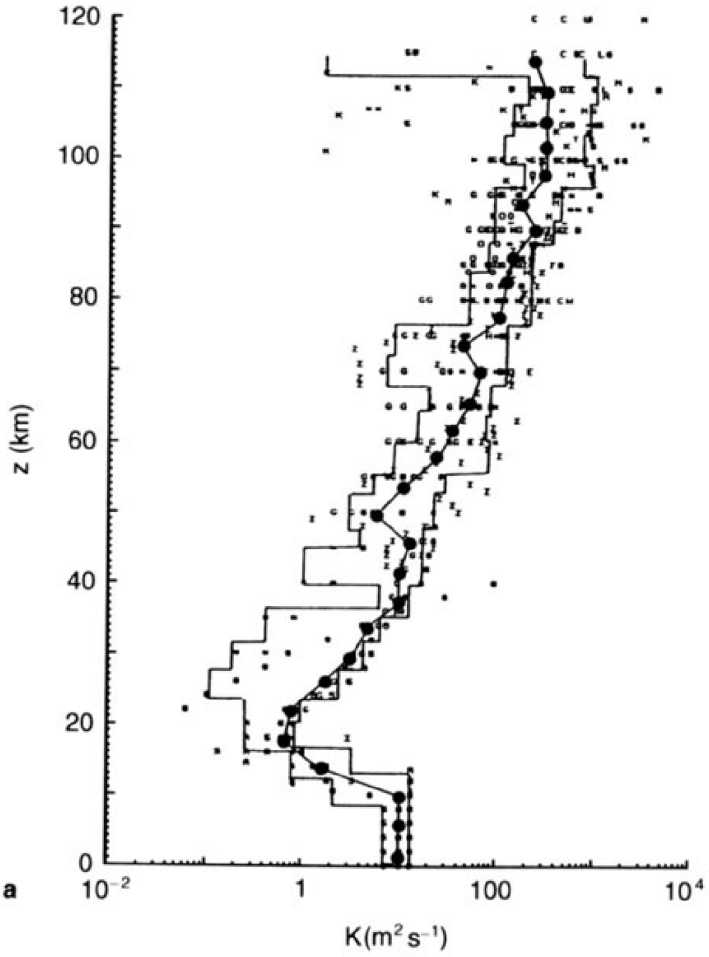

Figure 1.13: Collective of all K_{zz} profiles from all relevant references in Table 2 of Dieminger et al. (1996). No distinction has been made concerning latitude and season.

Turbulent patches can be understood to be similar to whitecaps that appear on the ocean surface from breaking of waves. The gravity waves are the primary drivers of the turbulence as the wind shears and temperature gradients induced by tides are generally too weak to lead to instabilities, however not negligible (Hodges Jr., 1967). The gravity waves also interact with each other and the background atmosphere resulting in complex non-linear interactions. Below, the discussion focuses around the turbulence due to gravity waves as this will be the main subject of Chapter 5.

Turbulence is important in the MLT region of 90-110 km (Dieminger et al., 1996; Hocking, 1990) as above this altitude, the atmosphere becomes too viscous to support turbulence. It can affect the background atmosphere primarily via : a) mixing and

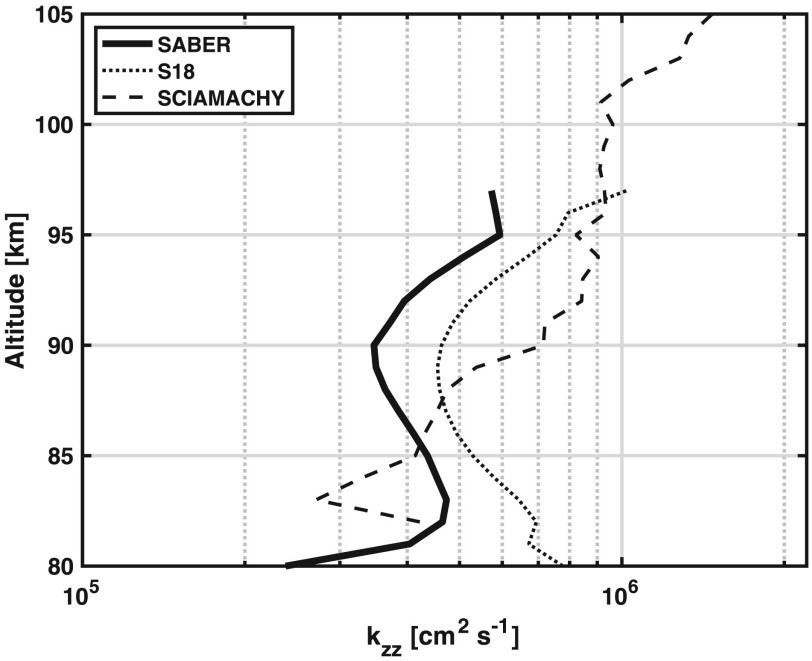

Figure 1.14: Estimated K_{zz} from SABER and SCIAMACHY instruments. S18 represents G. Swenson et al. (2018). (From G. R. Swenson et al. (2019)). Note 10^4 difference from Figure 1.13 due to different units.

diffusion of constituents, b) diffusion of heat and momentum, c) heating because of wave dissipation. There is evidence that the diffusion of heat in the thermosphere is larger than the heating due to wave dissipation which results in net cooling effect (Yigit & Medvedev, 2009). Because the turbulence acts on such small and varied scales, it is too small and computational expensive for models to capture, and therefore, it has to be parameterized in the different equations. This is typically done through a vertical momentum diffusion coefficient, also called as the eddy diffusion coefficient (K_{zz}) near the lower boundary of IT models (96-100 km) (in the equation of motion) and the heat diffusion coefficient, K_m (in the energy equation). Under realistic atmospheric conditions, these parameters should not be the same and the ratio for molecular diffusion has been found to be around 0.7 in the lower atmosphere (Dieminger et al., 1996). Since the exact ratio for turbulent diffusion remain controversial in the MLT (Fritts & Dunkerton, 1985; R. R. Garcia et al., 2014; Hocking, 1990), we use the same value for these coefficients in this study. Hence, we will refer to both of these coefficients as K_{zz}. There is evidence that turbulence occurs in patches roughly 30-80% of the time (Zimmerman & Murphy, 1977). Therefore, even though turbulence is intermittent, it should create sufficient turbulent motion to maintain the average K_{zz} (Dieminger et al., 1996).

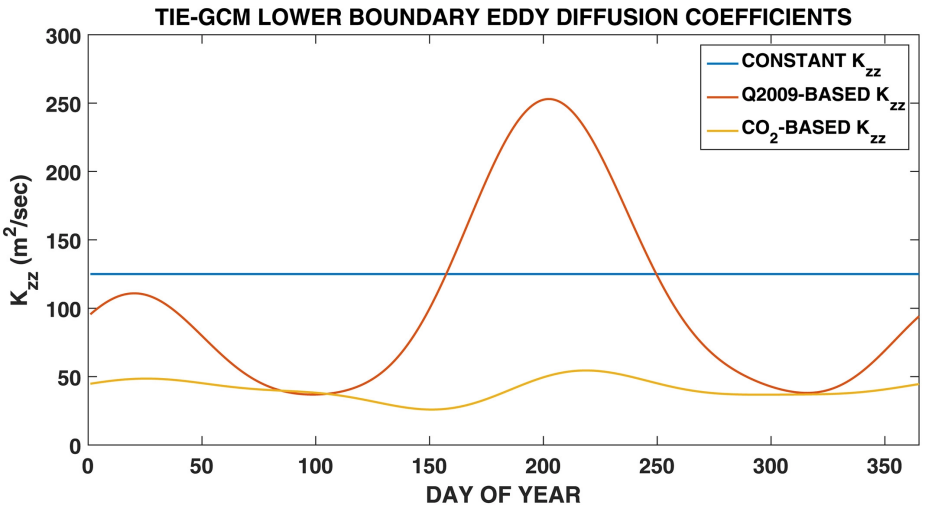

Figure 1.15: Seasonal variation of K_{zz} derived in two different studies. Q2009 represents Qian et al. (2009) and CO_2 based K_{zz} is from Salinas et al. (2016). (From Salinas et al. (2016))

K_{zz} is larger in the lower atmosphere, resulting in mixing and churning of air faster than what can be achieved by molecular diffusion. However, above 110 km, K_{zz} decreases while molecular diffusion increases, allowing molecular diffusion to dominate. These coefficients are illustrated in Figure 1.11. The transition region is the turbopause (also illustrated in Figure 1.1), above which the species in the IT region get separated by their mass. Figure 1.12 shows the photograph of a sodium vapor trail a sounding rocket and the transition from a turbulent to a diffusive regime of the atmosphere. This implies that until 100 km, the relative concentration of N_2 and O_2 in the atmosphere remains the same, 78% and 21%, respectively, decreasing with the same scale height. However, above this altitude regime, N_2 decreases much faster, resulting in a decrease in relative concentration of N_2.

Gravity waves of variety of periods, and amplitudes are also observed in the upper thermosphere, as traveling atmospheric and ionospheric disturbances (TADs and TIDs) (Miyoshi et al., 2018). They can either be internally generated in the thermosphere or be the result of direct penetration from the lower atmosphere. The effects of these propagating gravity waves in the thermosphere are not parameterized through K_{zz} at the lower boundary of IT models, and can be better estimated by an explicit gravity wave parameterization scheme (e.g., Yigit et al., 2008), and running the models in higher resolution. The global estimation of K_{zz} near the lower boundary of IT models is difficult, but local measurements from sounding rockets, incoherent scatter radars, meteor radars have been made. Figure 1.13 summarizes the values calculated

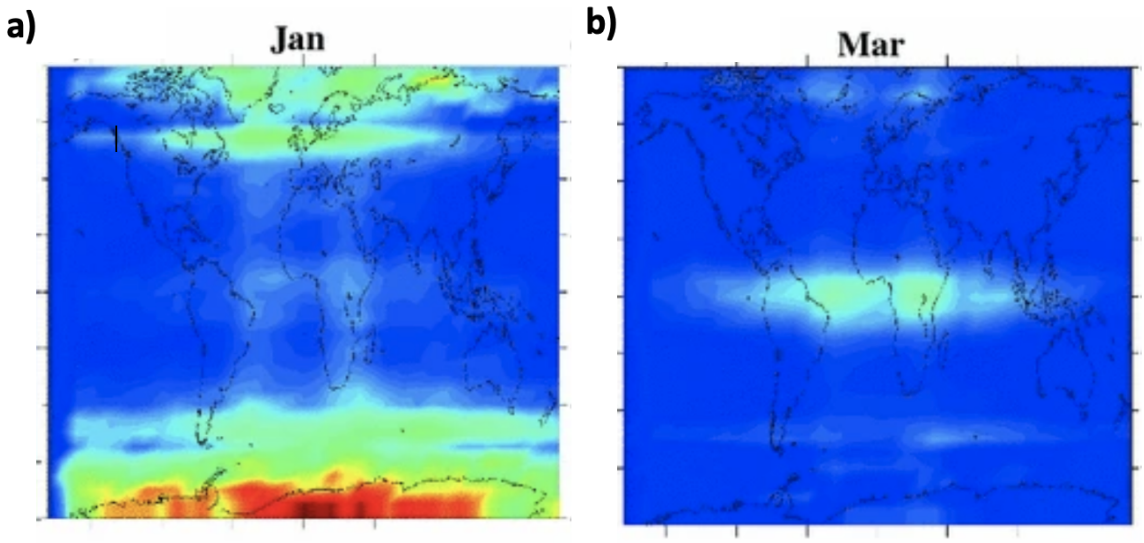

Figure 1.16: Global maps of gravity wave potential energies averaged in the 80-100 km using SABER data (2003-2007). From John & Kumar (2012)

from different studies (Dieminger et al., 1996). Recently, SABER instrument on the TIMED satellite has been used by G. R. Swenson et al. (2019) and Salinas et al. (2016) to find the globally averaged values of K_{zz}. Figure 1.14 shows the variation K_{zz} with height calculated by G. R. Swenson et al. (2019). Figure 1.15 shows the seasonal variation calculated by two different studies, from Salinas et al. (2016). These results show that globally averaged K_{zz} has a semiannual variation with larger values during solstices with the highest peak during northern summer. In the studies shown here, the average value is ∼50-100 m^2/s with significant variability. SABER data has also been used to study the spatial distribution of gravity wave activity in the MLT. Figure 1.16 shows the global map of gravity wave potential energies from John & Kumar (2012). During solstices, larger activity in summer high latitudes is observed, whereas during equinoxes, low latitudes show more wave activity (Preusse et al., 2009).

1.5 Outstanding Questions and Thesis Objectives

The focus of this thesis is to understand how the composition and turbulence in the lower atmosphere controls the upper atmosphere. As such, the major goal of this thesis is to answer the following questions:

- Since O is a minor species in the lower thermosphere but major above 200 km, does the O concentration in the MLT affect the upper thermospheric density,

temperature, and wind distributions? If so, what are the mechanisms that drive these changes?

- What are the primary processes through which the lower thermosphere drives the thermospheric and ionospheric semiannual oscillation (T-I SAO)? Does the long-term SAO depend on the MLT properties? Does a more realistic specification of the lower thermosphere composition and winds allow for a more accurate representation of the SAO?

- How does non-uniform mixing and diffusion in the MLT affect the thermospheric dynamics, composition and temperature? Is the effect of spatial variation of K_{zz} on the thermosphere different from using a globally uniform value of K_{zz}? Does using spatially varying K_{zz} improve the agreement of GITM with the data?

These questions are addressed by using the Global Ionosphere Thermosphere Model (GITM) and altering conditions near the bottom of the model to determine the effects on the rest of the domain.

1.6 Outline

The questions introduced in the previous section are investigated in the following chapters.

- The next chapter presents a brief overview of different models that are used for investigating the IT region. It also provides a brief overview of the models and datasets that are used in the following chapters of this thesis.

- In Chapter III the importance of MLT O on the IT region is investigated. This is interesting because satellite observations (Sounding of the Atmosphere using Broadband Emission Radiometry (SABER) instrument) show opposite latitudinal distribution of O in the MLT than previously thought, and the effects of this distribution on the upper atmosphere haven't received much attention. This is achieved by using a more accurate latitudinal distribution of O from the Whole Atmosphere Community Climate Model with thermosphere and ionosphere extension (WACCM-X) at the lower boundary of GITM and investigating the mechanisms through which this affects and improves the upper thermospheric state. This study is the first to use the improved specification of MLT [O]. It is found that the MLT [O] changes the upper thermospheric state through its effects on lower thermospheric dynamics and temperature.

- Chapter IV focuses on understanding how the MLT densities, temperature, and winds control the SAO in the IT region. GITM is used to investigate the amplitude and phase of SAO in the lower and upper thermosphere, for different lower boundary conditions, and when coupled with WACCM-X. It is found that the thermospheric spoon mechanism is the primary driver of T-I SAO. Using more realistic MLT specification from WACCM-X does not produce the right phase of T-I SAO, which hints towards a need to further improve the dynamics in the lower thermosphere.

- Chapter V aims at understanding the physical mechanisms through which non-uniform turbulent mixing in the MLT can change the IT state, as recent satellite observations have shown that the gravity wave activity has a latitudinal variation in the MLT region. This is achieved by introducing a spatial variation in the K_{zz} parameter in GITM. A sensitivity analysis is done for different seasons, K_{zz} values, and locations of the turbulent patch.

- Chapter VI concludes by summarizing all the findings and proposes several ideas for future work to improve IT modeling efforts and advance our understanding of vertical coupling mechanisms between Earth's lower and upper atmosphere.

- The Appendix at the end shows the results of my team project from the internship at NASA Frontier Development Lab program. This project aims at predicting the GNSS signal disturbances by using high resolution solar, magnetospheric and ionospheric data and employing supervised machine learning techniques.

CHAPTER II

Methodology

In the following chapters of this thesis, a combination of empirical models, physics-based models, and satellite observations are used. The physics-based models are used to primarily understand the physical mechanisms and the results are then validated using the empirical models and satellite observations. According to John von Neumann,

".. the sciences do not try to explain, they hardly even try to interpret, they mainly make models. By a model is meant a mathematical construct which, with the addition of certain verbal interpretations, describes observed phenomena. The justification of such a mathematical construct is solely and precisely that it is expected to work-that is, correctly to describe phenomena from a reasonably wide area."

The physics based (first-principles) models rely on solving equations that describe the behavior of the system via numerical methods. A simple example of such a model would be applying Newton's law of equations to find the acceleration of a body given the displacements with time as inputs. This means that numerical models need initial and boundary conditions, as well as drivers which can be provided based on empirical models, observational datasets or assumptions. Some of the physics-based models that have been widely used to study the Earth's upper atmosphere include the Global Ionosphere Thermosphere Model (GITM) (A. Ridley et al., 2006), NCAR Thermosphere Ionosphere Electrodynamics General Circulation Model (TIE-GCM), and the Thermosphere Ionosphere Mesosphere Electrodynamic General Circulation Model (TIME-GCM) (Dickinson et al., 1981, 1984).

Empirical modeling is a technique of modeling the behavior of a system based on the past experimental data and observations. Examples of upper atmospheric space weather empirical models are International Reference Ionosphere (IRI) (Bilitza, 2018), Horizontal Wind Model (HWM) (Drob et al., 2015), and NRLMSIS-00 (Picone et al., 2002). Empirical models are usually faster than the physics-based models and

represent nominal space weather conditions well, but lack accuracy during extreme and unusual events. With the advent of new satellite missions and large datasets, data assimilation techniques can be used in the physics-based models to improve their prediction accuracy, and are also becoming an integral part of space weather research (e.g., Eckermann et al., 2009; Siskind et al., 2014).

Machine learning (ML) algorithms have been widely used in the field of computer vision (Krizhevsky et al., 2017), fraud detection (Aleskerov et al., 1997), language translation (Cho et al., 2014), speech recognition (Hinton et al., 2012), and many others. In the last decade, some of the scientific disciplines such as astronomy, fluid dynamics, climate modeling have also utilized the capabilities of machine learning algorithms (e.g., George & Huerta, 2018; Kielty et al., 2018; Gagne II et al., 2020). The explosion of interest in the space weather community has happened recently (Camporeale, 2019). The applications that have received the most scrutiny are: forecast of geomagnetic indices, relativistic electrons at geosynchronous orbits, and solar eruptions (e.g., Bala et al., 2009; Fozzard et al., 1988; Fukata et al., 2002; Lethy et al., 2018; H. Wang et al., 2008; Wei et al., 2018; Wintoft et al., 2017). The advantage of machine learning models over that of first-principles space weather models is the speed and efficiency for forecasting applications, essentially due to large range of scales in space and time and thus enormous computational cost in the physics-based models (Camporeale, 2019).

As discussed in the previous chapter, the Ionosphere and Thermosphere (IT) is a tightly coupled complex system that has a range of inputs and drivers. Solving for and predicting the IT state is very relevant to modern day technologies, e.g., communication systems, interplanetary missions, tracking the position of satellites, and thus poses an ideal problem that can be solved by aforementioned techniques. We will start with a brief discussion of different IT models in the next section.

2.1 Ionosphere and Thermosphere Models

The earliest models that solved for the densities, momentum and energy of the thermosphere and ionosphere self-consistently were the Thermosphere General Circulation Models (TGCMs) (Dickinson et al., 1981, 1984). The TGCMs are three-dimensional codes with an empirical ionosphere that solve for mass mixing ratios of major neutral species O_2, N_2 and O and the minor species N(^2D), N(^4S), NO, He, and Ar. They use a pressure-based grid in the vertical direction, assuming hydrostatic equilibrium. They span the altitude domain of $\sim$95 to 600 km and did not include

2-way interaction with the ionosphere.

A self-consistent ionosphere was introduced in the Thermosphere Ionosphere General Circulation Model (TIGCM) (Roble et al., 1988), which solved for O^+ dynamics while assuming photochemical equilibrium for O_2^+, N_2^+, NO^+, and N^+. It was also coupled with other models for specifying auroral precipitation and high latitude electric fields (Roble & Ridley, 1987; Heelis et al., 1982). However, it did not solve for the electric fields generated as a result of neutral winds, also referred to as the ionospheric wind dynamo or low latitude electrodynamics, which was later included by (Richmond et al., 1992). The new model with a self-consistent low latitude electrodynamics, that cause the winds, currents and electric fields to interact is called the Thermosphere Ionosphere Electrodynamics General Circulation Model (TIE-GCM), and is used frequently to this day. This model was further extended into the mesosphere and upper stratosphere with added chemistry, CO_2 and OH, and called the Thermosphere Ionosphere Mesosphere Electrodynamics General Circulation Model (TIME-GCM) (Roble & Ridley, 1994). The lower boundaries of TIE-GCM and TIME-GCM are at 97 km and 30 km, respectively. The thermosphere ionosphere nested grid (TING) model was derived from the TIGCM but uses a nested grid within the grid cells for higher resolution in a small area (W. Wang et al., 1999, 2001). This helped in resolving small scale structures in the IT region.

Another model that has been widely used is the Coupled Thermosphere Ionosphere Model (CTIM) (T. J. Fuller-Rowell & Rees, 1980; Quegan et al., 1982; T. Fuller-Rowell & Rees, 1983; Rees & Fuller-Rowell, 1988, 1990; T. Fuller-Rowell et al., 1996). It is a three-dimensional model that solves for a self-consistent global thermosphere and a high latitude ionosphere, using solar, magnetospheric and tidal inputs. For the low-latitude ionosphere, it uses an empirical model by Chiu (1975). The thermospheric parameters are solved for in a Eulerian frame and the ionospheric parameters in a Lagrangian frame, and coupled together by interpolating the ion results on the thermospheric grid. This allows the ions to move along the field lines improving the mass flow between the opposite hemispheres. A newer version of this model that also includes the plasmasphere is called the Coupled Thermosphere Ionosphere Plasmasphere (CTIP). Along with a global thermosphere model, a high latitude ionosphere model, it also consists of a mid- and low-latitude ionosphere/plasmasphere model. The plasmasphere is modeled using individual flux tubes that are fixed in space and is based on the Bailey model (Bailey, 1983). Another improved version of this model is Coupled Thermosphere-Ionosphere-Plasmasphere electrodynamics (CTIPe) (Millward et al., 2001), which includes a self-consistent electrodynamics scheme for

low-latitude dynamo electric fields by Richmond et al. (1992). The Coupled Middle Atmosphere and Thermosphere (CMAT) general circulation model is built on top of the CTIP model extending down to 30 km in the mesosphere (Harris et al., 2002). A full chemical scheme for the mesosphere and thermosphere is included with gravity wave drag, and tidal forcing.

Another model that is widely used to model the ionosphere is SAMI3 (Sami3 is A Model of the Ionosphere) which is a three-dimensional physics-based model of the ionosphere, derived from an earlier two-dimensional version, SAMI2 (Huba et al., 2000). It spans a much larger altitude range, from 85 km to 20,000 km, and solves for seven ion species (H^+, He^+, N^+, O^+, N_2^+, NO^+, and O_2^+). The temperature equation is solved for three ion species (H^+, He^+, O^+) and for the electrons. The neutral composition for this model can be specified from both empirical models (e.g., NRLMSIS-00, HWM) or physics-based models (e.g., TIEGCM, TIMEGCM). It has a unique nonorthogonal, nonuniform, fixed grid with one axis that is aligned with the geomagnetic field of the Earth. It has recently been modified to import the thermospheric composition, temperature and winds from TIEGCM-ICON (Maute, 2017) to support the NASA Ionospheric Connection Explorer (ICON) mission (Huba et al., 2017)

One of the most widely used empirical models of the thermosphere is the Mass Spectrometer Incoherent Scatter Radar (MSIS) class of models. It outputs the neutral densities, mass density, and temperature and depends on the solar flux ($F_{10.7}$) and solar activity level (A_p) (Hedin, 1983, 1987, 1991; Picone et al., 2002; J. T. Emmert et al., 2020). The lower boundary for MSIS-86 is at 90 km (Hedin, 1987). This was improved in the later versions and extended from the surface to the exobase of the Earth. The version of MSIS that is used in the next two chapters is the NRLMSISE-00 (Picone et al., 2002). Similar to previous versions, it includes both ground-based and satellite data. It contains data from previous MSIS versions, such as from the incoherent scatter radars, mass spectrometer data, solar ultraviolet occultations, satellite drag measurements and satellite-borne accelerometer data. It also contains larger number of observations at high latitudes to improve the coverage of extreme geomagnetic storm events. For locations, geophysical conditions, and times not covered by the data, the model interpolates among and extrapolates the underlying data via fitting a set a parametric equations. In Chapter V, the newer version of MSIS, NRLMSIS 2.0 (J. T. Emmert et al., 2020) is used, which uses extensive new lower and middle atmosphere temperature, O, and H data, and thermospheric mass densities derived from satellite orbits.

2.1.1 GITM

In this section, a brief overview of another physics-based model, the Global Ionosphere Thermosphere Model (GITM) is provided, as this is the primary model used in the analyses in the next three chapters.

GITM is a 3D physics-based model that solves the Navier Stokes equations of continuity, momentum, and energy for the ionosphere and thermosphere of the Earth and was developed by A. Ridley et al. (2006). GITM is different from its predecessors because it uses an altitude-based grid in the vertical instead of using pressure coordinates. This allows for non-hydrostatic solutions and thus has the capability of representing the IT state in a more realistic way, especially when there are events that can cause sudden heating such as the aurora. The lower boundary of GITM is in the Mesosphere and the Lower Thermosphere (MLT) region at ∼97 km and the upper boundary is at ∼500 km. Depending on solar activity, because the vertical grid is defined depending on the scale height, the spacing increases with altitude, with it being less than 3 km in the lower thermosphere and over 10 km in the upper thermosphere. The resolution in the horizontal is flexible and can be changed by defining a higher number of grid cells in the latitudinal and longitudinal direction. GITM allows the decomposition of the domain into blocks and thus it can be run in a completely parallel configuration. It explicitly solves for the neutral densities O, O_2, N_2, N(^{2}D), N(^{2}P), N(^{4}S), NO, and He, and ion species, $O^+(^4S)$, $O^+(^2D)$, $O^+(^2P)$, O_2^+, N_2^+, NO^+, He^+, and N^+. All major neutral species have their own vertical velocity, but have the same velocity in the horizontal direction.

GITM is a flexible code and can be coupled with different models and datasets for inputs, initial condition and lower boundary. GITM is initialized using neutral densities and temperatures from MSIS and ion densities from IRI. The most common high latitude ionospheric electrodynamics models are, Assimilative Mapping of Ionospheric electrodynamics (AMIE) technique (Richmond & Kamide, 1988; Richmond et al., 1992), Weimer models (Weimer, 2005), empirical model by A. J. Ridley et al. (2000). Particle precipitation can be specified from T. J. Fuller-Rowell & Evans (1987), Hardy et al. (1987), Ovation SME (Mitchell et al., 2013), or Ovation Prime (P. T. Newell et al., 2009). It can also use inputs from global MHD models such as the Space Weather Modeling Framework (SWMF) (Tóth et al., 2005). It can use either an idealized dipole magnetic field or a realistic magnetic field from IGRF with the APEX coordinate system (Richmond, 1995). The lower boundary of GITM in its default configuration is specified using MSIS and Horizontal Wind Model (HWM) (Drob et al., 2015). In the first two chapters of this thesis, we specify the lower bound-

ary from a whole atmosphere model, WACCM-X instead, to provide more realistic estimates of neutral densities, temperature and winds. This allows for the variations from non-migrating tides, planetary waves, gravity waves to propagate up into the IT region.

2.1.1.1 GITM Equations

We describe the continuity, momentum and thermodynamic equations for neutral species here (see A. Ridley et al. (2006) for more details). The ion momentum equation is solved assuming a steady state using pressure gradient force, gravity, collisions with neutral winds, and electric fields. The advection in GITM is solved separately in the horizontal and vertical directions. In the horizontal direction, the continuity equation is :

$$\frac{\partial N_s}{\partial t} = -N_s \left(\frac{1}{r}\frac{\partial u_\theta}{\partial \theta} + \frac{1}{r cos\theta}\frac{\partial u_\phi}{\partial \phi} - \frac{u_\theta tan\theta}{r} \right) - \left(\frac{u_\theta}{r}\frac{\partial N_s}{\partial \theta} + \frac{u_\phi}{r cos\theta}\frac{\partial N_s}{\partial \phi} \right), \tag{2.1}$$

where, θ is latitude, ϕ is longitude, and the subscripts θ, ϕ denote the components in the respective directions. r is the radial distance measured from the center of the Earth. The subscript s denotes the species s, N is the number density, u is the horizontal velocity of all neutral species, and t is the time.

The eastward momentum equation is :

$$\begin{aligned} \frac{\partial u_\phi}{\partial t} + u_r\frac{\partial u_\phi}{\partial r} + \frac{u_\theta}{r}\frac{\partial u_\phi}{\partial \theta} + \frac{u_\phi}{r cos\theta}\frac{\partial u_\phi}{\partial \phi} + \frac{1}{r cos\theta}\frac{\partial \mathcal{T}}{\partial \phi} + \frac{\mathcal{T}}{r\rho cos\theta}\frac{\partial \rho}{\partial \phi} = \\ \frac{\mathcal{F}_\phi}{\rho} + \frac{u_\phi u_\theta tan\theta}{r} - \frac{u_r u_\phi}{r} + 2\Omega u_\theta sin\theta - 2\Omega u_r cos\theta \end{aligned} \tag{2.2}$$

The northward momentum equation is :

$$\begin{aligned} \frac{\partial u_\theta}{\partial t} + u_r\frac{\partial u_\theta}{\partial r} + \frac{u_\theta}{r}\frac{\partial u_\theta}{\partial \theta} + \frac{u_\phi}{r cos\theta}\frac{\partial u_\theta}{\partial \phi} + \frac{1}{r}\frac{\partial \mathcal{T}}{\partial \theta} + \frac{\mathcal{T}}{r\rho}\frac{\partial \rho}{\partial \theta} = \\ \frac{\mathcal{F}_\theta}{\rho} - \frac{u_\phi^2 tan\theta}{r} - \frac{u_\theta u_r}{r} - \Omega^2 r cos\theta sin\theta - 2\Omega u_\phi sin\theta \end{aligned} \tag{2.3}$$

Here, $\mathcal{F}_\phi$ and $\mathcal{F}_\theta$ represents the force due to viscosity and ion-neutral friction, Ω is the angular velocity of the Earth. $\mathcal{T}$ is the normalized temperature defined using the normalized temperature (T), the Boltzmann constant (k_B), and number density

weighted average mass ($\overline{m_n}$) as follows :

$$\mathcal{T} = \frac{k_B}{\overline{m_n}} T \tag{2.4}$$

The energy equation in the horizontal directions is as follows :

$$\frac{\partial \mathcal{T}}{\partial t} + \frac{u_\phi}{r cos\theta}\frac{\partial \mathcal{T}}{\partial \phi} + \frac{u_\theta}{r}\frac{\partial \mathcal{T}}{\partial \theta} + (\gamma - 1)\mathcal{T}\left(\frac{1}{r}\frac{\partial u_\theta}{\partial \theta} + \frac{1}{r cos\theta}\frac{\partial u_\phi}{\partial \phi} - \frac{u_\theta tan\theta}{r}\right) = 0 \tag{2.5}$$

where the source terms are included in the vertical energy equation.

In the vertical direction, the continuity equation is as follows :

$$\frac{\partial \mathcal{N}_s}{\partial t} = -\frac{\partial u_{r,s}}{\partial r} - \frac{2u_r}{r} - u_{r,s}\frac{\partial \mathcal{N}_s}{\partial r} + \frac{1}{N_s}\mathcal{S}_s \tag{2.6}$$

where

$$\mathcal{N}_s = ln(N_s) \tag{2.7}$$

Here, The subscript r denotes the component in the radial direction. $u_{r,s}$ is the vertical velocity of species s. The source term $\mathcal{S}_s$ for the species s includes the eddy diffusion (K_e) and chemical sources and losses (C_s) and is as follows :

$$\mathcal{S}_s = \frac{\partial}{\partial r}\left[N_s K_e \left(\frac{\partial N_s}{\partial r} - \frac{\partial N}{\partial r}\right)\right] + C_s \tag{2.8}$$

The vertical momentum equation is as follows :

$$\begin{aligned}\frac{\partial u_{r,s}}{\partial t} + u_{r,s}\frac{\partial u_{r,s}}{\partial r} + \frac{u_\theta}{r}\frac{\partial u_{r,s}}{\partial \theta} + \frac{u_\phi}{r cos\theta}\frac{\partial u_{r,s}}{\partial \phi} + \frac{k}{M_s}\frac{\partial T}{\partial r} + T\frac{k}{M_s}\frac{\partial \mathcal{N}_s}{\partial r} = g + \mathcal{F}_s \\ + \frac{u_\theta^2 + u_\phi^2}{r} + cos^2\theta\Omega^2 r + 2cos\theta\Omega u_\phi\end{aligned} \tag{2.9}$$

The vertical temperature equation is :

$$\frac{\partial \mathcal{T}}{\partial t} + u_r\frac{\partial \mathcal{T}}{\partial r} + (\gamma - 1)\mathcal{T}\left(\frac{2u_r}{r} + \frac{\partial u_r}{\partial r}\right) = \frac{k}{c_v \rho \overline{m_n}}\mathcal{Z} \tag{2.10}$$

Where, c_v is the specific heat at a constant volume. Here, the source term, $\mathcal{Z}$ contains the following terms :

$$\mathcal{Z} = Q_{EUV} + Q_{Chemistry} + Q_{CO_2} + Q_{NO} + Q_O + \frac{\partial}{\partial r}\left((\kappa_c + \kappa_{eddy})\frac{\partial T}{\partial r}\right) + Q_C \tag{2.11}$$

where Q_{EUV} is the heating of the thermosphere via solar ultraviolet radiation,

$Q_{Chemistry}$ is the chemical heating term, Q_{CO_2}, Q_{NO} and Q_O are radiative cooling terms for CO_2, NO and O, respectively. Q_C represents the collisional heating rates (frictional and heat transfer) from Zhu & Ridley (2016). κ_c and κ_{eddy} are molecular heat conductivity and eddy heat conductivity, respectively.

Numerically, GITM takes around a 2 second time step with 1° latitude resolution. In each time step, GITM solves for the vertical equations, horizontal equations, then adds all of the source terms. In the horizontal direction, the solver is a second order Rusanov solver with an MC limiter, while in the vertical direction, the solver is the AUSM 4th order solver.

2.2 Whole Atmosphere Models

Whole Atmosphere Modeling considers the dynamical and chemical coupling between the lower and the upper atmosphere of the Earth, and was discussed in detail by Akmaev (2011). There is a strong evidence of connections between lower and upper atmosphere (e.g., H.-L. Liu & Roble, 2002; Immel et al., 2006; Goncharenko, Chau, et al., 2010; Goncharenko, Coster, et al., 2010; Oberheide et al., 2011). The coupling between the lower and upper atmosphere can be achieved through different approaches.

One approach is to use boundary specifications from different models to couple them. These models can have boundaries somewhere in the atmosphere. In particular, this approach can be used to couple lower atmospheric model with an Ionosphere Thermosphere model to provide whole atmosphere modeling capabilities. This has been achieved before via using Navy Operational Global Atmospheric Prediction System-Advanced Level Physics High Altitude (NOGAPS-ALPHA) as a bottom boundary of TIE-GCM (Siskind & Drob, 2014). NOGAPS-ALPHA is a vertical extension of Navy's operational forecast model and specifies meteorological forcing and a complex spectrum of tides in TIE-GCM (Hoppel et al., 2008; Eckermann et al., 2009). TIME-GCM as discussed above, has a lower boundary in the stratosphere, and can be put into this category as it requires specification of tides and planetary waves from other models and data sources. A similar approach is used by SWMF that integrates numerical models of Solar Corona, Eruptive Event Generator, Inner Heliosphere, Solar Energetic Particles, Global Magnetosphere, Inner Magnetosphere, Radiation Belt, Ionosphere Electrodynamics, and Upper Atmosphere into a high performance coupled model (Tóth et al., 2005). It uses a control module to two-way couple different components via standardized interfaces. However, the SWMF has

not been extended down into the Earth's lower atmosphere yet, but does provide a useful framework for coupling different models.

The other approach is to use seamless models that use a single dynamic solver encompassing the physics from the surface to the exobase (R. Roble, 2013). The first self-consistent and seamless ground to exosphere model was developed by Miyoshi & Fujiwara (2003) which was derived from the model by Miyahara et al. (1993). This model has now evolved into the Ground to topside model of the Atmosphere and Ionosphere for Aeronomy (GAIA) (Jin et al., 2011). It has neutral, ionospheric and electrodynamic models and has comprehensive physical parameterizations (e.g., Fujiwara & Miyoshi, 2010), and has been validated against satellite observations (e.g., Jin et al., 2012). The Whole Atmosphere Model (WAM) (Akmaev et al., 2008; T. J. Fuller-Rowell et al., 2008) is derived from the U.S. National Weather Service Numerical Weather prediction model, Global Forecast System (GFS), which itself was based on the spectral model by Sela (1980). It encompasses the region from the surface to around 600 km and has been recently been coupled with another model, Ionosphere Plasmasphere Electrodynamics (Maruyama et al., 2016). This model has been validated against different observations (e.g., Lieberman et al., 2013; H. Wang et al., 2014) and is currently used for operational forecasts by National Oceanic and Atmospheric Administration (NOAA).

The Whole Atmosphere Community Climate Model with thermosphere and ionosphere extension (WACCM-X) is derived from the NCAR Whole Atmosphere Community Climate Model (WACCM), which in turn is a superset of the NCAR Community Atmospheric Model (CAM) (H. Liu et al., 2010; R. R. Garcia et al., 2007; Marsh et al., 2013; H.-L. Liu et al., 2018). It focuses on both climate and smaller time scales and thus is different from WAM which focuses on weather forecast time scales (Jackson et al., 2019). It also takes into account the neutral and ion chemistry much more extensively. As a part of Community Earth System Model (CESM), it can be run with different configuration of ocean, sea ice, and land components. It can be be run either in the Specified Dynamics (SD) or a free running configuration. In the SD configuration, the temperature, zonal and meridional winds, and surface pressure fields are specified in the troposphere and stratosphere from the Modern Era Retrospective Analysis for Research and Applications (MERRA) (Rienecker et al., 2011).

WACCM-X is a hydrostatic model and solves the Navier-Stokes equations in the coordinate system of latitude x longitude x pressure. The WACCM-X 2.0 version (used in this thesis) self-consistently solves for global electrodynamics, transport of

O^+ in the F-region, and electron and ion temperatures, and metastable O^+ chemistry and has high-cadence solar EUV capability (H.-L. Liu et al., 2018). However, it is currently limited in its capability to couple with only Heelis et al. (1982) for high latitude electric fields and is under active development. Solar spectra from the Flare Irradiance Spectral Model (FISM) (Chamberlin et al., 2007, 2008) is currently used as the default. Auroral precipitation is specified from the formulation by Roble & Ridley (1987) with slight modification based on the results by Y. Zhang & Paxton (2008) (H.-L. Liu et al., 2018). In the next two chapters, we use the first approach, where we couple an IT model (GITM) with a whole atmosphere model (WACCM-X) to capture the lower atmospheric variability.

One of the most complex parameterizations in an atmospheric model is the gravity wave specification. Proper representation of gravity waves is crucial to the accurate modeling of Earth's atmosphere as they affect the winds, temperature and composition at all heights. The gravity wave parameterization that is used in WACCM-X is based on the linear saturation theory by Lindzen (1981) and R. R. Garcia et al. (2007). Some other parameterizations schemes are Matsuno (1982), Medvedev & Klaassen (1995), Hines (1997) (See Yigit et al. (2008) for a detailed review). H.-L. Liu et al. (2014) demonstrated the impact of gravity waves at 100 km by using a fine-resolution (0.25° x 0.25°) version of WACCM. Miyoshi et al. (2018) showed that the GAIA simulation with a resolution of 1° x 1° produces fluctuations in ionospheric electron density which are not visible in coarser simulations. However, most of these gravity wave parameterization schemes are only suitable for the lower atmosphere. Yigit et al. (2008) developed a parameterization scheme that extends into the thermosphere and systematically accounts for the realistic dissipation in addition to breaking and saturation. Adoption of such a scheme in the IT models can provide better propagation and dissipation of gravity waves in the upper atmosphere similar to the seamless whole atmosphere models. This is also suggested as a project for future work in Chapter 6. In the next section, we provide a brief overview of different datasets that are used to validate model results in the next three chapters.

2.3 Datasets

2.3.0.1 SABER

Sounding of the Atmosphere using Broadband Emission Radiometry (SABER) is an instrument on NASA's Thermosphere Ionosphere Mesosphere Energetics Dynamics (TIMED) satellite. TIMED was launched in December 2001 and has an orbit with

74.1° inclination at an altitude of 630 km. The TIMED orbit precesses 180° in ∼ 60 days, This period is called the yaw period/cycle, and the satellite is rotated after each period to look into the opposite hemisphere (Ortland, 2017). The latitudinal coverage alternates between 82°N to 53°S and 53°N to 82°S, depending on the season. SABER is an infrared radiometer spanning 10 channels from 1.27 μm to 17 μm that scans Earth's limb every 58s. Its primary goal is to specify the temperature structure, energetics, and heating and cooling mechanisms in the MLT (Mlynczak, 1996, 1997). SABER provides global vertical profiles of temperature, pressure, geopotential height, volume mixing ratios, volume emission rates, and cooling and heating rates for several trace species in the MLT region (Russell III et al., 1999; Yee, 2003). The version of the dataset used in this thesis is V2.0. We use 10-year averaged [O] data to understand its temporal and spatial distribution at 97 km. Averages for each year are derived by binning the data into a day of the year and latitude grid. Then, 10 years of data are averaged together.

2.3.0.2 GUVI

Global Ultra-Violet Imager (GUVI) is a UV spectrograph with primary objectives of measuring thermospheric composition, temperature, and high-latitude particle precipitation. It provides cross-track scanned images of far ultraviolet emissions spanning the wavelengths 115-180 nm. This includes airglow emissions from [H]'s Lyman-α (121.6 nm), [O] (130.4 and 135.6nm) and N_2 Lyman-Birge-Hopefield bands (165 and 185 nm) (Paxton et al., 1999; Christensen et al., 2003; Yee, 2003). Originally, GUVI used a scanning mirror to sweep a 140° arc in the plane perpendicular to the orbit. This allowed for limb brightness profiles every ∼15s (Yee, 2003). The scanning mirror failed in 2007 and since then GUVI operates in the spectral stare mode at ∼47° from nadir (Meier et al., 2014). In this thesis, we use the height-integrated O/N_2 derived from GUVI measurements. Integrated O/N_2 is defined as the ratio of integrated [O] to [N_2] column densities, from the top of the atmosphere downward until the altitude where the N_2 column integrated density reaches 10^{21} m^{-2} (Strickland et al., 1995). We will henceforth refer to it simply as O/N_2. In this thesis, we use the zonal average for 2010. It is derived by binning the data into a day of the year and latitude grid. We use the level 3 GUVI data product which includes O/N_2, electron density profiles, estimated electron mean energy and energy flux in the auroral oval.

2.3.0.3 TIDI

TIMED Doppler Interferometer (TIDI) is a Fabry-Perot interferometer that measures global horizontal winds in the MLT region. It constructs a horizontal wind vector along two parallel tracks on both sides of the spacecraft. It has four telescopes that scan the airglow layers on the limb of the Earth along four orthogonal, azimuthal directions in front and rear of the spacecraft each at 45° from the orbit. The altitude resolution of the limb scans range from 2.5 km in the mesosphere to 25 km in the thermosphere. The spatial resolution is ∼750 km along the orbit track (Yee, 2003). In this thesis, we use TIDI data for 2010 to validate the meridional winds in the lower thermosphere. A 60-day average is determined by binning the data into an altitude and latitude grid. Level 3 vector data is used here which provides the meridional and zonal components of the neutral winds.

2.3.0.4 GNSS

Global Navigation Satellite System (GNSS) data is used to determine the line-integrated ionospheric electron density by measuring the propagation time difference between two different radio frequencies (Vierinen et al., 2016). The measurements are scaled by $10^{16}\mathrm{m}^{-2}$, also referred to as total electron content (TEC) units. This slant ionospheric TEC is converted into vertical total electron content (VTEC) by using a scaling factor proportional to the elevation angle of the satellite from the receiver (Vierinen et al., 2016). The data used in this thesis is downloaded from the CEDAR Madrigal database and is derived from a distributed network of ∼6000 worldwide GNSS receivers. The data that we use here has a spatial resolution of $1^\circ \times 1^\circ$ and a temporal resolution of 30 minutes. In this thesis, we use the zonally averaged TEC for 2010 for validation of ionospheric densities. It is derived by binning the data into a day of the year and latitude grid.

2.3.0.5 CHAMP and GRACE

CHAllenge Minisatellite Payload (CHAMP) and Gravity Recovery And Climate Experiment (GRACE) are both low-earth orbit satellites with a primary objective of making accurate measurements of Earth's gravity field. CHAMP was launched in 2000 into a ∼500 km, 87° inclination orbit (Reigber et al., 2002). The twin GRACE satellites were launched in 2002 in 89° inclination, 500 km altitude orbits, separated by ∼220 km in the same orbital plane (Tapley et al., 2004). All three satellites have highly accurate accelerometers that have been widely used to derive neutral

density measurements from atmospheric drag measurements (e.g., Lühr et al., 2004; S. Bruinsma et al., 2004; Sutton, 2011). In this thesis, we used neutral mass density datasets from 2007-2010 from these satellites to validate the mass density in the upper thermosphere. Averages for each year were derived by binning the data into a day of year and latitude grid.

2.3.0.6 Emmert Densities

J. T. Emmert (2015) studied the trends in globally averaged neutral mass density from 1967-2013. This dataset is derived from the orbits of ∼5000 objects between the altitude of 200-600 km (J. T. Emmert, 2009). The densities were derived from two-line elements (TLEs) compiled by the U.S. Air Force, estimating the ballistic coefficients and computing the average density for each object along the orbit relative to a reference model. These densities were then combined from different objects to produce a globally averaged density. This data has a resolution of 3-6 days with daily relative accuracy of ∼2% and absolute accuracy of 10%. In this thesis, we used the derived density data for 2010 at 400 km. We will henceforth refer to this dataset simply as 'Emmert ρ' or 'Emmert dataset'.

CHAPTER III

Impacts of Lower Thermospheric Atomic Oxygen on Thermospheric Dynamics and Composition Using the Global Ionosphere Thermosphere Model

This chapter focuses on understanding the role of MLT atomic oxygen, which is a minor species in the lower-middle thermosphere on the upper thermosphere. It gives an overview of how GITM is coupled with the whole atmosphere model, WACCM-X. It is published in the Journal of Geophysical Research: Space Physics, (Malhotra et al., 2020). The GITM runs are available in the University of Michigan's Deep Blue Data repository (Malhotra & Ridley, 2020).

The keypoints of this chapter are :

- SABER data shows that O number density between 95-100 km is higher in summer mid-high latitudes, opposite to the MSIS distribution.
- The atomic oxygen distribution between 95-100 km affects the winds, temperature, composition and dynamics in the middle-upper thermosphere.
- Correct lower thermospheric specification of atomic oxygen is important in modeling space weather and climate.

3.1 Introduction

The coupling between the lower atmosphere and the ionosphere-thermosphere (IT) system remains one of the biggest challenges in understanding and observing space weather. Numerous studies have been conducted over the past few decades to understand the dynamical and compositional changes in the IT densities and temperature because of the lower atmosphere (e.g., Shimazaki, 1967, 1968; Hagan & Forbes,

2002; Immel et al., 2006; X. Zhang et al., 2010a,b; Malhotra et al., 2016, and many others). The vertical coupling via gravity waves, planetary waves and atmospheric tides plays a crucial role in the momentum, energetics and composition of the IT system (Lindzen, 1981; Qian et al., 2009; Yamazaki & Richmond, 2013; Siskind et al., 2014). Because most space-based activities are in the thermosphere/ionosphere of either Earth or other planets, it is imperative to understand the physical processes affecting this region of the atmosphere. For example, ionospheric irregularities impacting communication systems (e.g., Kelly et al., 2014), such as equatorial bubbles, are thought to be seeded from the lower and middle atmosphere (Rottger, 1973; Hysell et al., 1990; Prakash, 1999).

In order to better understand how the lower atmospheric variability at various spatial and temporal scales propagates into the upper atmosphere, attempts have been made to develop whole atmosphere models, such as, the Whole Atmosphere Community Climate Model with Thermosphere and Ionosphere Extension (WACCM-X) (H.-L. Liu et al., 2018), the Ground to topside model of Atmosphere and Ionosphere for Aeronomy (GAIA) (Jin et al., 2011), the Whole Atmosphere Model (WAM) (Akmaev et al., 2008; T. J. Fuller-Rowell et al., 2008), and the Canadian Middle Atmosphere Model (CMAM) (Beagley et al., 1997). Apart from seamless atmospheric modeling, another approach to better understanding the lower atmospheric influences in the IT system is by coupling a lower atmosphere model with an IT/upper atmospheric model (e.g., R. Roble, 2013; Akmaev, 2011). While whole atmosphere models are more self-consistent, coupled models are better suited for isolating the effects of specific lower boundary conditions on the upper atmosphere (e.g., Hagan et al., 2009; Q. Wu et al., 2012).

For upper atmospheric models, lower boundary conditions are especially important for introducing compositional changes in the IT system, as the composition at 100-130 km map to higher altitudes because of diffusive equilibrium (Colegrove et al., 1966). Major constituents in the MLT are atomic oxygen (O), molecular nitrogen (N_2), and molecular oxygen (O_2). Between the altitudes 80-100 km, the lifetime of O changes from hours to several months and therefore O in the lower thermosphere becomes highly susceptible to dynamical transport by winds (Brasseur & Solomon, 1984; Smith et al., 2010). Changes in O concentration in this region map to total neutral densities at higher altitudes in the thermosphere as O becomes the major species above 200 km. It is also known that the electron density in the F region ionosphere is approximately proportional to O/N_2 because O acts as a source of free electrons while N_2 acts as the sink (Shimazaki, 1965, 1966).

In the upper thermosphere, a hemispheric asymmetry in the distribution of species is observed in solstice conditions. Higher concentrations of lighter species, for example, O and He are observed in the winter hemisphere, also called the 'winter bulge', whereas heavier species (e.g., O_2 and N_2) are concentrated in the summer hemisphere (e.g., Johnson, 1964; King, 1964; Keating & Prior, 1968; Reber et al., 1968; Johnson & Gottlieb, 1970, 1973; Johnson, 1973; Mayr et al., 1978). Two processes that are thought to be responsible for this redistribution are horizontal transport across the hemispheres and vertical transport. In the thermosphere, meridional wind circulation is dominated by interhemispheric winds from summer to winter due to the temperature gradient arising from asymmetrical solar heating between the hemispheres. Numerous studies (Mayr et al., 1978; Cageao & Kerr, 1984) have put forward the horizontal transport of O into the winter hemisphere by the meridional winds as the primary reason for the winter bulge. In the middle thermosphere, the vertical winds in the summer are largely upward whereas the vertical winds in the winter hemisphere are downward. This causes vertical transport of the species such that in the summer hemisphere, upward winds result in decrease of lighter species and increase of heavier species (Hays et al., 1973; Reber & Hays, 1973; Burns et al., 1989; Rishbeth, 1998; X. Liu et al., 2014; Jones Jr., Emmert, et al., 2018). The opposite happens in the winter hemisphere resulting in a relative increase of lighter species and decrease of heavier species. The importance of one mechanism versus the other (i.e., horizontal vs vertical transport) is still under investigation. T. J. Fuller-Rowell (1998) linked the two mechanisms by describing the mixing to be similar to a huge eddy, calling it the 'thermospheric spoon'. Sutton (2016) found that both phenomena are inherently linked with one another with convergent horizontal motion increasing downwelling and divergent motion increasing upwelling, thereby transporting light constituents both horizontally and vertically simultaneously.

In the mesosphere, the meridional circulation is in the same direction, from summer to winter, but driven by a different mechanism. Large westward gravity wave drag in the winter hemisphere and eastward gravity wave drag in the summer hemisphere causes the circulation to be from summer to winter through Coriolis force (Qian & Yue, 2017). Smith et al. (2010) used O mixing ratio at 0.0046 hPa ($\sim$84 km) from the Sounding of the Atmosphere using Broadband Emission Radiometry (SABER) instrument to show that there is a winter maximum in O which is likely linked to the above mentioned gravity wave driven downwelling in the winter. However, they observed the opposite hemispheric distribution at a lower pressure, 0.0008 hPa ($\sim$94 km) with higher O mixing ratio in the summer hemisphere and lower in

the winter hemisphere. The greatest variation was found to be at mid-latitudes with the phase of mid-latitude variation reversing between 84 and 94 km. The level of reversal was found to be at 0.001 hPa (∼93 km). The higher summer atomic oxygen concentration may be an indication that the summer upwelling circulation cell has reversed and there is a downward circulation cell above the mesopause (∼ 83-89 km) (Smith et al., 2010). Another reason may be enhanced molecular diffusion of O due to higher temperatures from higher altitudes (Smith et al., 2010). A similar reversal was also observed by J. P. Russell et al. (2004) using Wind Imaging Interferometer (WINDII) data and Sheese et al. (2011) using Optical Spectrograph and Infrared Imaging System (OSIRIS) data. Qian et al. (2017) found evidence of lower thermospheric winter to summer circulation using WACCM-X and SABER CO_2 data citing convergence in summer and divergence in winter about 10 km above the mesopause. It was explained to be forced by gravity waves (Lindzen, 1981; Rezac et al., 2015; Smith et al., 2011; H.-L. Liu, 2007). It is possible that this circulation is responsible for the distribution of atomic oxygen observed by Smith et al. (2010). Qian & Yue (2017) studied the impact of the lower thermospheric winter-to-summer circulation on the upper thermosphere by forcing the meridional and vertical winds of the NCAR Thermosphere-Ionosphere-Electrodynamics General Circulation Model (TIE-GCM) (Richmond et al., 1992; Qian et al., 2014, and references therein) in the altitude range of ∼97-110 km towards a winter-to-summer circulation. They found that upwelling decreases the upper-thermospheric O/N_2 in the winter hemisphere, whereas, downwelling increases it in the summer hemisphere, thus reducing the gradient between the two hemispheres.

This study reports the impact of changing the distribution of the lower thermospheric atomic oxygen on the upper thermosphere. This is done by changing the lower boundary condition for atomic oxygen in the Global Ionosphere Thermosphere Model (GITM) from an empirical model (MSIS) to a whole atmosphere model (WACCM-X). MSIS and WACCM-X have oppositely oriented atomic oxygen distributions in latitude, with WACCM-X having a distribution that is more consistent with observations. This is done while keeping other species' number densities, temperature, winds constant at the model lower boundary. This is different from Qian & Yue (2017) because our goal is to explain the mechanisms that are involved in lower-upper thermospheric coupling in the context of lower thermospheric O concentration rather than the winter-to-summer circulation.

3.2 Methodology

3.2.1 Models

3.2.1.1 Global Ionosphere Thermosphere Model (GITM)

GITM is a physics based three-dimensional spherical model that simulates the thermosphere and ionosphere by determining the density, momentum, and energy self-consistently (A. Ridley et al., 2006). GITM explicitly solves for the neutral densities of O, O_2, N(^{2}D), N(^{2}P), N(^{4}S), N_2, NO and He; and ion species O^+(^{4}S), O^+(^{2}D), O^+(^{2}P), O_2^+, N^+,N_2^+, NO^+ and He^+. It uses a stretched altitude grid from 100 km to 600 km that allows for non hydrostatic conditions to exist (Deng et al., 2008). The vertical grid spacing is less than 3 km in the lower thermosphere, and over 10 km in the upper thermosphere. It allows different models of high-latitude electric fields, auroral particle precipitation, and solar EUV inputs to be used. Here, we use the Weimer model, (Weimer, 2005) for the high latitude potential, FISM EUV empirical model, (Chamberlin et al., 2008) and NOAA POES Hemispheric Power driven model (T. J. Fuller-Rowell & Evans, 1987) as an estimate of power deposited in the polar regions by energetic particles.

3.2.1.2 Mass Spectrometer and Incoherent Scatter radar (MSIS)

In its default configuration, GITM uses the Mass Spectrometer and Incoherent Scatter radar model, NRLMSISE-00 (Hedin, 1983, 1987, 1991; Picone et al., 2002) as the thermospheric lower boundary condition on the number densities and temperature. NRLMSISE-00 is an empirical model that uses Fourier-modulated spherical harmonics in latitude, longitude, and time, and Bates-Walker (Walker, 1965) and cubic spline fits in the vertical to numerous satellite, ground based and rocket observations. NRLMSISE-00 has been widely used to understand vertical coupling between the lower atmosphere and the IT system (T. J. Fuller-Rowell, 1998; H. Liu et al., 2010; Qian et al., 2018; Weimer et al., 2018; Yue et al., 2019). Since it is an empirical model, it gives a good estimate of neutral densities and temperature for average conditions where observations exist. The inputs to MSIS are the solar flux proxy, F10.7 and geomagnetic activity level (Ap).

3.2.1.3 Whole Atmosphere Community Climate Model with Thermosphere and Ionosphere extension (WACCM-X)

WACCM-X is also a physics based model, covering the whole atmosphere starting from the surface to 2.5×10^{-9} hPa or $\sim$500 km in altitude (H. Liu et al., 2010; H.-L. Liu et al., 2018). It is based on the NCAR Whole Atmosphere Community Climate Model (WACCM) (R. R. Garcia et al., 2007; Marsh et al., 2013), which in turn is based on the NCAR Community Atmosphere Model (CAM) (S.-J. Lin, 2004). In this study, we use the Specified Dynamics configuration of WACCM-X, also known as SD-WACCM-X. In this configuration, dynamical fields (temperature, zonal and meridional winds and surface pressure) are specified in the troposphere and stratosphere from the Modern Era Retrospective Analysis for Research and Applications (MERRA) (Rienecker et al., 2011). WACCM-X can also be run without constraining the troposphere and stratosphere, also usually referred to as the free-running mode. Since we are only using the results from SD-WACCM-X here, we will refer to these simulations as WACCM-X. The horizontal resolution (latitude$\times$longitude) of the model is $1.9^\circ\times$ 2.5°, and the time step is 5 minutes. A detailed description of WACCM-X is given in H. Liu et al. (2010) and H.-L. Liu et al. (2018). Hourly averaged values are used in our study. WACCM-X is used as the lower boundary for GITM and the simulation results are compared with MSIS driven GITM. The version of Community Earth System Model (CESM) that is used in this study is 2.0.

WACCM-X solves the Navier Stokes equations in pressure coordinates whereas GITM solves them in altitude coordinates. WACCM-X outputs the mixing ratio for different species, whereas GITM uses number densities as boundary conditions. Therefore, the total neutral number density in WACCM-X is calculated from pressure and temperature fields (using the ideal gas law). WACCM-X also outputs the altitude corresponding to each pressure level at every grid cell. The total number densities and atomic oxygen mixing ratio in pressure coordinates are converted to altitude coordinates by linearly interpolating them to 95 km, 97.5 km and 100 km, thus putting them on a uniform altitude grid. The total number density is multiplied by the mixing ratio of atomic oxygen (also in altitude coordinates) to get number densities for atomic oxygen on the altitude grid.

3.2.2 GITM Simulations

Atomic oxygen number densities from MSIS and WACCM-X were used as inputs at the lower boundary of GITM. WACCM-X is expected to have significantly more

Table 3.1: Parameter values at the lower boundary - GITM w/ MSIS and GITM w/ WACCM-X

Parameter	Value
Temperature, T	150 K
Zonal Winds, U	0 m/s
Meridional Winds, V	0 m/s
Molecular Oxygen, O_2	1×10^{18} m^{-3}
Molecular Nitrogen, N_2	1×10^{19} m^{-3}
Nitric Oxide, NO	1×10^{14} m^{-3}

variability owing to non-migrating tides, planetary waves and gravity waves that propagate through the lower atmosphere to the thermosphere. On the other hand, because MSIS is an empirical model, it should provide a good estimate of average conditions but may not be as accurate in representing the impact of forcing from above (e.g., magnetospheric inputs) or forcing from below (e.g., atmospheric gravity waves). Also, at these altitudes, MSIS has only the mean component and migrating tides with a small dependence on F10.7 and Ap. It should be noted that real time-varying geospace conditions are used as inputs in these simulations.

To specify the lower boundary condition in GITM, two ghost cells below 100 km are used. In these cells, state values are specified. In order to not drive constant acceleration, a hydrostatic solution is used, where the density is set in the cell closest to 100 km (second cell), and the density in the lower cell is derived. In both the simulations, the temperature in both cells and across the globe were held constant at 150 K, while all components of the winds were held to be zero. For O_2, N_2, and NO, the number densities in the second cell are constant across the globe and specified in Table 3.1. For the minor species, He and N(^{4}S), MSIS is used to specify the number densities in both the simulations. For O, a zero gradient in altitude is used since O peaks in this region. Therefore, the O number densities in the first cell are same as in the second cell. O is allowed to have horizontal structure, such that, for the GITM w/ MSIS simulation, MSIS is used to specify the O number densities, whereas, for the GITM w/ WACCM-X simulation, the above mentioned linearly interpolated O number densities are used.

Hourly averaged WACCM-X O number densities are used. Since the timesteps in GITM are much smaller than the 1 hour time resolution of WACCM-X output, WACCM-X number densities are linearly interpolated in time between every hour. These number densities are linearly interpolated to GITM's second cell's altitude and

grid locations. MSIS O number density is computed at each GITM time step and location. The only difference between the two runs, GITM w/ MSIS and GITM w/ WACCM-X is the atomic oxygen between 95 - 100 km. This was specifically done to explore the effect of the O number density in the lower thermosphere on the system.

Results from the two simulations spanning 21 days, Jan 15, 2010 to Feb 04, 2010 are discussed here. Since, it took around 9 days for the model to achieve a nearly steady globally averaged O density at 200 km altitude, results from the last 12 days, Jan 24, 2010 to Feb 04, 2010 are discussed. The two simulations are referred to as GITM w/ MSIS and GITM w/ WACCM-X. This time period is chosen because it is a geomagnetically quiet time around solstice that results in a hemispherically asymmetric lower thermospheric O number density between MSIS and WACCM-X. Simulations results from June 24, 2010 to July 5, 2010 are also discussed here.

3.2.3 Data

In this study, SABER data is used to validate the lower thermospheric atomic oxygen in WACCM-X. We also use GUVI O/N_2 to validate the integrated thermospheric O/N_2 in GITM once the lower boundary atomic oxygen is changed from MSIS to WACCM-X. A brief description of the SABER and GUVI instruments is provided below for the interested reader.

3.2.3.1 SABER

Sounding of the Atmosphere using Broadband Emission Radiometry (SABER) is an instrument on Thermosphere-Ionosphere-Mesosphere Energetics and Dynamics (TIMED) satellite. Its primary goal is to quantify the energy budget of mesosphere and lower thermospheric (MLT) (Mlynczak, 1996, 1997). TIMED was launched in 2001 in a 74.1° inclination orbit at an altitude of 630 km (Russell III et al., 1999; Yee, 2003). It has a yaw period of ∼60 days in which the latitudinal coverage alternates between 82°N - 53°S and 53°N - 82°S. SABER has a vertical resolution of ∼2 km and horizontal resolution of ∼300 km depending on the limb geometry. SABER takes limb scan profiles of 10 spectral channels between 1.27 - 17μm, indicating the kinetic temperature of O and CO_2 in the MLT region (∼65-105 km) (Rezac et al., 2015).

O is generated by photodissociation of molecular oxygen by solar UV radiation and has two very bright fine structure lines, 63.184 μm (4.75 THz) and 145.525 μm (2.06 THz). However, both of these wavelengths are particularly hard to measure with the current state-of-the-art satellites instruments. Past and present technolo-

gies require a detection system cooled to cryogenic 4K temperatures, which poses a significant mission cost and lifetime overhead. D. L. Wu et al. (2016) described an emerging technique, THz limb sounder (TLS) using a Schottky–diode–based receiver which has good radiometric sensitivity at non-cryogenic temperature. Studies over the last few decades have used balloons (F. J. Lin et al., 1987; Mlynczak et al., 2004), rocket borne in-situ observations (von Zahn, 1967; Offermann, 1974; K. Grossmann & Offermann, 1978; Gumbel, 1997) and space station observations (K. U. Grossmann et al., 2000). Since there are no global observations made by observing radiant emission of O directly, SABER calculates O using indirect methods (Mlynczak, 1996, 1997; Rezac et al., 2015). During the daytime, O is derived using the emission of ozone (O_3) at 9.6 μm assuming that there is an equilibrium between the photolysis of O_3 and the recombination of O and O_2. During night, it is inferred from the emission of the vibrationally excitepd Meinel OH band, which is formed by the reaction between atomic hydrogen (H) and O_3. This measurement assumes that there is an equilibrium between this reaction and the recombination of O and O_2 (Mlynczak et al., 2013, 2018).

3.2.3.2 GUVI

The Global Ultraviolet Imager (GUVI) is an FUV hyperspectral imager aboard the TIMED satellite, measuring the terrestrial airglow from 120 to 180 nm (Christensen et al., 2003). Some of the objectives of GUVI are to make accurate observations of thermospheric temperature and composition and to understand the response of thermosphere ionosphere system to various energy fluxes. It measures in five far ultraviolet bands corresponding to emission features of H (121.6), OI(130.4), OI(135.6), and the N_2 LBH bands (Christensen et al., 1994; Paxton et al., 1999; Christensen et al., 2003). In the imaging mode, a scan mirror subsystem (Humm et al., 1998, 1999) scans the instantaneous field of view cross-track of the satellite once every 15s. The scan begins on the limb and covers 140°, i.e., 80° from nadir above the limb on the cold side of the satellite (away from the Sun) to 60° toward the warm side (Paxton et al., 2004). Since December 2007 when the scan mirror failed, GUVI only operates in the spectral stare mode at about 47° from nadir. In this mode, data are recorded continuously from all 176 spectral pixels for each of the 14 spatial pixels (Meier et al., 2014). The height integrated O/N_2 ratio referenced at a N_2 column integrated number density of 10^{17} cm^{-2} is obtained from the disk 135.6 nm and LBHS day glow data (Y. Zhang et al., 2004, 2014).

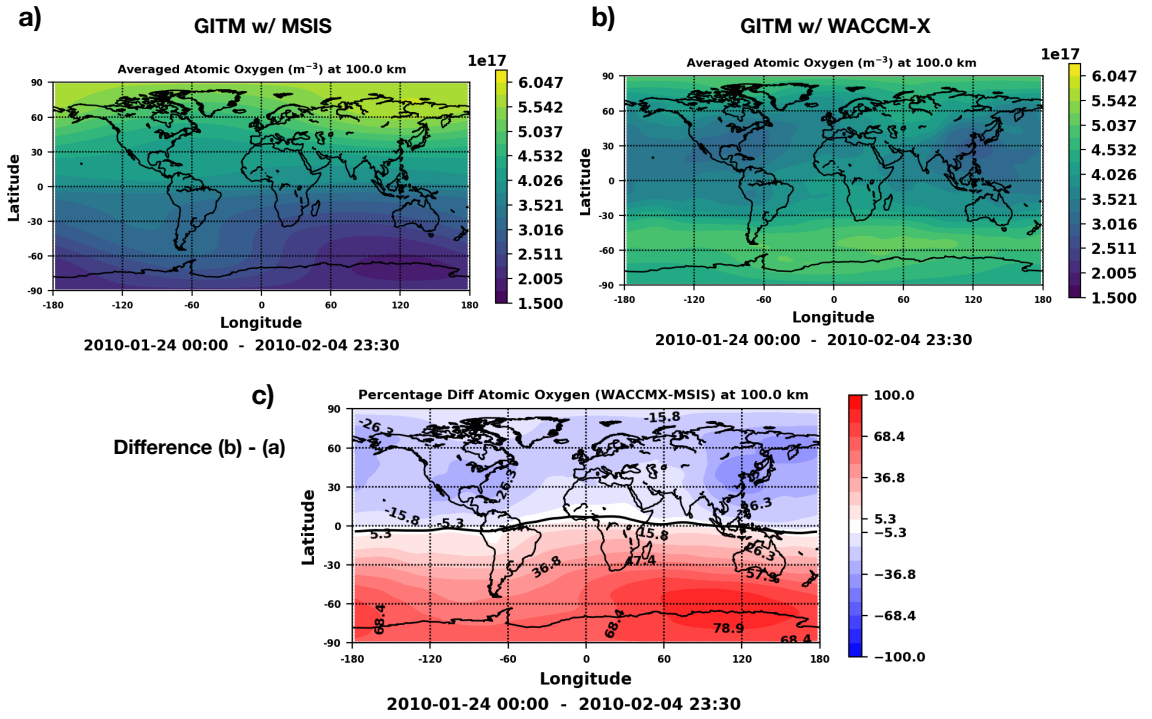

Figure 3.1: a) Atomic Oxygen for GITM w/ MSIS at 100 km averaged for time periods 01/24/2010 - 02/04/2010. b) Similar to a) but for GITM w/ WACCM-X. c) Averaged Difference in Atomic Oxygen at 100 km : GITM w/ WACCM-X (b) - GITM w/ MSIS (a). Note the thicker black line roughly parallel to the equator. This is the zero line where no difference is seen.

3.3 Results and Discussion

3.3.1 Lower Boundary Comparison

Figure 3.1 shows a comparison between atomic oxygen number densities of GITM w/ MSIS (Figure 3.1a) and GITM w/ WACCM-X (Figure 3.1b) at 100 km, averaged over the last 12 days of the simulation. For GITM w/ MSIS, O is higher in the northern winter whereas for GITM w/ WACCM-X, O is higher in the southern summer. Figure 3.1c shows the difference between panels b) and a) i.e., GITM w/ WACCM-X - GITM w/ MSIS. The absolute difference is larger in the summer hemisphere.

In order to determine which simulation result is closer to the observed O distribution, Figure 3.2a shows SABER atomic oxygen number densities at 100 km gridded in $4° \times 4°$ bins, averaged for January from 2002-2017. Figure 3.2b shows the number of

measurements in each bin. The high latitudes have lower numbers of measurements compared to middle-lower latitudes, because of the inclination of TIMED satellite. Long term averaging is helpful in reducing the uncertainty associated with the decrease in abundance of daytime ozone due to photolysis. The atomic oxygen number densities are larger in the summer (southern) hemisphere which is similar to Figure 3.1b for GITM w/ WACCM-X. The summer hemisphere number density maximum is at different latitudes, with the SABER maximum occurring at higher latitudes than the WACCM-X maximum. Because of the lower number of SABER measurements at high summer latitudes, there is a greater statistical uncertainty associated with the measurements. Another source of uncertainty is the accuracy of the temperature at 100 km, through the recombination rate coefficient in the steady-state chemical expression used to derive atomic oxygen from ozone (Mlynczak et al., 2013). Lastly, SABER daytime ozone has a likely high bias as reported by Smith et al. (2013). Thus, the absolute magnitude of SABER data is different from both MSIS and WACCM-X. SABER values are ∼3 times the model values, resulting in a larger gradient between the hemispheres. Using WACCM-X O number densities as an approximation for the true O number density distribution, this study focuses on explaining the large-scale effects of the O number density distribution at the mesopause on the thermosphere.

As an aside, MSIS was developed using data from a wide variety of in-situ satellite measurements in the upper themosphere (Hedin, 1987, 1991; Picone et al., 2002) and did not include measurements of O in this region. At around 100 km, a hemispheric gradient in the atomic oxygen number density in MSIS is predicted, with lower O number density in the summer hemisphere, similar to the observations in the middle-upper thermosphere (Reber & Hays, 1973). However, in the region between 90 - 150 km, limited observations were available, primarily being temperature and total neutral density measurements inferred from rockets and incoherent scatter radars. NRLMSISE-00 did not include the SABER measurements in its fitting procedure because TIMED hadn't been launched yet. In MSIS, below the turbopause (∼105 km), the number densities were extrapolated using the average molecular weight of the atmosphere assuming a perfectly mixed atmosphere along with a correction factor to account for chemical and dynamical flow effects on various species. Below the turbopause, these chemical dynamical correction factors imply that the atmosphere is not fully mixed until ∼80 km or lower. Between 120 km and 105 km, the number densities are a meld of their fully mixed and diffusively separated values along with the correction factor. The correction factor for O does not take into account the dynamical/chemical effects that lead to larger summer atomic oxygen, thus explaining

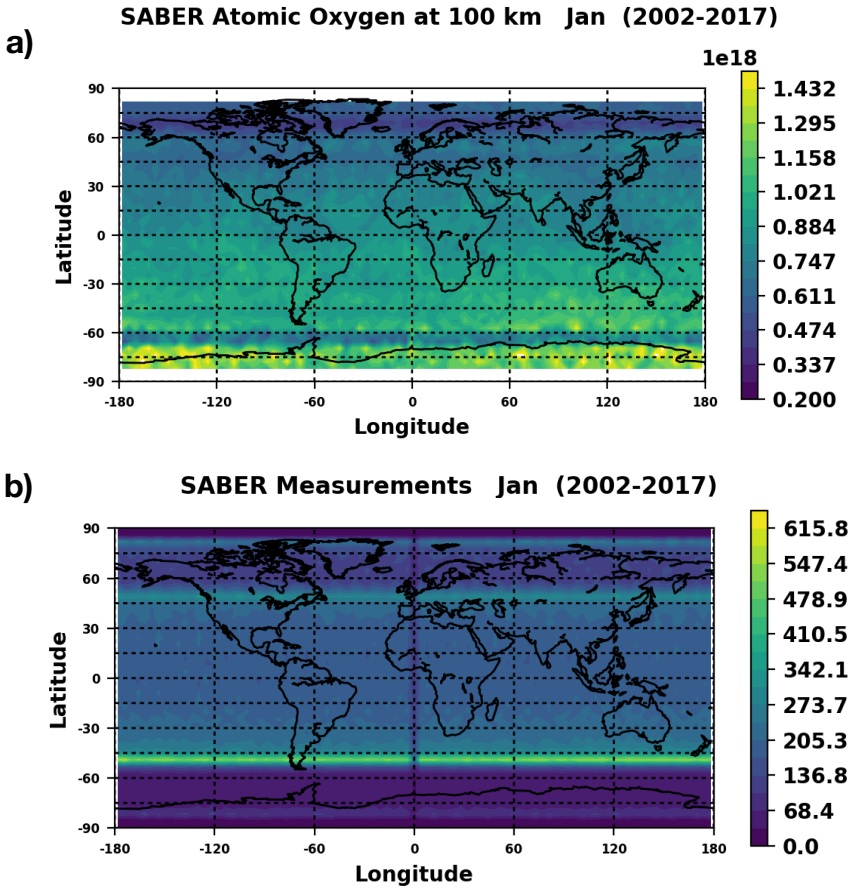

Figure 3.2: a) Atomic oxygen for SABER in number m^{-3} at 100 km for the month of January binned together for the years 2002-2017. The bin size is $4° \times 4°$. b) Number of measurements in each bin for the month of January for 2002-2017.

the similar hemispheric gradient of atomic oxygen number density in the upper as well as the lower thermosphere.

However, O departs from diffusive and fully mixed equilibrium in the mesosphere and lower thermosphere due to chemistry, eddy mixing and dynamic transport, which is highlighted by the incorrect O distribution in MSIS, as compared to both WACCM-X results and SABER observations. One of the reasons for the O reversal in SABER data is suggested by Smith et al. (2010) through the effect of temperature and molecular diffusion. Higher temperatures in the summer hemisphere may lead to molecular diffusion of O from higher to lower altitudes resulting in high O concentration. The transport of O via lower thermosphere winter to summer circulation suggested by Qian & Yue (2017) and Rezac et al. (2015) may also be the reason for this reversal. Another contribution to high summer O can be from the eddy turbulence or eddy diffusion. Eddy diffusion is a macroscopic description of flow induced by the gravity wave motion (Hodges, 1969). However, previous studies suggest that other tidal and wave activity can contribute to the mixing and turbulence in this region (Salinas et al., 2016; Jones Jr. et al., 2017). Numerous observational (e.g., Fukao et al., 1994; Kirchhoff & Clemesha, 1983a; Sasi & Vijayan, 2001) and modeling studies (e.g., Qian et al., 2009; Pilinski & Crowley, 2015; Salinas et al., 2016) have found that eddy diffusion coefficient is larger in summer and smaller in winter. However, the exact magnitude of the eddy diffusion term near the turbopause still remains elusive. We have yet to achieve a universal model for specifying the eddy diffusion coefficient. It is possible that larger eddy diffusion during summer leads to downward transport of O into the lower thermosphere resulting in the increase of summer O/N_2.

3.3.2 Effect on Lower - Upper Thermosphere

Figure 3.3 shows GITM zonally averaged meridional winds in the thermosphere from 100 km to 275 km. Figure 3.3a and 3.3b are the winds for GITM w/ MSIS and GITM w/ WACCM-X, respectively. Winds vectors comprising of both vertical (scaled by 50) and meridional winds components are overlaid on the contour plots. The general circulation remains similar between the two simulations. Between 100 - 120 km, winds are equatorward and above 160 km the circulation is dominated by summer to winter winds with upwelling in summer and downwelling in winter at mid-high latitudes.

Figure 3.3c is the difference between the zonally averaged meridional winds, GITM w/ WACCM-X - GITM w/ MSIS. As mentioned previously, the only difference between the two simulations is the atomic oxygen distribution below 100 km. The

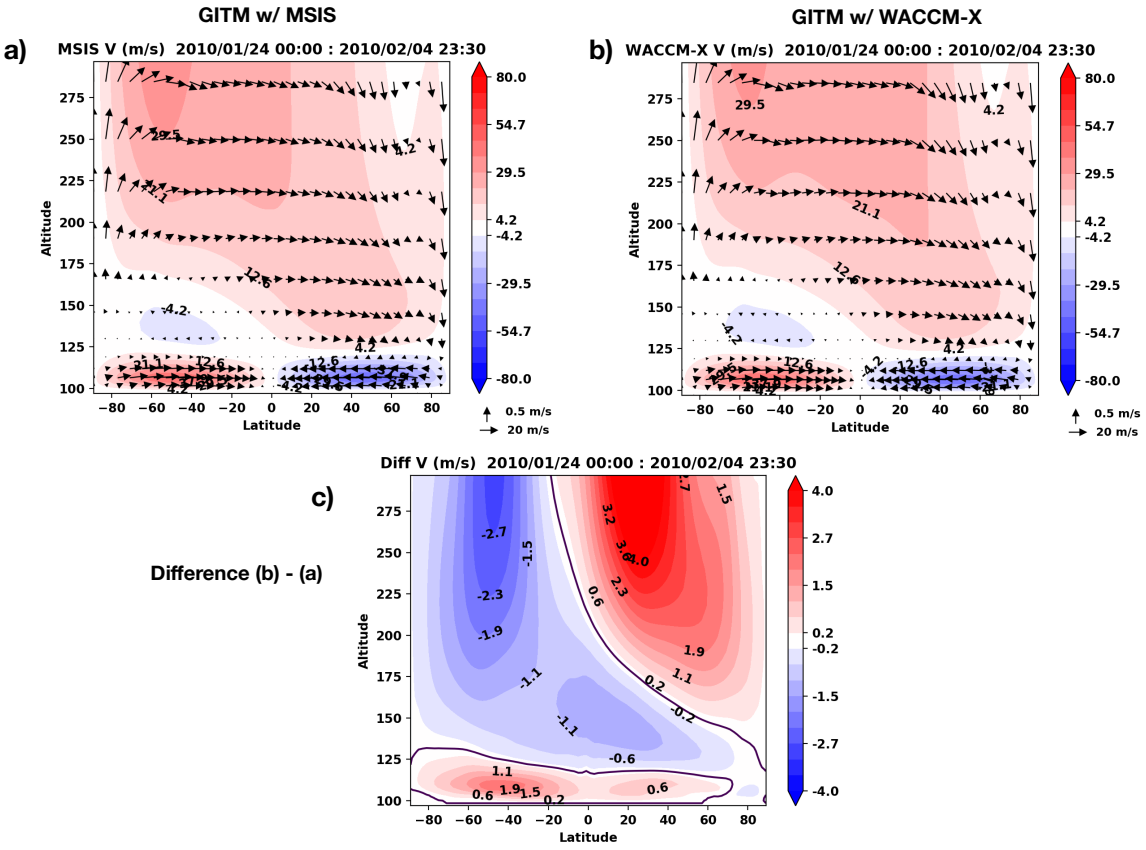

Figure 3.3: a) The contours indicate the zonally averaged meridional wind in m/s for GITM w/ MSIS averaged for 01/24/2010 - 02/04/2010. Positive values indicate northward wind while negative values indicate southward wind. The arrows signify a vector sum of meridional and vertical winds (scaled by $\times$ 50). b) Similar to a) but for GITM w/ WACCM-X. c) Averaged difference in meridional winds, GITM w/ WACCM-X (b) - GITM w/ MSIS (a). Note the thicker black contour line. This is the zero line where no difference is seen.

difference in Figure 3.3c is positive in the region between 100-120 km. This indicates that GITM w/ WACCM-X has larger equatorward winds in the summer (southern) hemisphere, whereas GITM w/ MSIS has larger equatorward winds in the winter (northern) hemisphere. This is because of the difference in latitudinal O number density gradient between the two simulations such that, the winds induced by the lower boundary O gradient superimpose on the main equatorward circulation cells. Thus, because of the opposite O distribution, the hemisphere with larger equatorward winds simply reverses.

The forces affecting the winds in the thermosphere can be understood by investigating the contribution of force terms of the horizontal momentum equation. The northward momentum equation in GITM is as follows (A. Ridley et al., 2006):

$$\frac{\partial u_\theta}{\partial t} = -u_r \frac{\partial u_\theta}{\partial r}^{(1)} - \frac{u_\theta}{r}\frac{\partial u_\theta}{\partial \theta}^{(2)} - \frac{u_\phi}{r cos\theta}\frac{\partial u_\theta}{\partial \phi}^{(3)} - \frac{k_b}{\overline{m_n} r}\frac{\partial T}{\partial \theta}^{(4)} - \frac{T}{r\rho}\frac{k_b}{\overline{m_n}}\frac{\partial \rho}{\partial \theta}^{(5)} + \frac{\mathscr{F}_\theta}{\rho}^{(6)} - \frac{{u_\phi}^2 tan\theta}{r}^{(7)} - \frac{u_\theta u_r}{r}^{(8)} - \Omega^2 r cos\theta sin\theta^{(9)} - 2\Omega u_\phi sin\theta^{(10)} \tag{3.1}$$

where θ denotes the north latitude, ϕ denotes east longitude, r is the radial distance from the center of the Earth, u is the neutral velocity, Ω is the angular velocity of the planet, k_b is the Boltzmann constant, m_n is the number density weighted average mass, T is the neutral temperature and ρ is the mass density. $\mathscr{F}_\theta$ is the force due to ion-neutral friction and viscosity in θ direction. The superscript for each term is for notation purposes only. Terms (1), (2), and (3) on the right represent the advective terms from the total derivative of velocity. Terms (7) and (8) are the velocity terms due to the spherical coordinates. Terms (4) and (5) represent the force arising from pressure gradient. Terms (9) and (10) are the centrifugal and Coriolis force terms, respectively.

Figure 3.4 shows the zonally and temporally averaged centrifugal (3.4a), Coriolis (3.4b), pressure gradient (3.4c), and ion drag (3.4d) forces from GITM w/ MSIS. It should be noted that these figures represent the force terms on the right side of equation 3.1 with the appropriate sign. Clearly, on average, the centrifugal and pressure gradient forces dominate this region of the thermosphere. Below 120 km, near the boundary of the model, the pressure gradient force in Figure 3.4c is weak owing to a nearly constant boundary condition on number densities (except O), temperatures, and winds. Thus, the two equatorward circulation cells between 100 - 120 km are driven by centrifugal force shown in Figure 3.4a. In the middle thermosphere, between

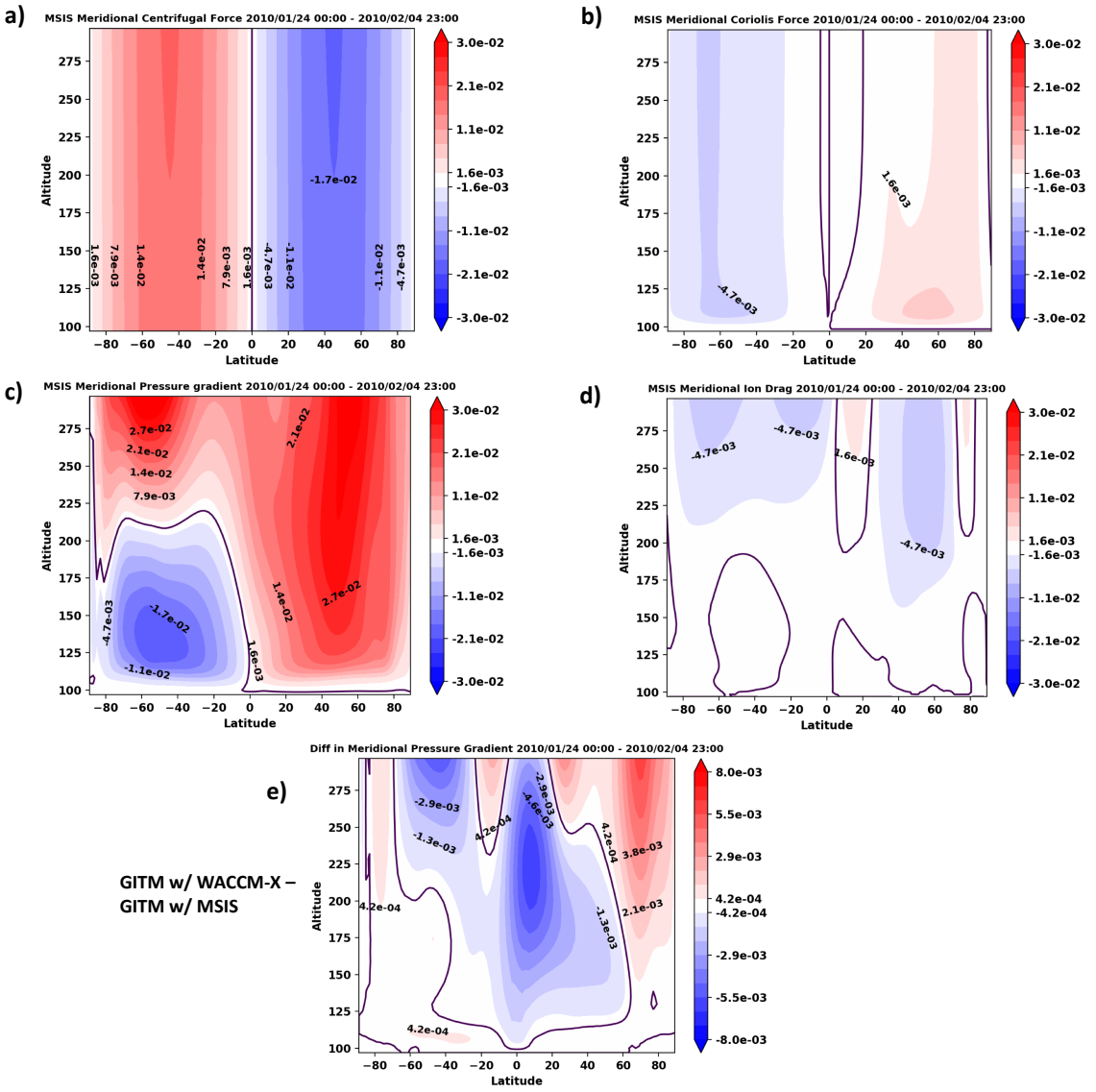

Figure 3.4: a) The contours indicate the force terms of northward momentum equation in m/s^2 for GITM w/ MSIS, zonally averaged for 01/24/2010 - 02/04/2010. b) Similar to a) but for Coriolis force. c) Similar to a) but for pressure gradient force. Positive values indicate that the pressure is increasing from north to south. d) Similar to a) but for Ion Drag. e) Averaged difference in meridional pressure gradient forces, GITM w/ WACCM-X - GITM w/ MSIS. Note the thicker black contour line. This is the zero line where no difference is seen.

125 - 200 km, the winds can develop creating a pressure bulge and can cause a redistribution of the temperature and densities to create oppositely directed forces that cancel the centrifugal force. A more-precise boundary condition on the pressure would have a bulge at the equator, such that the latitudinal gradient in pressure more closely balances the centrifugal force (i.e., an oblate-spheroid atmosphere instead of a perfect sphere). We refer to this as the poleward directed pressure gradient force. Above this altitude range, the pressure gradient force is from the summer to winter because of the temperature gradient, driving the main circulation. Coriolis force shown in Figure 3.4b is weak and acts opposite to the centrifugal force. Ion drag shown in Figure 3.4b is also weak and has a significant magnitude only above 200 km, where it acts mostly against the main circulation.

Figure 3.4e shows the difference between the pressure gradient forces of GITM w/ WACCM-X and GITM w/ MSIS. The differences corresponding to other force terms are negligible and are not shown here. Between 100-120 km, a small difference exists between the simulations which can be largely attributed to the density gradient difference. This difference results in the wind differences shown in Figure 3.3c. GITM w/ WACCM-X (GITM w/ MSIS) has weaker pressure gradient force in the summer (winter) hemisphere. More O at summer high latitudes in GITM w/ WACCM-X weakens the poleward directed pressure gradient force which increases the acceleration due to centrifugal force, resulting in stronger winds as compared to GITM w/ MSIS. Similarly, GITM w/ MSIS has weaker poleward directed pressure gradient force and larger acceleration due to centrifugal force in the winter hemisphere. The wind difference between 140 and 200 km altitude will be discussed later. It is important to note that the change in lower boundary O only changes the magnitude of the winds and does not change the direction of the wind. The transition to the upper thermospheric summer to winter circulation starts above 120 km, resulting in high atomic oxygen in the winter hemisphere above this altitude in both the simulations. This was also observed by K. U. Grossmann et al. (2000) at an altitude of 140 km using CRISTA experiments.

Figure 3.5 shows the zonally averaged temperature for the two simulations. Figures 3.5a and 3.5b are the temperature plots for GITM w/ MSIS and GITM w/ WACCM-X, respectively while 3.5c is the percent difference between the two. The temperature shows a similar pattern between Figures 3.5a and 3.5b. The temperatures are the lowest in the high latitude region in the 100-120 km altitude range. This can be attributed to the adiabatic and advective cooling due to the equatorward circulation cells as shown previously in Figure 3.3. Above this altitude, there

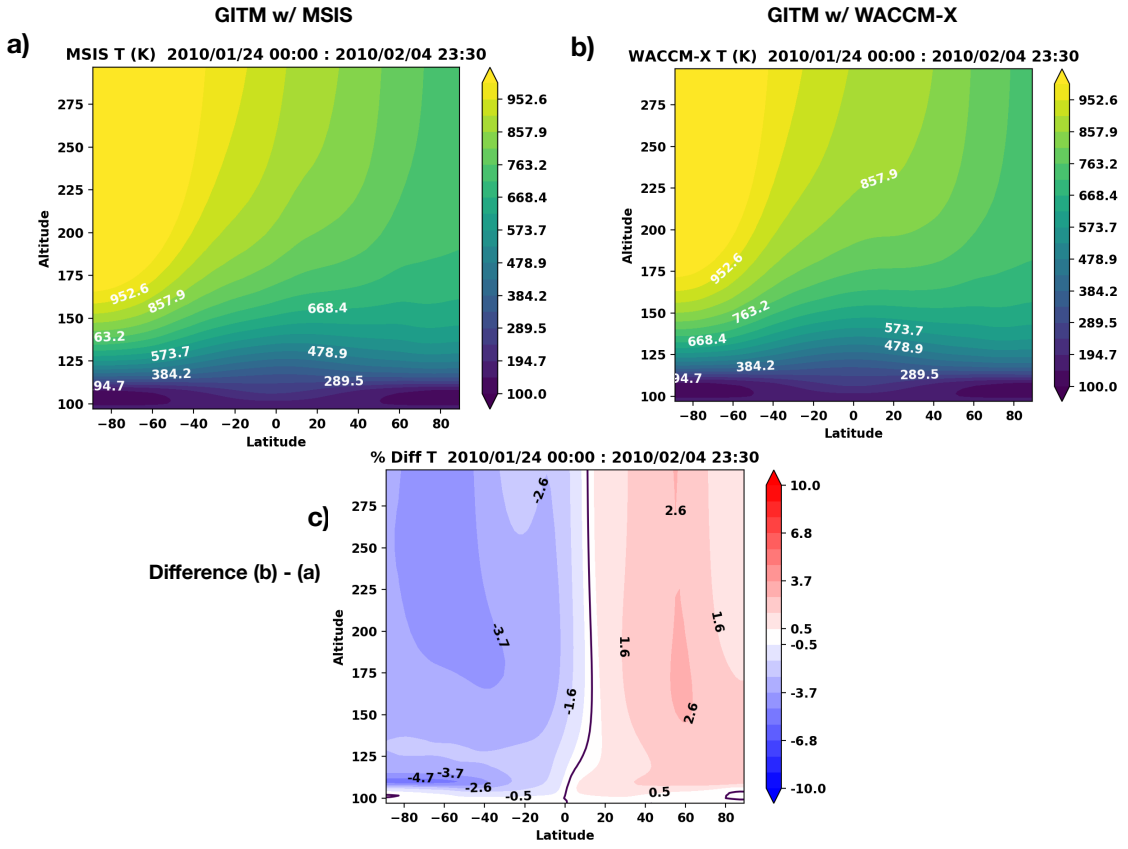

Figure 3.5: a) The contours indicate the temperature in K for GITM w/ MSIS zonally averaged for 01/24/2010 - 02/04/2010. b) Similar to a) but for GITM w/ WACCM-X. c) Zonally averaged percentage difference in temperatures GITM w/ WACCM-X (b) - GITM w/ MSIS (a). Note the thicker black contour line. This is the zero line where no difference is seen.

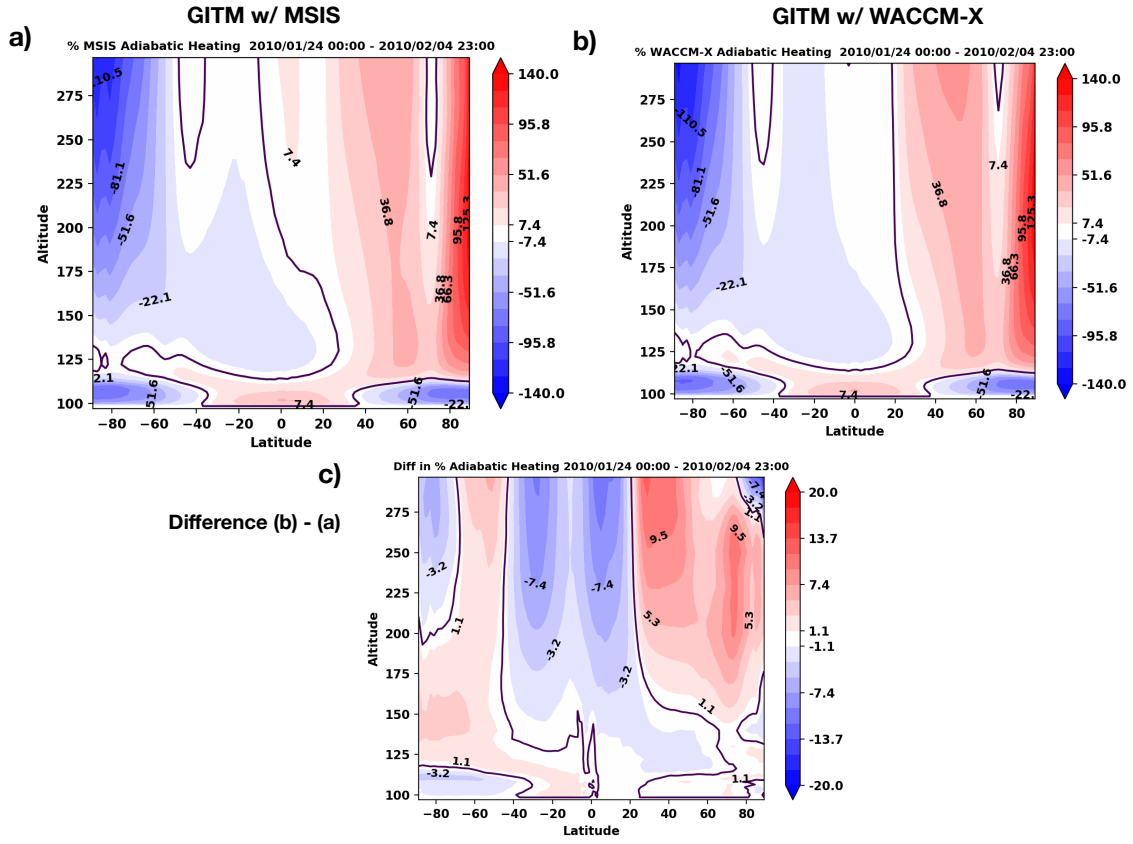

Figure 3.6: a) The contours indicate the percent Adiabatic heating per day (normalized by temperature) for GITM w/ MSIS zonally averaged for 01/24/2010 - 02/04/2010. b) Similar to a) but for GITM w/ WACCM-X. c) Zonally averaged Difference in adiabatic heating GITM w/ WACCM-X (b) - GITM w/ MSIS (a). Note the thicker black contour line. This is the zero line where no difference is seen.

is a sharp increase in the temperature with temperatures rising up to 1000 K in summer (southern) hemisphere. As seen in Figure 3.5c, the temperature difference between the two simulations starts at altitudes slightly above 100 km. In the summer hemisphere, GITM w/ WACCM-X has a lower temperature, while in the winter hemisphere, GITM w/ MSIS has a lower temperature. The temperature difference is as high as 5% (35 K) in the southern hemisphere. Thus, reversing the O number density distribution at the lower boundary leads to a change in lower thermospheric temperature, i.e., lower thermospheric temperatures occur at latitudes with higher O concentrations.

Figures 3.6a and 3.6b show the zonally averaged percent adiabatic heating per day (normalized by temperature) for GITM w/ MSIS and GITM w/ WACCM-X, respectively. For both the simulations the overall heating pattern remains similar.

In the lower thermosphere, between 100-120 km, the high latitudes have adiabatic cooling, and the lower latitudes have adiabatic heating. The reason for this is the equatorward wind cells as mentioned before and shown in Figure 3.3. Above 125 km, the summer hemisphere experiences adiabatic cooling (due to diverging winds), and the winter hemisphere gets warmer (due to converging winds) because of the summer to winter circulation. The difference between the two simulations is shown in Figure 3.6c. Between 100-120 km, in the summer hemisphere, GITM w/ WACCM-X has more adiabatic cooling because of larger equatorward winds. Similarly, in the winter hemisphere, GITM w/ MSIS has a tiny bit more adiabatic cooling. Above this altitude region, the adiabatic heating difference shows a roughly similar pattern as the wind difference of Figure 3.3c. In the summer hemisphere, except at middle-high latitudes, GITM w/ WACCM-X has more adiabatic cooling while in the winter hemisphere, GITM w/ MSIS has more adiabatic cooling. It should be noted that adiabatic heating differences in Figure 3.6c do not exactly correspond to the temperature difference of Figure 3.5c. This is because of the contribution of other terms of the energy equation.

Figures 3.7a and 3.7b show the percent difference between the two simulations for advective and radiative heating per day (normalized by temperature), respectively. For both GITM w/ MSIS and GITM w/ WACCM-X, advective heating shows similar heating patterns (not shown here), and largely follows the meridional wind patterns of Figure 3.3. Meridional winds in the upper thermosphere advect fluid parcels of higher temperature from summer to winter, resulting in heating in the winter hemisphere, whereas equatorward winds in the lower thermosphere advect fluid parcels of lower temperature from higher latitudes, resulting in cooling at lower latitudes. The difference between the two simulations as shown in Figure 3.7a is small relative to the adiabatic heating differences, and largely follows the meridional wind differences at mid-latitudes of Figure 3.3. The radiative cooling comes from a combination of CO_2 cooling in the 100-120 km altitude range, NO cooling in the 100-150 km range and O cooling above that. In the summer hemisphere, GITM w/ WACCM-X has larger O and therefore, less total radiative heating (more cooling), and in the winter hemisphere, GITM w/ MSIS has larger O and thus less radiative heating. The sum of these three terms, Figures 3.6c, 3.7a and 3.7b largely explains the temperature difference observed in Figure 3.5c, as the radiative heating mostly compensates for the anomalous differences (e.g., GITM w/ MSIS has larger adiabatic cooling in summer mid-high latitudes) in Figure 3.6c. The contribution of other terms of the energy equation are analyzed as well (not shown here) : (a) the difference between the two simulations for auroral heating is negligible in comparison to the above mentioned

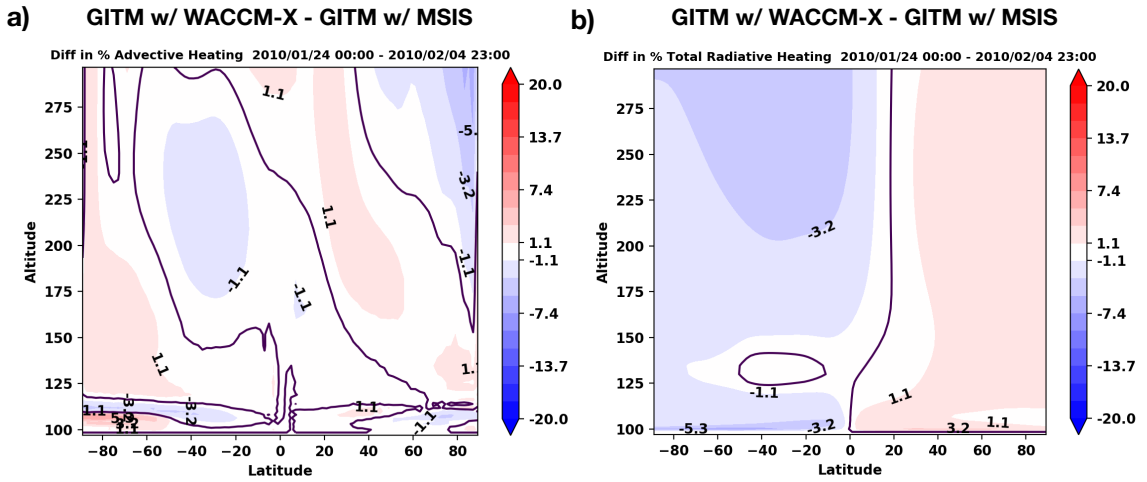

Figure 3.7: a) The contours indicate the difference in percent Advective heating per day (normalized by temperature), GITM w/ WACCM-X - GITM w/ MSIS, zonally averaged for 01/24/2010 - 02/04/2010. b) Similar to a) but for Radiative heating. Note the thicker black contour line. This is the zero line where no difference is seen.

terms, (b) chemical heating difference has a significant magnitude and reinforces the temperature differences in Figure 3.5c, (c) the molecular conduction heating and Joule heating differences have an opposite distribution as the other terms and mainly contribute in reducing the magnitude of the overall heating difference. The sum of these individual heating terms do not exactly correspond to the temperature distribution of Figure 3.5c, indicating the non-linearity of the thermospheric dynamics.

Figure 3.8 shows the mean height profiles of temperature, O, N_2, and O/N_2 separated into northern and southern hemispheres averaged poleward of $\pm$ 30° latitude. The red and blue curves are for GITM w/ WACCM-X and GITM w/ MSIS simulations, respectively. Larger differences between the curves exist in the summer (southern) hemisphere for all parameters. Figure 3.9 shows the percentage difference between the two simulations for temperature, O, N_2 and the electron density. Figures 3.8a and 3.9 show that the difference in temperature between the two simulations remains roughly constant with altitude. The effect of the change in temperature on neutral number densities can be understood using diffusive equilibrium as a rough guide (e.g., Schunk & Nagy, 2009).

$$n_s(z) = n_s(z_o) \times \frac{T_s(z_o)}{T_s(z)} \times e^{-\int_{z_o}^{z} \frac{(dz')}{H_s}}, \tag{3.2}$$

$$H_s = \frac{k_B T_s}{m_s g} \tag{3.3}$$

where n_s(z) and $T_s(z)$ are the number density and temperature at altitude z, respectively. $n_s(z_o)$ and $T_s(z_o)$ are the number density and temperature at a reference altitude z_o, respectively. H_s is the scale height for each species and is directly proportional to temperature, T_s and inversely proportional to the mass of the species, m_s. k_B is the Boltzmann constant and g is the acceleration due to gravity. We can break equation 3.2 into two contributing terms, the temperature ratio term, $\frac{T_s(z_o)}{T_s(z)}$ and the scale height term $e^{-\int_{z_o}^{z} \frac{(dz')}{H_s}}$ (This is just for nomenclature; the scale height term depends on temperature too).

For N_2 (assuming z_o to be at 100 km), number densities are the same between the two simulations at 100 km ($n_s(z_o)$) and the entire difference arises because of different distributions of O at the boundary. The temperature at the lower boundary ($T_s(z_o)$) is also the same between the simulations. In the southern hemisphere, GITM w/ WACCM-X has lower temperature ($T_s(z)$) (Figure 3.5) resulting in larger temperature ratio term, causing an increase in N_2 number densities. Whereas, the scale height term is smaller causing a decrease in N_2 number densities. The effect of these two terms

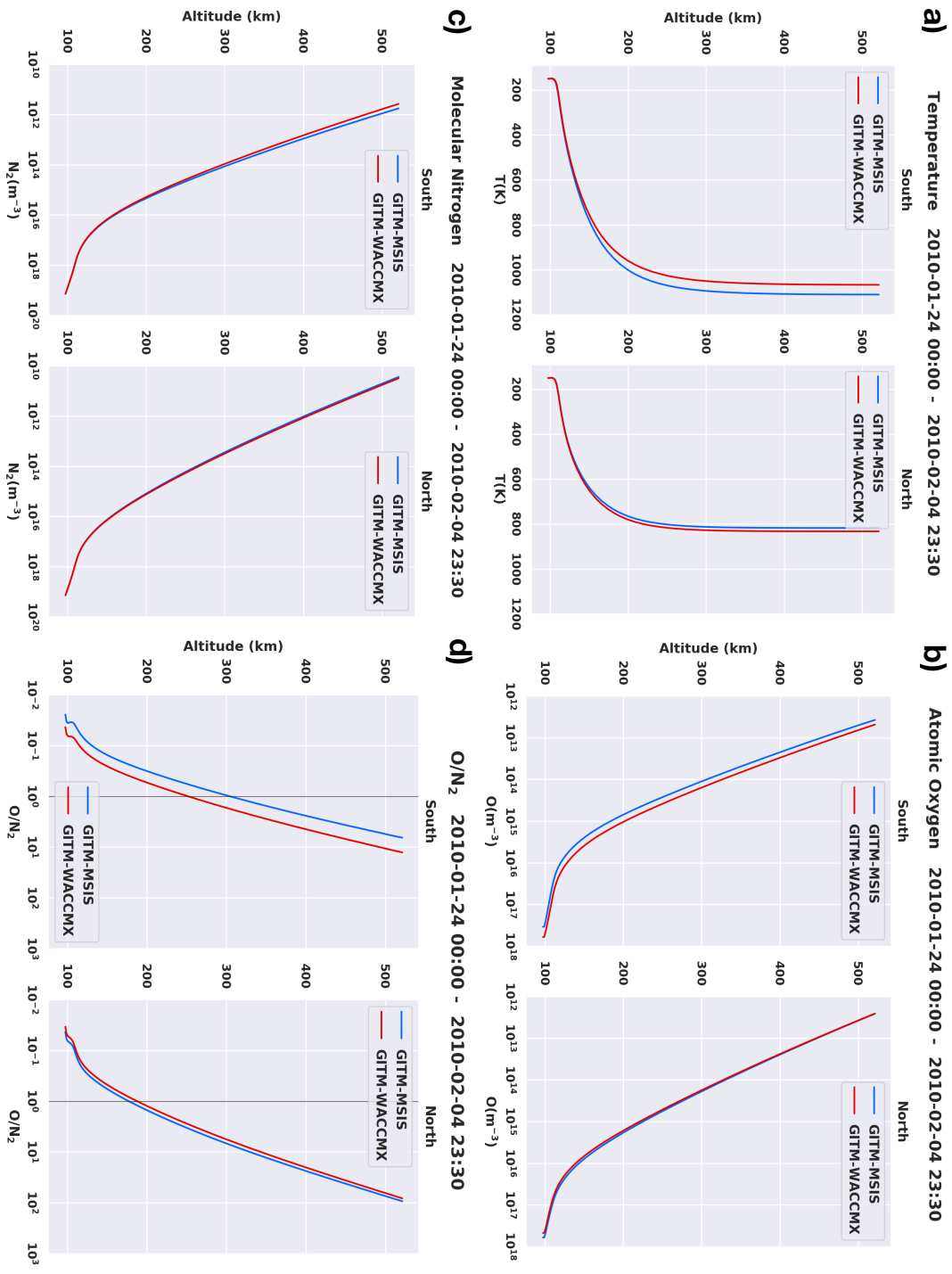

Figure 3.8: Height profile for a) Temperature (K), b) Atomic Oxygen (m^{-3}), c) Molecular Nitrogen (m^{-3}), d) O/N_2 averaged for 01/24/2010 - 02/04/2010. The x-axis indicates the values of each parameter while y-axis is the altitude. The red (blue) curves are for GITM w/ WACCM-X (MSIS). Each parameter is divided into northern and southern hemisphere, and cosine-weighted averaged for latitudes 30° - 90°. The black vertical line in d) indicates where O/N_2 is 1

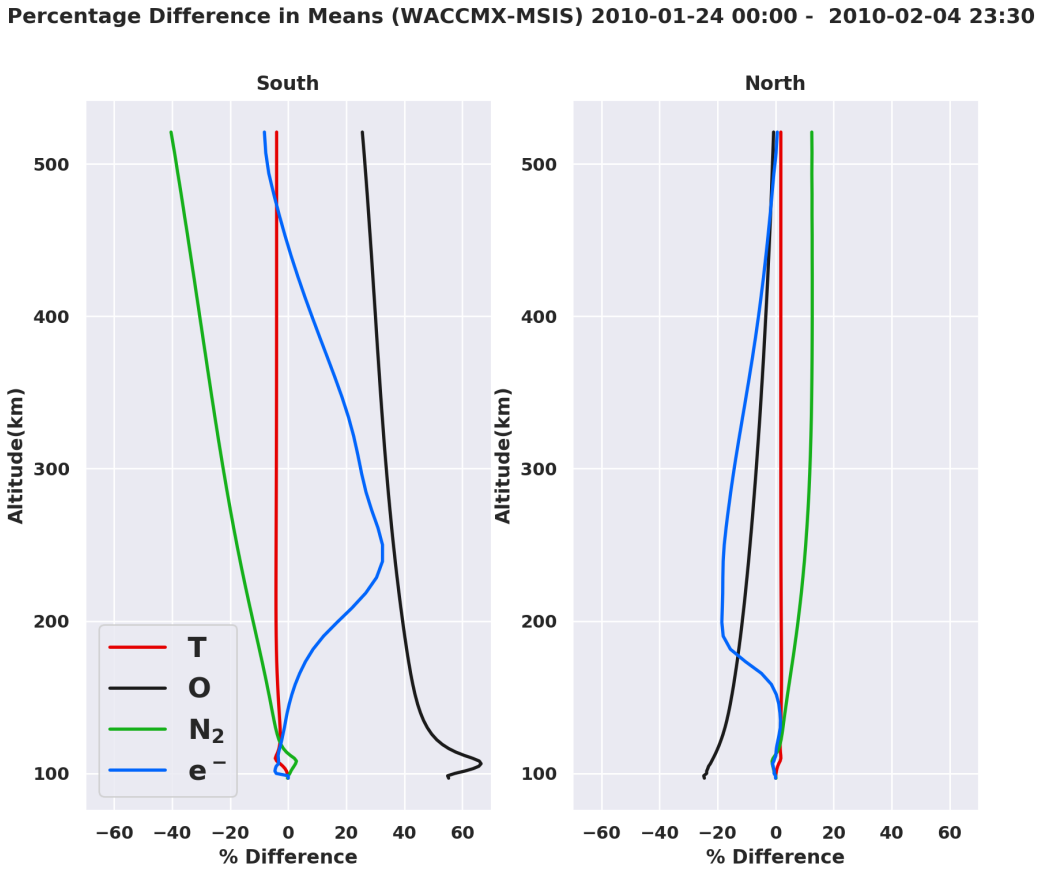

Figure 3.9: Height profile for the percentage difference in GITM w/ WACCM-X - GITM w/ MSIS for Temperature (red), O (black), N_2 (green), electron density (blue). These profiles are averaged for 01/24/2010 - 02/04/2010 and cosine-weighted averaged for latitudes 30° - 90° and divided into northern and southern hemisphere.

cancel each other and as a result, the difference in N_2 number densities between the two simulations is small in the lower thermosphere. In the upper thermosphere, the difference in the temperature ratio terms between the simulations remains the same, while the difference in the scale height terms becomes larger because of the integrated effect of exponential. As a result, N_2 decreases faster for GITM w/ WACCM-X in the southern hemisphere, because of lower temperature and smaller scale height. Therefore, the difference in N_2 between the two simulations increases with height as seen in Figure 3.9. The percentage difference of N_2 reaches about $\sim$10% in the northern hemisphere and $\sim$-30% in the southern hemisphere.

For the atomic oxygen profile in Figure 3.8b, the lower boundary number density term ($n_s(z_o)$) is important because the two simulations have different O at the lower boundary. The difference is as large as $\sim$50% at 100 km as seen in Figure 3.9. Moreover, the contribution of the temperature ratio term reinforces the difference in $n_s(z_o)$ between the two simulations. In the lower thermosphere, at southern latitudes, GITM w/ WACCM-X has larger $n_s(z_o)$ and larger temperature ratio term because of the lower temperature, which results in increased O. However, in the upper thermosphere, as the scale height term becomes important, a lower temperature and thus a lower scale height has the opposite effect on O as it acts to decrease the O number densities faster (also observed for N_2 above). Similarly, GITM w/ MSIS has higher temperature in this hemisphere resulting in larger scale height and a slower decrease. Therefore, the difference between the simulations reduces in magnitude with altitude in Figure 3.9. For the northern hemisphere, the difference between $n_s(z_o) \times \frac{T_s(z_o)}{T_s(z)}$ at lower altitudes is small as also shown in Figure 3.1. In the lower thermosphere, this term dominates. However, with increasing altitude, the effect of scale height causes the O number densities for the two simulations to become very close in magnitude and eventually at higher altitudes causes the difference to reverse. It should also be noted that the lower thermosphere is dominated by dynamics and the diffusive equilibrium reasoning here is used as a rough guide to understand the vertical profiles of different species.

Figure 3.8d shows the height profiles for O/N_2. O/N_2 increases with altitude due to larger rate of decrease of N_2 as compared to O (N_2 has smaller scale height because of its larger mass). In the southern hemisphere, GITM w/ WACCM-X has larger O and smaller N_2 resulting in larger O/N_2 which affects the electron density. In the northern hemisphere, the situation is reversed where GITM w/ MSIS has larger O/N_2 and electron density. Figure 3.9 also shows the percentage difference in height profile of electron density between the two simulations. The difference ranges

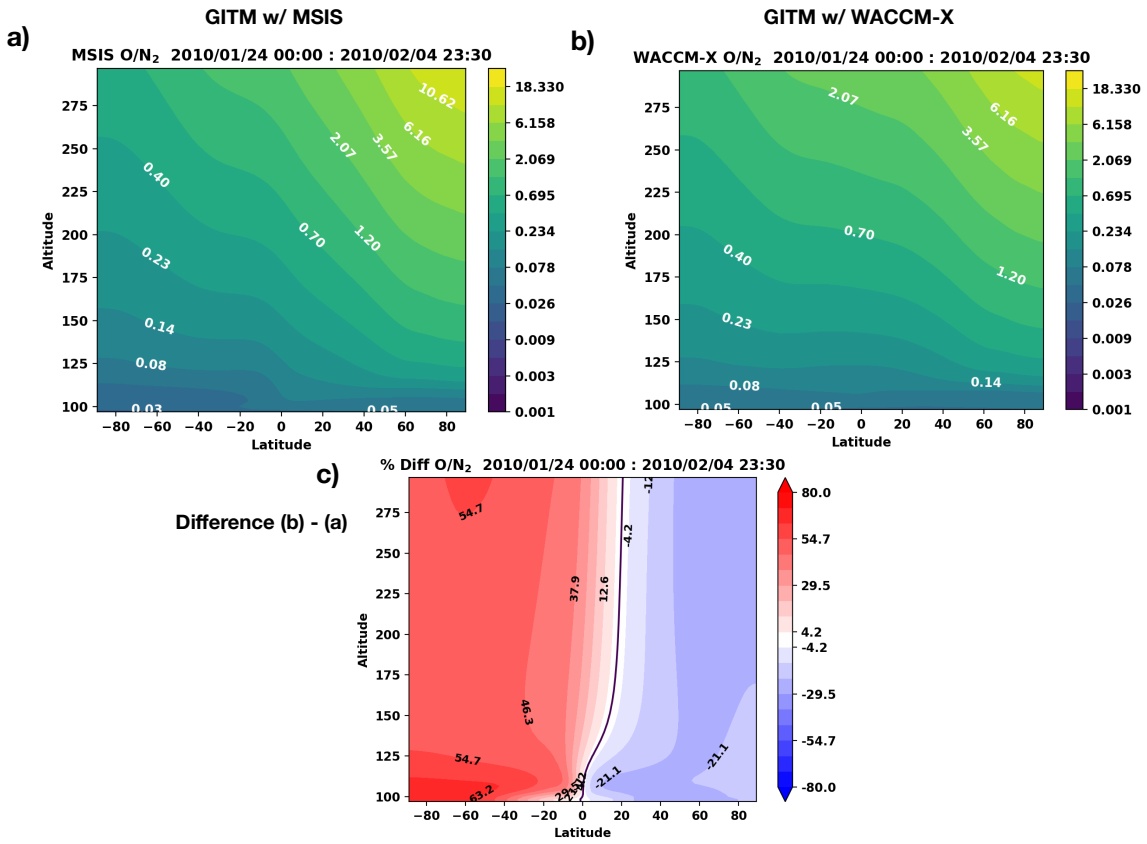

Figure 3.10: a) The contours indicate the O/N_2 for GITM w/ MSIS averaged for 01/24/2010 - 02/04/2010 using a logarithmic colorscale. b) Similar to a) but for GITM w/ WACCM-X. c) Averaged Difference in O/N_2 GITM w/ WACCM-X (b) - GITM w/ MSIS (a). Note the thicker black contour line. This is the zero line where no difference is seen.

between 10 - 40% at F-region altitudes and follows the O/N_2 difference in both the hemispheres.

Contour plots for O/N_2 are shown in Figure 3.10. Above ~120 km, both simulations show similar patterns in O/N_2 with larger values in the winter hemisphere. This is indicative of the summer to winter circulation shown in Figure 3.3. Figure 3.10c shows the percent difference between the two simulations. The difference is as large as 60% between the two simulations in the lower thermosphere in the southern hemisphere. The effect of lower thermospheric O distribution superimposes on the overall O/N_2 distribution in the upper thermosphere, leading to increases in O/N_2 in the hemisphere with larger lower thermospheric O. The effect of using O number densities from WACCM-X is to decrease the overall O/N_2 gradient between the two hemispheres. This result is similar to that observed by Qian & Yue (2017). When

comparing the global averages, GITM w/ WACCM-X has higher O/N_2, resulting in larger electron density.

Above 125 km, as shown in Figure 3.3, the winds are dominated by northward interhemispheric winds. Figure 3.3c showed that the winds in the upper thermosphere are slower for GITM w/ WACCM-X in the southern hemisphere and faster in the northern hemisphere. From Figure 3.10c, GITM w/ WACCM-X has ∼20-30% more O/N_2 than GITM w/ MSIS in the equatorial region. This mainly comes from +∼20% in O and -∼10% difference in N_2. It can be observed from Figure 3.4e that GITM w/ WACCM-X has smaller northward directed pressure gradient in most of the summer and winter hemisphere at mid-latitudes and larger at higher latitudes in the winter hemisphere. The latitudinal gradient of higher equatorial O in GITM w/ WACCM-X leads to slower northward winds in the summer hemisphere and faster northward winds in the winter hemisphere as compared to GITM w/ MSIS which has higher winter O. This change in interhemispheric winds is in equilibrium with the reduced O/N_2 gradient for GITM w/ WACCM-X. Because the thermosphere is a non-linear system, changes in densities, temperatures, and winds further affect the transport and density distribution. Only the first order impact of lower thermospheric O distribution on the upper thermosphere is considered here.

Figure 3.11 shows a comparison between integrated O/N_2 for the two simulations and GUVI observations. As mentioned previously, using GITM w/ WACCM-X decreases the gradient in O/N_2 between the two hemispheres. Figure 3.11 shows O/N_2 is higher for GITM w/ WACCM-X in the southern hemisphere and lower in the northern hemisphere as compared to GITM w/ MSIS. In both hemispheres, GITM w/ WACCM-X matches with GUVI observations (Figure 3.11c) better. We would expect the correction of N_2 and other parameters in the lower thermosphere to bring the model results even closer to the observations. It was shown by Perlongo et al. (2018) that GITM has lower summer electron densities than the GPS TEC observations in both the northern and southern mid-latitudes. Using GITM w/ WACCM-X at the lower boundary, this will potentially be corrected as the electron density depends on the O/N_2.

When the opposite solstice (i.e., June) is considered, the opposite behavior is observed. Figure 3.12 shows atomic oxygen distributions and O/N_2 for the month of June. GITM w/ WACCM-X and SABER number densities are similar in O distribution, although they are off in magnitude, while the MSIS driven simulation has the opposite gradient in O. Figure 3.12d shows the height profile of difference in O/N_2 between the two simulations. This is opposite of Figure 3.10c. Thus, the opposite O

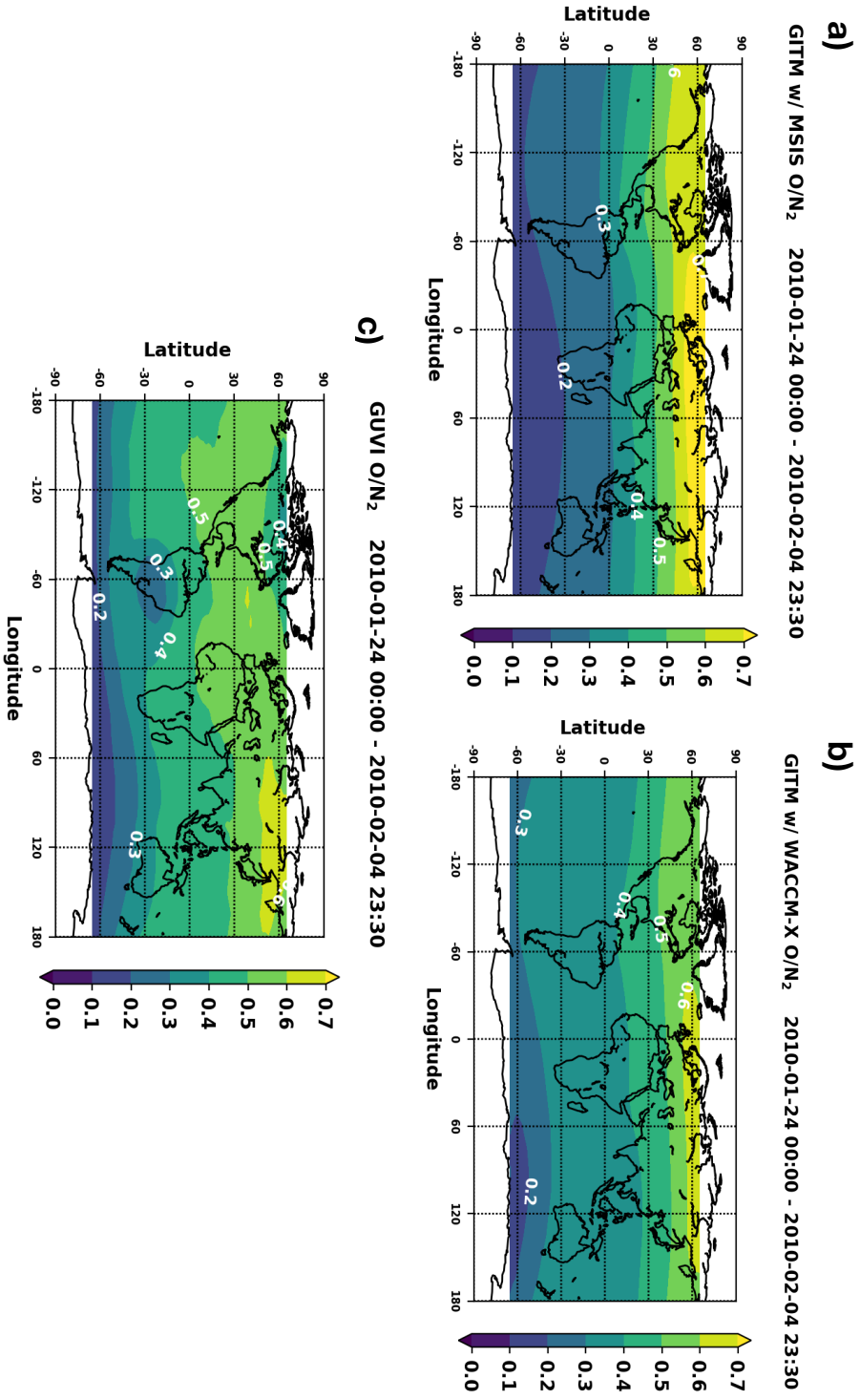

Figure 3.11: Integrated O/N_2 with a reference altitude of 10^{17} cm^{-2} for a) GITM w/ MSIS, b) GITM w/ WACCM-X, c) TIMED GUVI data. The O/N_2 in GITM are sampled at GUVI times and locations.

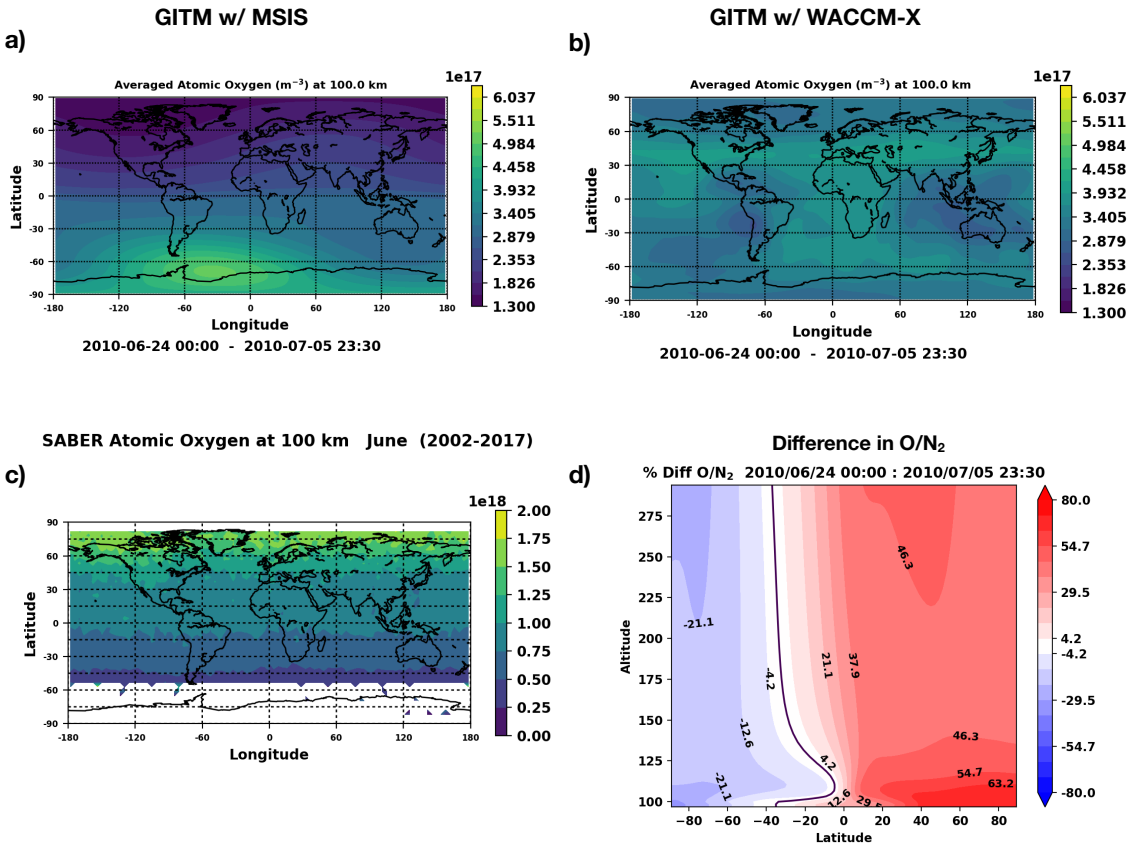

Figure 3.12: Atomic Oxygen (m^{-3}) at 100 km averaged from 06/24/2010 - 07/05/2010 for a) GITM w/ MSIS, b) GITM w/ WACCM-X. c) Atomic Oxygen for SABER in m^{-3} interpolated at 100 km for the month of January binned together for the years 2002-2017. The bin size is $4° \times 4°$. d) Averaged Difference in O/N_2 GITM w/ WACCM-X - GITM w/ MSIS for 06/24/2010 - 07/05/2010. Note the thicker black contour line. This is the zero line where no difference is seen.

distribution in the lower thermosphere affects both solstices in a similar, but opposite, way.

As mentioned above, the decrease in O/N_2 gradient in GITM w/ WACCM-X is consistent with the results obtained by Qian & Yue (2017). They explained the mechanism via vertical mixing due to lower thermospheric winter to summer circulation but did not show the species distribution in the lower thermosphere as a result of this circulation. Whereas this work starts with the species distribution in the lower thermosphere to observe the impact on the upper thermosphere. It is found that the O distribution at the mesopause affects the upper thermosphere in a more direct way than just through molecular diffusion : it impacts the wind and temperature distributions which subsequently changes the scale heights of molecular species. It is also found that using this distribution increases the global O/N_2 which is opposite to the result obtained by Qian & Yue (2017). However, this difference depends on the lower thermospheric species distribution from WACCM-X in our study and thus will change depending on the variability of the phenomena leading to this distribution.

3.4 Conclusions

Variations in O in the mesosphere and the lower thermosphere affect the composition and dynamics of the upper thermosphere as it becomes a major species above 200 km. Previous studies (J. P. Russell et al., 2004; Smith et al., 2010; Rezac et al., 2015) have shown that the summer hemisphere has higher atomic oxygen concentration in the lower thermosphere (90-100 km). Qian et al. (2017) suggested that the lower thermosphere winter to summer circulation is responsible for the high summer concentration of CO_2 in this region. In this study, we investigate the effect of the MLT O distribution on the composition and dynamics of the middle-upper thermosphere using an ionosphere-thermosphere model, GITM. Conventionally, GITM uses O distribution that is higher in winter from MSIS at its lower boundary. We change the lower boundary O distribution to be higher in summer, as specified by WACCM-X, which also matches better with the observations from SABER. We find that the reversal of O hemispheric concentration changes the magnitudes of the winds between 100-120 km due to the differences in pressure gradients. The hemisphere with larger O number densities has larger equatorward winds resulting in adiabatic cooling in that hemisphere. Larger radiative cooling in that hemisphere also leads to the cooling of that hemisphere. Other terms of the temperature equation such as advective, chemical, auroral, Joule and molecular conduction heating also change and affect the

temperature distribution. Overall, the lower temperature decreases the scale height of N_2 and other molecular species in the hemisphere with more lower thermospheric O, resulting in a reduction of their number densities at higher altitudes. We also find that the averaged O densities at 100 km in both MSIS and WACCM-X are much lower than SABER. If these O densities would have been much closer to SABER, we would expect higher O in the thermosphere in both the simulations. We would also expect a net lower temperature in the thermosphere due to larger radiative cooling, which would then also change the wind magnitudes.

In January, the southern hemisphere has larger atomic oxygen in GITM w/ WACCM-X (and SABER data) as compared to GITM w/ MSIS, larger equatorward winds, more adiabatic and radiative cooling, lower temperature and lower N_2. This results in an increased O/N_2 and electron densities in the southern (summer) hemisphere in the GITM w/ WACCM-X simulation. The opposite behaviour is observed in the northern (winter) hemisphere. The change in O/N_2 is as large as 63% in the summer hemisphere in the lower thermosphere. This also slows down the northward interhemispheric winds in the summer hemisphere and speeds them up in the winter hemisphere. It is found that the vertical column integrated O/N_2 in GITM w/ WACCM-X matches the TIMED GUVI O/N_2 measurements better in both the hemispheres, as GITM w/ MSIS tends to understimate O/N_2 in the summer and overestimate it in the winter hemisphere. We would expect the correction of other mesopause boundary drivers within GITM such as N_2 and temperature to further improve the agreement between model results and the observations.

The results of this study are summarized in Figures 3.13 and 3.14.

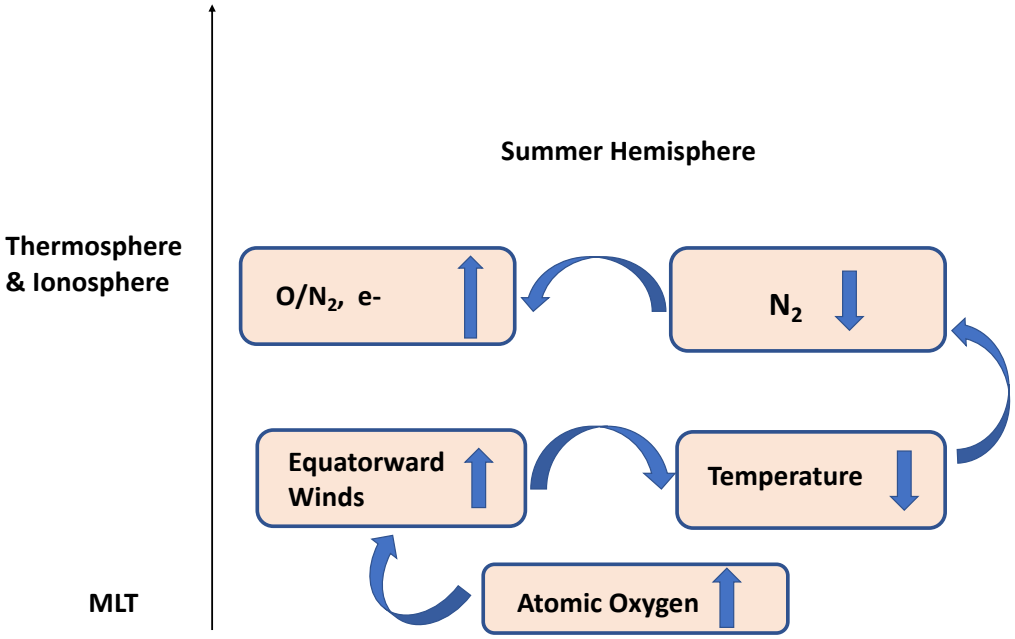

Figure 3.13: Illustration summarizing the results of this study in the summer hemisphere.

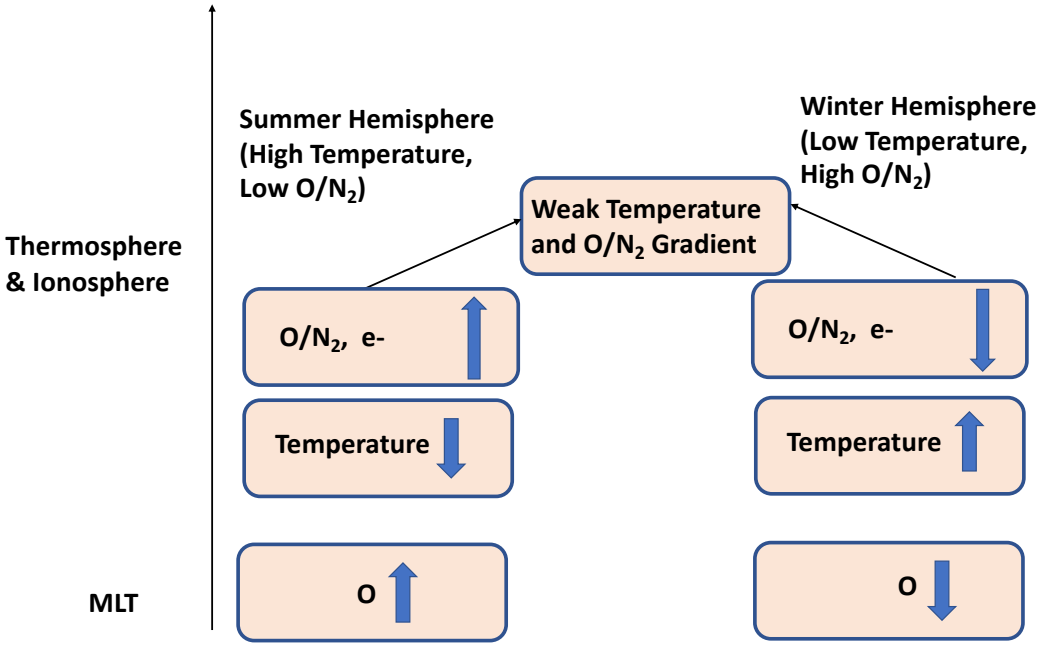

Figure 3.14: Illustration summarizing the results of this study in both the hemispheres.

CHAPTER IV

Impacts of Lower Thermospheric Atomic Oxygen and Dynamics on Thermospheric Semiannual Oscillation Using GITM and WACCM-X

This chapter investigates the role of the MLT composition and dynamics on the middle-upper thermospheric semiannual oscillation. It is currently under review in the Journal of Geophysical Research: Space Physics. The GITM and WACCM-X runs are available in the University of Michigan's Deep Blue Data repository (Malhotra & Ridley, 2021).

The keypoints of this chapter are :

- GITM successfully reproduces the T-I SAO with equinoctial maxima, using both constant and MSIS [O] at lower boundary.
- Atomic oxygen at ∼97-100 km from SABER has an SAO with maxima at solstices and at summer mid-high latitudes.
- Using SABER-like [O] from WACCM-X at GITM lower boundary reverses the T-I SAO, because of solstitial accumulation of [O] at lower latitudes.

4.1 Introduction

The Earth's atmosphere is an open system with complex interplay between internal and external drivers resulting in complicated non-linear coupling mechanisms. The region above 100 km is usually referred to as the Earth's upper atmosphere with the neutral thermosphere coexisting with the partly ionized ionosphere. Both the thermosphere and ionosphere exhibit several periodic variations in densities and temperature ranging across many time scales from minutes to a few years (Rishbeth,

2007). These include variations due to gravity waves (e.g., S. L. Bruinsma & Forbes, 2008; Miyoshi et al., 2014), tides (e.g., Forbes et al., 2009; Hagan et al., 2009), planetary waves (Sassi et al., 2016), annual and semiannual oscillation (e.g., Jones Jr., Emmert, et al., 2018), quasi-biennial oscillation (e.g., Malhotra et al., 2016), and 11-year solar cycle (e.g., J. T. Emmert et al., 2008; Burns et al., 2015). Amongst the long term variations, the thermospheric and ionospheric annual oscillation (T-I AO) and the semiannual oscillation (T-I SAO) have the largest magnitudes and were initially observed in neutral densities derived from satellite drag measurements by Paetzold & Zschörner (1961). The global T-I AO has a minimum in neutral densities in July and has partially been attributed to the changing distance between the Sun and the Earth (Volland et al., 1972), and is still under investigation. In this study, we mainly focus on the T-I SAO. We will briefly review some of the pioneering works on T-I SAO in the following section.

4.1.1 Previous Work

The global T-I SAO has maxima in April and October and minima in January and July, and was initially attributed to the semiannual effect of geomagnetic activity (Paetzold & Zschörner, 1961). However, the SAO in geomagnetic activity itself was not well understood at the time (e.g., Bartels, 1932; Boller & Stolov, 1970). Amongst many theories, the Russell-McPherron (R-M) effect (C. T. Russell & McPherron, 1973) has been studied widely to explain the semiannual variation in geomagnetic activity. In this mechanism, during equinoxes, the magnetic field of the Sun in the ecliptic plane has larger southward magnitude at Earth in the Geocentric Solar Magnetospheric (GSM) coordinates, resulting in stronger reconnection events. Walterscheid (1982) suggested that the semiannual variation in temperature (Joule Heating) due to R-M effect is responsible for the globally averaged SAO in mass density. After Paetzold & Zschörner (1961), several other studies observed the SAO signature in O/N_2, atomic oxygen (O), temperature and the ionospheric F2 layer (e.g., King-Hele, 1966, 1967; King-Hele & Kingston, 1968; Jacchia et al., 1969; T. J. Fuller-Rowell, 1998; Rishbeth et al., 2000; Rishbeth & Mendillo, 2001). The amplitude of the global T-I SAO has been recorded to be $\sim$15% in mass density at 400 km and ionospheric Total Electron Content (TEC) relative to the global annual average (J. Emmert, 2015; Jones Jr. et al., 2017). The T-I SAO was initially reproduced using temperature variations by the Jacchia series of thermospheric models (Jacchia, 1965, 1970). However, it was later observed that the temperature variations could not completely explain the SAO amplitude in thermospheric density and composition at solar minimum (G. Cook

& Scott, 1966; G. Cook, 1967; G. E. Cook, 1969b). G. E. Cook (1969a) reported on the SAO in mass density at 90 km using rocket data and suggested that the source of T-I SAO is possibly in the mesosphere or the stratosphere. Jacchia (1971) and Jacchia (1977) later updated their thermospheric model such that the T-I SAO was considered as a density variation rather than purely a temperature variation.

An internal thermospheric mechanism called the 'thermospheric spoon' (TSM) was proposed by T. J. Fuller-Rowell (1998) using the Coupled Thermosphere Ionosphere Model (CTIM) (T. Fuller-Rowell et al., 1996). According to this mechanism, at solstices, due to the tilt of the Earth, the temperature gradient between the two hemispheres results in a global-scale, summer-to-winter interhemispheric circulation. It is also marked by upwelling in the summer and downwelling in the winter. This circulation acts as a large-eddy resulting in a much more mixed thermosphere and a smaller scale height during solstices. Jones Jr., Emmert, et al. (2018) showed using controlled simulations of Thermosphere Ionosphere Mesosphere Electrodynamics General Circulation Model (TIME-GCM) that the magnitude of SAO reduces to 2% relative to the annual average when the tilt of the Earth is reduced to 0°, thus proving that the obliquity of the Earth is the largest factor for the SAO in the Earth's upper atmosphere. The TSM also results in larger densities of lighter species, such as atomic oxygen and helium, in the winter hemisphere (Mayr & Volland, 1972; Mayr et al., 1978; Cageao & Kerr, 1984; T. J. Fuller-Rowell, 1998; Rishbeth & Müller-Wodarg, 1999) via vertical and horizontal transport. The lifetime of O increases to several months in the MLT. As a result, it becomes susceptible to dynamic effects above the MLT region (Brasseur & Solomon, 1984). Higher [O] in the winter have been observed at altitudes as low as 140 km (K. U. Grossmann et al., 2000). Sutton (2016) showed that the meridional transport of lighter species is linked with vertical upwelling and downwelling in the two hemispheres, along with horizontal divergence and identified these as the primary mechanisms for the accumulation of light species at high winter latitudes.

As stated above, the IT system has many external drivers. One such driver is the lower atmosphere. Soon after its discovery in the upper thermosphere, the SAO was found in the lower thermosphere and near the mesopause (e.g., G. E. Cook, 1969b,a; King-Hele & Kingston, 1968; King-Hele & Walker, 1969; Groves, 1972). Waves propagating up from the lower atmosphere can couple linearly and non-linearly with the background atmosphere or with each other and significantly affect the T-I SAO (R. E. Newell, 1966; Volland et al., 1972). Eddy diffusion has historically been used in atmospheric models to parametrize the effects of subgrid-scale gravity wave

mixing and breaking on the background densities, temperature and winds (Hodges, 1969). Qian et al. (2009) and Qian et al. (2013) using Thermosphere Ionosphere Electrodynamics General Circulation Model (TIE-GCM) observed that the magnitude of SAO in neutral densities, composition, and peak electron density and height can be improved by introducing a seasonal variation in the eddy diffusion parameter (K_{zz}) at the lower boundary of the model, with a primary maximum during summer and minima during the equinoxes. A larger value of K_{zz} in the mesosphere and lower thermosphere (MLT) during the solstices will result in higher concentration of molecular species and lower concentration of lighter species, thus, decreasing the O/N_2, mean scale height, and total density in the thermosphere. The amplitude of SAO in K_{zz} has been under investigation by G. Swenson et al. (2018) and G. R. Swenson et al. (2019). It has recently been realized that the K_{zz} by Qian et al. (2009) represents net cumulative coupling from the lower atmosphere (see Jones Jr. et al. (2017)) as Salinas et al. (2016) found the amplitude of SAO in K_{zz} derived from SABER CO_2 to be much smaller.

In fact, Jones Jr. et al. (2017) pointed out that K_{zz} due to gravity waves may not be a primary driver for SAO in the lower thermosphere but may only affect the phase of SAO. Tidal dissipation from the lower thermosphere also affects the T-I SAO (Siskind et al., 2014; Jones Jr. et al., 2017). Jones Jr. et al. (2017) used TIME-GCM to analyze the contribution of different terms in the globally averaged O continuity equation. They found that the SAO in [O] is forced by a cumulative effect of the advective, tidal and diffusive transport of O. O is the major species above 200 km, therefore, any long-term variations are directly manifested in neutral and ionospheric densities in the upper atmosphere. Jones Jr., Emmert, et al. (2018) suggested that the upper mesospheric O chemistry might play an important role in the return branch of the thermospheric spoon circulation, but recently showed its effects to be negligible on the T-I SAO amplitude (Jones Jr. et al., 2021). Qian et al. (2017) and Qian & Yue (2017) showed that lower thermospheric winter-to-summer residual circulation can also affect the amount of upwelling and downwelling at higher latitudes, thereby affecting the T-I SAO.

4.1.2 Scope and Approach

First principles IT models such as TIE-GCM (Richmond et al., 1992) and Global Ionosphere Thermosphere Model (GITM) (A. Ridley et al., 2006) have been widely used to study the contribution of the lower atmosphere to T-I SAO (e.g., Qian et al., 2009, 2013; Salinas et al., 2016; Q. Wu et al., 2017). This is because their lower

boundaries are at roughly 95 km or slightly above, therefore providing an opportunity to study the effect of different (imposed) lower boundary assumptions. Another category of models are the whole atmosphere models, e.g., Whole Atmosphere Model (WAM) and Whole Atmosphere Community Climate Model with thermosphere and ionosphere extension (WACCM-X), that simulate the entire atmospheric column (i.e., ground-to-space) and thus include physical and chemical processes that IT models do not have. These models are invaluable in understanding the coupling of lower atmospheric phenomena and the IT system. The use of both types of models has the potential to significantly advance our understanding of the contribution of the lower atmosphere to the IT system. The coupling of the lower atmosphere with an IT model can be achieved through multiple mechanisms, for example, by specifying large-scale MLT winds, densities and temperatures at the lower boundary, by introducing variations in eddy diffusion parameter, and by including migrating and non-migrating tides (and other waves) in the state variables.

The motivation for this study is to better understand how the T-I SAO is controlled by the [O] and winds distribution in the MLT region. It is important because the variations due to dynamics in the lower thermosphere map to higher altitudes via diffusive equilibrium (Picone et al., 2013). This goal is achieved through the alteration of GITM's lower boundary, which is typically specified by the empirical model, Mass Spectrometer and Incoherent Scatter Radar Model (MSIS). However, there is a huge uncertainty regarding the dynamics, turbulence, neutral densities near the lower boundary of GITM. This is because, the lower boundary of GITM is in the MLT at $\sim$97 km, which lacks long-term, global observations. Therefore, in order to improve the SAO, we use the whole atmosphere model, WACCM-X as the lower boundary for GITM and compare the effect on the T-I SAO relative to MSIS driven GITM. There is evidence that since WACCM-X includes the physical mechanisms of the lower atmosphere, it best represents the MLT state and thus the thermosphere more accurately (Dunker et al., 2015; McDonald et al., 2015; J. Liu et al., 2018; Qian et al., 2018; Huba & Liu, 2020). The use of WACCM-X is also motivated by different spatial and temporal variations of [O] in the lower thermosphere between MSIS and WACCM-X. The opposite latitudinal distribution in MSIS as compared to SABER data and WACCM-X has been previously studied (Malhotra et al., 2020). At $\sim$95-100 km, MSIS shows a winter maxima, whereas SABER and WACCM-X show summer maxima (J. P. Russell et al., 2004; Smith et al., 2010; Sheese et al., 2011; Malhotra et al., 2020). Moreover, the global mean of [O] within WACCM-X in the MLT is almost 180° out-of-phase with MSIS. We investigate the effects of these opposite latitudinal

and temporal [O] variations on the T-I SAO. We also study the effects of having no SAO at the lower boundary, and the effects of constraining the dynamics in the lower thermosphere towards WACCM-X.

4.2 Methodology

4.2.1 Models

4.2.1.1 Global Ionosphere Thermosphere Model (GITM)

GITM is a physics based first principles model developed at the University of Michigan by A. Ridley et al. (2006) that self-consistently solves the Navier Stokes equations for neutral, ion, electron densities, dynamics, and temperatures in the IT region. It uses a three dimensional spherical grid with longitude, latitude and altitude as the coordinate system with the lower boundary in the MLT at ∼97 km and the upper boundary at ∼500-600 km. In its default mode, MSIS and Horizontal Wind Model (HWM) are used for initial and lower boundary conditions. The IT state in GITM depends on the external drivers of the model, such as solar Extreme Ultraviolet (EUV) inputs, solar wind parameters, energetic electron precipitation, and high latitude electrical fields. It can couple with other empirical and physics based estimates for these inputs. In the configuration used in this study, GITM uses the Weimer model (Weimer, 2005) for high-latitude potential, Flare Irradiance Spectral Model (FISM) EUV model (Chamberlin et al., 2008) for estimates of solar irradiance at different wavelengths and NOAA POES hemispheric power-driven model (T. J. Fuller-Rowell & Evans, 1987) for estimates of energetic particle precipitation. The version of HWM used in this study is HWM14 (Drob et al., 2015).The GITM simulations in this study have a resolution of 2° × 4° (latitude×longitude), and roughly a third of scale height in altitude.

4.2.1.2 Whole Atmosphere Community Climate Model with Thermosphere and Ionosphere Extension (WACCM-X)

WACCM-X is a whole atmosphere model that is built on top of the Whole Atmosphere Community Climate Model (WACCM) and covers the atmospheric region from the surface to the 500-700 km (H. Liu et al., 2010; H.-L. Liu et al., 2018). WACCM itself is built on top of the Community Atmosphere Model (CAM) (S.-J. Lin, 2004) and is a part of Community Earth System Model (CESM). WACCM-X uses a conventional spatial grid of latitude, longitude and pressure. It includes self-

consistent neutral dynamics, electrodynamics, F-region ion transport and solves for ion/electron temperatures. Gravity waves are parameterized from both orographic and non-orographic sources and thus can be used for studying the coupling of IT system with both geomagnetic drivers and the lower atmosphere (H.-L. Liu et al., 2018). In this study, we use WACCM-X 2.0 in the Specified Dynamics (SD) configuration in our simulations and will refer to it simply as WACCM-X. In the SD configuration, temperature, winds and surface pressure in the troposphere and stratosphere are specified from the Modern Era Retrospective Analysis for Research and Applications (MERRA) dataset (Rienecker et al., 2011). The simulations used in this study have a horizontal resolution of $1.9^\circ \times 2.5^\circ$ (latitude×longitude).

Here we use the hourly averaged WACCM-X output files. WACCM-X outputs the mixing ratios of different species on a pressure grid with temperature, altitude, and winds. Total number density is derived from pressure and temperature using the ideal gas law. Vertical motion (ω) is output in the units of Pa/s and is converted to vertical wind, W in m/s as follows :

$$W = -\frac{\omega}{\rho g}, \tag{4.1}$$

where ρ is the total mass density and g is the acceleration due to gravity (assumed constant with altitude). Since GITM uses an altitude grid, the WACCM-X total number density is logarithmically interpolated to an altitude grid in each grid cell. This altitude grid is uniformally defined from 95 km to 152.5 km. Other parameters such as mixing ratios, temperature and winds are linearly interpolated onto this altitude grid. The mixing ratios and total number densities are then multiplied to output the number density for each species on this new grid.

4.2.1.3 Mass Spectrometer and Incoherent Scatter Radar Model

The MSIS-class models (Hedin et al., 1977; Hedin, 1983, 1987, 1991) are empirical models of composition, temperature, and neutral density of Earth's atmosphere, derived from ground, rocket and satellite-based measurements. MSISE-86 covers the altitude region from 90 km to the exobase, while MSISE-90 has the lower boundary at the surface. These models were a significant improvement over the Jacchia-class models, which were also empirical models that estimated total mass density from orbital decay of objects that flew from 1961-1970 (Jacchia, 1965, 1970, 1971). NRLMSISE-00 (Picone et al., 2002) also extends from the ground to the exobase and includes additional data spanning 1965-1983 from the Jacchia models. This includes data from

Table 4.1: GITM Runs

Simulation	Density Lower Boundary Condition	Winds Lower Boundary Condition
G/MSIS	MSIS	HWM
G/NOSAO	MSIS with AO and SAO set to 0	0
G/WX	WACCM-X	WACCM-X
G/NUDGE	WACCM-X	Nudged to WACCM-X till 140 km

satellite accelerometers, incoherent scatter radars, mass spectrometers, solar ultraviolet occultation, and drag measurements up to the mid-to-late 1990s. It also contains more data covering high latitudes and extreme cases of geomagnetic forcing. In this study, we use NRLMSISE-00 for the lower boundary condition in GITM. A new, improved NRLMSIS 2.0 model (J. T. Emmert et al., 2020), that ingests SABER [O] measurements has recently been released, and much better represents MLT [O]. At the time of writing this manuscript, all the simulations were already completed with the NRLMSISE-00. We do plan to change the lower boundary in GITM to NRLMSIS 2.0 in the future. In this manuscript, we will refer to NRLMSISE-00 simply as MSIS.

4.2.2 GITM Simulations

The GITM simulations used in this study are for 2010 and use measured time-varying geospace indices to specify high-latitude and solar EUV drivers so that the results can be validated against observational datasets. This year was chosen because it was a geomagnetically quiet year during a solar minimum, which emphasizes the lower atmospheric effects on the upper thermosphere. The lower boundary of GITM is controlled by two ghost cells in altitude below 100 km which are filled with densities, temperatures and winds. These are then used in the solvers for the first couple of lower cells in GITM, so that they control the dynamics in these cells. Table 4.1 summarizes these simulations. All these simulations use a K_{zz} value of 300 m^2/s that is constant with time.

The default configuration is the G/MSIS simulation. In this configuration, for neutral densities, only the second ghost cell nearest to 100 km is specified from MSIS. For the first cell, a hydrostatic solution for most neutral densities is projected from the second cell so as to not drive constant non-zero acceleration. [O] and T are specified from MSIS and kept the same in both the cells. Horizontal winds are specified by HWM in the second cell and determined in the first cell similar to densities using the gradients from cells above. Since HWM only has horizontal winds, the vertical velocity for all species is determined in both the cells so as to have zero flux through the lower boundary, i.e., the value in the first (second) ghost cell is the opposite of

the value in the second (first) real cell. In the second simulation, G/NOSAO, we use GITM in its default configuration, but MSIS has the AO and SAO flags turned off for both symmetrical and asymmetrical components. The horizontal winds in the second cell are zero. In the first cell, they are non-zero and determined as discussed above.

In the third simulation, G/WX, we use WACCM-X as the lower boundary condition. For densities, similar to the default configuration, values are specified in the second cell only and hydrostatic condition is enforced in the first cell. [O] is same in both the cells. However, for winds (including the vertical winds) and temperatures, values are specified in both the cells from WACCM-X. Thus, there is a vertical flux of winds and temperature in this simulation, resembling more realistic atmospheric conditions.

In the fourth simulation, G/NUDGE, the lower boundary conditions are identical to the G/WX simulation, but from 100 km to 140 km, GITM winds (full dynamical fields) are nudged towards WACCM-X winds. The vertical weighting function (ζ) for the nudging is similar to that used by Maute et al. (2015) and is as follows :

$$\zeta = cos^2 \left[\frac{\pi}{2} \left(\frac{z - z_{lb}}{z_{max} - z_{lb}} \right) \right], \tag{4.2}$$

where z_{lb} and z_{max} are 100 km and 140 km, respectively. The nudging technique is similar to that used by J. C. Wang et al. (2017) :

$$X(\lambda, \theta, z, t) = (1 - \alpha\zeta(z))X_G(\lambda, \theta, z, t) + \alpha\zeta(z)X_W(\lambda, \theta, z, t), \tag{4.3}$$

where X represents zonal wind, meridional wind and vertical wind fields. X_G and X_W represents the model fields from GITM and WACCM-X, respectively. In this technique, the GITM fields are constrained by the dynamics fields of equation 4.3. The use of vertical profile implies that nudging is the strongest at 100 km and weakest at 140 km. This allows for a smooth transition from WACCM-X lower thermospheric dynamics to GITM dynamics in this simulation. α represents the relaxation factor and was discussed in detail by Jones Jr., Drob, et al. (2018), and is defined as -

$$\alpha = G\Delta t, \tag{4.4}$$

where G represents the inverse of relaxation time. α=1, implies that GITM fields are overwritten at every model time-step. Here we use a relaxation time of 60s. The model time-step, Δt in GITM varies and is on average $\sim$2s. This implies α would on average have a value of $\sim$0.03.

4.2.3 Datasets

We use a number of different datasets to validate the phase and amplitude of T-I SAO produced by the different simulations.

4.2.3.1 Sounding of the Atmosphere using Broadband Emission Radiometry (SABER)

SABER is an instrument on NASA's Thermosphere Ionosphere Mesosphere Energetics Dynamics (TIMED) satellite. SABER provides global vertical profiles of temperature, pressure, geopotential height, volume mixing ratios, volume emission rates, and cooling and heating rates for several trace species in the MLT region (Mlynczak, 1996, 1997; Russell III et al., 1999; Yee, 2003). The version of the dataset used in this study is V2.0 (Panka et al., 2018). We use 10-year averaged [O] data to understand its temporal and spatial distribution at 97 km. Averages for each year are derived by binning the data into a day of the year and latitude grid. Then, 10 years of data are averaged together.

4.2.3.2 Global Ultra-Violet Imager (GUVI)

GUVI is a UV spectrograph with primary objectives of measuring thermospheric composition, temperature, and high-latitude particle precipitation (Paxton et al., 1999; Christensen et al., 2003; Yee, 2003). In this study, we use the height-integrated O/N_2 derived from GUVI measurements. Integrated O/N_2 is defined as the ratio of integrated O to N_2 column densities, from the top of the atmosphere as defined by a model or the altitude of the satellite, downward until the altitude where the N_2 column integrated density reaches 10^{21} m^{-2} (Strickland et al., 1995). We will henceforth refer to it simply as O/N_2. In this study, we use the global average for 2010. It is derived by binning the data into a day of the year and latitude grid. We use the level 3 GUVI data product.

4.2.3.3 TIMED Doppler Interferometer (TIDI)

TIDI is a Fabry-Perot interferometer that measures global horizontal winds in the MLT region (Yee, 2003). In this study, we use TIDI data for 2010 to validate the meridional winds in the lower thermosphere. A 60-day average is determined after binning the data into an altitude and latitude grid. Level 3 vector data is used here.

4.2.3.4 Global Navigation Satellite System (GNSS)

GNSS data is used to determine the line-integrated ionospheric electron density by measuring the propagation time difference between two different radio frequencies (Vierinen et al., 2016). The measurements are scaled by $10^{16}\mathrm{m}^{-2}$, also referred to as total electron content (TEC) units. This slant ionospheric TEC is converted into vertical total electron content (VTEC) by using a scaling factor proportional to the elevation angle of the satellite from the receiver (Vierinen et al., 2016). The data that we use here has a spatial resolution of $1^{\circ}\times\ 1^{\circ}$ and a temporal resolution of 30 minutes. In this study, we use the global mean TEC for 2010 for validation of the ionospheric SAO. It is derived by binning the data into a day of the year and latitude grid.

4.2.3.5 Challenging Minisatellite Payload (CHAMP) and Gravity Recovery and Climate Experiment (GRACE)

CHAMP and GRACE are low-earth orbit satellites with a primary objective of making accurate measurements of Earth's gravity field Reigber et al. (2002); Tapley et al. (2004). They have highly accurate accelerometers that have been widely used to derive neutral density measurements from atmospheric drag measurements ?e.g.>Luhr04, Bruinsma04, Sutton11. In this study, we use neutral mass density datasets from 2007-2010 from these satellites to validate the mass density SAO in the upper thermosphere. Averages for each year were derived by binning the data into a day of year and latitude grid.

4.2.3.6 Emmert Dataset

J. T. Emmert (2015) studied the trends in globally averaged neutral mass density from 1967-2013. This dataset is derived from the orbits of $\sim$5000 objects between the altitude of 200-600 km (J. T. Emmert, 2009). This data has a resolution of 3-6 days with daily relative accuracy of $\sim$2% and absolute accuracy of 10%. In this study, we use the derived density data for 2010 at 400 km. We will henceforth refer to this dataset simply as 'Emmert ρ' or 'Emmert dataset'.

4.3 Results

4.3.1 Motivation

Figure 4.1 shows the normalized integrated O/N_2, integrated vertical TEC and mass density (ρ) for G/NOSAO and G/MSIS simulations, compared with different observational datasets and empirical models for 2010. The thin lines are the daily averages for all data, and the thicker lines indicate fitted values. The fitted curves are derived by fitting a least squares annual and semiannual variation to the data. The red vertical lines indicate the solstices and equinoxes. All the values are normalized as specified below,

$$v_{norm} = \frac{v - \overline{v}}{\overline{v}} \times 100, \tag{4.5}$$

where $\overline{v}$ represents the global annual average of value, v (where v is ρ, TEC or O/N_2). In Figure 4.1a, an SAO with equinoctial maxima and an amplitude of 18% (with respect to its annual average) is observed in the GUVI O/N_2 data. The amplitude of SAO for different data are determined by fitting a semiannual variation. Since, O/N_2 is an integrated value, it largely reflects the lower IT state at ∼140 km, as the densities decrease exponentially with altitude (Yu et al., 2020). G/NOSAO shows smaller SAO amplitude as compared to G/MSIS, which is in better agreement with the GUVI data and pure MSIS, thus demonstrating the importance of appropriate lower boundary SAO. The amplitude of SAO for GUVI is larger than that of MSIS. We can also compare the SAO phase of different simulations by analyzing their day of maxima and minima. The phase of both the simulations agrees well with the observations.

Figure 4.1b shows the TEC for the two simulations compared with GNSS data. TEC being an integrated quantity has the largest contribution from the peak electron density altitude at ∼250-300 km. The amplitude of SAO in GNSS TEC data is ∼13%, which is consistent with the climatological value calculated by J. T. Emmert et al. (2014) . This is much less than that observed in GUVI O/N_2. Similar to Figure 4.1a, using MSIS as the lower boundary increases the SAO amplitude in GITM. There is also a small phase difference between the simulations and the GPS data, with GITM leading (peak earlier in the year) the data during March and June. G/MSIS lags behind the G/NOSAO, and is in better agreement with the phase of GNSS data.

Figure 4.1c shows the mass densities at ∼400 km for both the simulations compared with those from the CHAMP and GRACE satellites (normalized at 400 km). The densities for CHAMP and GRACE are averaged between 2007-2010 because of

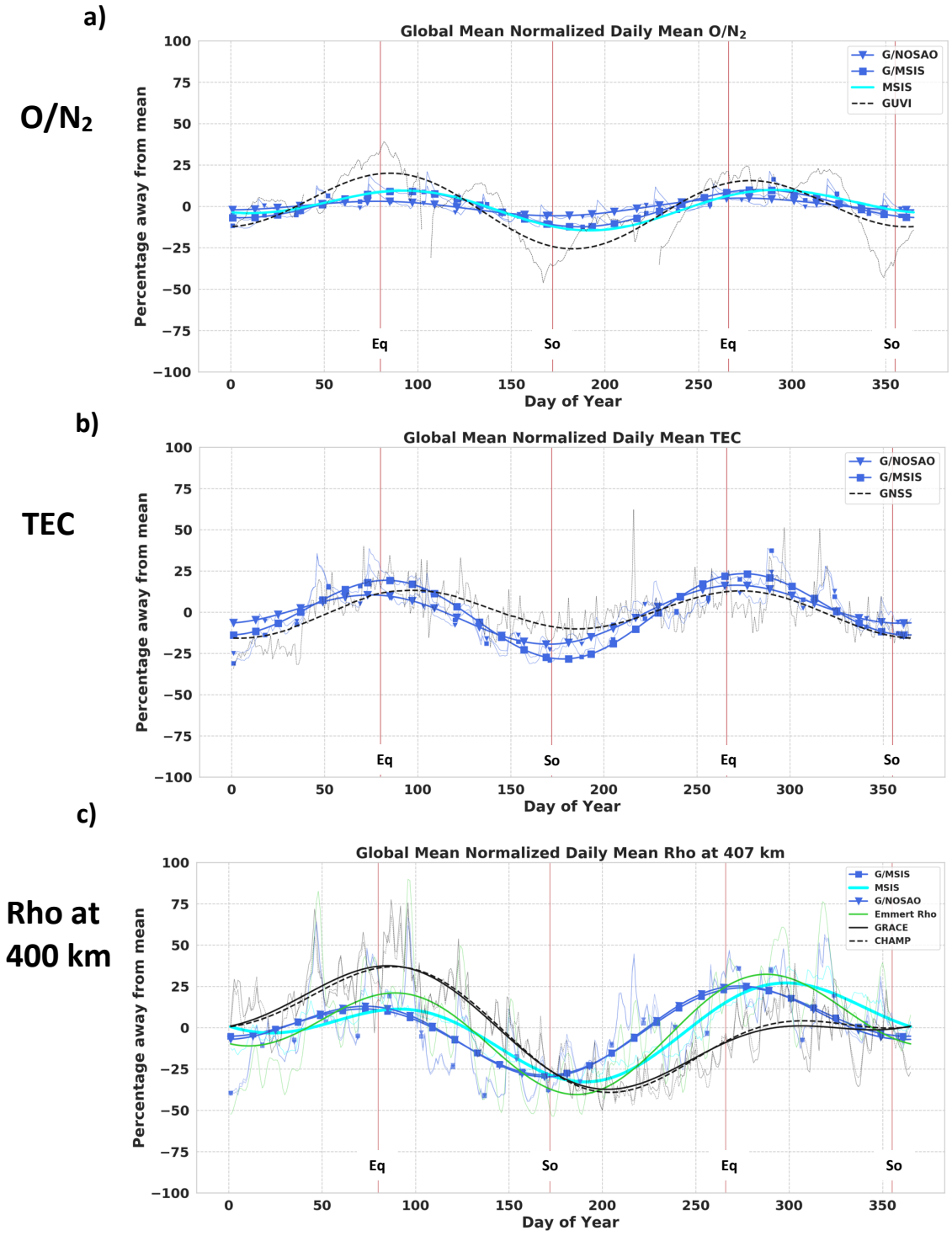

Figure 4.1: Diurnally Averaged Normalized a) O/N_2, b) TEC, c) ρ at 400 km, for GITM simulations, MSIS and observational datasets. CHAMP and GRACE datasets are normalized to 400 km and averaged for 2007-2010 because of data gaps in 2010. The thin lines indicate the raw data and the thicker lines indicate the fitted values. The red vertical lines indicate the days of equinoxes (day 80 and day 266) and solstices (day 172 and 355).

data gaps in 2010. We also show values from the Emmert dataset and the MSIS empirical model. In this altitude region, G/NOSAO and G/MSIS show agreement in both the SAO phase and amplitude. CHAMP and GRACE mass densities also agree well with each other. The largest disagreement is in the phase of the SAO. Both the model simulations lead the observations and empirical model, especially during June and September. Comparing with the Emmert data, GITM simulations have smaller deviations from the mean. An equinoctial asymmetry is also prominent in ρ and not in O/N_2 and TEC, hinting at its origin in the middle-upper thermosphere. MSIS, Emmert data and GITM simulations have larger (smaller) densities during September (March) equinox, whereas CHAMP and GRACE have smaller (larger) values during this time. A similar observation was made by Lei et al. (2012) in the CHAMP and GRACE data, namely that the densities are larger during March than those around September during periods of high and moderate solar actvitiy. Since CHAMP and GRACE data are averaged for 2007-2010, it is possible it does not accurately represent the thermospheric state during a geomagnetic quiet time (2010 for our purposes).

Note the phase of GUVI and GNSS data leads the CHAMP data, indicating that there is a phase progression in the T-I SAO with altitude that GITM is unable to capture. For example, GUVI and GPS data show a September maxima closer to equinox (day 266), whereas, the September maximum for CHAMP ρ is around day 280-300. Moreover, the phase progression with altitude is not uniform for different times of the year, and is more prominent during June and September. This is different from the inference by Yue et al. (2019) as they observed that the phase of the SAO in height-resolved O/N_2 stays the same between the lower and upper thermosphere. An annual asymmetry is also quite noticeable for all the parameters shown in Figure 4.1. Lower O/N_2, TEC, and ρ are observed at June solstice as compared to the December solstice.

These results reveal that GITM is able to reproduce SAO in the IT region without necessarily having an SAO at the lower boundary, but with lower amplitude and leading phase. This is not necessarily the case with other ionosphere-thermosphere models whose lower boundaries are between 95-100 km (e.g., TIE-GCM see Qian et al. (2009) and Jones Jr. et al. (2021)). In the absence of a composition or eddy diffusion SAO imposed at the model lower boundary, the only major driver of the SAO is the thermospheric spoon mechanism. The disagreements in the amplitude and phase might be due to the contribution from the lower atmosphere. In the next section, we discuss the distribution of [O] in the MLT.

4.3.2 Lower Boundary Conditions

Figures 4.2a and 4.2b show 10-year averaged O number density from SABER at 85 km and 97 km, while Figures 4.2c and 4.2d show the area-weighted global averages at each altitude. The global averages are only for the latitude region spanning $\pm 55^{\circ}$ because of missing data at high latitudes. Using a longer term average for satellite data reduces biases due to incomplete longitudinal sampling, tidal phases, missing data, etc, thus increasing the statistical significance.

The latitudinal distribution of [O] reverses between the two altitudes, consistent with what Smith et al. (2010) showed using an earlier version of the SABER [O] data. At 85 km, the higher latitudes show an annual variation with larger [O] during winter. This is because of the gravity wave induced summer-to-winter meridional circulation in the mesosphere, and downwelling in winter (e.g. Lindzen, 1981; Holton, 1983; R. R. Garcia & Solomon, 1985). The lower latitudes show an SAO with maxima around the equinoxes which is similar to the mesospheric semiannual oscillation (MSAO) in zonal winds in the equatorial mesosphere (R. R. Garcia et al., 1997). The SAO in zonal winds has been found to be driven by momentum deposition by gravity waves that are selectively filtered by the stratospheric winds (Burrage et al., 1996). However, the mechanism for the SAO at 85 km in [O] is still under investigation. The lifetime of O in this altitude region is too short to be affected by a wind circulation of such a long period. Smith et al. (2010) suggested that the seasonal variation in the amplitude of the migrating diurnal tide might be a more likely source. It was demonstrated by Jones Jr. et al. (2014) that tides induce a net increase in [O] during equinoxes close to the equator via tidally induced advective transport. Figure 4.2c shows that at 85 km, the global average is dominated by the SAO with maxima closer to the equinoxes. This is because the high latitude AO in both the hemispheres is out of phase and cancels out, which then reinforces the lower latitudinal SAO in the global means.

At 97 km, the AO at higher latitudes reverses with larger [O] during the summer (J. P. Russell et al., 2004; Smith et al., 2010; Sheese et al., 2011; Malhotra et al., 2020). The mechanism responsible for these summer maxima is still under investigation (Smith et al., 2010; Qian et al., 2017; Rezac et al., 2015; Malhotra et al., 2020). The effect of this reversal on the upper thermosphere was discussed by Malhotra et al. (2020). It can also be observed that the SAO at 97 km at lower latitudes is almost non-existent, and is smaller than that observed by Smith et al. (2010). This difference might arise because of different years that are included in the averages or different versions of SABER data. In Figure 4.2d, a small intra-annual variation is observed

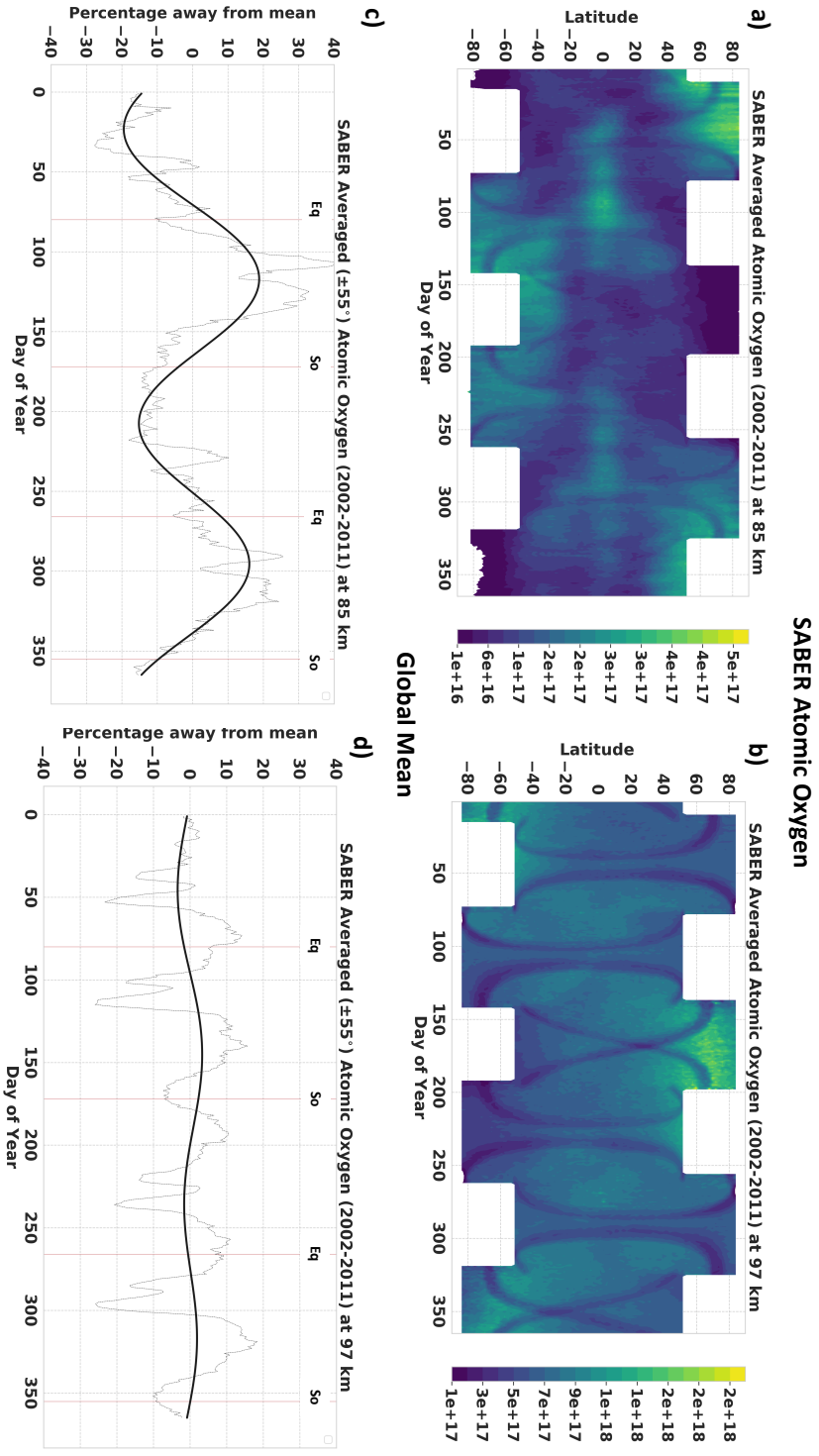

Figure 4.2: [O] for SABER in m^{-3}, averaged for 2002-2011, binned by day of the year and latitude a) at 85 km, b) at 97 km. Area-weighted normalized global means spanning ±55° c) at 85 km, d) 97 km.

with maxima around solstices in the global mean [O]. The high latitude AO in the two hemispheres do not completely cancel each other out, resulting in net maxima closer to the solstices. It should be noted that these plots represent averaged values over a 10 year period. The global averages for individual years can have deviations from this average. The amplitude of smoothed intra-annual variation is $\sim$20% at 85 km and decreases to $<\sim$3% at 97 km. Note that if high latitude SABER data is also included in the calculation of global average [O], this amplitude increases and SAO peaks a little later in the year.

Figures 4.3a and 4.3b illustrate the latitudinal distribution of [O] at $\sim$97 km for MSIS and WACCM-X in 2010, respectively. WACCM-X shows more temporal and spatial variations, which is indicative of atmospheric variations including gravity waves, non-migrating tides, and planetary waves propagating up from the lower atmosphere. The latitudinal distribution of [O] in WACCM-X matches better with the SABER data at 97 km in Figure 4.2b. Both show annual variation at higher latitudes with maxima in summer and minima in winter. MSIS, on the other hand, has higher [O] during winter. This is because the [O] for MSIS in the MLT is extrapolated from higher altitudes assuming mixed equilibrium below the turbopause ($\sim$105 km) with a correction factor for chemistry and dynamics. The version of MSIS used here, NRLMSISE-00 did not have [O] observations in the MLT region as SABER had not been launched when it was created. Most of the observations in this region are of neutral densities and temperature from rockets and incoherent scatter radars. Therefore, the correction factors in MSIS do not account for the processes responsible for high latitude summer [O] in the MLT. The summer MLT maximum in [O] at high latitudes is better represented in MSIS2.0 (see Figure 11 of J. T. Emmert et al. (2020)). At low latitudes, WACCM-X and MSIS show a larger amplitude SAO than what SABER observed. A possible explanation for this might be the larger uncertainty in SABER [O] at these altitudes (Mlynczak et al., 2013; Smith et al., 2013).

Figure 4.3c compares the area-weighted global mean [O] for MSIS, WACCM-X and SABER data at 97 km. The [O] for MSIS and WACCM-X is for 2010, whereas the SABER data is the average for 2002-2011 shown previously in Figure 4.2d. The global mean [O] for both SABER and WACCM-X shows an SAO with maxima closer to solstices, whereas [O] for MSIS shows an SAO with 180 degree phase shift (maxima around equinoxes). In MSIS, the high latitude AO in both the hemispheres cancels out with each other resulting in minima at solstices. For WACCM-X, at equinoxes, low [O] at high latitudes result in minima at equinoxes relative to solstices. The SAO amplitude is lower and also in agreement between WACCM-X and SABER.

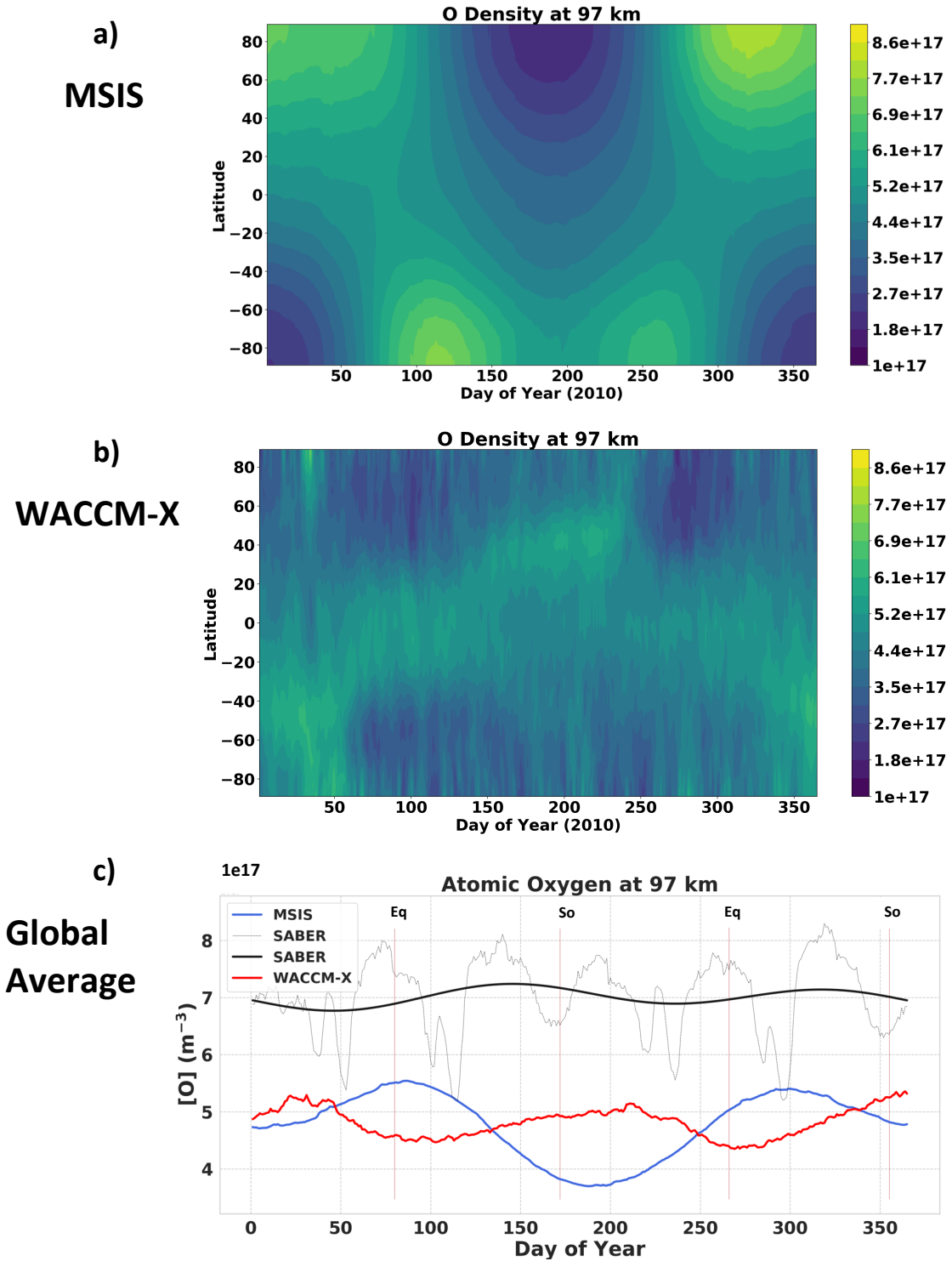

Figure 4.3: Diurnally averaged [O] in m^{-3} for 2010 for a) MSIS, b) WACCM-X at 97 km. c) Area-weighted globally and diurnally averaged [O] at 97 km. For SABER, the thin black line indicates the raw data and the thicker black line indicates the fitted values. SABER data is similar to that of Figure 4.2 and thus is the long-term average for 2002-2011.

The overall magnitude of [O] for SABER however exceeds that of both MSIS and WACCM-X. Note, MSIS2.0 [O] at 97 km are roughly a factor of 2 higher than what is shown in Figure 3c (see J. T. Emmert et al. (2020) Figures 11-13).

Since the latitudinal distribution of [O] for WACCM-X is similar to SABER, the lower boundary of GITM was changed to WACCM-X in 2010 to assess its effects on the T-I SAO. We cannot directly use SABER at the lower boundary of GITM because of the lack of measurements at high latitudes. As specified in Section 2, we also use other parameters from WACCM-X in GITM. The temporal and latitudinal variation for these parameters are not much different between MSIS and WACCM-X, and are shown in the supporting information. Therefore, our results primarily signify the implications of different [O] distribution at the lower boundary. In the next few sections, we will analyze the results of different simulations, starting with a comparison of meridional winds in the thermosphere.

4.3.3 Dynamics

Figure 4.4 shows the 16-day averaged meridional winds for HWM, WACCM-X and different GITM simulations at June solstice (June 21±8 days). We take a multi-day average to eliminate short term variations due to tides and planetary waves, such that the winds in this figure represent background meridional winds. All GITM simulations show a higher altitude summer-to-winter thermospheric circulation starting from around ∼140 km which roughly agrees with HWM and WACCM-X winds. Both HWM and WACCM-X although have larger wind speeds at summer high latitudes. However, the wind patterns in the lower thermosphere are different between the different models. In the lower thermosphere, between 100-120 km, two equatorward circulation cells are observed in G/NOSAO, G/MSIS, and G/WX simulations. These circulation cells are observed in GITM throughout the year and were shown to be driven by the centrifugal force (Malhotra et al., 2020). Comparing Figures 4.4d and 4.4e, we see that changing the lower boundary from MSIS to WACCM-X affects the magnitude of the winds in the lower thermosphere, but does not change their direction. HWM and WACCM-X winds, on the other hand, show a region with winter-to-summer circulation which has previously been observed to be caused by residual gravity waves during solstices (Qian et al., 2017). HWM primarily has Wind Imaging Interferometer (WINDII) data in this altitude regime. Being a global IT model, GITM does not resolve gravity waves. Therefore, it does not have the requisite forcing for this opposite lower thermospheric circulation, and hence relies on realistic boundary conditions. G/NUDGE demonstrates the effect of constraining the

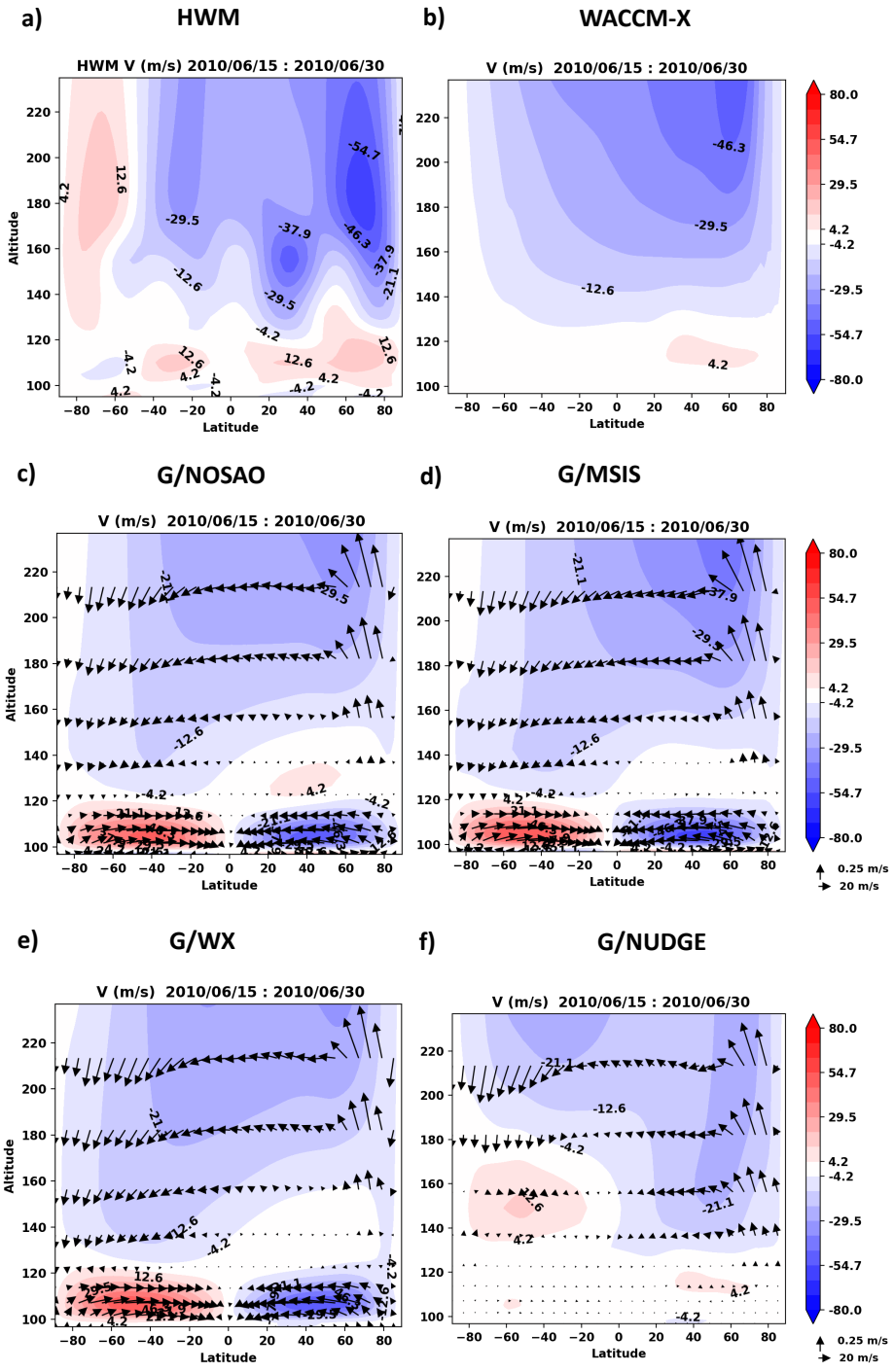

Figure 4.4: Latitude-Altitude cross-section of zonally and diurnally averaged meridional winds in m/s for 2010/06/15 - 2010/06/30 for a) HWM, b) WACCM-X, c) G/NOSAO, d) G/MSIS, e) G/WX, f) G/NUDGE. The negative values depict southward winds. Vectors indicate a sum of of meridional and vertical winds (scaled by $\times$ 50).

winds in GITM with WACCM-X up to 140 km. Between 100-120 km, G/NUDGE shows winter-to-summer circulation similar to pure WACCM-X and HWM.

As an aside, during equinoxes (not shown here), GITM simulations continue to show the equatorward circulation cells below 120 km. During this time, HWM and WACCM-X also show a similar circulation pattern. This has also been previously observed in the High Resolution Doppler Imager (HRDI) and WINDII wind measurements onboard the Upper Atmosphere Research Satellite (UARS) (McLandress et al., 1996; S. P. Zhang et al., 2007). It is possible that, because of absence of strong residual gravity wave forcing during equinoxes, the centrifugal force dominates the momentum budget in this region at equinoxes, resulting in net equatorward winds in the lower thermosphere.

Figure 4.5 shows the 60-day-averaged meridional wind for TIDI data near December and June solstices. In Figure 4.5a, between 90-100 km, northward winds indicate the mesopause summer-to-winter circulation during December solstice. The horizontal line at 97 km indicates the lower boundary of GITM. Above 100 km, southward winds depict the winter-to-summer residual circulation. Similar meridional wind patterns are also observed during June solstice in Figure 4.5b in the opposite direction, potentially signifying an AO in meridional winds in the lower thermosphere. Recently, Dhadly et al. [2020] showed similar oscillations at midlatitudes, as well as an SAO, and high order intra-annual oscillations in middle thermospheric in situ measurements of the horizontal neutral winds from the Gravity Field and Steady-State Ocean Circulation Explorer (GOCE) accelerometer. HWM and WACCM-X agree with the TIDI data between 100-120 km, and thus nudging the GITM dynamics towards WACCM-X should improve the thermospheric modeling and SAO in GITM. However, it is worth noting that the magnitude of the winds in the winter-to-summer circulation is much larger in TIDI data during both solstices. In the next section, we will reveal the effect of different thermospheric dynamics on the amplitude and phase of T-I SAO of the simulations.

4.3.4 Global Mean Intra-Annual Variations

Figure 4.6 reveals the averaged normalized O/N_2, TEC, and [O] and ρ at $\sim$400 km for GITM simulations compared with different datasets and models for 2010. This comparison was shown for G/NOSAO and G/MSIS previously in Figure 4.1. Similar to Figure 4.1, thin lines are the daily averages for all data, and the thicker lines indicate fitted values. The parameters are normalized with respect to annual means as specified in equation 4.5. The amplitudes and phases for different model runs and

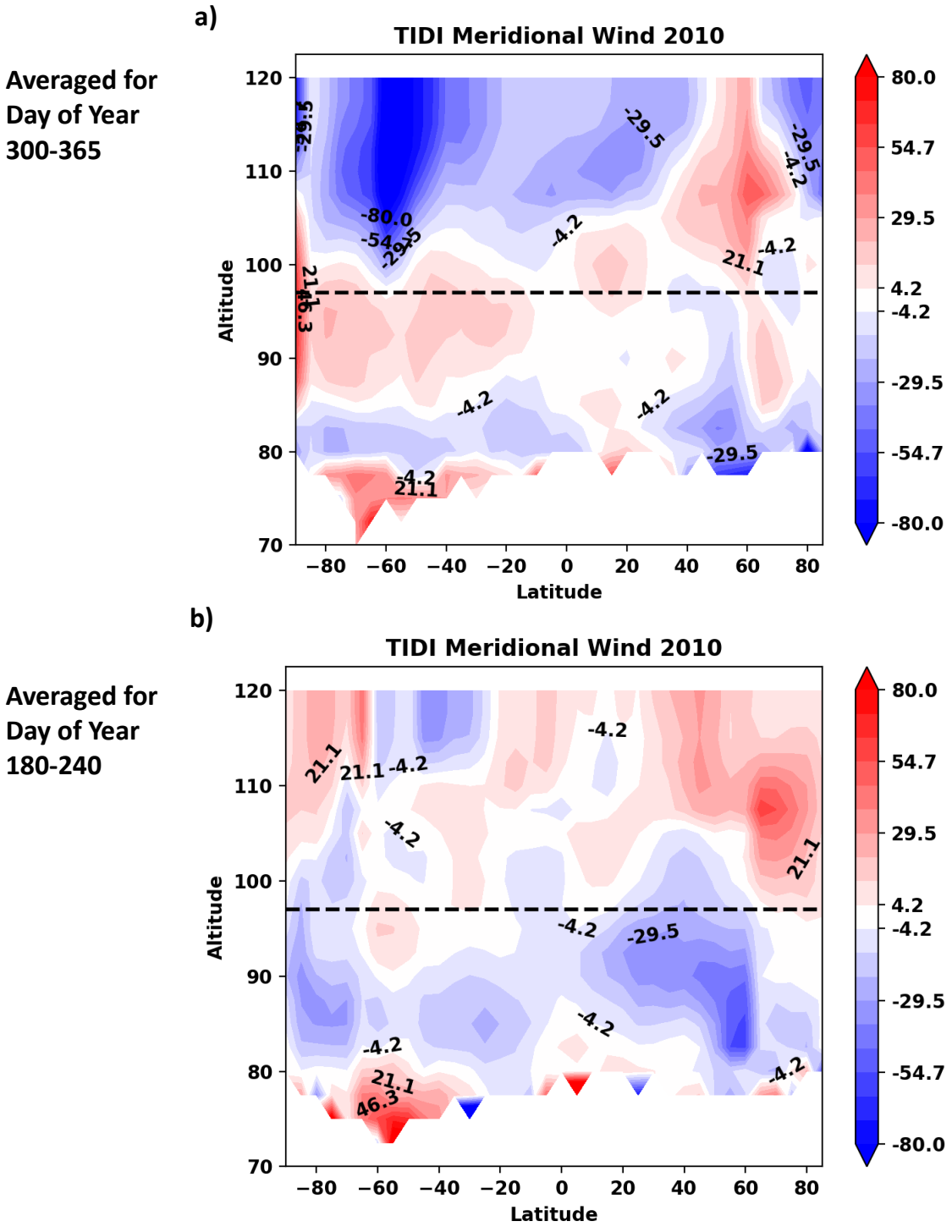

Figure 4.5: Averaged meridional winds in m/s for TIDI binned by latitude and altitude for days of the year a) 300-365 b) 180-240 in 2010. The dashed black horizontal line indicates the altitude of lower boundary of GITM, ∼97 km.

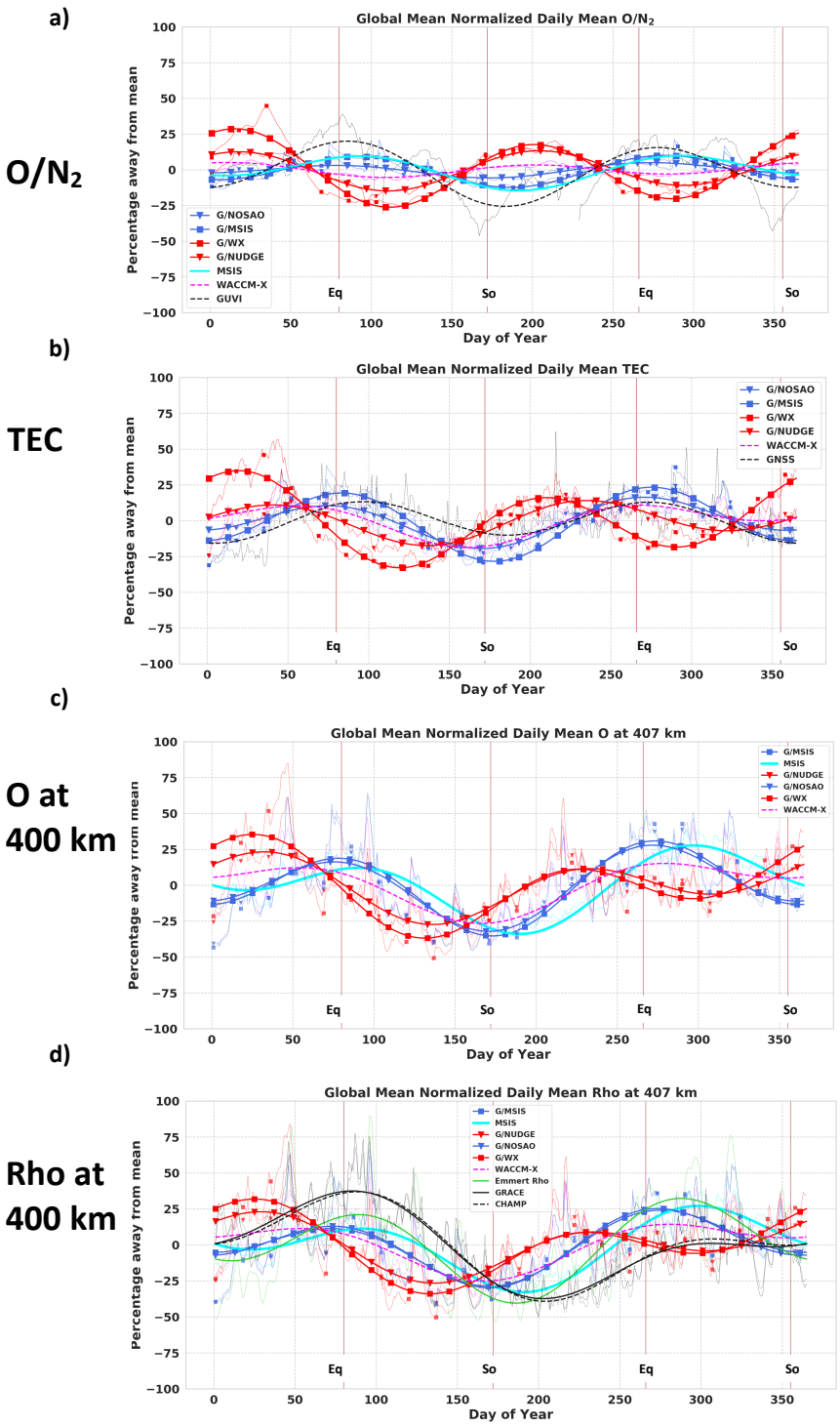

Figure 4.6: Diurnally averaged, normalized (area-weighted) global means a) O/N_2, b) TEC, c) [O] at 407 km, d) ρ at 407 km, for different GITM simulations, WACCM-X model, MSIS, and observational datasets. The thin lines indicate the raw data and the thicker lines indicate the fitted values. Similar to Figure 4.1, CHAMP and GRACE datasets are normalized to 400 km and averaged for 2007-2010. The red vertical lines indicate the days of equinoxes and solstices.

observations are also summarized in Table 4.2.

Figure 4.6a shows the daily averaged and fitted O/N_2. The black line represents the averaged O/N_2 measurements from GUVI data. The phase of the SAO in G/MSIS and G/NOSAO match best with the GUVI data and the MSIS model, with equinoctial maxima. Using MSIS at the lower boundary (G/MSIS) is not enough, as it produces a smaller SAO amplitude in comparison to GUVI observations. While WACCM-X [O] compares well with SABER in the MLT, using WACCM-X at the lower boundary of GITM (G/WX) reverses the phase of SAO in O/N_2, shifting the maxima closer to solstices. Using dynamics from WACCM-X in the lower thermosphere (G/NUDGE) reduces the amplitude of this out-of-phase SAO, but does not completely correct it.

The phase shifts and amplitudes in TEC, and globally averaged [O] and ρ in Figures 4.6b, c and d show similar model differences as the O/N_2, with maxima and minima for G/WX and G/NUDGE almost midway between solstices and equinoxes. At 400 km, the major neutral constituent is O, and thus, ρ primarily represents variations in [O]. However, for neutral density at 400 km, there are more observational datasets to validate the simulations against. The densities from Emmert dataset, CHAMP and GRACE peak around equinoxes (with an equinoctial asymmetry) similar to that of G/NOSAO and G/MSIS. The phase difference of both G/WX and G/NUDGE simulations from G/MSIS in these figures is lower when compared to that for O/N_2. This hints towards phase progression of SAO with altitude in G/WX and G/NUDGE simulations towards equinoctial maxima due to the effect of thermospheric spoon mechanism. The summer-to-winter meridional wind speeds increase with altitude in the lower-middle as shown in Figure 4.4, resulting in decrease of solstitial densities relative to equinoctial densities. This will be more clear in Figure 4.7 where we show variations in phase of SAO with altitude.

The WACCM-X model also has an SAO that is out-of-phase in the lower thermosphere as seen in O/N_2 (Figure 4.6a). However, it has the correct phase in TEC, [O], and ρ at 400 km, with peaks at the equinoxes. This implies that the phase shifts towards equinoctial maxima in the lower-middle thermosphere. Nudging GITM dynamics to WACCM-X up to 140 km reduces the amplitude of oppositely-phased SAO in G/NUDGE, but is not enough to completely correct the phase and shift the phase to equinoctial maxima. This reduction in the amplitude of the opposite SAO signifies primarily the contribution of the lower thermospheric residual circulation. Qian & Yue (2017) showed that the residual circulation results in upwelling and reduction of O/N_2 in winter, and downwelling and its increase in summer. This leads to an overall reduction of the global mean O/N_2 by 18% during solstices. Comparison of

Model Run	ρ at 400 km		O/N_2		TEC	
	SAO Amplitude (%)	SAO Phase	SAO Amplitude (%)	SAO Phase	SAO Amplitude (%)	SAO Phase
G/NOSAO	18.2	82	3.9	84	12.9	81
G/MSIS	16.6	83	9.6	95	21.0	87
G/WX	18.9	34	23.1	16	25.2	22
G/NUDGE	14.9	38	12.9	19	12.2	46
WACCM-X	10.0	76	4.2	14	9.4	70
MSIS	17.5	104	9.3	100		
GRACE	16.2	97				
CHAMP	17.3	101				
Emmert Dataset	25.6	97				
GUVI			18.2	89		
GNSS					12.9	95
TIE-GCM, w/ Q09	16.2	122			26.5	129
TIME-GCM Standard	12.8	114			19.7	106

Table 4.2: SAO Amplitude and Phase for different model runs and observations. The amplitude is determined by fitting a least squares semiannual variation to the data. Phase is the day of first maxima. TIE-GCM and TIME-GCM values are from Jones Jr. et al. (2017).

G/NUDGE with G/WX, shows a similar reduction in the global mean for all parameters in Figure 4.6 around both June and December solstices. Further explanation of these differences is beyond the scope of this manuscript.

In summary, using WACCM-X at the lower boundary in GITM reverses the phase of the SAO in both thermospheric and ionospheric parameters, such that it does not agree with the observations, despite the SABER-like [O] distribution at the lower boundary. This can be wrongly directly linked with the solstitial peaks in the global mean of [O] at 97 km in WACCM-X. However, O is not in diffusive equilibrium above 97 km, but in fact is driven by the dynamics and chemistry in the lower thermosphere.

Figure 4.7 compares the altitudinal progression of the [O] and ρ SAO amplitudes and phases. For [O] at 100 km, MSIS and G/MSIS have the largest amplitude of 15%, with maxima at around equinoxes (day 100). Both G/WX, G/NUDGE and the WACCM-X model start with a much lower amplitude of around 5%, with maxima near solstices (day 10), which are in better agreement with the amplitude and phase of SABER data at 100 km. G/NOSAO starts with an amplitude of $\sim$0. WACCM-X shows a minimum at around $\sim$120 km, above which the amplitude increases monotonously. The amplitude of SAO in WACCM-X remains lower than other simulations also causing much lower amplitude in G/NUDGE, at $\sim$10-15%. WACCM-X transitions from solstitial maxima to equinoctial maxima in the 100-200 km altitude region. In the upper thermosphere, G/MSIS, G/NOSAO and G/WX have the largest amplitudes of $\sim$25%, which is greater than that of MSIS. Since, there are limited observations of [O] in the thermosphere, there is an uncertainty regarding which simulation represents the correct SAO amplitude. A similar amplification of the SAO with altitude for different neutral species was depicted by Picone et al. (2013) because of the variation in temperature. Thus, it is possible that different temperature structure between the simulations leads to different amplification factors of the SAO. When considering the importance of SAO at the lower boundary, G/NOSAO catches up with other simulations above 300 km. However, the absence of lower boundary SAO results in much smaller amplitude below 300 km. Hence, our results indicate that it is necessary to have an SAO in composition and winds at the lower boundary of IT models for better agreement with the observations in the lower-middle thermosphere, otherwise it can lead to underestimation of the SAO in this region. Recent work by Jones Jr. et al. (2021) using the TIE-GCM showed that including MSIS2.0 composition improved the globally-averaged mass density SAO at 400 km in the TIE-GCM (although the TIE-GCM amplitude was notably smaller than observed).

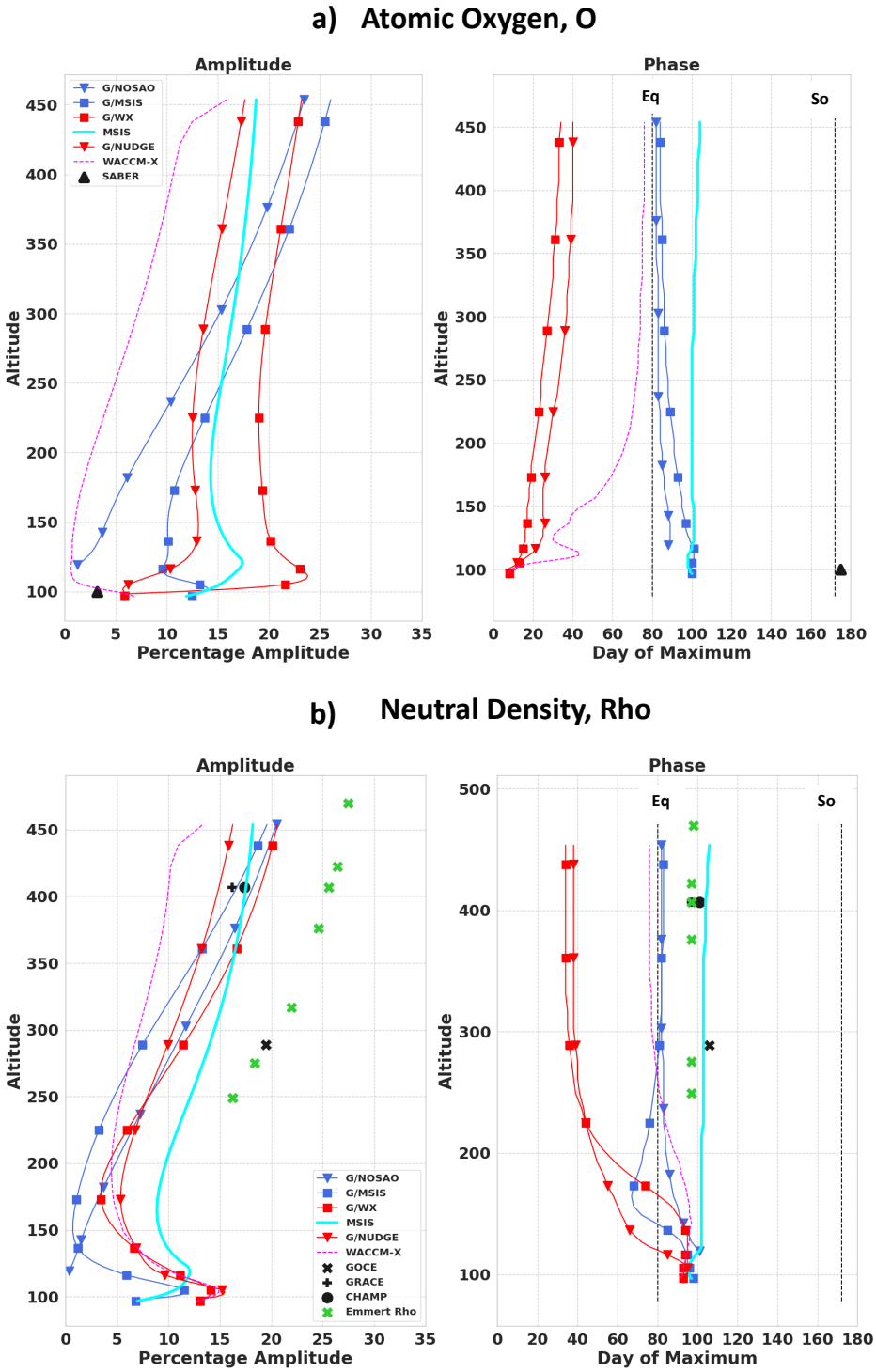

Figure 4.7: SAO Amplitudes and phases with altitude for a) [O] b) ρ, for different GITM simulations, WACCM-X model, MSIS, and observational datasets. SAO Amplitudes and phases are calculated from least squares fits to normalized daily averages of Figure 4.6. The phase signifies the day of first maximum. The vertical dashed black lines indicate the day of equinox (March 21) and solstice (June 21).

The phase for [O] largely remains constant with altitude for all of the simulations. G/MSIS and G/NOSAO continue to have maxima at equinox in the upper thermosphere, which leads the MSIS SAO, as observed previously in Figure 4.1c. G/WX and G/NUDGE have maxima near the solstices progressing towards equinoxes with altitude. As stated before, we believe that this is due to the effect of summer-to-winter thermospheric circulation that pushes the thermosphere towards a more mixed state at solstices. This phase progression is most apparent between 100-300 km, above which it does not change much. This is because the thermospheric spoon mechanism is more dominant in this altitude region. Above ∼300 km, O is in diffusive equilibrium and thus the SAO phase is constant at higher altitudes.

Figure 4.7b shows the variation of SAO phase and amplitude for ρ. Above 200 km, O is the major species and hence the SAO in ρ primarily reflects the variations in [O]. At 100 km, all the simulations start with a maxima at ∼day 90 (equinox) because of the dominance of the N_2 density. The SAO in ρ for G/MSIS and G/NOSAO has almost a constant phase with altitude displaying an equinoctial maxima, fairly consistent with MSIS and TIME-GCM simulations by Jones Jr. et al. (2017). Pure WACCM-X also exhibits a constant SAO phase above 100 km, peaking at equinox. This is because of the dominant equinoctial maxima in N_2 in the lower-middle thermosphere and equinoctial maxima in [O] above 200 km. In G/WX and G/NUDGE, the phase shifts from equinoctial (due to N_2) towards solstitial maxima at ∼200-250 km (because of O). The model runs that show the correct phase, i.e., the equinoctial peaks (WACCM-X, G/MSIS, G/NOSAO), lead all observational datasets (MSIS, CHAMP, GRACE, Emmert data, and GOCE). These observational datasets peak at a similar time around ∼day 100, while model simulations peak at ∼day 80. The amplitude of the SAO for ρ increases with altitude similar to that of [O]. The amplitude for the GITM simulations reaches a maximum of ∼20% and is in better agreement with CHAMP and GRACE, whereas the amplitude is much larger in the Emmert and GOCE data. The SAO in temperature at 400 km (not shown here) has an amplitude of ∼<3% with phase for G/NOSAO and G/MSIS at ∼day 70-80 and at ∼50-60 for G/WX and G/NUDGE.

A similar analysis was done by Jones Jr. et al. (2017) (see Figure 2) for different TIME-GCM simulations. Table 4.2 shows the SAO amplitudes and phases for standard TIME-GCM and TIE-GCM with Qian et al. (2009) eddy diffusion variation (TIE-GCM w/ Q09). Comparing with our G/MSIS simulation, for both TEC and ρ at 400 km, G/MSIS peaks earlier in the year (day 83) as compared to these two simulations from Jones Jr. et al. (2017) (day 106 and 122). The phase of the obser-

vations (GPS, CHAMP, GRACE, and Emmert dataset) lies between these different models. For the SAO amplitudes, these three model runs have larger amplitudes than the GNSS TEC (∼13%). Comparing the ρ at 400 km, both TIE-GCM w/ Q09 and G/MSIS agree with the SAO amplitude of CHAMP and GRACE (∼16-17%). To further understand the differences between our simulations, we will analyze the latitudinal distribution of thermospheric densities in the next section.

4.3.5 Global Distribution

Figure 4.8 illustrates the latitudinal distribution of [O] at ∼150 km. G/NOSAO and G/MSIS show a similar variation, with equinoctial maxima at lower latitudes. At solstices, larger [O] is observed in the winter hemisphere because of the interhemispheric summer-to-winter circulation. At ∼day 180, by comparing the summer minima in the northern hemisphere between these two simulations, we see that G/MSIS has a minima spanning a larger latitudinal region. Similar behavior is observed starting from ∼day 350 in the southern hemisphere. This is because G/MSIS as shown in Figure 4.3 starts with the summer minima and winter maxima at the GITM lower boundary. The interhemispheric meridional circulation adds to this depletion in summer and accumulation in winter. This can result in an underestimation and overestimation of [O] in summer and winter, respectively (Malhotra et al., 2020).

G/WX and G/NUDGE also show large winter [O]. Thus, GITM is able to reverse the opposite latitudinal variation of [O] from larger values in the summer at ∼97 km to larger in winter at ∼150 km. There is also an increase in summertime [O], and thus decrease in the summer-to-winter gradient at solstices similar to G/NOSAO. The features of primary importance in these figures are the low latitude maxima at solstices in 4.8c and 4.8d that result in the 180° phase shift in the global mean SAO (shown in Figure 4.6). G/NUDGE has a similar latitudinal distribution as G/WX, but the absolute [O] densities are much larger for both equinoxes and solstices. In Figure 4.6, the parameters were normalized, leading to an overall decrease of the SAO amplitude in G/NUDGE. In contrast with Figures 4.8c and 4.8d, the WACCM-X model in Figure 4.8e exhibits stronger winter maxima. However, similar to both G/WX and G/NUDGE simulations, the summer-winter gradient is low. [O] from MSIS is shown here for consistency. We do not expect MSIS to have the correct distribution at these altitudes because of lack of [O] observations. It shows deep summer minima at mid-high latitudes that cancels out the winter maxima of the opposite hemisphere, resulting in equinoctial peaks in the global means.

Figure 4.9 shows neutral density at ∼400 km (resembles major species, [O] at 400

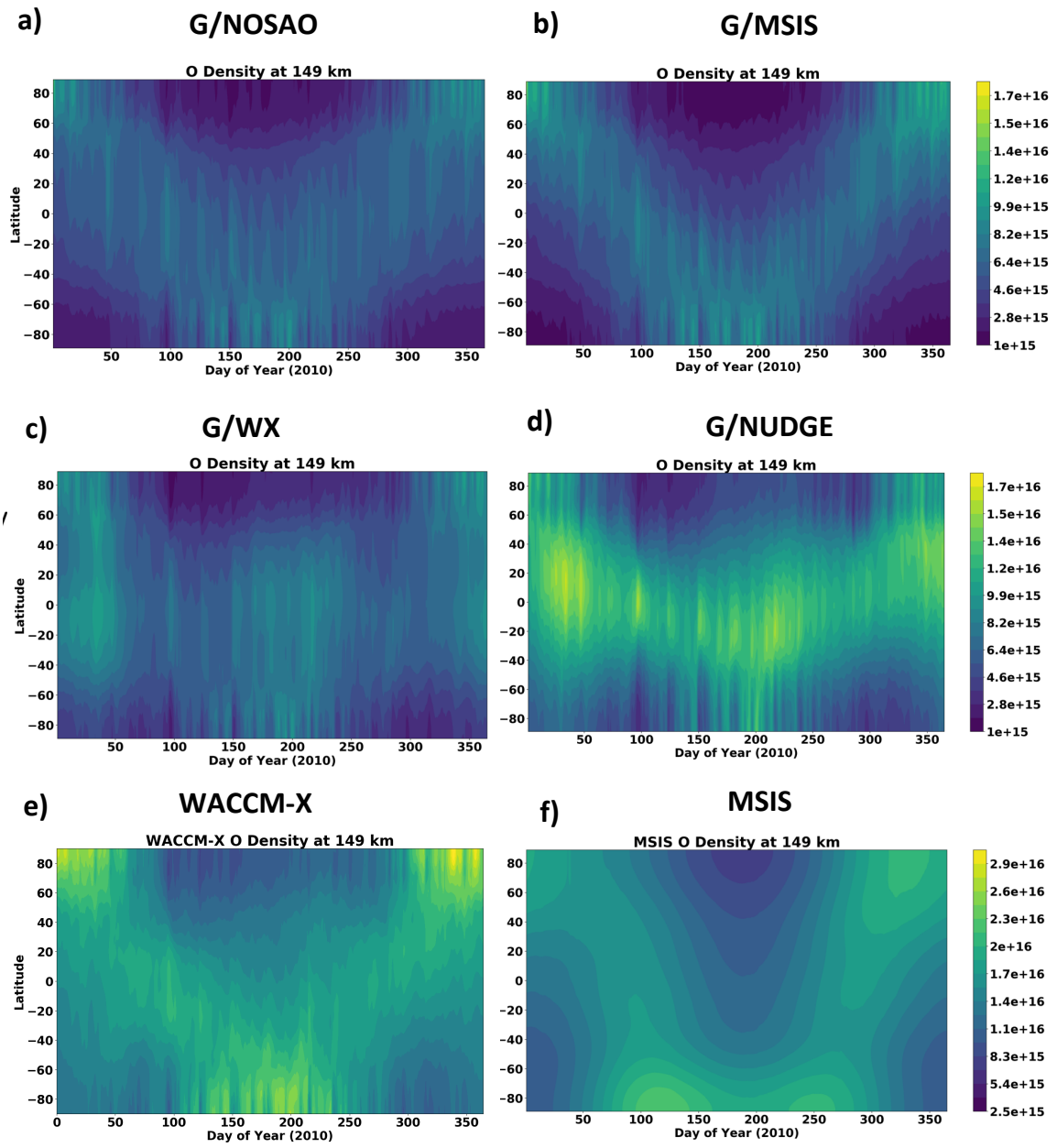

Figure 4.8: Diurnally averaged distribution of [O] with latitude in m^{-3} at 149 km for 2010 for a) G/NOSAO, b) G/MSIS, c) G/WX , d) G/NUDGE, e) WACCM-X, f) MSIS empirical model.

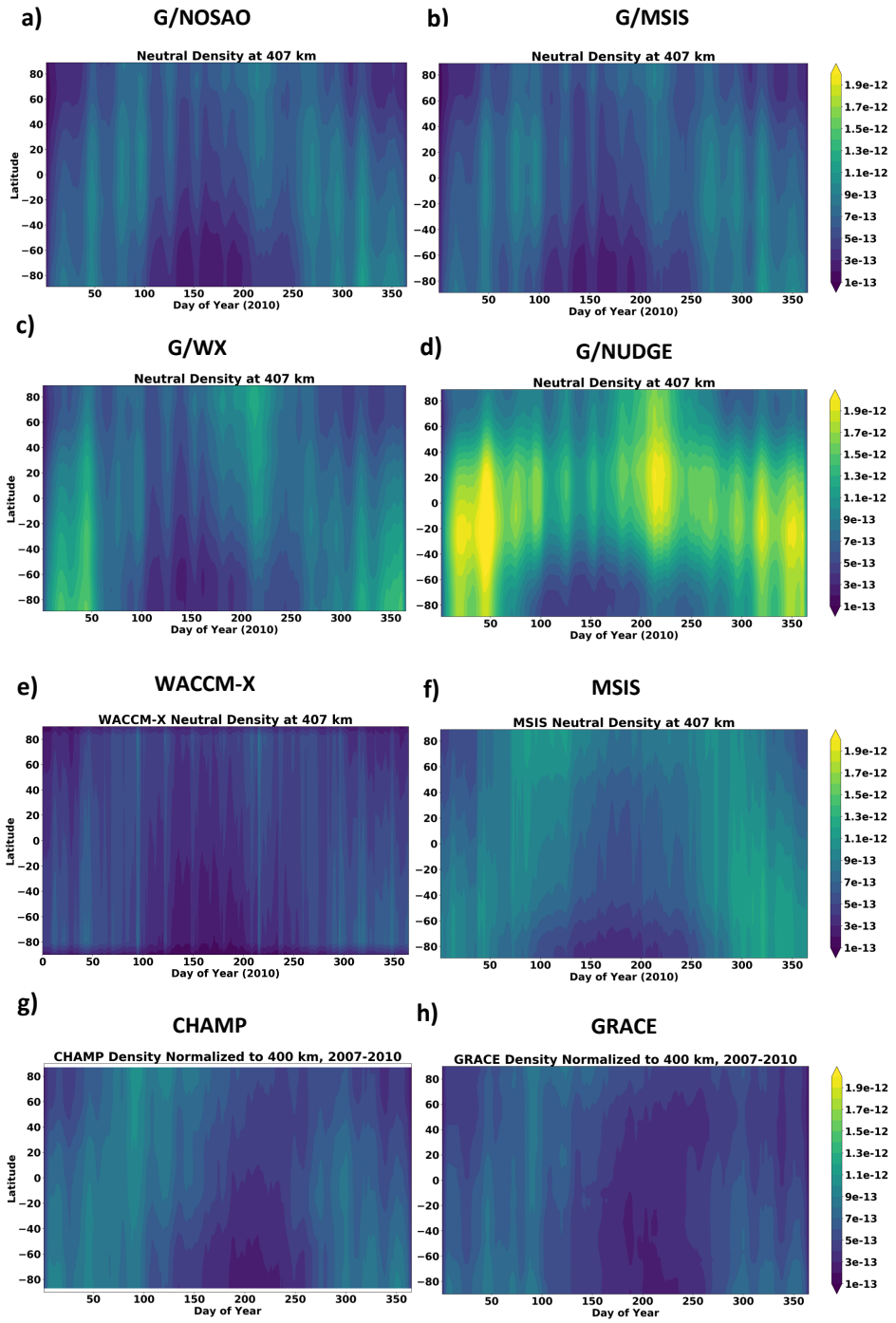

Figure 4.9: Diurnally averaged distribution of ρ with latitude in m^{-3} at 400 km for a) G/NOSAO, b) G/MSIS, c) G/WX , d) G/NUDGE, e) WACCM-X, f) MSIS empirical model. g) CHAMP, h) GRACE. CHAMP and GRACE datasets are normalized to 400 km and averaged for 2007-2010.

km) from all our model simulations, as well as CHAMP and GRACE observations. The high latitude winter maxima observed for [O] at ∼150 km has transitioned to high latitude summer maxima at ∼400 km in this figure. This is because above ∼300-400 km, the effect of larger summer temperatures dominates over that of compositional changes due to thermospheric spoon mechanism (J. Emmert, 2015). The ρ for G/WX and G/NUDGE have the correct annual oscillation at high latitudes, however, the maxima at lower latitudes is at solstices, similar to [O] at ∼150 km. Thus, the intra-annual variation in [O] stays the same at lower latitudes above ∼150 km. The latitudinal distribution of G/NOSAO and G/MSIS agrees with MSIS, CHAMP and GRACE data, with slight phase differences. Comparing the absolute values of [O] and ρ in the Figures 4.8 and 4.9, it should be noted that the difference amongst the various GITM simulations is largest during solstices. Thus, major phase differences between the global means of the simulations in Figure 4.6, arise because of a relative increase in low latitude [O] during solstices in the lower thermospheric altitude region in G/WX and G/NUDGE.

It is worth mentioning that the results by a previous study by Malhotra et al. (2020) showed that using high summer [O] from WACCM-X at the lower boundary improves the O/N_2 agreement of GITM with the GUVI data during January and June. The WACCM-X driven GITM simulation showed a decreased O/N_2 gradient between the summer and winter hemispheres. We observe similar results in this study in Figure 4.8. However, it was not inferred from that study that the equatorial increase in [O] has the potential to reverse the global mean SAO. This raises the question, if WACCM-X represents the MLT state more accurately, how and why does the phase of T-I SAO reverse in GITM ? What are the additional processes in the lower thermosphere that are required to correct this discrepancy? We will henceforth look at the differences between the simulations during June solstice, when they are the largest.

4.3.6 June solstice

The panels on the left in Figure 4.10 show the averaged latitude-height distribution for temperature, whereas the panels on the right show the latitudinal gradient in temperature, for GITM simulations and WACCM-X around June solstice. Positive temperature gradient signifies larger temperature towards north (summer) and vice-versa. We show only G/MSIS and G/WX simulations here because G/MSIS shows a similar distribution as the G/NOSAO, and G/NUDGE is similar to WACCM-X. Overall, thermospheric temperature is larger in GITM than in WACCM-X. In the

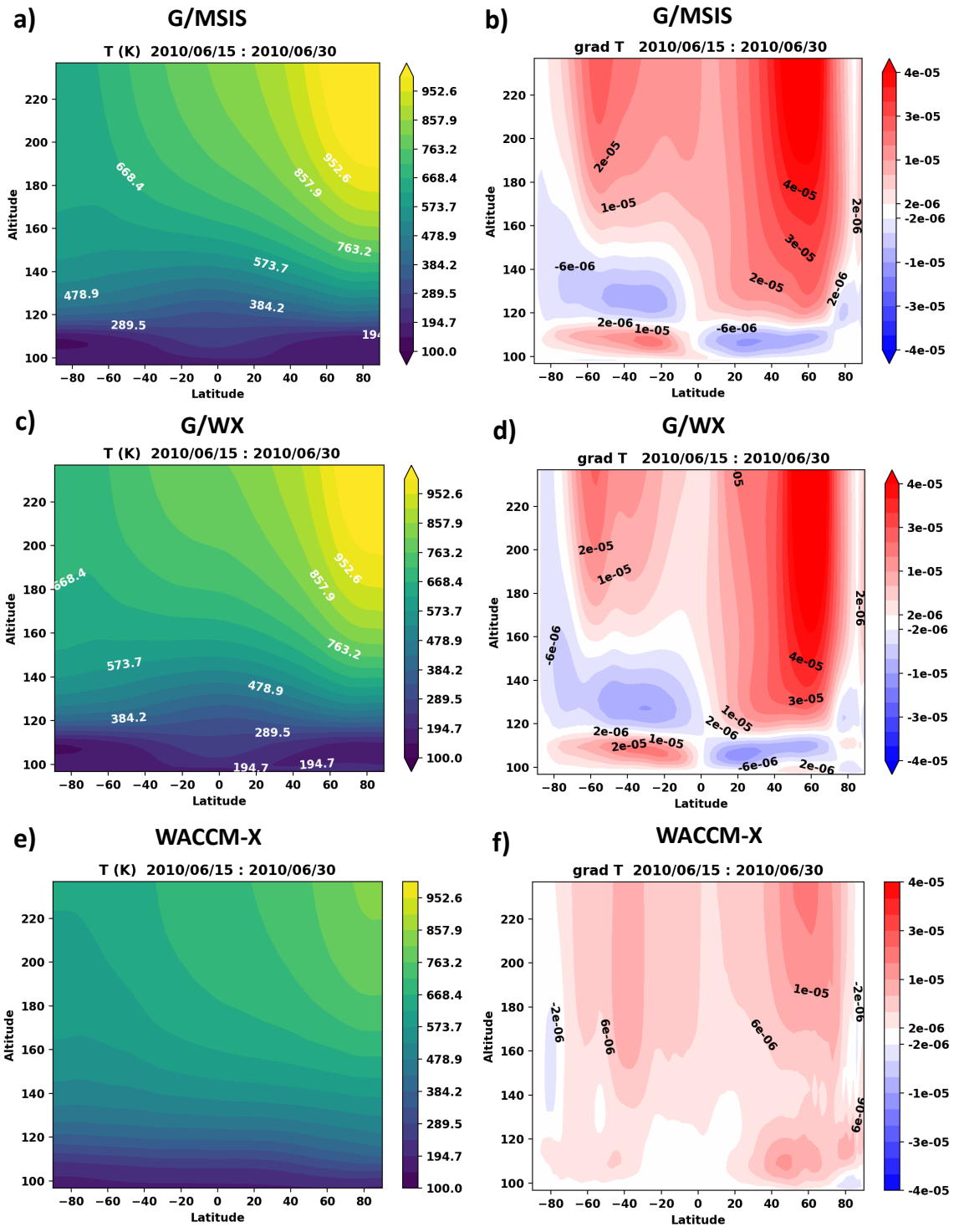

Figure 4.10: Latitude-Altitude cross-section of zonally and diurnally averaged Temperature in K for 2010/06/15 - 2010/06/30 for a) G/MSIS, c) G/WX, e) WACCM-X. Gradient in Temperature for each corresponding simulation is shown in the panel on the right. A positive gradient indicates that the temperature is larger towards the north.

lower thermosphere, between 100-120 km, GITM shows low temperatures at high latitudes. This is because of the adiabatic cooling due to equatorward circulation cells shown in Figure 4.4.

Above 140 km, WACCM-X has the weakest temperature gradient between the two hemispheres. It shows positive temperature gradient at all heights. GITM on the other hand shows a large positive gradient in both the hemispheres. As compared to G/MSIS, the gradient is lower at equatorial latitudes in G/WX. A possible explanation for this difference was discussed by Malhotra et al. (2020). As discussed in that study, high summer [O] from WACCM-X at the lower boundary of GITM changes the wind magnitudes between 100-120 km. This high summer [O] leads to larger equatorward winds, resulting in more adiabatic cooling. Similarly, lower winter [O] produces relatively slower equatorward winds resulting in less adiabatic cooling. This effect introduced near the lower boundary of the model has implications on the temperature structure of the whole thermosphere, resulting in the lowering of the summer temperature and relative increase in the winter temperature, thereby reducing the summer-to-winter gradient. These differences in gradients have a direct implication on the meridional and vertical winds, as the effectiveness of the thermospheric spoon mechanism depends on the temperature gradient between the two hemispheres (Jones Jr., Emmert, et al., 2018).

Figure 4.11 compares the zonal mean meridional and vertical winds and their variations with altitude for G/MSIS and G/WX simulations. The panel on the top (bottom) show the meridional (vertical) winds at summer high latitudes, 73°N. For HWM and WACCM-X, only the meridional winds are shown here. Above 120 km, the meridional winds transition to the summer-to-winter circulation, and thus are southward. These winter-directed meridional winds are accompanied by upwelling in summer (lower panel). The southward meridional wind and upwelling is the weakest for G/WX simulation because of weaker temperature gradient at equatorial latitudes. Above 140 km, WACCM-X (and HWM) show large southward winds despite the smaller temperature gradient. It is possible that the momentum sources from subgrid processes, e.g., breaking gravity waves at $\sim$140 km increase the magnitude of interhemispheric winds in WACCM-X. Another possible reason for weaker GITM winds might be stronger ion drag and viscosity. Note the momentum terms that contribute to GITM meridional winds were shown in Figure 4 of Malhotra et al. (2020). They showed that WACCM-X driven GITM had smaller winter-directed pressure gradient force at low latitudes, similar to the results shown in Figure 4.10. In the next section, we analyze the transport terms that contribute to the distribution

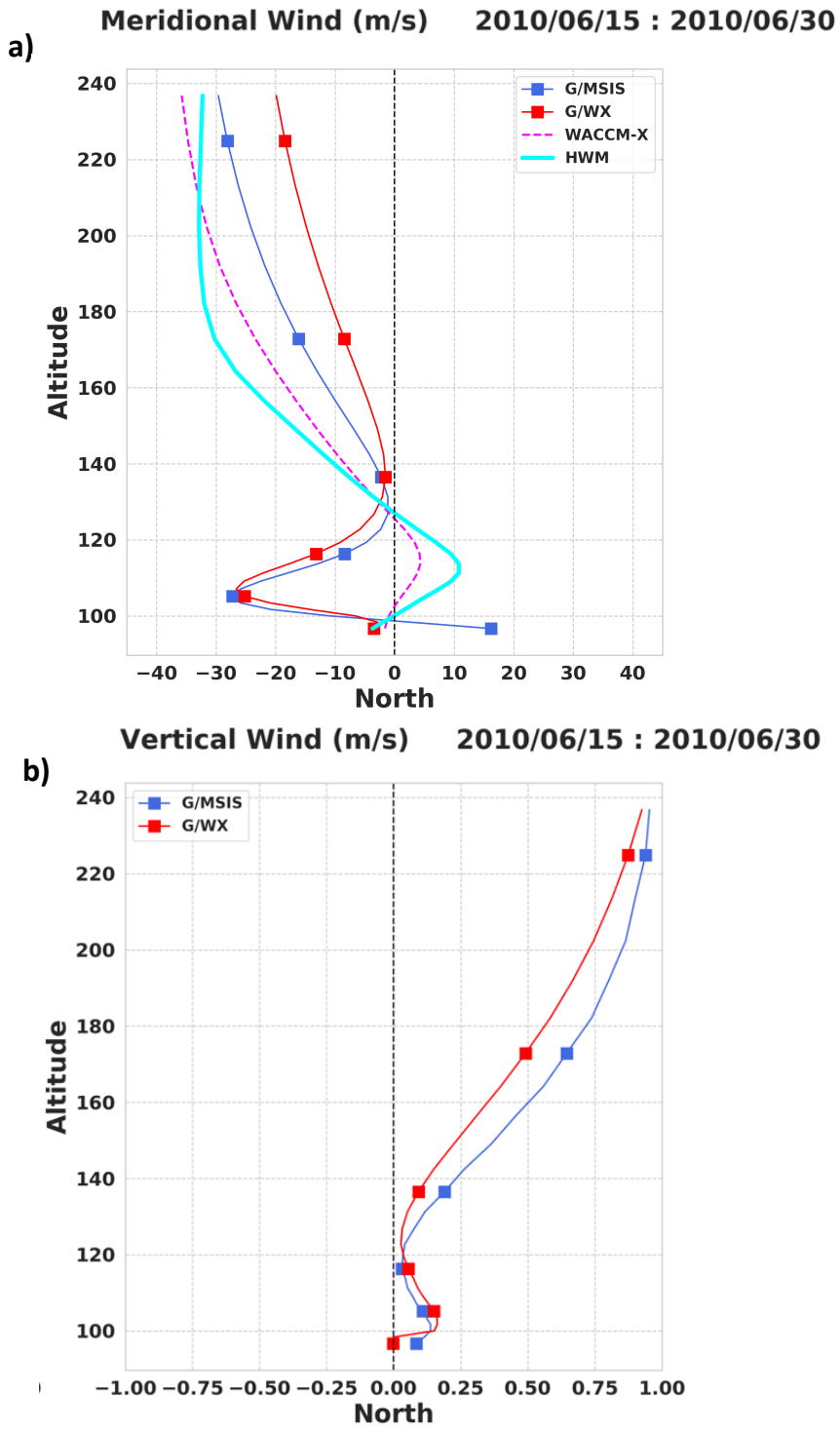

Figure 4.11: Zonal Averages for a) Meridional Winds and b) Vertical winds in m/s for different GITM simulations, WACCM-X and HWM, at 73°N. The winds are diurnally averaged for 2010/06/15 - 2010/06/30.

of [O] in the lower thermosphere and provide evidence that low latitude accumulation and incorrect global mean SAO in both G/WX and G/NUDGE simulations are linked to weaker meridional and vertical winds in the summer hemisphere.

4.4 Discussion

The continuity equation in the vertical direction in GITM can be written as,

$$\frac{\partial \mathcal{N}_s}{\partial t} = -\underbrace{\frac{\partial u_{r,s}}{\partial r}}^{(a)} - \underbrace{\frac{2u_r}{r}}^{(b)} - u_{r,s}\underbrace{\frac{\partial \mathcal{N}_s}{\partial r}}^{(c)} + \frac{1}{N_s}\mathcal{S}_s^{(d)} \tag{4.6}$$

where

$$\mathcal{N}_s = ln(N_s) \tag{4.7}$$

Following the notation from A. Ridley et al. (2006), r is the radial distance measured from the center of the Earth. The subscript r denotes the component in the radial direction. $u_{r,s}$ is the vertical velocity of species s. N_s is the number density of species s. The source term $\mathcal{S}_s$ for the species s includes the eddy diffusion and chemical sources and losses. Terms (a) and (b) signify the divergence of the vertical velocity and term (c) represents the vertical advection. Here, we demonstrate these terms only for [O]. For the vertical continuity equation, we show the sum of terms (a), (b) and (c). These terms collectively are referred to as the transport terms. Amongst the source terms, the eddy diffusion terms has negligible effect above 120 km. Eddy diffusion acts on the thermospheric densities primarily at ∼100 km, but the effect is much smaller than the transport terms. The chemical source term for [O] shows equinoctial peaks and thus does not provide an explanation for the opposite SAO in G/WX and G/NUDGE. This is because of larger chemical loss of [O] during solstices in G/WX and G/NUDGE simulations relative to other simulations and is shown in the supporting information.

The continuity equation in the horizontal direction is :

$$\frac{\partial N_s}{\partial t} = -N_s\underbrace{\left(\frac{1}{r}\frac{\partial u_\theta}{\partial \theta} + \frac{1}{rcos\theta}\frac{\partial u_\phi}{\partial \phi} - \frac{u_\theta tan\theta}{r}\right)}^{(e)} - \underbrace{\left(\frac{u_\theta}{r}\frac{\partial N_s}{\partial \theta} + \frac{u_\phi}{rcos\theta}\frac{\partial N_s}{\partial \phi}\right)}^{(f)}, \tag{4.8}$$

where, θ is latitude, ϕ is longitude, and the subscripts θ, ϕ denote the components in the respective directions. The first grouping on the right, labeled (e), is the divergence term, while the second, labeled (f), is the horizontal advection term. These are added together and considered as the horizontal transport terms below.

Figure 4.12 shows the latitudinal distribution of the horizontal (top panels) and

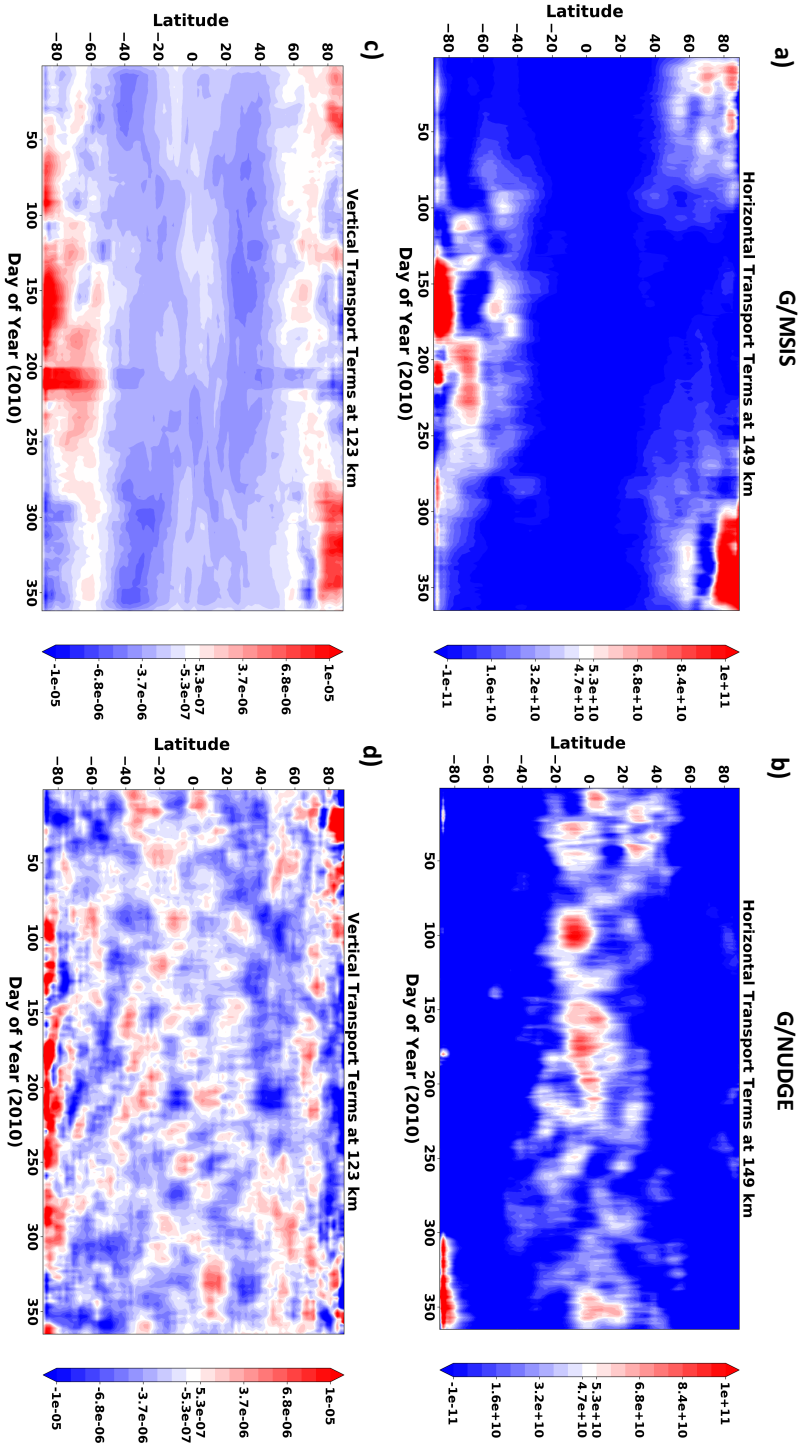

Figure 4.12: Diurnally averaged (15 day rolling mean) zonal means of transport terms. The panels on the left (right) are for G/MSIS (G/NUDGE). The top (bottom) panels are the horizontal (vertical) transport terms at 149 (123) km. Vertical transport terms have the units of s^{-1} and the horizontal transport terms have the units of $m^{-3}s^{-1}$.

vertical transport (bottom panels) terms that lead to the global distribution of [O] at ∼150 km shown in Figure 4.8. The panels on the left show the terms for G/MSIS while panels on the right are for the G/NUDGE. We only show G/MSIS and G/NUDGE, as we expect similar inference for G/NOSAO and G/WX, respectively. The magnitudes are different for the vertical and horizontal terms because the vertical continuity equation uses $\mathcal{N}_s$ as shown in equation 5.2. G/MSIS shows high [O] accumulation in the winter high latitudes via both horizontal and vertical transport. G/NUDGE shows weaker winter accumulation driven exclusively by vertical transport. This is a result of weaker upwelling, as shown in Figure 4.11. Alternatively, the horizontal transport term shows an accumulation at lower latitudes during solstices. This is because of weaker meridional winds in the summer hemisphere for G/WX and G/NUDGE simulations. Since, WACCM-X has larger meridional winds, it does not show equatorial accumulation of [O]. It was also demonstrated by X. Liu et al. (2014) that horizontal transport affects the peak location of the winter He bulge. We infer that weaker interhermispheric meridional transport in the summer hemisphere is the primary cause of the equatorial accumulation of [O] at solstices and the opposite phase of global mean SAO. Note, we also interpret similar results for January solstice (not shown here). The major difference between January and June meridional winds is that the wind magnitudes are much weaker for January relative to June.

It can be suggested that since WACCM-X has the right phase of [O] and ρ in the upper thermosphere, the nudging altitude in GITM should be increased to above 140 km where WACCM-X wind speeds increase to achieve the right phase of SAO. However, the WACCM-X model has the wrong SAO phase in the lower thermosphere as observed in global mean O/N_2. Yue et al. (2019) showed that GUVI data has an SAO in both [O] and O/N_2 that are in phase between the lower (8.4×10^{-4} Pa) and upper thermosphere (6.35×10^{-6} Pa), and have equinoctial peaks. Similar results were also obtained by Yu et al. (2020). Using the GITM altitude grid, we estimate 8.4×10^{-4} Pa to be ∼140-160 km. Even though the phase of the SAO is correct in WACCM-X at 400 km, it is not until 200 km that the SAO completely transitions from solstitial maxima to equinoctial maxima. GITM on the other hand is unable to correct this as it has lower meridional wind speeds and transport. This suggests that there are mechanisms missing in both models that could be responsible for the phase transition of the SAO in [O] from solstitial maxima to equinoctial maxima. Jones Jr. et al. (2017) noted that this phase transition in the global mean SAO in TIME-GCM occurs between ∼90-100 km. The amplitude of the SAO decreases to a minimum at 90 km, which is similar to the low amplitude observed by SABER in

Figure 4.2d. However, the transition altitude in TIME-GCM is much lower, as we still observe solstitial maxima in SABER [O] at 97 km. Considering the results by Yue et al. (2019) and Jones Jr. et al. (2017), in order to have the right phase of the SAO in integrated O/N_2, the global SAO should transition to equinoctial maxima in the lower thermosphere below ∼140 km. However, mechanisms driving this transition are not well understood. Jones Jr. et al. (2017) also observed a similar phase reversal between 90-100 km in the advective flux divergence, which was represented by a combination of meridional and vertical mean transport. This provides a hint that dynamics in the lower thermosphere might be driving this transition.

Given the results shown herein, we offer the following thoughts about certain processes that can improve the amplitude and phase of the SAO in IT models such as GITM :

- We introduce a seasonal variation in K_{zz} at the GITM lower boundary as a possible solution. This seasonal variation is similar to that used by Qian et al. (2009) in TIE-GCM. Even though seasonally varying K_{zz} decreases the O/N_2 at solstices and increases it during equinoxes, it is not enough to completely reverse the phase of the oppositely-phased SAO. We also ran a simulation using WACCM-X version 2.1 at the lower boundary of GITM and got similar results as G/WX shown in this study. The temporal variation of global mean O/N_2 and ρ at 400 km for both of these simulations are provided in the supporting information.

- HWM winds have relatively larger summer-to-winter interhemispheric winds in the lower thermosphere. Thus, the lower thermospheric meridional wind magnitudes can be increased in GITM to be in better agreement with HWM. Additionally, Jones Jr., Emmert, et al. (2018) demonstrated that the thermospheric spoon mechanism is most effective in the altitude regime where the thermosphere is transitioning from a fully mixed state to that of diffusively separated state. This can be achieved by reducing ion drag and/or viscosity in GITM, or nudging the meridional winds to HWM. The exact magnitude of winds in this region remains to be studied as more thermospheric wind observations are made over the next few decades.

- We also observe that winter-to-summer winds between ∼100-120 km are much larger in TIDI data than in HWM and WACCM-X. In our G/NUDGE simulation, we found that this circulation results in the lowering of global mean O/N_2, [O], ρ during solstices. If this residual circulation in WACCM-X and GITM is

more accurately represented such that the magnitude of the winds are in agreement with TIDI data, the solstitial maxima seen in the G/WX and G/NUDGE simulations could decrease significantly.

Thus, the correct lower boundary conditions for GITM should be SABER/WACCM-X-like [O], with additional mechanisms that represent the state of lower thermospheric dynamics more accurately.

4.5 Summary and Conclusions

The T-I SAO is a large intra-annual density (mass and plasma) variation with maxima during equinoxes and minima during solstices. It is successfully reproduced in most global whole atmosphere models. However, IT models need estimates of the MLT state via accurate specification of lower boundary conditions for producing the right amplitude and phase of SAO in the thermosphere. This is especially difficult as there are limited global sources to validate the winds, composition, and temperature in the MLT. It has recently been shown that lower atmospheric perturbations from gravity waves and tides can affect and improve (in some studies) the modeling of T-I SAO in the global IT models. This study explores a possible solution to improving the amplitude and phase of T-I SAO in GITM.

Our results show that GITM successfully reproduces the T-I SAO from first principles when no SAO is present at the lower boundary. This demonstrates that the SAO is primarily driven by the internal thermospheric horizontal and vertical transport. Using the densities and temperature from MSIS (MSIS-00) and winds from HWM (HWM14) at the lower boundary improves the amplitude and phase of SAO, especially in the lower thermosphere. However, there are still some disagreements between models and data regarding its phase and amplitude. For example, summer densities are underestimated and winter densities are overestimated during solstices, and the phase of SAO in ρ at 400 km leads the observations, especially during June and September.

Another problem is that the lower boundary condition in [O] specified at $\sim$100 km by MSIS does not match data in this region from SABER. The [O] from SABER (at 97-100 km) has larger densities at solstices and at summer mid-high latitudes, opposite to that of MSIS. It was found that [O] from WACCM-X at $\sim$100 km matches the data better and was then used as lower boundary condition in GITM. The seasonal and latitudinal variations of other parameters are the same between MSIS and WACCM-X in this altitude region. Using GITM driven by the opposite [O] distribution from

WACCM-X (G/WX) corrects for the summer-winter gradient. However, it does not improve the SAO at higher altitudes, but rather shifts its phase by 180°, such that the maxima shift to the solstices in the thermosphere. This is especially interesting, since the pure WACCM-X model has the appropriate phase of the upper thermospheric SAO, when compared to data. Nudging the dynamics in GITM towards WACCM-X up to 140 km (G/NUDGE), reduces the amplitude of this oppositely-phased SAO, but does not completely correct it.

We reveal that in G/WX and G/NUDGE simulations, the maxima in global mean [O] during the solstices are a result of the accumulation of [O] at lower latitudes. We show evidence that this is a result of of weaker temperature gradients, and ultimately weaker meridional and vertical winds in the summer hemisphere. The pure WACCM-X model also has the wrong phase of the SAO in the lower thermosphere, as it transitions from solstitial maxima towards equinoctial maxima between the altitudes ranging from 100-200 km. Since, several studies have shown that the global mean [O] and O/N_2 in the lower thermosphere have equinoctial maxima, we suggest that the phase transition from solstitial to equinoctial maxima in the global mean SAO should occur in the altitude region of ∼100-140 km.

Since the [O] distribution in WACCM-X is correct at 97-100 km, there must be additional mechanisms that decrease solstitial densities and nudge the phase of SAO towards equinoctial maxima in the lower thermosphere. These could include stronger thermospheric spoon circulation, stronger lower thermospheric residual circulation during solstices, and a seasonal variation in K_{zz}. It is also possible that sub-grid processes such as gravity wave breaking could act as a momentum source for the meridional winds, enhancing the meridional transport during the solstices. The exact mechanisms that drive the phase transition of the SAO in the lower thermosphere are currently unknown and will be the subject of future studies.

Our results emphasize the importance of accurate representation of the MLT state and dynamics in the lower thermosphere in IT models for better modeling of T-I SAO, and thus agree with the appraisal by Picone et al. (2013). We infer that the lower thermospheric region between 100-150 km is a complex and important region, as this is where the effect of the larger scale neutral dynamics is strongest. Finally, as new models and datasets are introduced, it becomes crucial to validate them with the older models and datasets; this can help in addressing the gaps in our knowledge of the physical mechanisms in the IT region.

The results of this study are summarized in Figures 4.13 and 4.14.

Figure 4.13: Illustration summarizing the observations of this study.

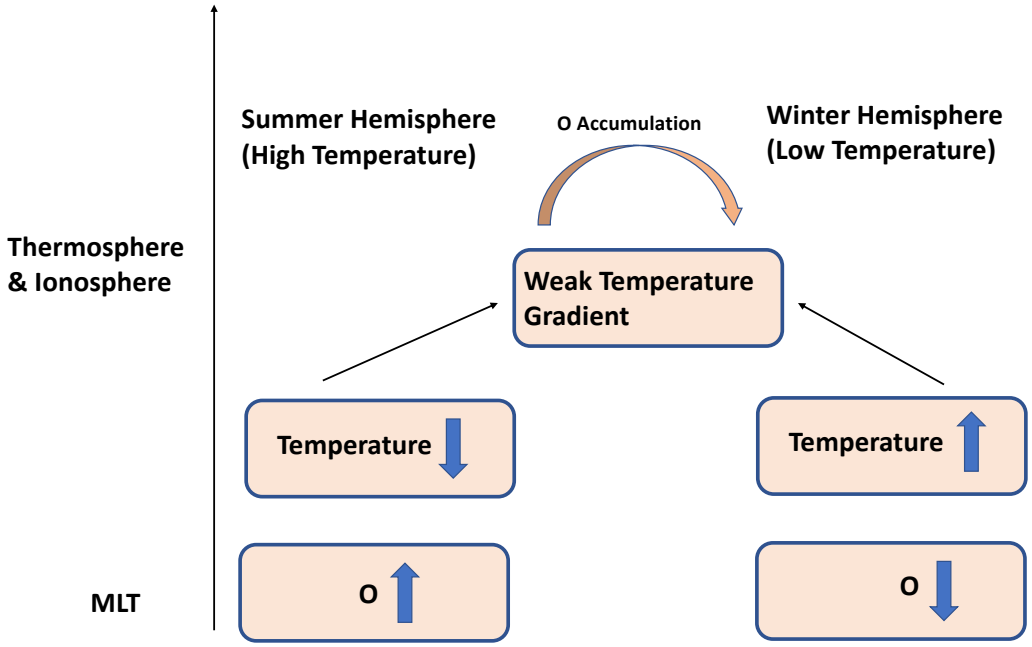

Figure 4.14: Illustration summarizing the results and conclusions of this study.

4.6 Supporting Information for "Impacts of Lower Thermospheric Atomic Oxygen and Dynamics on Thermospheric Semi Annual Oscillation using GITM and WACCM-X"

Contents :

1. Text Describing Figures 4.15, 4.16, and 4.17
2. Figures 4.15, 4.16, 4.17

Text in Support of Figures S1, S2, and S3

Figure 4.15 shows the densities and winds for MSIS and WACCM-X at the lower boundary of GITM. It demonstrates that the seasonal and latitudinal distribution of these parameters is similar between the two models and thus the largest difference between G/MSIS and G/WX is because of different [O] distributions.

Figure 4.16 shows the distribution of production and loss terms for O at 149 km for different GITM simulations. Panels (e), (f), and (g) show the net chemical source term that is used in the vertical continuity equation. This term is the difference between the production and loss terms for [O]. It can be inferred from these panels that the chemical source term though significant is not the cause of opposite SAO in G/WX and G/NUDGE simulations, because maxima at equinoxes in the globally averaged source terms are observed here. This is because of larger losses during solstices in both these simulations, arising from larger [O] during this time.

Figure 4.17 shows the intra-annual variations in daily averaged and fitted O/N_2 and ρ at 400 km for GITM simulations compared with WACCM-X, MSIS and different datasets. Here, we show two more simulations than the main manuscript. G/EDDY uses a seasonally varying eddy diffusion coefficient, K_{zz} with WACCM-X 2.0 density and dynamics at the lower boundary of GITM. The seasonal variation in K_{zz} is similar to that used by Qian et al. (2009). In comparison with G/WX, high K_{zz} in June results in much larger decrease in O/N_2 and ρ than in January, and there is a relative increase during equinoxes. G/WX 2.1 uses the latest version of WACCM-X, 2.1 and shows similar results as GITM driven with WACCM-X 2.0 (G/WX).

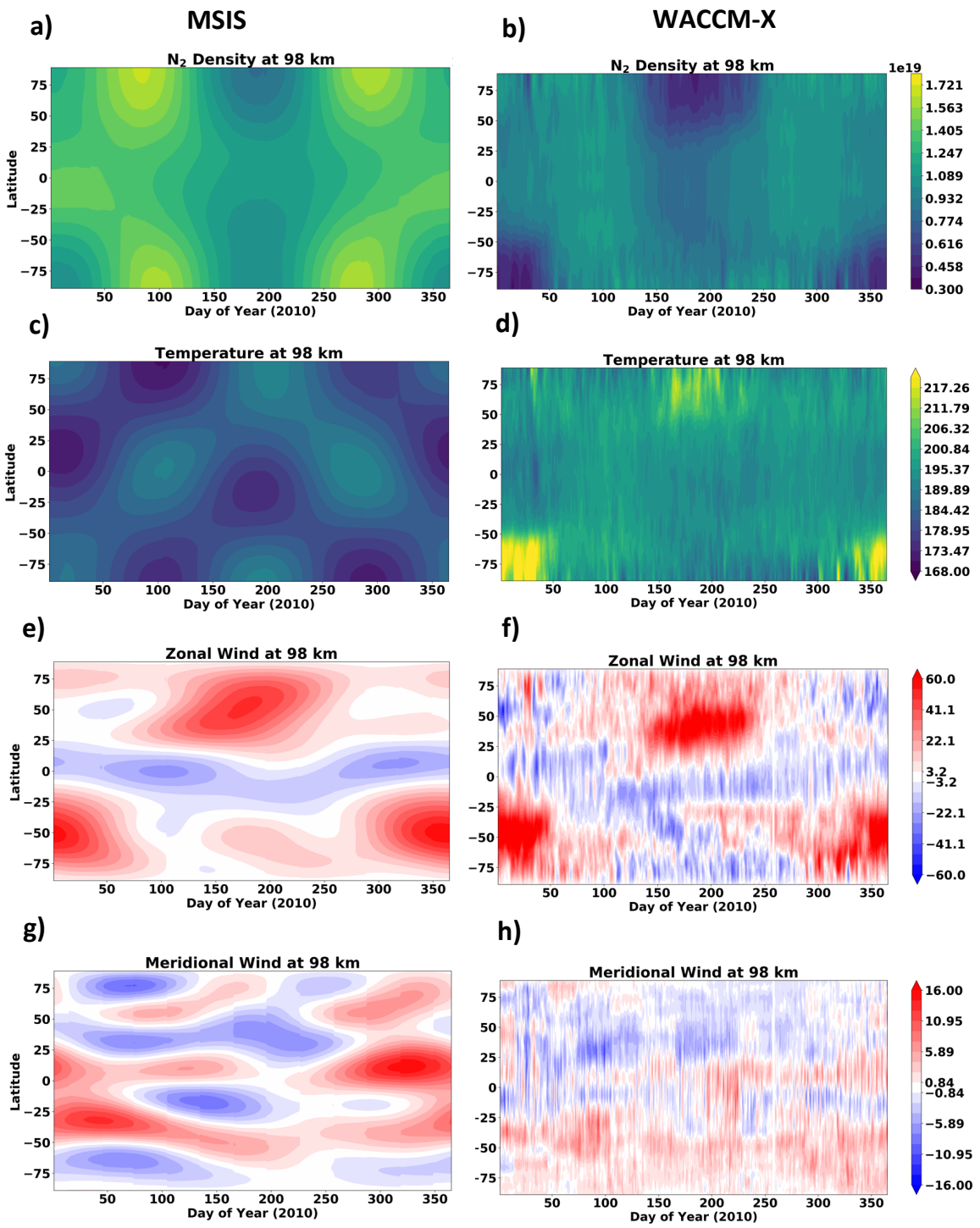

Figure 4.15: Diurnally averaged zonal mean quantities at the lower boundary (98.3 km) for MSIS in the left panel and WACCM-X in the right panel. (a), (b) N_2 density is in m^{-3}. (c), (d) Temperature is in K. (e), (f) Zonal Wind is in m/s. (g), (h) Meridional wind is in m/s.

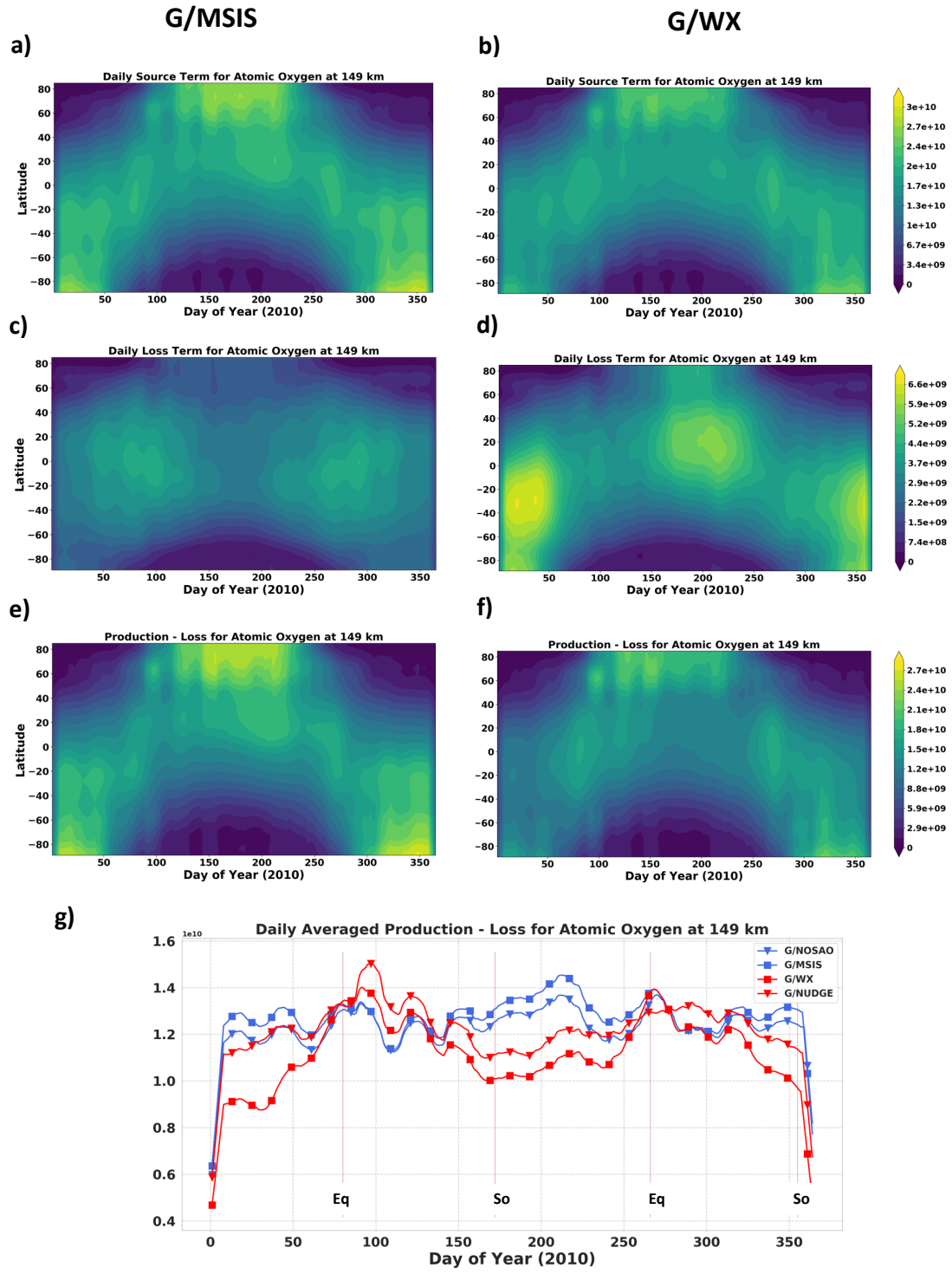

Figure 4.16: Diurnally averaged zonal mean chemical production ((a) and b)), loss ((c) and d)) and the difference between production and loss terms ((e) and f)) for O at 149 km. The panels on the left are for G/MSIS and the panels on the right are for G/WX, g) Global mean of the difference between production and loss terms for different simulations. The red vertical lines indicate the days of equinoxes and solstices.

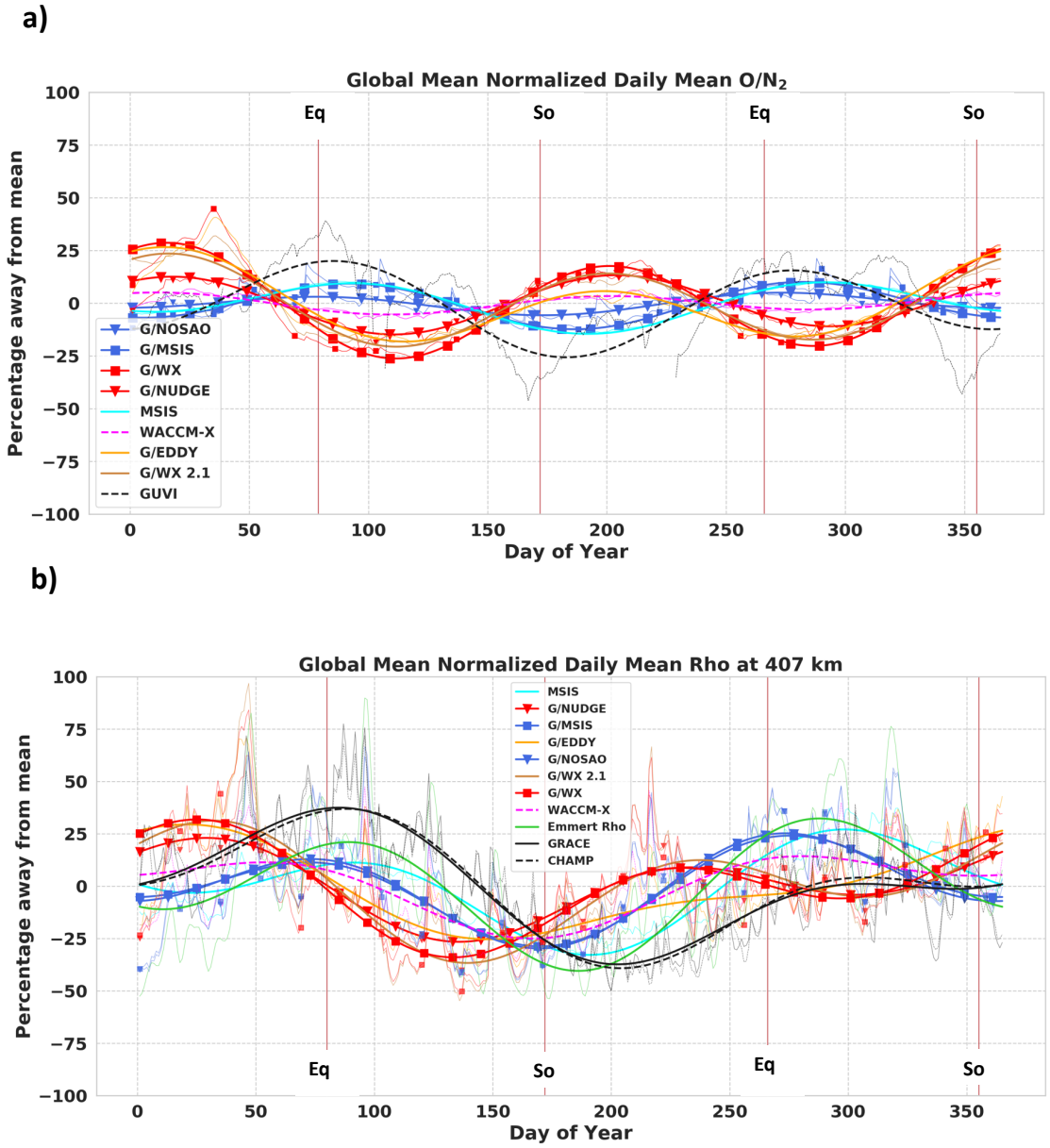

Figure 4.17: Diurnally averaged, normalized global means for a) O/N_2, b) ρ at 407 km, for different GITM simulations, WACCM-X model, MSIS, and observational datasets. The thin lines indicate the raw data and the thicker lines indicate the fitted values. CHAMP and GRACE datasets are normalized to 400 km and averaged for 2007-2010. The red vertical lines indicate the days of equinoxes and solstices.

CHAPTER V

Impacts of Spatially Varying Eddy Diffusion Coefficient in the Lower Thermosphere on the Ionosphere and Thermosphere Using GITM - Sensitivity Study

This goal of this chapter is to understand the effects of spatially non-uniform turbulent mixing in the MLT region on the Earth's upper atmosphere. The keypoints of this chapter are :

- Non-uniform MLT turbulent mixing introduces spatial variability in IT state.
- The net decrease of global O/N_2 and TEC is small and depends on the area of turbulent patch.
- During solstices, a larger decrease in O/N_2 is observed in the winter hemisphere of the IT region.

5.1 Introduction

The thermosphere couples with the electromagnetically forced ionosphere and magnetosphere and neutral dominated lower atmospheric regions. Even though geomagnetic disturbances account for the largest variability during geomagnetically active times (and at high latitudes), the geospace environment is in geomagnetically quiet condition most of the time, rendering the thermosphere highly susceptible to wave and turbulent forcings from the lower atmosphere. This can include short and longer term variations from tides, planetary waves, or gravity waves (Forbes, 1996; R. F. Garcia et al., 2016; Immel et al., 2006; Malhotra et al., 2016; Yigit & Medvedev,

2017). These forcings from the lower atmosphere can also change the background conditions of the ionosphere and thermosphere (IT) which can further modulate the way IT system responds to large geomagnetic forcings (Rees & Fuller-Rowell, 2011; X. Liu, 2013).

Gravity waves (GWs) play a crucial role in vertically coupling the different layers of the Earth's atmosphere. They are essentially generated in the troposphere and stratosphere by numerous mechanisms, such as topography (e.g., Nastrom et al., 1987; Nastrom & Fritts, 1992), and convective and frontal activity (e.g., Clark et al., 1986; Fritts & Nastrom, 1992), because of imbalances between gravity and atmospheric buoyancy forces. As they propagate higher in the atmosphere, their amplitude increases (because of the decrease in density), as a result of which they can become unstable (Fritts & Rastogi, 1985). This can result in non-linear wave breaking, turbulence and deposition of wave momentum and energy in the upper atmosphere (Hodges Jr., 1967; Fritts & Alexander, 2003), thus changing the background winds, thermal structure and composition. For example, the cold summer mesopause anomaly is a result of adiabatic expansion due to meridional circulation induced by the GW drag (Andrews et al., 1987; R. R. Garcia & Solomon, 1985; Lindzen, 1981). Because of the large amplitude of GWs in the mesosphere and lower thermosphere (MLT), turbulence resulting from their breaking can be quite large in this region (e.g., Fukao et al., 1994; X. Liu et al., 2014). However, above this region, the atmosphere becomes too viscous to sustain turbulence. The transition from the region dominated by eddy turbulence (mesosphere) to the region dominated by molecular diffusion (IT) is also called as the turbopause (between 90-120 km) (Vlasov & Kelley, 2014). Specifically, the turbopause is the boundary where eddy diffusivity roughly equals molecular diffusivity.

IT models such as the Global Ionosphere Thermosphere Model (GITM) (A. Ridley et al., 2006) and Thermosphere-Ionosphere-Electrodynamics General Circulation Model (TIE-GCM) (Dickinson et al., 1981, 1984) are often used to understand the evolution and physical mechanisms responsible for the state of IT system. The lower boundary of these IT models represents the state of MLT which also contains the turbopause. Thus, to improve the IT modeling, the spatial and temporal variation of the background state (e.g., Malhotra et al., 2020), atmospheric waves (e.g., Q. Wu et al., 2012), and of turbulence (Qian et al., 2009) should be correct at the lower boundary of the models. Most global circulation models do not resolve GWs because of their coarse resolution. The models that can resolve some portion of GW spectrum are restricted by the computing constraints and a large spatial and temporal spectrum

of GWs. The effects of turbulence in the thermosphere are thus often parameterized by a diffusion parameter, called the eddy diffusion coefficient (K_{zz}), in the continuity and energy equations of the IT models (e.g., A. Ridley et al., 2006; Qian et al., 2009). Turbulence in the MLT modifies the thermospheric state through its influence on the thermal balance via wave dissipation (causing heating), thermal diffusion (causing cooling), and compositional change via increased mixing (Demaeyer & Vannitsem, 2018). There is evidence that the primary effect on the temperature of IT is cooling (Yigit & Medvedev, 2009). It also results in upward transport of molecular species into the thermosphere, increasing their relative concentration, and vice-versa for lighter species. These changes in composition introduced in the lower thermosphere can map to higher altitudes through diffusive equilibrium (e.g., Malhotra et al., 2020).

Various in-situ and remote sensing observational platforms, such as rockets, lidars, and radars have historically been used to calculate the value of K_{zz} in the MLT region, and several studies have reported the value of K_{zz} that ranges between 10 - 100 m^2/s (e.g., Danilov & Kalgin, 1996; Fukao et al., 1994; Justus, 1967; H.-L. Liu, 2021; Kurosaki et al., 1996; Triplett et al., 2018). A few studies (e.g., Johnson & Wilkins, 1965; Strobel et al., 1985; Vlasov & Kelley, 2015) have calculated the upper limits of K_{zz} to be around the same range. However, some other experimental studies have reported values of energy dissipation rate between 100-1,000 mW/kg, which correspond to larger values of K_{zz}, ranging between 100 - 1000 m^2/s (e.g., Bishop et al., 2004; R. R. Garcia & Solomon, 1985; G. Lehmacher & Lübken, 1995; G. A. Lehmacher et al., 2006, 2011; A. Z. Liu, 2009; Szewczyk et al., 2013). The globally averaged K_{zz} calculated from the satellite observations of atomic oxygen (O) and carbon dioxide (CO_2) from the Sounding of the Atmosphere using Broadband Emission Radiometry (SABER) instrument has also been reported to be $\sim$ 30 - 100 m^2/s (Salinas et al., 2016; G. R. Swenson et al., 2019). Several of these studies have also reported a seasonal variation in K_{zz} with larger values during solstices (with maxima in summer) (Fukao et al., 1994; R. R. Garcia & Solomon, 1985; Kirchhoff & Clemesha, 1983b; Lubken, 1997; Kurosaki et al., 1996; Sasi & Vijayan, 2001).

Even though the seasonal variation of K_{zz} has been widely studied, its spatial variation largely remains a mystery. H.-L. Liu et al. (2014) showed using Whole Atmosphere Community Climate Model with thermosphere and ionosphere extension (WACCM-X) high-resolution simulations that the GW structures on the order of tens to 100 km in the MLT generated from a tropical cyclone are spatially non-uniform. In fact, with a non-uniform wave field and background atmosphere, it is expected

that the resulting turbulence in the wave-breaking region would be non-uniform as well (Fritts & Dunkerton, 1985; H. L. Liu et al., 1999). However, since there are not many global observations of turbulence, we can really only use the measurements of GW activity to approximate the spatial variation of turbulence. GW potential energy indicates the intensity of GWs and can be strongly related to the amplitude of breaking GWs and thus GWs induced K_{zz} (Lindzen, 1981). Kurosaki et al. (1996) found that the seasonal variability of eddy diffusion derived from VHF Doppler radar is similar to that of the GW activity derived by Tsuda et al. (1990) and R. R. Garcia & Solomon (1985) and supported the hypothesis that turbulence is primarily generated by GW breaking. With the advent of space-based MLT observations, space-borne instruments (e.g., SABER) have also been widely used to study GW morphology and climatology in the stratosphere and mesosphere (e.g., Fetzer & Gille, 1994; Preusse et al., 2008; Ern et al., 2004; Frohlich et al., 2007). Recent studies have found that the GW activity in the MLT region varies spatially with seasons (John & Kumar, 2012; Preusse et al., 2009; Walterscheid & Christensen, 2016). John & Kumar (2012) using temperature variances from SABER showed that the GW activity during the equinoxes is larger at low latitudes and larger at polar latitudes during solstices (with maxima in summer). It is likely that there can be more regions of enhanced GW wave activity where the amplitudes of GWs might be too small to be observed by SABER (X. Liu et al., 2017)

As GWs propagate up from their sources in the troposphere and stratosphere, they also propagate away from their sources horizontally because of which the shears due to localized sources tend to smear out, resulting in more band-like/zonally symmetric GW variances (e.g., Ern et al., 2011, 2013; Preusse et al., 2009; Trinh et al., 2018). Thus, the specific source regions of GWs become less important than a general background of GWs in the atmosphere (Trinh et al., 2018). The goal of this study is to better understand the sensitivity of the IT region to the spatial variation of K_{zz}. This is done using the IT model, GITM, with different settings and spatial distributions for K_{zz}. We introduce latitudinal bands (longitudinally uniform) of 30° width at equatorial and polar latitudes during different seasons similar to the observations by John & Kumar (2012). We investigate the mechanisms through which a non-uniform global distribution of K_{zz} can alter the dynamics and thermal structure of the thermosphere, and how these effects compare to when a globally uniform value of K_{zz} is used.

5.2 Methodology

5.2.1 Global Ionosphere Thermosphere Model (GITM)

GITM is a physics-based IT model that solves the continuity, momentum and energy equation to estimate the IT state (neutral, ion, and electron densities, temperature, and dynamics) given specific inputs and model parameters (A. Ridley et al., 2006). It is a 3D model with latitude, longitude, and altitude as the coordinate systems. The altitude grid allows for studying non-hydrostatic responses of the IT system. The lower boundary of GITM is at ∼97 km and the upper boundary is at ∼500 km. The vertical grid resolution is roughly 30% of the scale height of the thermosphere: it is less than 3 km in the lower thermosphere and up to 10 km in the upper thermosphere. The horizontal resolution is flexible and can be changed depending on the use case. It solves for the neutral densities of O, O_2, N(^{2}D), N(^{2}P), N(^{4}S), N_2, NO and He; and ion species O^+(^{4}S), O^+(^{2}D), O^+(^{2}P), O_2^+, N^+, N_2^+, NO^+ and He^+. The neutral species have the same velocity in the horizontal direction and different in the vertical. For the simulations shown in this study, GITM uses a horizontal resolution of $2^\circ \times 4^\circ$ (latitude × longitude).

GITM can be coupled with different models for drivers, initial conditions and boundary conditions. In the simulations used in this study, we use NRLMSIS2.0 for initial and lower boundary conditions (J. T. Emmert et al., 2020) for neutral densities, and Horizontal Wind Model (HWM14) (Drob et al., 2015) for neutral horizontal winds. We use the default configuration for the external drivers: Weimer model (Weimer, 2005) for high latitude electric fields, Flare Irradiance Spectral Model (FISM) (Chamberlin et al., 2008) for solar extreme ultraviolet irradiance at different wavelengths, and NOAA POES hemispheric power driven model (T. J. Fuller-Rowell & Evans, 1987) for estimates of high latitude energetic particle precipitation.

5.2.2 GITM Eddy Diffusion Parameterization

The eddy diffusion parameter is included in the continuity and the thermodynamic equations of GITM to parameterize the effects of eddy mixing and eddy conduction, respectively. The vertical continuity equation is as follows:

$$\frac{\partial \mathcal{N}_s}{\partial t} = -\frac{\partial u_{r,s}}{\partial r} - \frac{2u_r}{r} - u_{r,s}\frac{\partial \mathcal{N}_s}{\partial r} + \frac{1}{N_s}\mathcal{S}_s \tag{5.1}$$

where

$$\mathcal{N}_s = ln(N_s) \tag{5.2}$$

Here, the subscript r denotes the component in the radial direction. $u_{r,s}$ is the vertical velocity of species s. N_s is the number density of species s. The source term $\mathcal{S}_s$ for the species s includes the contribution of eddy diffusion (K_e) and chemical sources and losses (C_s) and is as follows:

$$\mathcal{S}_s = \frac{\partial}{\partial r}\left[N_s K_e \left(\frac{\partial N_s}{\partial r} - \frac{\partial N}{\partial r}\right)\right] + C_s \tag{5.3}$$

The vertical component of the thermodynamic equation is:

$$\frac{\partial \mathcal{T}}{\partial t} + u_r \frac{\partial \mathcal{T}}{\partial r} + (\gamma - 1)\mathcal{T}\left(\frac{2u_r}{r} + \frac{\partial u_r}{\partial r}\right) = \frac{k_B}{c_v \rho \overline{m_n}} \mathcal{Z} \tag{5.4}$$

where c_v is the specific heat at a constant volume, ρ is the neutral mass density, γ is the ratio of specific heats. $\mathcal{T}$ is the normalized temperature defined using the temperature (T), the Boltzmann constant (k_B), and number density weighted average mass ($\overline{m_n}$) as follows:

$$\mathcal{T} = \frac{k_B}{\overline{m_n}} T \tag{5.5}$$

The source term, $\mathcal{Z}$ contains the following terms:

$$\mathcal{Z} = Q_{EUV} + Q_{chem} + Q_{NO} + Q_O + Q_{CO_2} + \frac{\partial}{\partial r}\left((\kappa_c + \kappa_{eddy})\frac{\partial T}{\partial r}\right) + Q_C \tag{5.6}$$

where Q_{EUV} is the heating of the thermosphere via solar ultraviolet radiation, Q_{chem} represents the chemical heating, Q_{NO}, Q_O, Q_{CO_2} are radiative cooling terms for NO, O, and CO_2. Q_C represents the collisional heating rates (frictional and heat transfer) from Zhu & Ridley (2016). κ_c is the molecular heat conductivity and κ_{eddy} is the heat conductivity due to eddy diffusion.

In this study, we use the same value for the turbulent momentum and heat diffusivity in the equations 5.3 and 5.6, i.e., $K_e = \kappa_{eddy} = \mathrm{K}_{zz}$. The ratio of turbulent momentum to heat diffusivity is called the turbulent Prandtl number. Under realistic atmospheric conditions, these parameters should not be the same (Fritts & Dunkerton, 1985; R. R. Garcia et al., 2014; Hocking, 1990; Justus, 1967; A. Z. Liu, 2009; McIntyre, 1989) and the Prandtl number for molecular diffusion has been found to be around 0.7 in the lower atmosphere (Dieminger et al., 1996). Since the value of turbulent Prandtl number remains controversial in the MLT (Fritts & Dunkerton, 1985; R. R. Garcia et al., 2014; Hocking, 1990), we use the same value for these coefficients (Prandtl number=1) in this study. More detailed discussion of other physical and chemical processes included in GITM is provided in A. Ridley et al. (2006).

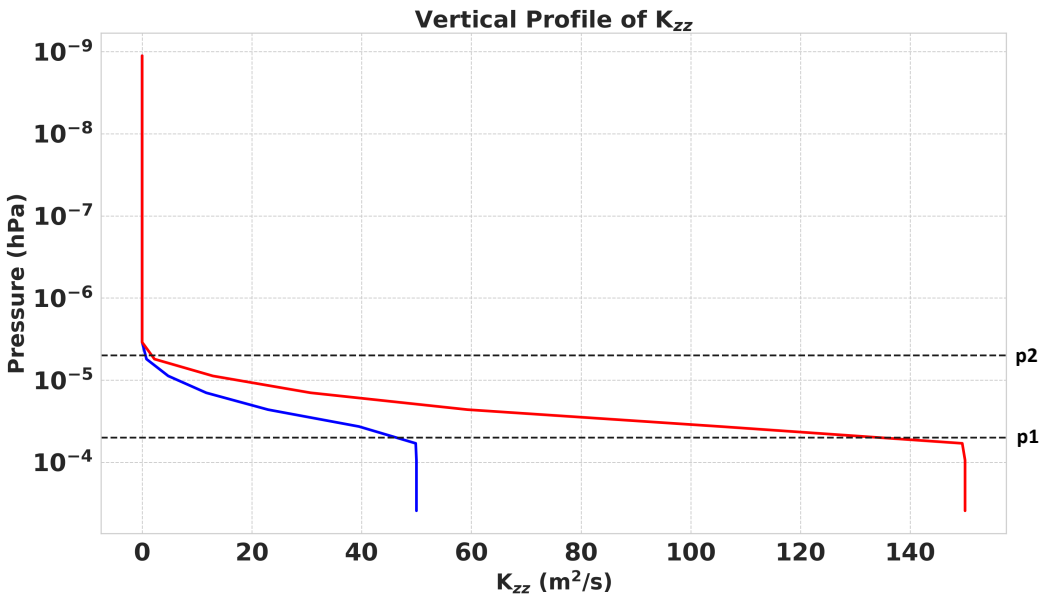

Figure 5.1: Vertical profile of the K_{zz} parameter for one of the simulations, when K_{zz} is set to 50 m^2/s or 150 m^2/s at the lower boundary of GITM. Here. p1 = 5×10^{-5} hPa and p2 = 5×10^{-6} hPa. These values are also indicated by dashed black horizontal lines. Slight deviation of the profile from these values is because of the uncertainty introduced by interpolation.

Figure 5.1 shows the vertical profile for K_{zz} used in this study. Here, we define two pressure levels. Pressure $p1$ defines the pressure up to which K_{zz} remains constant, while $p2$ defines the upper altitude limit of eddy diffusion in GITM, above which K_{zz} is zero. Between $p1$ and $p2$, K_{zz} decays linearly. The vertical profile (in pressure coordinates) stays the same in all of our simulations, thus assuming the turbopause to be at the same pressure level, while only changing the magnitudes of K_{zz}. Here, we use $p1 = 5 \times 10^{-5}$ hPa, and $p2 = 5 \times 10^{-6}$ hPa.

5.2.3 Simulations

The simulations used in this study are run for 15 - 17 days depending on the month with the results shown here being the diurnal averages of last 1-2 days of the simulations. This is done because GITM takes $\sim$ 10 - 12 days to achieve diurnal reproducibility. Three time periods are chosen for this analysis: around March Equinox (2010/03/15 - 2010/04/02), around June Solstice (2010/06/15 - 2010/07/02), and around December solstice (2010/12/15 - 2010/12/30). We use time-varying geomagnetic indices (F10.7, IMF, HP) representing realistic conditions. Here, the results are primarily shown as the differences between perturbed simulations with spatially varying K_{zz} and control simulations with globally uniform K_{zz}. These are collectively referred to as "configurations". Table 5.1 summarizes the different GITM configurations and the corresponding simulations that are differenced in each.

We use the spatially non-uniform K_{zz} that is inspired from the gravity wave activity distribution provided in Figure 9 of John & Kumar (2012). In John & Kumar (2012), during equinoxes, weak activity at equatorial latitudes is observed, whereas, larger activity at high latitudes (especially in summer) is observed during solstices. The exact values of K_{zz} and how it relates to the gravity wave activity observed in these studies will be investigated in future studies. Here, we assume a value of 50 m^2/s for background K_{zz} in the MLT, taking into consideration the recent evidence of K_{zz} values of $\sim$ 30 - 60 m^2/s (e.g., H.-L. Liu, 2021; Salinas et al., 2016; G. R. Swenson et al., 2019; Triplett et al., 2018), and larger values ranging between 150-200 m^2/s to represent intermittent patches of high turbulent activity in latitudinal bands (longitudinally uniform) of 30° width.

The distribution of K_{zz} near the lower boundary for certain configurations is also shown in Figure 5.2. From Table 5.1 and Figure 5.2, the C1 configuration around March equinox has larger K_{zz} (150 m^2/s) at equatorial latitudes, and a smaller value (50 m^2/s) everywhere else. The C2 configuration has the same K_{zz} as C1, but with turbulent heat conduction off in both the perturbed and control simulations. The

Model Configuration	Month	Perturbed Simulation	Globally averaged K_{zz} for the Perturbed Simulation	Control Simulation
C1	NH Spring Equinox	K_{zz} = 150 m^2/s for -15° <= lat <= 15° K_{zz} = 50 m^2/s elsewhere	74.2 m^2/s	K_{zz} = 50 m^2/s
C2	NH Spring Equinox	Same as C1, Turbulent Conduction off	74.2 m^2/s	K_{zz} = 50 m^2/s, Turbulent conduction off
C3	NH Spring Equinox	Same as C1	74.2 m^2/s	K_{zz} = 74.2 m^2/s
C4	NH Winter Solstice	K_{zz} = 150 m^2/s for lat >= 60° K_{zz} = 50 m^2/s elsewhere	53.6 m^2/s	K_{zz} = 50 m^2/s
C5	NH Summer Solstice	K_{zz} = 150 m^2/s for lat >= 60° K_{zz} = 50 m^2/s elsewhere	56.6 m^2/s	K_{zz} = 50 m^2/s
C6	NH Summer Solstice	K_{zz} = 200 m^2/s for lat >= 60° K_{zz} = 100 m^2/s for -15° <= lat <= 15° K_{zz} = 200 m^2/s for lat <= -60° K_{zz} = 50 m^2/s elsewhere	83.6 m^2/s	K_{zz} = 50 m^2/s

Table 5.1: GITM Runs with different spatial variations of K_{zz}. For each model configuration, the control simulation with uniform K_{zz} is subtracted from the perturbed simulation with non-uniform K_{zz}. 'NH' is the abbreviation for the northern hemisphere.

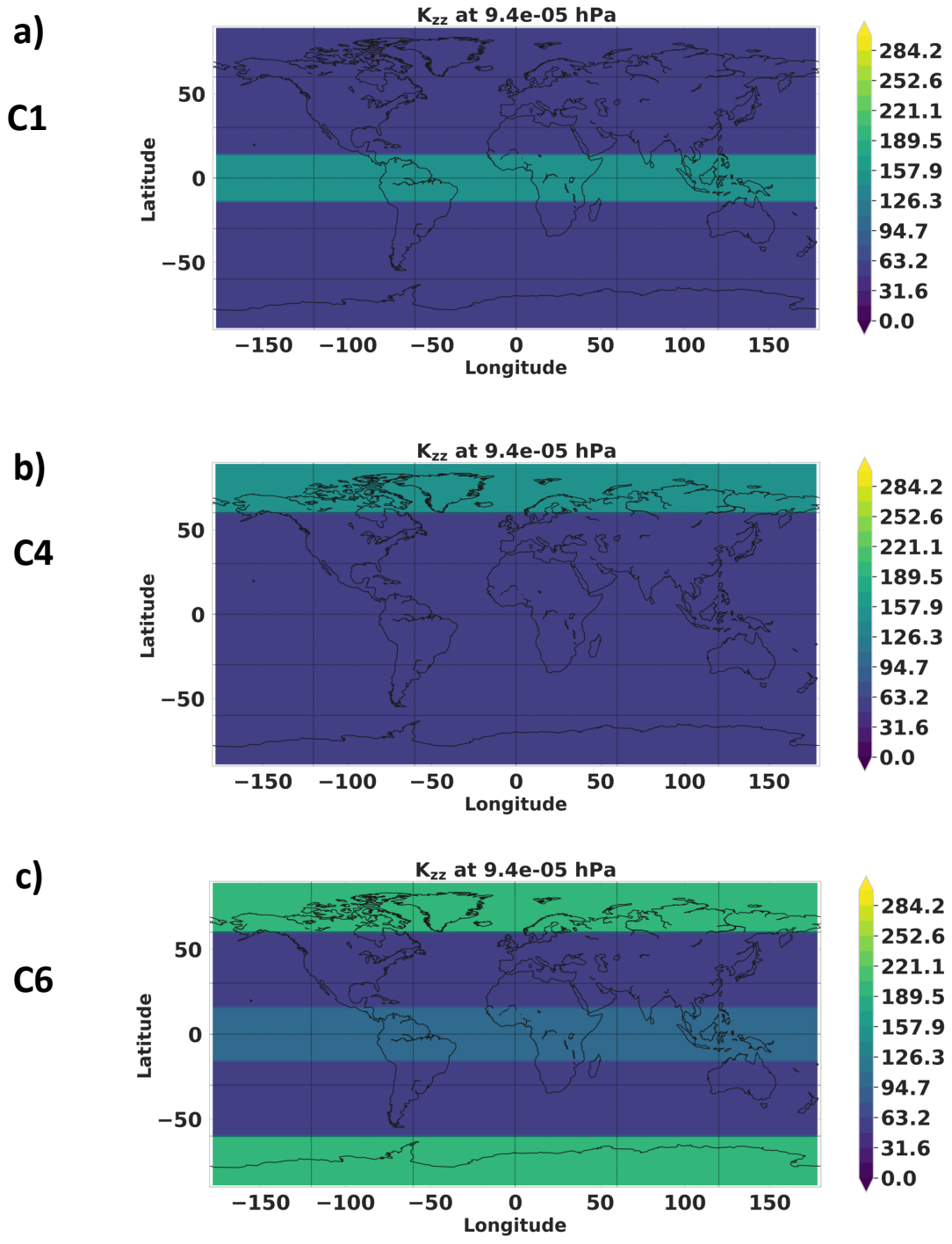

Figure 5.2: Spatial variation of K_{zz} (in m^2/s) for different configurations, a) C1, b) C4, and c) C6, near GITM lower boundary.

C3 configuration has the perturbed simulation similar to C1, however, K_{zz} for the control simulation is adjusted such that its value is equal to the globally averaged K_{zz} of the perturbed simulation (74.2 m^2/s). This configuration aims to understand the net effect of spatially varying K_{zz} without changing the global mean of K_{zz}. The C4 configuration is run during December solstice, and has larger K_{zz} of 150 m^2/s in the polar regions, and 50 m^2/s everywhere else. The C5 configuration is similar to C4 but run during June solstice. C4 and C5 configurations are run to understand any seasonal differences in the IT response to the MLT K_{zz} variation. The C6 configuration is run during June solstice, with K_{zz} variation resembling the gravity wave activity observed by John & Kumar (2012) during solstices. They observed larger values in the summer hemisphere relative to the winter hemisphere. However, in our effort to understand the seasonal differences, we use the same value at polar latitudes in both the hemispheres, with a relatively smaller value (but still enhanced from the background) in the equatorial region.

5.3 Results

Figure 5.3 shows the background conditions (diurnally and zonally averaged) for the control simulation of C1 configuration ($K_{zz} = 50$ m^2/s everywhere). The distributions of $[N_2]$ and [O] are symmetric around the equator. At ~ 200 km, O becomes the major species in the thermosphere. The temperature is slightly larger in the northern hemisphere as it is transitioning from spring to summer during this time. The meridional winds are weak and relatively unstructured. The equatorward cells in the lower thermosphere are because of the dominating centrifugal force near the lower boundary of the model (Malhotra et al., 2020). Similar circulation cells were also observed by McLandress et al. (1996) and S. P. Zhang et al. (2007) in the High Resolution Doppler Imager (HRDI) Wind Imaging Interferometer (WINDII) data onboard the Upper Atmosphere Research Satellite (UARS). These cells are directly responsible for the low temperatures in the high latitude region in the lower thermosphere via adiabatic divergence.

5.3.1 Equinox Simulations

Figure 5.4 shows the K_{zz} for configuration C1. As discussed above, the vertical profile of K_{zz} is such that it is maximum in the lower thermosphere and gradually decreases to 0 at higher altitudes. Thus, the perturbed and control simulations differ in their K_{zz} distribution at only low latitudes and low altitudes.

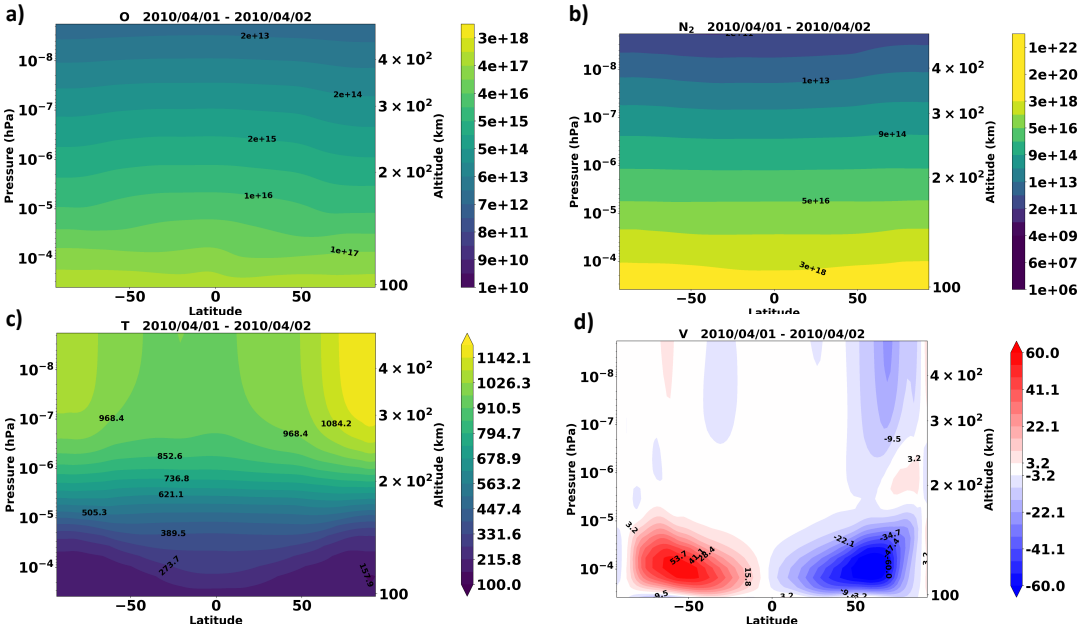

Figure 5.3: Diurnal and zonal means of a) O number density in m^{-3}, b) N_2 number density in m^{-3}, c) Temperature in K, and d) Meridional wind in m/s for the control simulation of the C1 configuration.

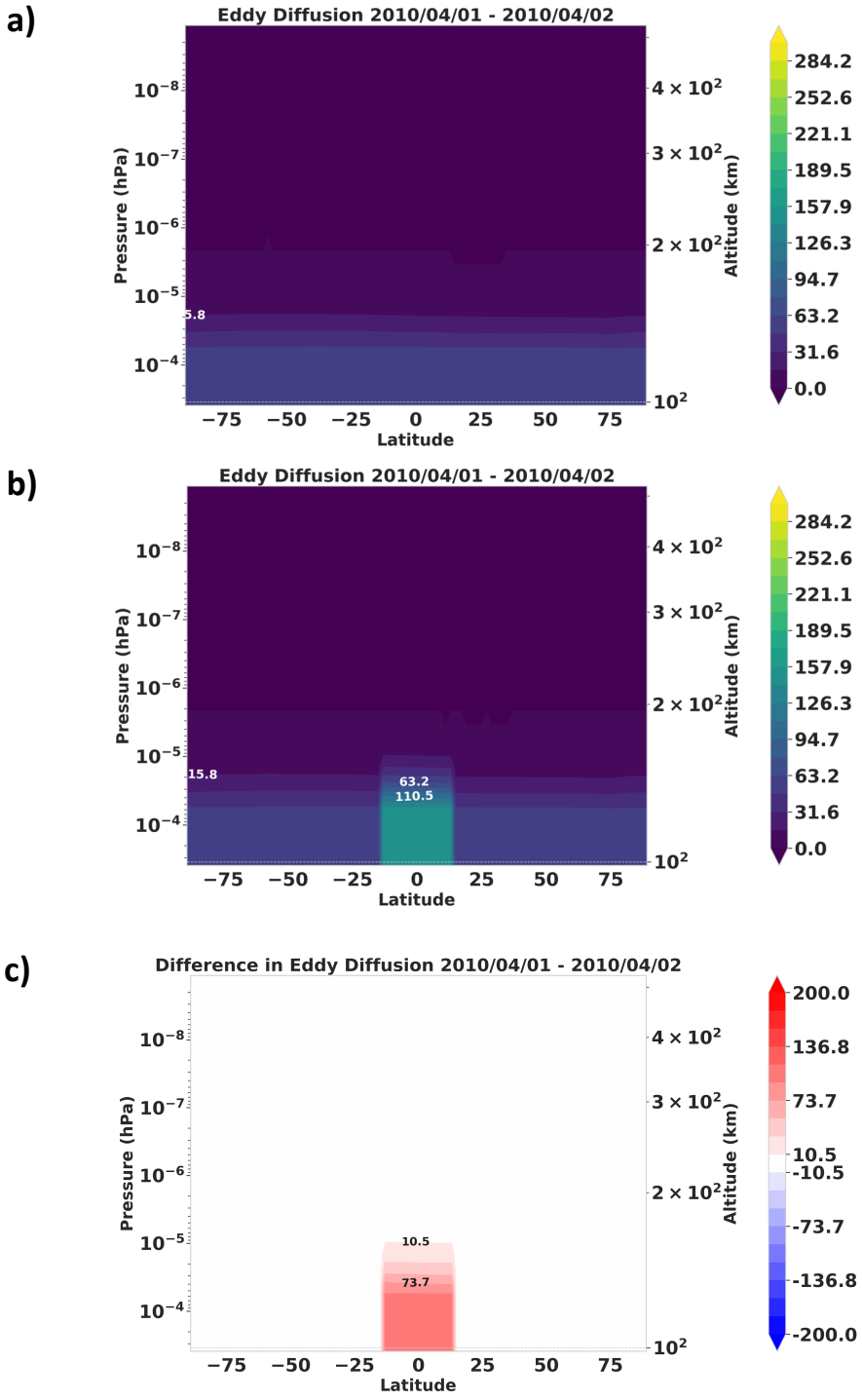

Figure 5.4: Diurnal and zonal means of K_{zz} for configuration C1; a) Control simulation with K_{zz} = 50 m^2/s throughout the globe at the lower boundary, b) Perturbed simulation with K_{zz} = 150 m^2/s at low latitudes (-15° <= lat <= 15°) and 50 m^2/s everywhere else at the lower boundary. c) Difference between a) and b).

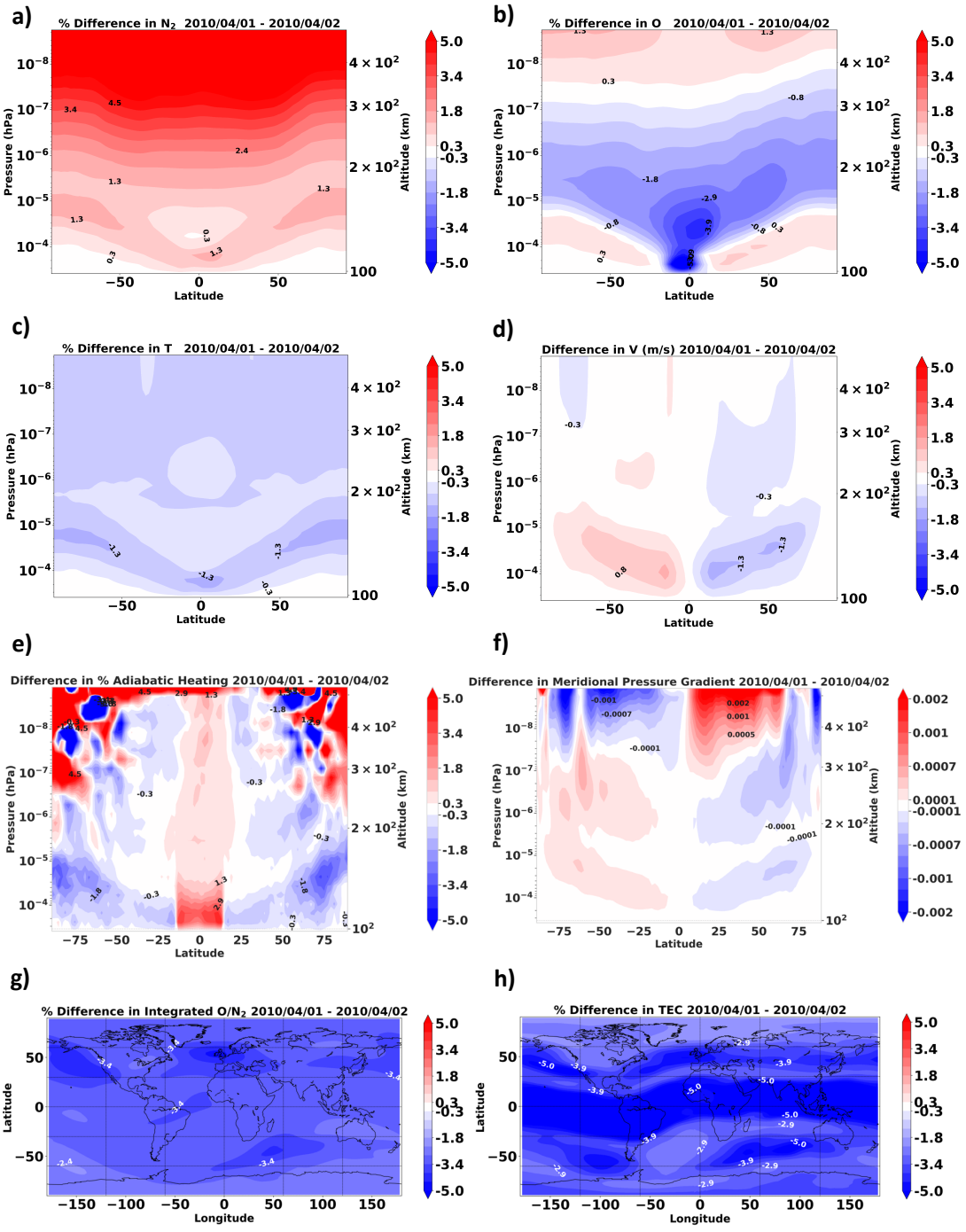

Figure 5.5: Difference between the diurnal and zonally averaged quantities of the perturbed simulation and the control simulation of C1 configuration. Percent difference between the a) N_2 number density, b) O number density, c) Temperature. d) Difference between the meridional winds in m/s. e) Difference between the percent adiabatic heating (normalized by temperature and in per day units). f) Difference between the meridional pressure gradient in m/s^2. Percent difference between the g) integrated O/N_2, and h) TEC.

Figure 5.5 shows the difference in the diurnally and zonally averaged IT state between the perturbed simulation and the control simulation of the C1 configuration. The temperature decreases by up to 1-2% at all latitudes. [O] decreases and [N_2] increases because of the vertical mixing introduced by the larger K_{zz} in the perturbed simulation. A large value of K_{zz} drives the upwelling of N_2 rich air into the thermosphere, thus increasing its relative concentration in the thermosphere, with the opposite occuring for the lighter species, such as O. However, there is an additional significant effect on N_2 due to the temperature change: because of the ideal gas law, on a constant pressure surface, a decrease in temperature is accompanied by an increase in the density (Burns et al., 2015). Since, N_2 is the major species in the lower thermosphere, its density increases on a constant pressure level. Above 200 km, as O becomes the major species, it shows the similar increase.

An equatorward meridional circulation is also induced because of the change in pressure gradients in the lower thermosphere, as shown in Figures 5.5d and 5.5f. It is likely that the primary driver of these winds (and the pressure gradients) is the decrease in [O] and temperature near the equatorial latitudes. In Figure 5.5e, these circulation cells cause adiabatic cooling at high latitudes, which is also then reflected in the larger [N_2] in the lower thermosphere at polar latitudes. There is a corresponding adiabatic heating in the equatorial region, which serves to nullify some of the cooling effects due to the vertical conduction increase near the equator. Pressure levels are used as the vertical coordinate to interpret the mixing effects of eddy diffusion, thus eliminating any differences that arise because of upwelling or downwelling due to temperature changes. In the altitude grid, a decrease in all species is observed because of the decrease in temperature and scale heights, with a subsequent contraction of the atmosphere. A net decrease is observed in the integrated O/N_2 and the total electron content (TEC). Integrated O/N_2 is defined as the ratio of integrated O to N_2 column densities, from the top of the atmosphere (upper limit of the model), downward until the altitude where the [N_2] column integrated density reaches 0.8×10^{21} m^{-2} (Strickland et al., 1995). Conventionally, for analyzing GITM results, a value of 10^{21} m^{-2} has been used (e.g., Malhotra et al., 2020). However, we have found that using 0.8×10^{21} m^{-2} yields better match with the GUVI O/N_2 during certain times. We will henceforth refer to the integrated O/N_2 simply as O/N_2. The TEC is in TEC units, which implies that it is scaled by 10^{16} m^{-2} (Vierinen et al., 2016). We observe a maximum decrease of up to $\sim 5\%$ in [O], $\sim 8\%$ in N_2, resulting in $\sim 5\%$ decrease in O/N_2 and up to 8% in TEC.

An interesting observation here is that even though we introduce a large value

of K_{zz} in a small area at the model lower boundary, a localized decrease (in the vicinity of region with large K_{zz}) in both [O] and temperature is more dominant in the lower thermosphere (below $p2$ where $K_{zz} \neq 0$). At higher altitudes, the effect of eddy mixing becomes latitudinally uniform and the horizontal gradients decrease. With increasing altitude, diffusion and horizontal transport (advection) of O can lead to spreading of these differences globally. A combination of thermal diffusion, conduction (both eddy and molecular), adiabatic cooling (below 200 km), and lower collisional heating (i.e., frictional and ion heat transfer) above 200 km (because of decrease in O density) causes a global decrease in the temperature. In this figure, we show only the adiabatic term. Mathematically, from equation 5.3 and 5.6, the effect of eddy mixing on temperature and density depends on the vertical gradient of K_{zz} in the lower thermosphere (in addition to vertical gradient of neutral densities). As shown in Figure 5.1, since K_{zz} decreases above pressure level $p1$ (Figure 5.1), it acts as a sink in the continuity equation and a cooling term in the thermodynamic equation. On the other hand, below pressure $p1$, where K_{zz} is constant, a slight increase in [O] and temperature is observed, because of the dominance of vertical gradients of temperature and neutral density terms. Thus, we can infer from this figure that the total impact of turbulence on the IT region is through both the vertical mixing of neutral species and the conduction of heat. However, it is worthwhile to understand which of these mechanisms dominates.

Figure 5.6 shows the C2 configuration that aims to understand the relative importance of eddy mixing versus the eddy conduction. The eddy thermal conductivity is set to zero in these simulations. Thus, the net change in these simulations is only due to the vertical mixing of neutral species. Here, we observe that [O] decreases throughout the globe similar to C1. However, in the lower thermosphere, it has a more localized decrease in the vicinity of the region with large K_{zz}, with a net decrease of smaller magnitude. Similar to C1, above 200 km, [O] increases gradually because of the mild decrease in temperature. Temperature shows a negligible decrease, with the spatial variation different from C1. Meridional winds show negligible difference in the lower thermosphere because of almost zero difference in pressure gradients. The equatorward winds between 200-300 km induce adiabatic cooling at high latitudes (Figure 5.6e), which is reflected in a very small decrease in mid- to high-latitude temperatures above 200 km. $[N_2]$ increases by a small amount in this region because of the decrease in temperature. Overall, there is a net decrease of 1-2% in O/N_2 and up to 4% in TEC, with the largest decrease at equatorial latitudes. It should be noted that changes in TEC do not exactly correlate with those in O/N_2. In fact, TEC

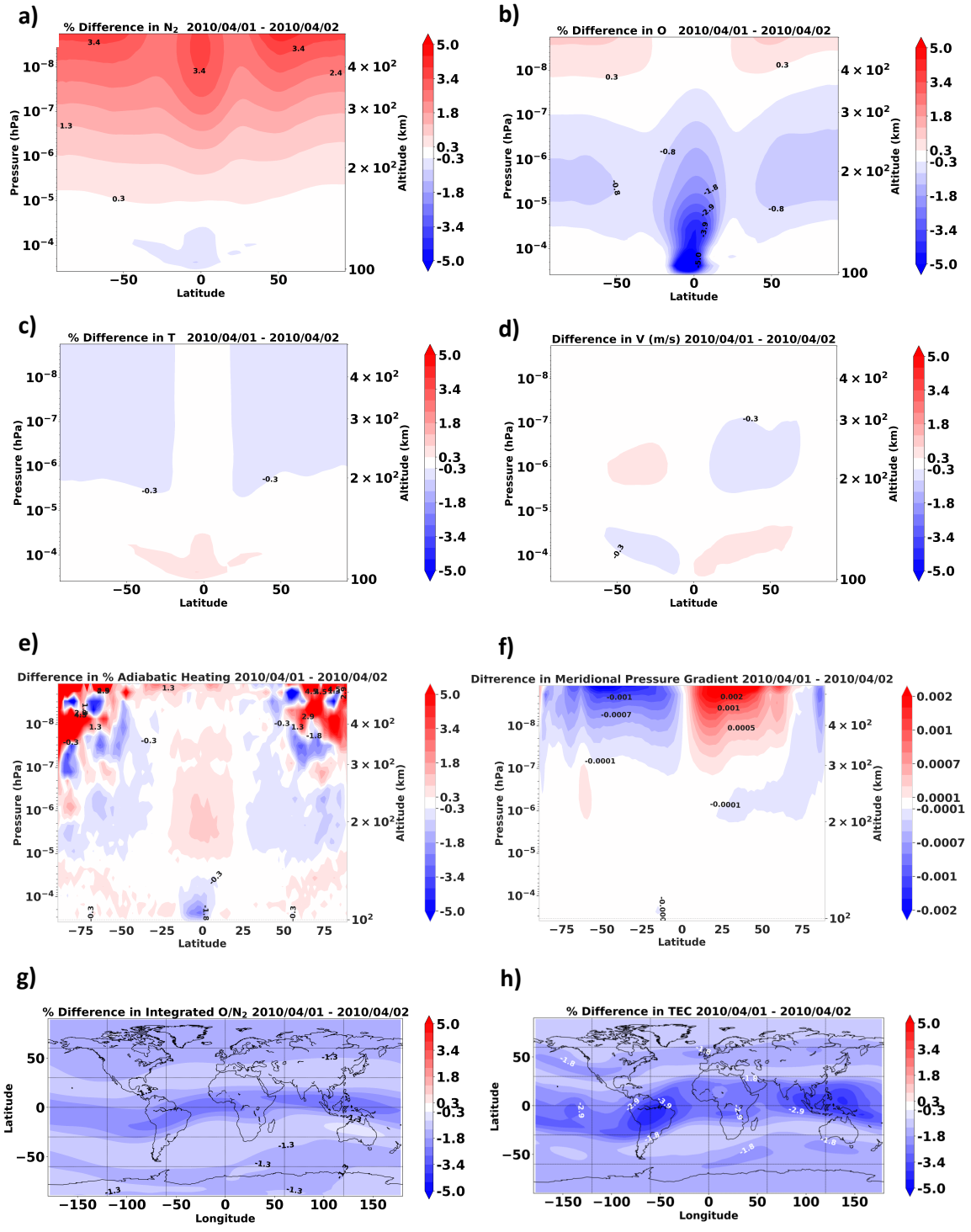

Figure 5.6: Same as Figure 5.5 but for C2 configuration (April 2010), in which the turbulent conduction is turned off for both the perturbed and control simulations. The perturbed simulation has a K_{zz} = 150 m^2/s at equatorial latitudes (-15° <= lat <= 15°), and 50 m^2/s everywhere else. The control simulation has K_{zz} = 50 m^2/s everywhere.

shows larger longitudinal variation as along with photodissociation and recombination, it also depends on other factors, such as the changes in zonal winds in relation to the magnetic field geometry.

By comparing the results from the C1 and C2 configurations, we infer that the eddy conduction term through the thermodynamic equation plays a dominant role relative to the eddy sink term in the continuity equation, in changing the global IT state. This is assuming that both the turbulent thermal conduction and momentum diffusivity are the same, i.e. the turbulent Prandtl number is 1. One important point is that the impact on the thermosphere is less localized when eddy conduction is included. The molecular diffusion coefficients of neutral species depend on the temperature. Thus, it is likely that negligible temperature differences in the C2 configuration, might result in negligible differences in molecular diffusion, and thus, a more localized decrease of [O].

It is worth noting that in both C1 and C2 configurations, the K_{zz} value was raised at low latitudes in the perturbed simulation, such that the global average K_{zz} also increased relative to the control simulation. These global averages are shown in the fourth column of Table 5.1. To understand the net effect of latitudinal variation of K_{zz}, we also ran a configuration with the same global mean K_{zz} for the perturbed and control simulations (74.2 m^2/s). Figure 5.7 shows the results for this C3 configuration. Figure 5.7a shows the difference in K_{zz} for this configuration. K_{zz} is larger for the perturbed simulation at low latitudes and smaller than the control simulation everywhere else. Not all plots are shown in this case because of very small differences between the simulations. Comparing with the C1 configuration, the global difference is much smaller with 1 - 2% decrease in O/N_2 and a maximum of $\sim 4\%$ decrease in TEC, with a larger decrease near low latitudes. A decrease in [O] and almost negligible impact on temperature is observed. Small differences in temperature are induced because of the induced meridional circulation. Thus, the spatial distribution of K_{zz} is less important in a globally averaged sense, and one can achieve almost similar impact on the global thermosphere by using a globally uniform value. However, using a spatially non-uniform K_{zz} does introduce some latitudinal variability in the IT state, especially in TEC. Under realistic conditions, an increase in localized turbulence will raise the global mean K_{zz} as well, resembling the IT state changes of C1 more closely.

5.3.2 Solstice Simulations

Figure 5.8 shows the differences in thermospheric quantities for configuration C4, in which the perturbed simulation has larger K_{zz} of 150 m^2/s at polar latitudes north

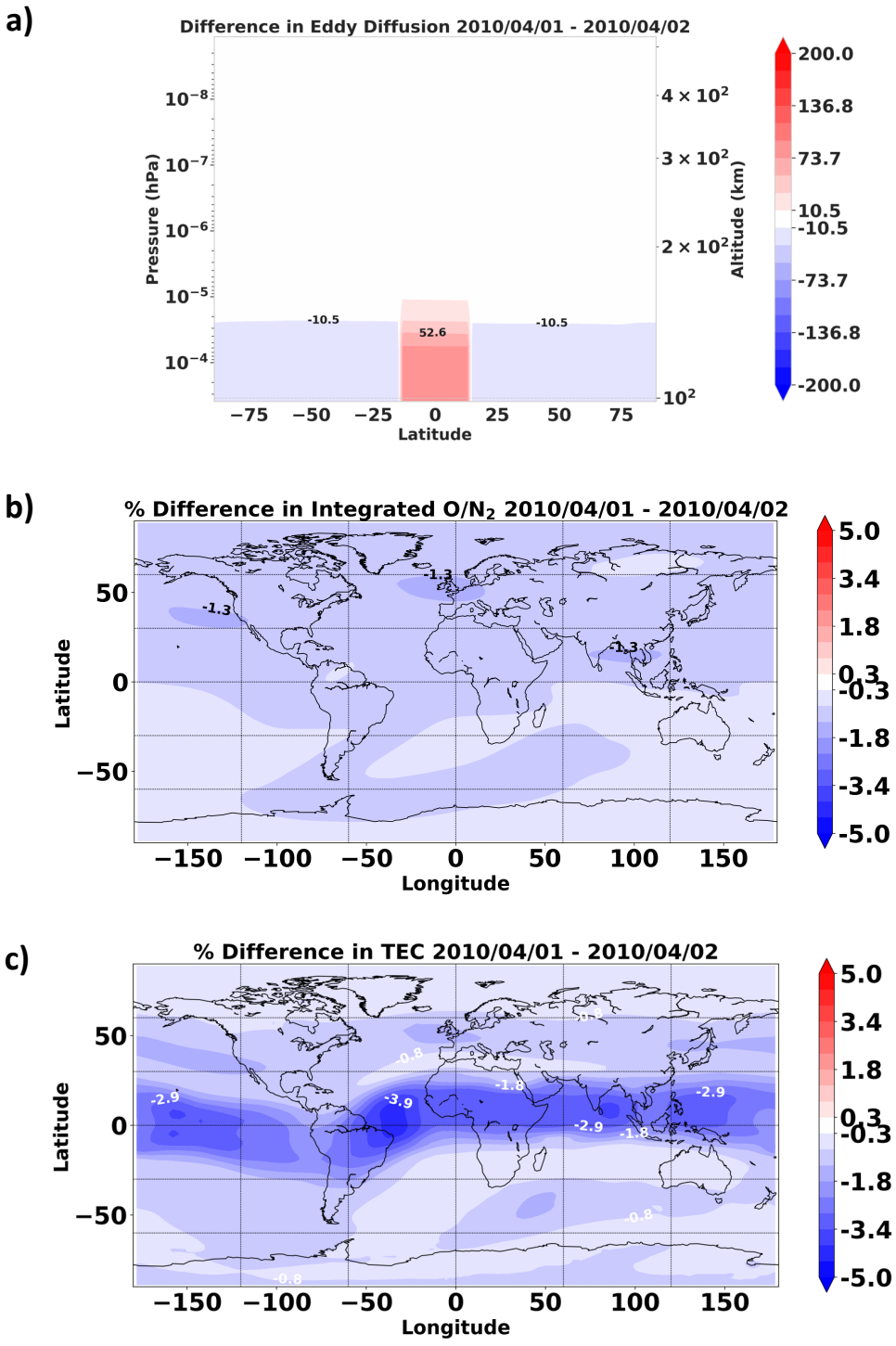

Figure 5.7: Difference between the diurnal and zonally averaged quantities of the perturbed simulation and the control simulation of C3 configuration. a) Difference in K_{zz} in m^2/s. Percent difference in g) integrated O/N_2, and h) TEC. In this configuration, the perturbed simulation has a K_{zz} = 150 m^2/s at equatorial latitudes (-15° <= lat <= 15°), and 50 m^2/s everywhere else. The control simulation has K_{zz} = 74.2 m^2/s everywhere.

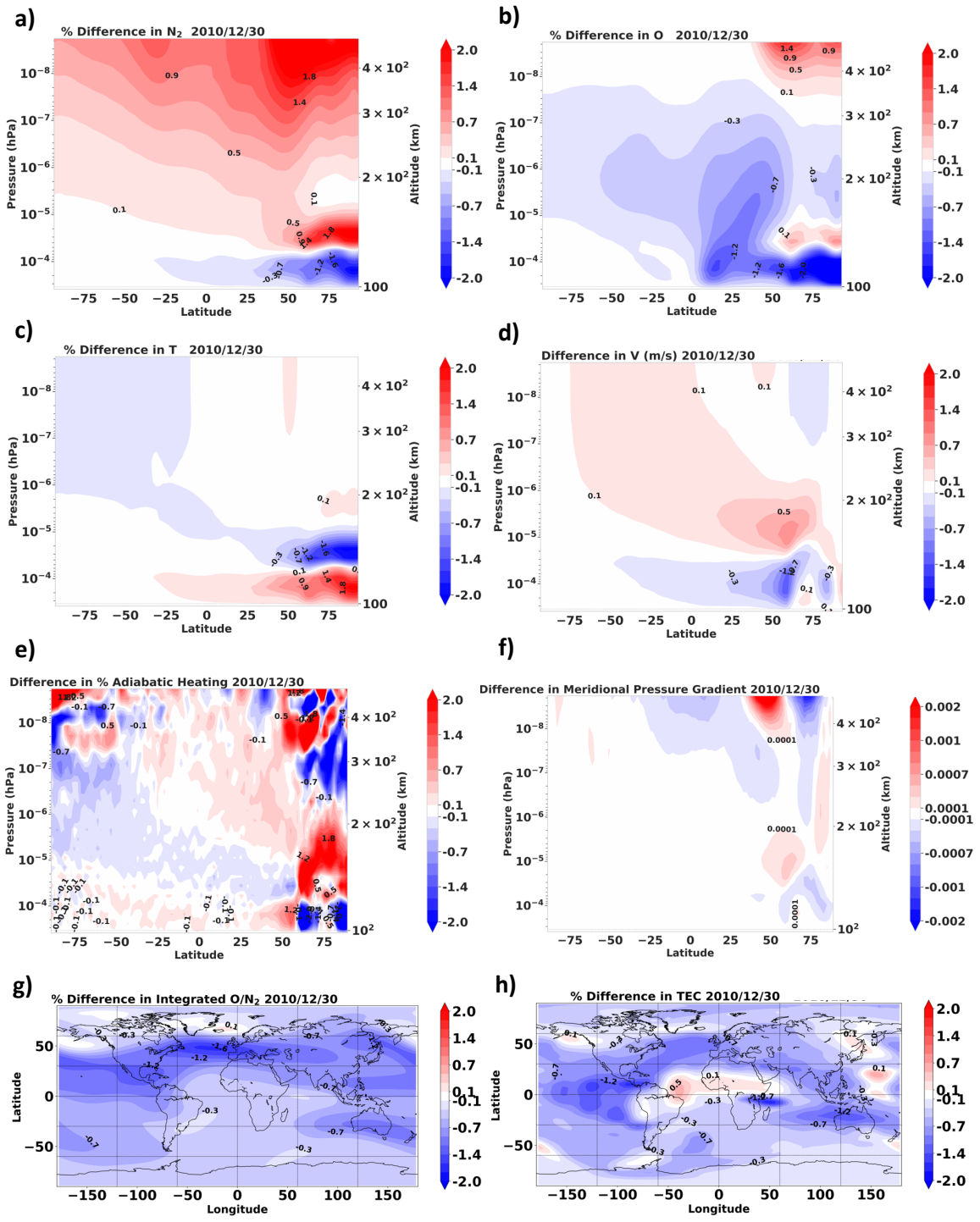

Figure 5.8: Similar to Figure 5.5 but for configuration C4 (for Dec 2010). In this configuration, the perturbed simulation has a K_{zz} = 150 m^2/s at polar latitudes (lat >= 60°), and 50 m^2/s everywhere else. The control simulation has K_{zz} = 50 m^2/s everywhere.

of 60°N (Northern Hemisphere winter). The scales in this figure are different from the previous figures because of smaller differences. Above pressure $p1$ (5×10^{-5} hPa), [O] decreases by up to 2% in the northern hemisphere mid-high latitudes via eddy mixing. This decrease is more localized as compared to the C1 configuration. Changes in densities lead to pressure gradients that induce weak summer-to-winter meridional winds with magnitudes of maximum $\sim$ 1.2 m/s in the middle-upper thermosphere. A weak winter to summer circulation is induced in the lower thermosphere below pressure $p1$. This is similar to the lower thermospheric circulation indicated by H.-L. Liu (2007), Rezac et al. (2015), Smith et al. (2011), Qian et al. (2017), and Qian & Yue (2017), which is because of the momentum deposition by residual gravity waves that penetrate into the lower thermosphere. Our results here indicate that sub-grid scale turbulence due to gravity wave breaking at high winter latitudes (manifesting as increased vertical diffusion and thermal conduction) can also contribute to this circulation. Thus, introducing a larger winter K_{zz} can improve the dynamics in the lower thermosphere in GITM, as well as in the upper thermosphere, where the induced winds add to the background summer to winter circulation.

A small patch of temperature decrease is also observed at high latitudes above pressure $p1$ because of eddy conduction. However, above 200 km, surprisingly, the opposite hemisphere has a larger temperature decrease. This is because the changes in meridional winds induce adiabatic cooling in the summer hemisphere and heating in the winter hemisphere. The other terms such as collisional heating and molecular conduction also contribute to this difference (not shown here). An increase in $[N_2]$ similar to previous configurations is also observed in both the hemispheres. O/N_2 and TEC decrease by up to 2%, with larger decrease in the winter hemisphere.

Overall, the net decrease is much smaller in magnitude in comparison to when a high K_{zz} latitudinal band is introduced at lower latitudes in configuration C1. This is because a 30° latitudinal band at polar latitudes has a smaller area as compared to a latitudinal band of similar width at low latitudes. This can also be understood by comparing the globally averaged K_{zz} of perturbed simulations in C4 and C1 configurations in Table 5.1. The globally averaged K_{zz} of 53.6 m^2/s of C4 is much smaller than that of the 74.2 m^2/s of C1 configuration, leading to smaller differences relative to the control simulations (K_{zz} = 50 m^2/s).

Figure 5.9 shows the results for configuration C5. This configuration is run during June (northern hemisphere summer) but has the same increase in K_{zz} in the northern hemisphere as configuration C4 and aims to investigate seasonal differences in the response of thermosphere to the same eddy mixing (i.e., summer increase instead of

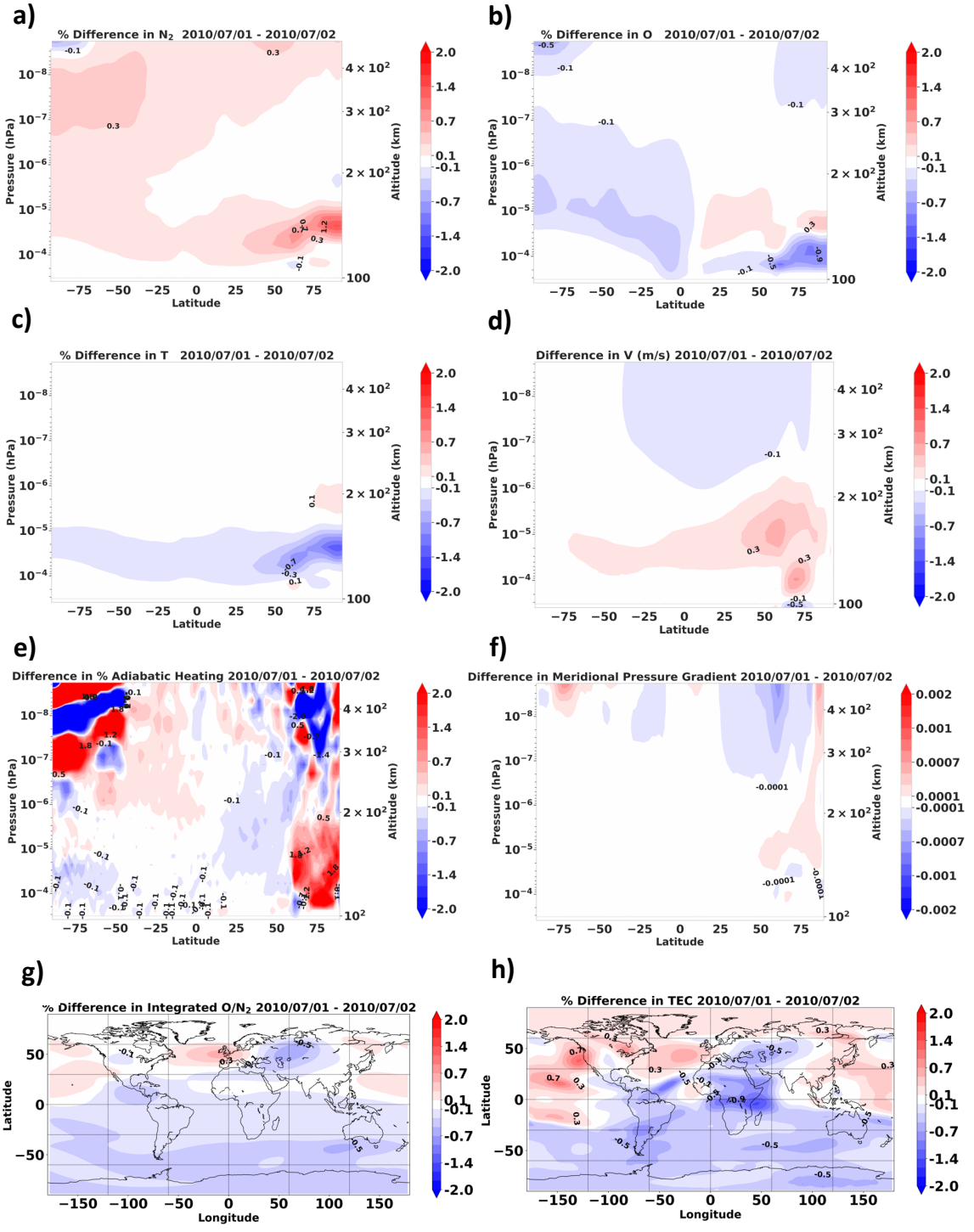

Figure 5.9: Similar to Figure 5.5 but for configuration C5 (July 2010). In this configuration, the perturbed simulation has a K_{zz} = 150 m^2/s at polar latitudes (lat >= 60°), and 50 m^2/s everywhere else. The control simulation has K_{zz} = 50 m^2/s everywhere.

winter increase). In this case, the differences are smaller than those in configuration C4 (Figure 5.8). The decrease in [O] in the lower thermosphere is less than 1%. At higher altitudes, a slightly larger decrease in the opposite hemisphere is observed. This is because the effect of vertical mixing on composition as shown in equation 5.3, depends on the vertical gradient of [O] and the total neutral density, which can also be understood as the gradient in O/N_2. The vertical gradient of O/N_2 is larger in the winter because of the summer-to-winter winds that lead to accumulation of [O] in the winter (and $[N_2]$ in the summer) hemisphere via thermospheric spoon mechanism (T. J. Fuller-Rowell, 1998). This results in a more effective vertical mixing and decrease of [O] in the winter hemisphere. In the summer hemisphere, a small patch of increased [O] is observed between 100-200 km. This is because in the summer hemisphere, as [O] is depleted (low O/N_2), eddy mixing acts in the opposite sense, increasing its relative concentration. These processes can be understood as a dynamic balance between the terms $\frac{\partial N_s}{\partial r}$ and $\frac{\partial N}{\partial r}$ in equation 5.3 or $\frac{\partial O/N_2}{\partial r}$. The primary purpose of eddy mixing is to mix the neutral species similar to the lower atmosphere. Weak meridional pressure gradients and winds are induced similar to Figure 5.8, but in the opposite direction. Temperature shows a small decrease due to eddy conduction at high summer latitudes in the lower thermosphere and a negligible change in the rest of the globe. O/N_2 and TEC show a net increase in the summer (decrease in the winter) hemisphere, with smaller magnitudes as compared to the C4 configuration. Thus, comparing configurations C4 and C5, changes in the K_{zz} in the winter hemisphere have a significantly larger ramification than similar changes in the summer hemisphere.

Figure 5.10 shows the results for configuration C6, which is a combination of polar and equatorial increases in K_{zz} during northern summer solstice conditions. In this case, K_{zz} is 200 m^2/s in the polar regions, 100 m^2/s in the equatorial regions, and 50 m^2/s everywhere else. [O] decreases at all latitudes, but with much larger decrease at equatorial latitudes despite smaller K_{zz}. This is because of the area difference between high and low latitudes. Between 100-200 km, the decrease in [O] is slightly larger in the winter hemisphere at low-mid latitudes, as compared to the summer hemisphere (similar to the C4 and C5 results). The temperature decreases, and $[N_2]$ increases at all heights. Below 200 km, equatorward meridional winds are also induced because of the corresponding pressure gradient changes (Figures 5.10d and 5.10f). The winds induced in the winter hemisphere (Southern Hemisphere) have slightly larger magnitudes that cause larger decrease in the high latitude winter temperature, which is reflected in the $[N_2]$ difference as well. The net decrease in O/N_2 is up to $\sim 4\%$ and in TEC is up to $\sim 8\%$. Both O/N_2 and TEC show a larger decrease in the winter

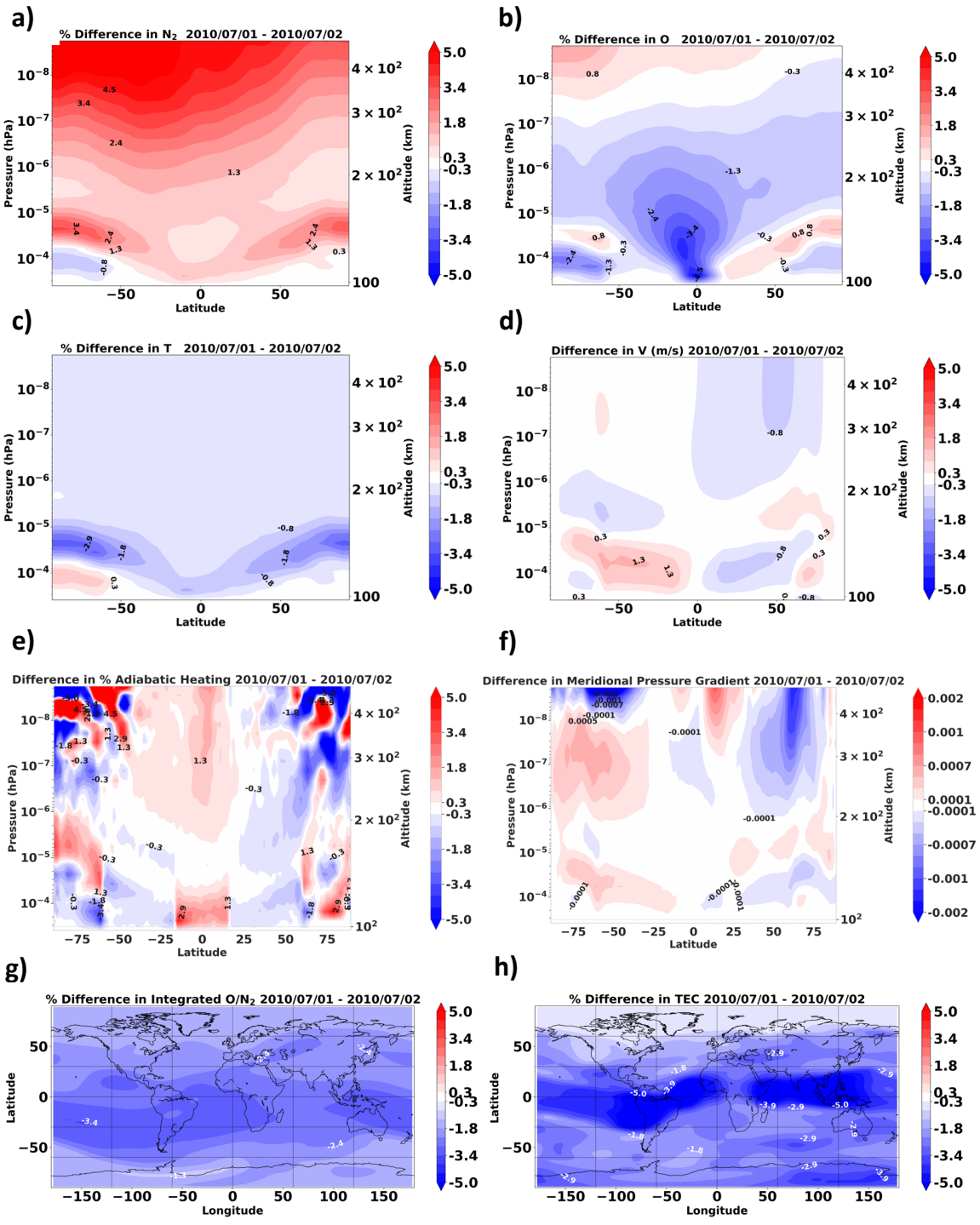

Figure 5.10: Similar to Figure 5.5 but for configuration C6 (July 2010). In this configuration, the perturbed simulation has a K_{zz} = 200 m^2/s at polar latitudes (lat >= 60° and lat <= -60 m^2/s), 100 m^2/s at equatorial latitudes (-15°<=lat<=15°) and 50 m^2/s everywhere else. The control simulation has K_{zz} = 50 m^2/s everywhere.

hemisphere. We also ran a configuration similar to C6 but with a larger polar K_{zz} in the summer hemisphere (not shown here), similar to the distribution of gravity wave activity shown in John & Kumar (2012). Our results for this configuration were similar to that of C6, with larger differences in the winter hemisphere.

5.3.3 Comparison with GOCE

The largest differences in this study are observed in configuration C1 (around March equinox) in Figure 5.5. In order to explore whether the changes in localized increase in K_{zz} improve the global IT simulations or not, we compare the neutral mass density (ρ) from this configuration with GOCE densities at $\sim$ 270 km. We do not show comparison for other time periods as the difference between the perturbed and control simulations are small and within observational uncertainty. Figure 5.11 shows the ρ for the perturbed simulation (a), control simulation (b), and GOCE ρ averaged for 9 days around this time (c). A longer term average is done to reduce short term variability due to tides and planetary waves, and to thus obtain background densities. Panels d) and e) show the percent difference of GOCE ρ from the control and perturbed simulations, respectively. Both GITM and GOCE have larger ρ at low latitudes, which is typical of this time period (equinoxes). In panel d), GITM has larger ρ as compared to the GOCE observations across the globe, with larger differences in the Southern Hemisphere. Using a large equatorial K_{zz} in the perturbed simulation reduces this difference at equatorial latitudes and in the northern hemisphere, as shown in panel e). It should be noted that tuning some other parameters, e.g., photoelectron heating, neutral heating, and thermal conductivity (Burrell et al., 2015; Pawlowski & Ridley, 2009), in the model can further improve the agreement between GITM ρ and GOCE data. This data-model comparison shows that while altering the localized K_{zz} alters the differences, those changes are quite small, and it is most likely other effects that are the main drivers of the differences between the model and the data.

5.4 Discussion

We also ran simulations with varying equatorial K_{zz} (K_{zz} = 150, 300, 450, 600 m^2/s.) and a constant background K_{zz} of 50 m^2/s. The spatial variation is thus similar to that of the perturbed simulation in configuration C1. Figure 5.12 shows the O/N_2, TEC, ρ at 272 km for these simulations, averaged over the whole globe, northern high latitudes (lat>=60°N), southern high latitudes (lat<=-60°N), and equatorial

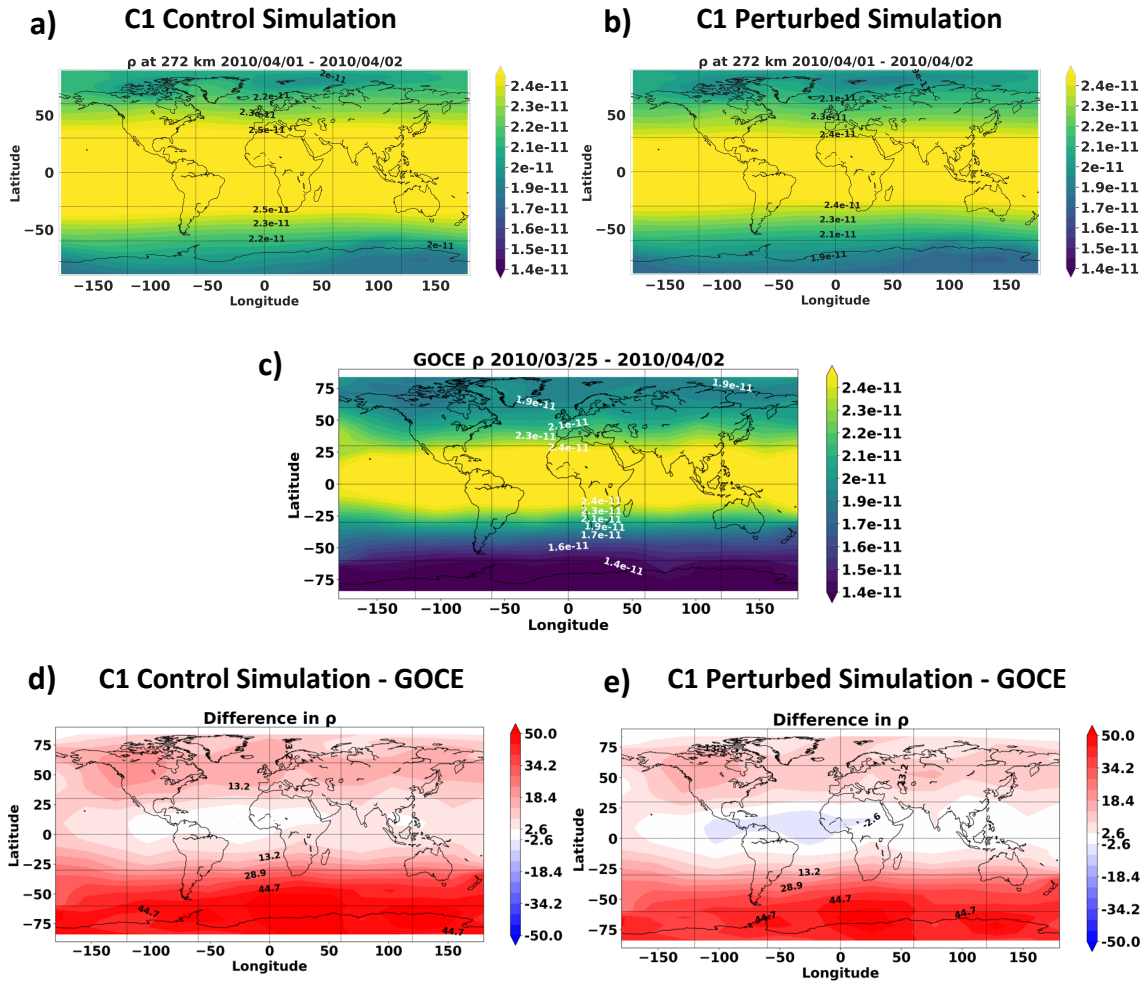

Figure 5.11: Comparison between ρ from GOCE and GITM simulations of C1 configuration. a) ρ at 272 km for the control simulation of C1, b) ρ at 272 km for the perturbed simulation of C1, c) GOCE ρ. d) Percent difference between the control simulation of C1 and GOCE. e) Percent difference between the perturbed simulation of C1 and GOCE.

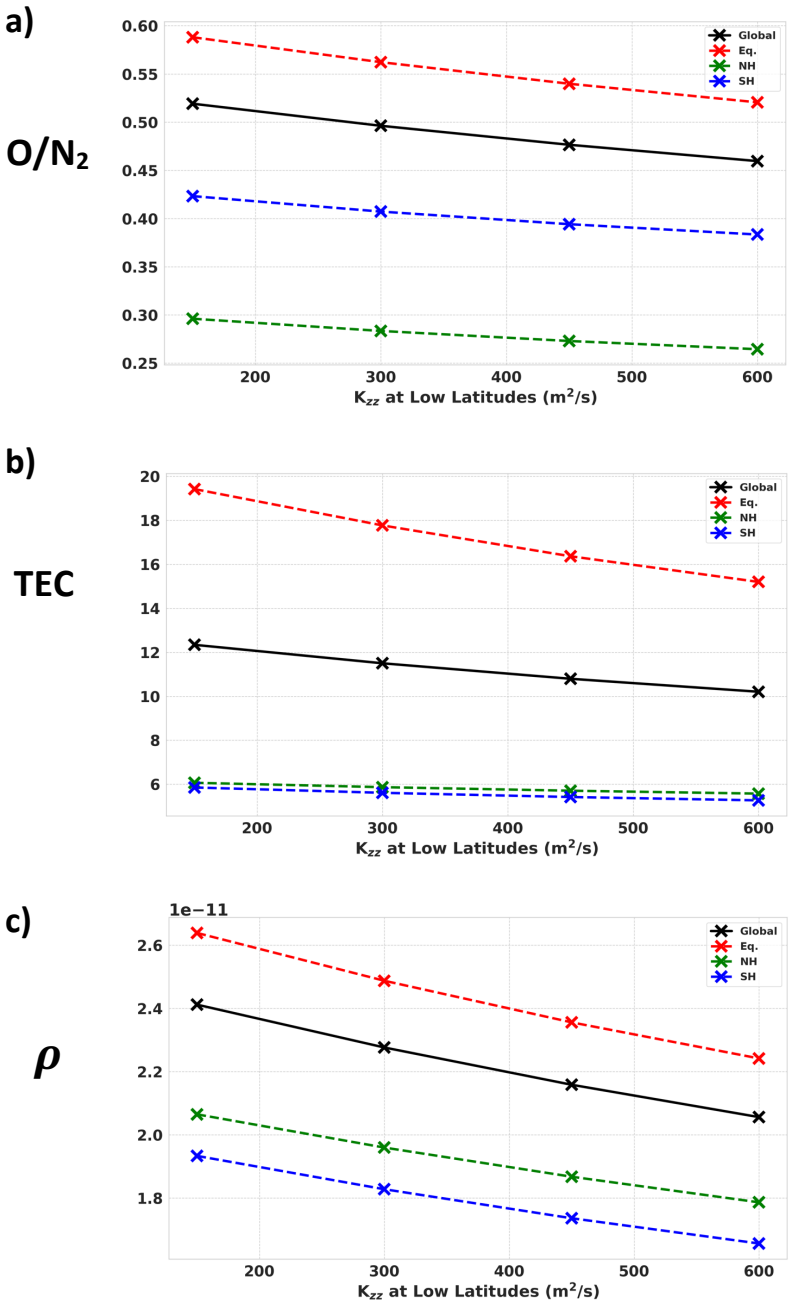

Figure 5.12: Change in the IT quantities with increasing K_{zz} at low latitudes. The x-axis data points represent simulations with low latitude K_{zz} = 150 m^2/s, 300 m^2/s, 450 m^2/s, and 600 m^2/s (globally averaged K_{zz} = 74.2 m^2/s, 110.6 m^2/s, 147 m^2/s, 183.4 m^2/s, respectively). The spatial variation is similar to that of C1, where K_{zz} is raised at only lower latitudes (-15° <= lat <= 15°) and is 50 m^2/s everywhere else. These simulations are run for 18 days and the quantities are averaged for the last two days of the simulations. a) O/N_2 averaged over the whole globe, northern high latitudes (lat>=60°N), southern high latitudes (lat<=-60°N), and equatorial latitudes (-15°<=lat<=15°). b) Similar to a), but for TEC. c) Similar to a), but for ρ at 272 km.

latitudes (-15°<=lat<=15°). The globally averaged K_{zz} is also increasing linearly for each of these simulations ($\overline{K_{zz}}$ = 74.2 m^2/s, 110.6 m^2/s, 147 m^2/s, 183.4 m^2/s, respectively). We observe that as K_{zz} increases linearly, O/N_2, and ρ decrease linearly too in all the regions. For TEC, the decrease is localized in the equatorial region and is almost negligible at high latitudes in either of the hemispheres. As K_{zz} increases from 150 to 600 m^2/s (and globally averaged K_{zz} increases by ∼147%), globally averaged O/N_2 drops by ∼11.5%, TEC drops by 20%, and ρ drops by 14.6%. While this latitudinal band of larger K_{zz} is relatively wide, it is not clear how tropospheric weather activity or orographic features or dynamics in the stratosphere would map spatially to the turbulence in the MLT.

What is clear is that using larger values of K_{zz} (even locally, especially in the winter hemisphere) induces larger changes in the densities, temperature and winds of the upper atmosphere of the Earth. However, the exact value of K_{zz} remains controversial and varies depending on the measurement technique. For example, Triplett et al. (2018) using rocket-borne ionization gauge measurements measured K_{zz} values as low as 10 m^2/s, whereas the values measured by A. Z. Liu (2009) using Na wind/temperature lidar reached greater than 900 m^2/s in summer. Moreover, in-situ and localized measurements (e.g., A. Z. Liu, 2009) often report larger magnitudes of turbulence, as compared to the satellite measurements (e.g., Salinas et al., 2016; G. R. Swenson et al., 2019). Turbulence occurs 30 - 80% of the time, and the global rate of diffusion depends on the temporal and spatial frequency of turbulent patches (Hocking, 1990; Zimmerman & Murphy, 1977). Therefore, even if turbulence is intermittent, a high spatial and temporal frequency can be sufficient to maintain a net turbulent motion and average K_{zz}. Thus, a possible explanation for this discrepancy is that some instruments might have measured locally enhanced values of diffusion coefficients because of local breaking GWs which might be different from the global diffusion coefficients. In fact, some ground-based measurements have reported larger K_{zz} in winter as compared to summer (e.g., Danilov & Kalgin, 1996). Since, different instruments capture different spectrum of gravity waves, the seasonal variation can be different across the spectrum (Preusse et al., 2009).

We also ran a simulation with large K_{zz} over the continental US (not shown here) and observed negligible global changes in the thermosphere. However, this does not imply that turbulence over the USA is irrelevant to the IT state. Comparing our last configurations C6 with C4 and C5, it can be observed that smaller patches of high K_{zz} can produce a net large effect on the thermosphere, especially if turbulence persists for protracted periods of time. Thus, even though the effect of isolated large

K_{zz} patch over USA is small, it can add to other turbulent patches across the globe to produce similar effects in the upper thermosphere and seasonal variations in the global mean diffusion coefficients.

Finally, the differences observed in this study are small and depend on the assumed perturbed and background values of K_{zz}. Walterscheid & Christensen (2016) observed larger variances in the SABER data than John & Kumar (2012) in the altitude region of 95-115 km, but agreed on the spatial distribution of GW activity. Thus, the actual values of intermittent and localized K_{zz} might be larger than those assumed in this study. We also observed in configuration C3, that the net global effects of non-uniform K_{zz} are quite small and may only be of significant importance if IT spatial variability is relevant to the application or topic of research. Thus, when globally averaged quantities are important, uniform K_{zz} can be equally effective.

5.5 Summary and Conclusions

The eddy diffusion parameter (K_{zz}) is often used in the IT models to parameterize the effects of gravity wave (GW) induced turbulence on the upper atmosphere and ionosphere. It is used in the continuity equation where it largely acts as a sink for [O], and a source for [N_2] at higher altitudes. It also induces net cooling in the thermosphere via conduction, thus modifying the thermal structure of the atmosphere. The seasonal variation of K_{zz} has been well studied and it has been found to maximize during summer. However, the spatial variation of K_{zz} is still unclear and its linear and non-linear effects on the IT warrant further investigation.

Recent studies, such as John & Kumar (2012), Walterscheid & Christensen (2016), and Preusse et al. (2009), have used SABER measurements to study the spatial variation of GW activity in the MLT region. John & Kumar (2012) showed larger GW potential energy in the summer hemisphere during solstices and at equatorial latitudes during equinoxes. It remains to be studied how the GW potential energy is linked to the turbulence in this region. These global GW observations with their innovative analysis methods can provide constraints for the K_{zz} parameterization used in the IT models, thus improving the treatment of the effects of turbulence on IT. We use the results from these studies to modify the spatial distribution of K_{zz} in the lower thermosphere of GITM for different seasons. We introduce turbulent patches of 30° latitudinal width in which K_{zz} ranges between 150 - 200 m^2/s, with a low value for the background K_{zz}. These perturbed simulations are then compared with control simulations of globally uniform K_{zz}. The vertical profile of K_{zz} is such

that it stays constant until 5×10^{-5} hPa pressure level (roughly 120 km altitude) and decreases linearly to zero above that. This vertical profile stays the same in all our simulations. We compared the IT state for the control and perturbed simulations and the conclusions reached by altering the horizontal distribution of K_{zz} include :

- During equinoxes, when a large K_{zz} is introduced at equatorial latitudes (background K_{zz} is the same as that of the control simulation), a decrease in [O] (because of eddy mixing), T (because of eddy conduction), and an increase in $[N_2]$ at a constant pressure level is observed throughout the globe. This induces changes in pressure gradient forces and meridional winds which further feedback into temperature via adiabatic processes. A net change of 5-8% in O/N_2 and TEC is observed. Comparison with GOCE data reveals better agreement with the perturbed simulation. The conduction through turbulent mixing plays a more important role in modifying the IT state globally, as when turbulent conduction is turned off in both the perturbed and control simulations, more localized changes in the vicinity of equatorial latitudes are observed.

- If the globally averaged K_{zz} of the perturbed simulation is kept the same as the control simulation, the net effect of introducing spatial variation in K_{zz} is small and within 2-4% in globally averaged O/N_2 and TEC. However, it introduces spatial variability in both latitude and longitude which is important for improving the modeling of smaller-scale features in the IT.

- When larger K_{zz} is introduced at polar latitudes, the net global effect is relatively small. The global effect on the IT state depends on the area of the turbulent patch, and thus the globally averaged K_{zz}.

- When K_{zz} is raised in the winter hemisphere, a decrease in the winter O/N_2 and TEC is observed. This is because the advection of O is more effective in changing the winter composition because of larger O/N_2 vertical gradient (a result of thermospheric spoon circulation). When K_{zz} is raised in the summer hemisphere, instead an increase in [O], O/N_2, and TEC in the summer hemisphere, and a decrease in the rest of the globe is observed. This is because the thermospheric spoon mechanism reduces [O] in the summer hemisphere. Eddy mixing then acts in the opposite sense to mix the atmosphere, increasing its relative concentration. This is also illustrated in Figure 5.13. Thus, the effects of MLT turbulence on the thermosphere are dependent on its background state and composition.

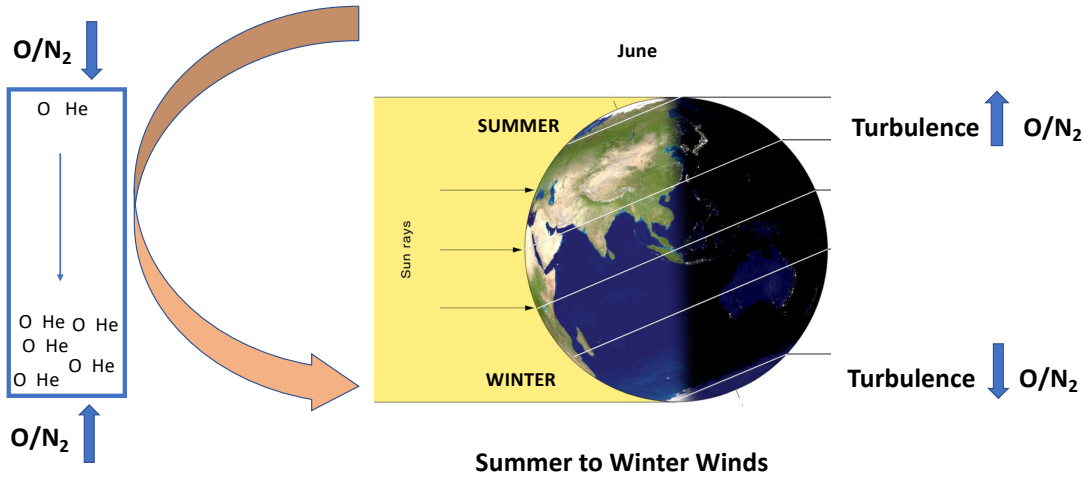

Figure 5.13: Illustration summarizing the results of configuration C5.

- If a combination of equatorial and polar patches of large K_{zz} are introduced during solstices, a decrease in O/N_2 and TEC of up to 4-8% is observed again. This hints that if turbulence occurs in patches, its effects on the IT region can add up to produce a larger global change. A significant spatial variation with larger differences in the winter hemisphere is observed.

To better predict the state of the thermosphere and space weather, our analysis and results delineate the need for more targeted modeling studies to understand the linkage between GW activity in the MLT and the resulting momentum diffusion and conduction. Eventually, using spatially varying turbulence in the IT models has the potential to improve the estimation of smaller-scale structures in the IT system, and therefore should be taken into consideration.

CHAPTER VI

Conclusions and Future Work

6.1 Conclusions

This dissertation focuses on understanding some of the fundamental processes through which the mesosphere and lower thermosphere (MLT) region interacts and controls the properties of Ionosphere and Thermosphere (IT) of the Earth. We used the global circulation model, Global Ionosphere Thermosphere Model (GITM) to investigate the mechanisms that drive this coupling and several satellite observational datasets to validate the model outputs. Through each research project discussed in Chapters III, IV, and V, we have attempted to answer the outstanding questions posed in the first chapter. This thesis is also innovative in its approach as all three projects used term analysis of the GITM equations to analyze the role of different physical mechanisms.

- **Outstanding Question** : Since atomic oxygen (O) is a minor species in the lower thermosphere but major above 200 km, does the O concentration in the MLT affect the upper thermospheric density, temperature, and wind distributions? If so, what are the mechanisms that drive these changes?

  Findings : At the start of this thesis, it was identified that the MLT [O] has opposite latitudinal distribution between Mass Spectrometer Incoherent Scatter (MSIS) and Whole Atmosphere Community Climate Model with thermosphere and ionosphere extension (WACCM-X). MSIS has higher [O] in the winter hemisphere while WACCM-X has higher [O] in the summer hemisphere, which matched the observations from the Sounding of the Atmosphere using Broadband Emission Radiometry (SABER) instrument much better. In this study, the sensitivity of the upper thermosphere to lower thermospheric O was investigated. WACCM-X was used to drive the lower atmospheric boundary

of O in GITM between $\sim$ 95 - 100 km and the results were compared with the conventional MSIS-driven GITM. It was found that the reversal of [O] distribution changes the pressure distribution between 100-120 km, such that the hemisphere with larger [O] has stronger equatorward winds, and lower temperature mainly due to adiabatic and radiative cooling. This changes thermospheric scale heights such that the hemisphere with more [O] has lower [N_2] and thus enhanced integrated O/N_2. This behavior is observed in the opposite hemisphere when MSIS is used as the lower boundary for GITM. Overall, O/N_2 for WACCM-X-driven GITM matches better with the Global Ultraviolet Imager (GUVI) data. Thus, the impact of lower thermospheric [O] on IT was found to be not just through diffusive equilibrium, but also through secondary effects on winds and temperature.

- **Outstanding Question** : What are the primary processes through which the lower thermosphere drives the thermospheric and ionospheric semiannual oscillation (T-I SAO)? Does the long-term SAO depend on the MLT properties? Do more realistic drivers in the lower thermosphere allow for a more accurate representation of the SAO?

  Findings : The second study (Chapter IV) identified that the year-long temporal variation of O is also opposite between MSIS and WACCM-X at 97-100 km. The [O] from WACCM-X has maxima at solstices similar to [O] from SABER. The densities and dynamics from WACCM-X were then used to drive the GITM at its lower boundary, and compared with the MSIS-driven GITM. The focus was on the modeling of the T-I SAO. It was found that using MSIS at the lower boundary yields a thermospheric SAO with equinoctial maxima. The study also revealed that GITM is able to reproduce a T-I SAO without an SAO variation at the lower boundary of GITM. Thus, the thermospheric spoon mechanism is the primary driver of T-I SAO. However, both of these simulations had lower amplitude and slightly phase-shifted T-I SAO when compared with the satellite observations. It was also found that when WACCM-X is used to drive GITM instead, the phase of T-I SAO shifts to maximize around solstices. Nudging the dynamics in GITM towards WACCM-X, reduces the amplitude of the oppositely-phased SAO but does not completely corrects its phase. It was identified that during solstices, WACCM-X-driven GITM has a smaller temperature gradient between the hemispheres and weaker meridional and vertical winds in the summer hemisphere. This leads to accumulation of [O] at

lower latitudes due to weaker meridional transport, resulting in solstitial maxima in global means. WACCM-X itself has the right phase of SAO in the upper thermosphere, but the wrong phase at lower altitudes. The exact mechanisms that can correct the phase of SAO in IT models while using SABER-like [O] in the MLT are currently unknown and warrant further investigation. Possible solutions to solving this discrepancy will be discussed in the next section.

The research projects presented in both Chapters III and IV are the first to report the sensitivity of an IT model to the latitudinal and temporal distribution of MLT [O] that is observed in both the SABER data and the WACCM-X model.

- **Outstanding Question** : How does the non-uniform mixing and diffusion in the MLT affect the thermospheric dynamics, composition and temperature? Is the effect of spatial variation of K_{zz} on the thermosphere different from using a globally uniform value of K_{zz}? Does using spatially varying K_{zz} improve the agreement of GITM with the data?

  Findings : There is currently no well-known study that has attempted to understand the effects of spatially non-uniform eddy mixing (K_{zz}) on the IT region, while constraining it by previous measurements of K_{zz} and SABER global gravity wave (GW) activity in the MLT. This research project was inspired from a few recent studies that reported non-uniform and spatially variable MLT GW activity extracted from the SABER measurements. In this project, latitudinal bands of large K_{zz} at low latitudes during equinoxes and at high latitudes during solstices were introduced, and the results were compared with the control simulations of uniform global K_{zz}. It was found that the primary effect of non-uniform K_{zz} is in introducing spatial variability in the IT, and that the net change in globally-averaged thermospheric quantities is small, being within 2-4%. The net effect of K_{zz} depends on the area of the turbulent patch and spreads globally when K_{zz} at low latitudes in increased. This effect is much smaller and localized in one hemisphere when the K_{zz} at high latitudes is raised. It was also revealed that when turbulent conduction is turned off, the changes in the IT state are more localized in the vicinity of the turbulent patch. Overall, at a constant pressure surface, a decrease in O, temperature, O/N_2, TEC and an increase in N_2 are observed. Meridional winds are also affected via changes in pressure gradient forces across the globe. During solstices, the IT state of the winter hemisphere exhibits larger changes, due to more effective compositional change of O through vertical advection.

Over the course of these research projects, new analysis codes have been written in python that can be easily used to plot GITM results and perform term analysis on the output files. The older version of MSIS (NRLMSIS-00) has been replaced by the newer version NRLMSIS 2.0, and a framework has been laid out for coupling WACCM-X with GITM. Despite these research endeavors, there are several open questions and model improvements that can be made, some of which are suggested as potential research projects in the next section.

6.2 Future Work

The research presented in this thesis highlights the importance of using correct and realistic boundary conditions for temperature, winds, and densities in the IT models. Presented here are questions that need to be still addressed and ideas regarding possible improvements of GITM to better represent the variability of lower atmosphere in the IT region :

- The first study identified that the latitudinal distribution of [O] in the MLT is larger in the summer hemisphere which is opposite of the distribution in both the mesosphere and middle-upper thermosphere. The mechanisms that drive this summer maximum are not currently known, which warrants further investigation using term analysis in WACCM-X. Some possible mechanisms may include larger K_{zz}/turbulence in summer, advection due to lower thermospheric winter-to-summer circulation, or enhanced summer molecular diffusion that advects [O] down from the thermosphere into the MLT.

- In the second study, it was found that the T-I SAO reverses and shows solstitial maxima when GITM uses more realistic latitudinal and temporal distribution of [O] from WACCM-X. Thus, further investigation of processes that can help in correcting the phase of T-I SAO is warranted. It was suggested that certain mechanisms such as stronger interhemispheric meridional winds, stronger residual circulation, seasonal variation in eddy diffusion, and momentum from breaking gravity waves, can reduce the solstitial maxima in the lower thermosphere. An exhaustive research project devoted to test the role of each of these processes while adjusting their relative magnitudes would be useful in answering this outstanding question

- In the second study, an exhaustive investigation of SAO drivers and properties was done. However, there are other intra-annual variations in the IT that re-

main to be understood well. This includes the annual oscillation (June solstice has lower globally averaged densities as compared to the December solstice), hemispheric asymmetry, and equinoctial asymmetry. Among the simulations ran in this study, the simulation that used flat/no SAO (G/NOSAO) at the lower boundary of GITM produced surprisingly decent agreement with the observations. This simulation may be extremely useful in understanding the origin of these asymmetries and isolate them without the contribution of lower atmosphere. These results may then be compared with those of the G/MSIS simulation.

- In the last study, it was observed that spatially non-uniform turbulence can introduce spatial variability in the IT region. However, not all GWs break in the MLT. A portion of the GW spectrum leaks into the upper atmosphere and can often be observed in thermospheric and ionospheric properties (Hocke & Schlegel, 1996; H. Liu et al., 2017; Park et al., 2014). These waves can seed plasma instabilities in the ionosphere that can generate equatorial ionospheric plasma bubbles often observed in the evening sector (Fritts et al., 2008; Abdu et al., 2009). Another source of thermospheric GWs are the secondary waves that are generated by the thermospheric body forces induced by dissipating GWs (Vadas, 2007). The effect of these waves cannot be modeled in an IT model without explicitly including a parameterization scheme that is suitable for the thermosphere. Most of the GW parameterization schemes (e.g., Lindzen, 1981; R. R. Garcia et al., 2007) are suitable for the lower atmosphere. Yigit & Medvedev (2009) recently developed a parametrization scheme that extends into the thermosphere and accounts for the realistic dissipation of GWs in addition to breaking and saturation. Attempts to use this scheme in the Mars version of GITM are ongoing. A research project aimed at including this scheme in the Earth version of GITM would be a great step forward in improving the representation of GWs in the IT region. This would require extending the lower boundary of GITM down to lower altitudes to provide background atmosphere for the GWs to propagate. This can be done either by using MSIS for the lower atmospheric state, or by extending the numerical solver (which would be a major undertaking).

- In the last study, certain values of K_{zz} based on some previous studies were assumed. It would be groundbreaking to calculate realistic values and spatial variability of K_{zz}. G. Swenson et al. (2018), G. R. Swenson et al. (2019),

and Salinas et al. (2016) used 1-D models and SABER observations to derive globally averaged K_{zz} in the MLT. Using a similar methodology, long-term averaged observations of SABER [O] and [CO_2], and winds from Wind Imaging Interferometer (WINDII), it is possible to determine a more realistic spatial distribution of K_{zz} by solving the model code in a latitude and longitude grid cell, instead of using global means. This SABER-derived K_{zz} can further be compared with K_{zz} from WACCM-X and the gravity wave potential energy from John & Kumar (2012) and Preusse et al. (2009).

In closing, the Earth's atmosphere is a complex, non-linear, and dynamic system. The research presented here has underscored the importance of lower atmospheric variability and turbulence in controlling the background IT state. Despite being a minor species, atomic oxygen in the MLT also plays a crucial role in controlling the IT dynamics and the T-I SAO. As human presence in this region continues to increase, it becomes imperative to be able to predict the IT state accurately. Thus, continued research efforts to answer the open questions highlighted in the presented studies, and improvement of lower atmospheric representation in the IT models is warranted.

APPENDIX

APPENDIX A

Prediction of GNSS Phase Scintillations: A Machine Learning Approach

This project shows the results from an internship project at the NASA Frontier Development Lab program, hosted by the SETI Institute and the NASA Ames Research Center. It was accepted at Machine Learning for the Physical Sciences workshop of NeurIPS 2019 (Lamb et al., 2019).

A.1 Abstract

A Global Navigation Satellite System (GNSS) uses a constellation of satellites around the earth for accurate navigation, timing, and positioning. Natural phenomena like space weather introduce irregularities in the Earth's ionosphere, disrupting the propagation of the radio signals that GNSS relies upon. Such disruptions affect both the amplitude and the phase of the propagated waves. No physics-based model currently exists to predict the time and location of these disruptions with sufficient accuracy and at relevant scales. In this paper, we focus on predicting the phase fluctuations of GNSS radio waves, known as *phase scintillations*. We propose a novel architecture and loss function to predict 1 hour in advance the magnitude of phase scintillations within a time window of ± 5 minutes with state-of-the-art performance.

A.2 Introduction

A global navigation satellite system (GNSS) is a constellation of satellites around the Earth used for accurate navigation, timing and positioning. GNSS refers to a

large category of commercial products like the Global Positioning System (GPS). As a society, we are becoming increasingly dependent on GNSS technology, with a recent study estimating losses of $1 billion per day in case of an extended outage (O'Connor et al., 2019). Therefore it becomes imperative to predict disruptions to GNSS signals with good spatial and temporal resolution.

GNSS signals are high frequency radio waves that propagate through the ionosphere before they reach ground-based receivers. The frequency of these signals is of the order of GHz and they therefore interact with small scale ionospheric irregularities (i.e. sharp gradients in ion and electron densities). This causes the signals to exhibit rapid amplitude and phase variations known as *scintillations*, causing uncertainty in position and loss of lock in severe cases (Kintner et al., 2007). Interactions between the sun and the Earth's ionosphere are extremely non-linear, which makes the prediction of space weather effects challenging. Because of the complex nature of the problem, a complete theory of ionospheric irregularities and signal scintillation does not yet exist, which limits the prediction capabilities of physics-based models (Priyadarshi, 2015).

In this study, we focus on predicting phase scintillations at high latitudes, using data from Global Positioning System (GPS) receivers in the Canadian High Arctic Ionospheric Network (CHAIN) obtained between 2015-2017. At high latitudes, the dominant source of ionospheric irregularities and therefore scintillations is solar-driven storms and substorms (geomagnetically active periods). One very visible manifestation of these high energy inputs from the sun is the aurora, which has also been shown to correlate with these scintillations (Aarons et al., 2000; van der Meeren et al., 2015).

Phase scintillations are an uncommon yet severe phenomenon. Over the course of 2015-2016, only 0.0091% of the minute basis samples from CHAIN exhibited scintillations over the threshold of 0.1, which is the value above which the GNSS signal reliability decreases (McGranaghan et al., 2018). Therefore, the event task is sparse, rendering standard techniques incapable of predicting accurately in time and magnitude. In addition, due to errors in hardware, 22% of data in the years 2015-2017 are missing, further complicating the prediction task.

We propose a method for predicting scintillations from time-series of physical measurements, incorporating two key novelties: (a) we account for the sparsity of scintillations with a custom loss function; (b) we handle missing data values with binary masks that inform our model which values are missing. We outperform the current state of the art by making predictions 1 hour in advance with a total skill score (TSS, discussed below) of 0.64. To the best of our knowledge we are the first

to treat the prediction problem as a regression problem, rather than classifying the existence of phase scintillations, as per the current state of the art.

A.2.1 Related Work

There is no physics based model capable of performing accurate predictions of timing and magnitude of phase scintillations with relevant spatial and temporal scales. Previous data-driven approaches include de Lima et al. (2015) where the authors predict scintillations in equatorial latitudes; we note that their results are not directly comparable to our task, as the physics guiding ionospheric scintillations on high latitudes differ from the equatorial. In Jiao et al. (2013) the authors characterize the climatology of scintillations using statistical analysis but do not predict them in the future. The only known predictive model, McGranaghan et al. (2018) only classifies the occurrence of scintillations 1 hour in advance. Our work is the first to treat phase scintillation prediction as a regression problem, and the first to account for event sparsity and missing data.

A.3 Methodology

Dataset: We study the high latitude Canadian sector ($50° - 70°$ geographic latitude) between mid-October 2015 and end-February 2016. We use solar activity parameters such as solar wind speed (Vsw), interplanetary magnetic field components such as (IMF Bz, By), F10.7, Sym-H, etc. and geomagnetic activity indices such as Kp, AE to characterize the global influence of solar activity on Earth's magnetosphere and ionosphere (Editors: Russell & Kivelson, 2005). For local ionospheric state information pertaining to the high latitude Canadian sector, we are using the CARISMA (Canadian Array for Realtime Investigations of Magnetic Activity) magnetometer dataset, the Canadian High Arctic Ionospheric Network for ionospheric total electron content (TEC) and scintillation index measurements. In summary, we have 39 features in a minute-cadence dataset. We use the first 75000 points (until mid-January) as our training data, while we reserve the latter 75000 points as our test set.

Masking: Due to measurement errors, faulty equipment and other natural phenomena, 22% of the data are corrupted and logged as `NaN`. For each feature, we substitute any NaN values with the mean value of that feature across all non-NaN observations. We indicate such substitutions with a binary (1/0) mask, which is provided as an additional feature. Including a mask for each feature therefore doubles the total number of features. This approach resembles that of Che et al. (2018), except that we do not

decay the substituted value towards the mean as the vast majority of our observations exhibit small variation from the mean.

Sparsity and Loss Function: As discussed above, phase scintillations are a rare phenomenon. Given the extreme sparsity of our positive phase scintillation values, standard regression loss functions would find their minimum by predicting values around the mean, and failing to predict high phase scintillation events. We introduce a custom loss function defined in equation (A.1). The loss function has two components: (i) the Mean Absolute error (MAE) between the predicted output and ground truth; (ii) a dynamic range penalty that incentivizes the range of the output sequence to match the range of the true sequence. With both components, the model is encouraged to match both the mean and variance of the true sequence. In the following expression for the loss L, the sum, max and min are computed over a batch X, Y of predictions and ground truth respectively:

$$L = \frac{\sum_i \|y_i - x_i\|}{N} + \lambda \left(\text{DynRange}(Y) - \text{DynRange}(X)\right) \tag{A.1}$$

$$\text{DynRange}(X) = \max(X) - \min(X) \tag{A.2}$$

In our experiments we found that setting $\lambda = 0.1$ provided the best performance.

Architecture: Figure A.1 shows the proposed architecture. In addition to the time-series data for time t we also include observations from $t-120$ min to t min to inform the model of the historical changes in the values. Thus, the dimensionality of our input is $History \times Features$; in our case 120×40. We condition our model to predict 1 hour in advance. We note that filter sizes decrease and then slightly increase in order to create a small bottleneck in feature space such that noisy information is excluded from the final layers. The aforementioned mask is appended to our input as an extra channel.

A.4 Results

Figure A.2 shows our results over the whole testing dataset of 75000 minute samples, as well as a zoomed version over 5000 minute samples. The test time-points do not overlap with the training time-points. It is evident that the prediction follows closely the ground truth but fails to accurately predict the magnitude of high intensity phase scintillations. Fig A.2(b) shows that despite the mismatch in absolute magnitude, our model successfully predicts a phase scintillation larger than the mean. We also note a small delay in the order of 2-3 minutes in our predictions. Fig A.2(a)

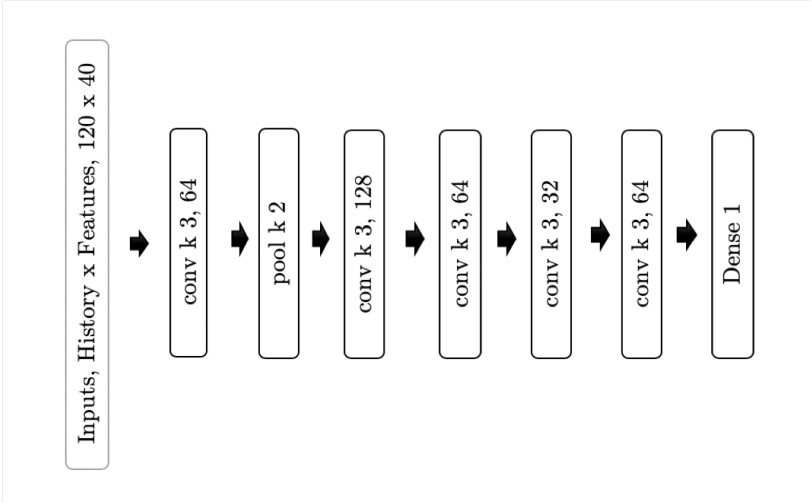

Figure A.**1:** Proposed convolutional architecture. Input timeseries is passed through the convolutional layers and a single output neuron produces the prediction. `k`: is the size of the convolutional kernel, while the following number corresponds to the filters

shows that the predicted sequence has the same peak behaviour as the ground truth. Fig A.3 shows the predictions over the whole test set to make the predicted time series more clear without the scaling of Fig. A.2.

For ease of comparison against existing techniques such as McGranaghan et al. (2018), which approached the prediction task as one of classification, we quantitatively assess the performance of our model by first casting it as a binary classification task and then applying two classification metrics. To cast as binary classification, we say that a scintillation occurs if a threshold of 0.1 in the scintillation index is exceeded (this choice of threshold follows that chosen in Jiao et al. (2013)). The metrics we use to assess this are the total skill score (TSS) as defined in McGranaghan et al. (2018) and equation (A.3), and the Heidke skill score as discussed in Hyvarinen (2014). The Heidke skill score takes values in $(-\inf, 1]$, and the TSS takes values in $[-1, 1]$. In both cases, a score of 0 means no predictive capability. Our model scores 0.34 on the Heidke skill score, showing some predictive ability. The model of McGranaghan et al. (2018) performed classification with a TSS of 0.49, while our model achieves a TSS of 0.64, outperforming the current state of the art.

$$TSS = \frac{TP}{(TP + FN)} - \frac{FP}{(FP + TN)} \tag{A.3}$$

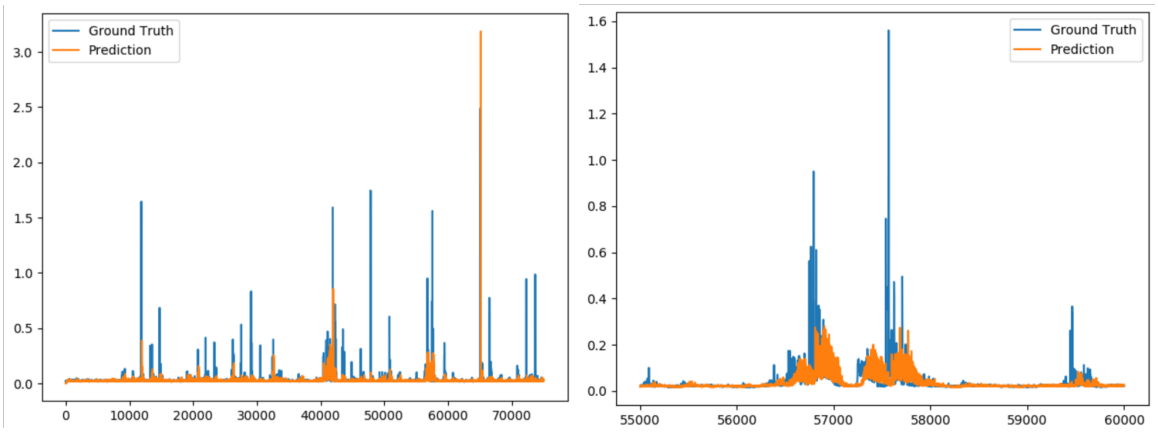

Figure A.2: (a) Results over 75000 minute interval (b) Results zoomed in a 5000 min interval

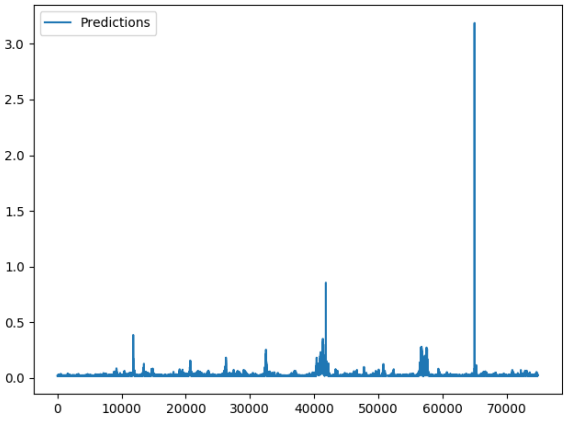

Figure A.3: Predictions over 75000 points of test set; Note that predicted sequence exhibits same peak behaviour as ground truth.

A.5 Conclusions

GNSS products like GPS are vital to modern day operations; from navigation to high-frequency trading in the stock markets — all of which can be disrupted by scintillations in the signals. In this paper we proposed a novel methodology for predicting GNSS phase scintillations 1 hour in advance. We introduced a custom loss function and a method of dealing with missing and incomplete data. We further improved the current state of the art by 0.15 in skill score and demonstrated our method's predictive capability. We believe that additional data sources driven by the same physical phenomena, like auroral images, can further improve the skill score.

This project was conducted during the 2019 NASA Frontier Development Lab (FDL) program, a public-private partnership between NASA, the SETI Institute, and commercial partners. We wish to thank, in particular, NASA, Google, Intel, ElementAI and SRI, for supporting this project.

BIBLIOGRAPHY

BIBLIOGRAPHY

Aarons, J., Lin, B., Mendillo, M., Liou, K., & Codrescu, M. (2000). Global positioning system phase fluctuations and ultraviolet images from the polar satellite. *Journal of Geophysical Research: Space Physics*, *105*(A3), 5201-5213.

Abdu, M. A., Alam Kherani, E., Batista, I. S., de Paula, E. R., Fritts, D. C., & Sobral, J. H. A. (2009). Gravity wave initiation of equatorial spread f/plasma bubble irregularities based on observational data from the spreadfex campaign. *Annales Geophysicae*, *27*(7), 2607–2622. Retrieved from `https://angeo.copernicus.org/articles/27/2607/2009/` doi: 10.5194/angeo-27-2607-2009

Akmaev, R. A. (2011). Whole atmosphere modeling: Connecting terrestrial and space weather. *Reviews of Geophysics*, *49*(4). Retrieved from `https://agupubs.onlinelibrary.wiley.com/doi/abs/10.1029/2011RG000364` doi: 10.1029/2011RG000364

Akmaev, R. A., Rowell, T. J. F., Wu, F., Forbes, J. M., Zhang, X., Anghel, A. F., ... Juang, H. (2008). Tidal variability in the lower thermosphere: Comparison of Whole Atmosphere Model (WAM) simulations with observations from TIMED. *Geophysical Research Letters*, *35*(3). Retrieved from `https://agupubs.onlinelibrary.wiley.com/doi/abs/10.1029/2007GL032584` doi: 10.1029/2007GL032584

Aleskerov, E., Freisleben, B., & Rao, B. (1997). Cardwatch: a neural network based database mining system for credit card fraud detection. In *Proceedings of the ieee/iafe 1997 computational intelligence for financial engineering (cifer)* (p. 220-226). doi: 10.1109/CIFER.1997.618940

Andrews, D. G., Holton, J. R., & Leovy, C. B. (1987). *Middle atmosphere dynamics*. Elsevier, New York.

Bailey, G. (1983). The effect of a meridional e ÃŮ b drift on the thermal plasma at l = 1.4. *Planetary and Space Science*, *31*(4), 389-409. Retrieved from `https://www.sciencedirect.com/science/article/pii/003206338390154X` doi: https://doi.org/10.1016/0032-0633(83)90154-X

Bala, R., Reiff, P. H., & Landivar, J. E. (2009). Real-time prediction of magnetospheric activity using the boyle index. *Space Weather*, *7*(4). Retrieved from `https://agupubs.onlinelibrary.wiley.com/doi/abs/10.1029/2008SW000407` doi: https://doi.org/10.1029/2008SW000407

Bartels, J. (1932). Terrestrial-magnetic activity and its relations to solar phenomena. *Terrestrial Magnetism and Atmospheric Electricity*, *37*(1), 1-52. Retrieved from https://agupubs.onlinelibrary.wiley.com/doi/abs/10.1029/TE037i001p00001 doi: 10.1029/TE037i001p00001

Beagley, S., de Grandpre, J., Koshyk, J., McFarlane, N., & Shepherd, T. (1997). Radiative dynamical climatology of the first generation Canadian middle atmosphere model. *Atmosphere-Ocean*, *35*(3), 293-331. Retrieved from https://doi.org/10.1080/07055900.1997.9649595 doi: 10.1080/07055900.1997.9649595

Bilitza, D. (2018). Iri the international standard for the ionosphere. *Advances in Radio Science*, *16*, 1–11. Retrieved from https://ars.copernicus.org/articles/16/1/2018/ doi: 10.5194/ars-16-1-2018

Bishop, R. L., Larsen, M. F., Hecht, J. H., Liu, A. Z., & Gardner, C. S. (2004). Tomex: Mesospheric and lower thermospheric diffusivities and instability layers. *Journal of Geophysical Research: Atmospheres*, *109*(D2). Retrieved from https://agupubs.onlinelibrary.wiley.com/doi/abs/10.1029/2002JD003079 doi: https://doi.org/10.1029/2002JD003079

Boller, B. R., & Stolov, H. L. (1970). Kelvin?helmholtz instability and the semiannual variation of geomagnetic activity. *Journal of Geophysical Research (1896-1977)*, *75*(31), 6073-6084. Retrieved from https0://agupubs.onlinelibrary.wiley.com/doi/abs/10.1029/JA075i031p06073 doi: 10.1029/JA075i031p06073

Brasseur, G., & Solomon, S. (1984). *Aeronomy of the middle atmosphere*. D.Reidel, Dordrecht.

Bruinsma, S., Tamagnan, D., & Biancale, R. (2004). Atmospheric densities derived from champ/star accelerometer observations. *Planetary and Space Science*, *52*(4), 297-312. Retrieved from https://www.sciencedirect.com/science/article/pii/S003206330300237X doi: https://doi.org/10.1016/j.pss.2003.11.004

Bruinsma, S. L., & Forbes, J. M. (2008). Medium- to large-scale density variability as observed by champ. *Space Weather*, *6*(8). Retrieved from https://agupubs.onlinelibrary.wiley.com/doi/abs/10.1029/2008SW000411 doi: https://doi.org/10.1029/2008SW000411

Burns, A. G., Killeen, T. L., & Roble, R. G. (1989). Processes responsible for the compositional structure of the thermosphere. *Journal of Geophysical Research: Space Physics*, *94*(A4), 3670-3686. Retrieved from https://agupubs.onlinelibrary.wiley.com/doi/abs/10.1029/JA094iA04p03670 doi: 10.1029/JA094iA04p03670

Burns, A. G., Solomon, S. C., Wang, W., Qian, L., Zhang, Y., Paxton, L. J., ... Liu, H. L. (2015). Explaining solar cycle effects on composition as it relates to the

winter anomaly. *Journal of Geophysical Research: Space Physics*, *120*(7), 5890-5898. Retrieved from https://agupubs.onlinelibrary.wiley.com/doi/abs/10.1002/2015JA021220 doi: 10.1002/2015JA021220

Burrage, M. D., Vincent, R. A., Mayr, H. G., Skinner, W. R., Arnold, N. F., & Hays, P. B. (1996). Long-term variability in the equatorial middle atmosphere zonal wind. *Journal of Geophysical Research: Atmospheres*, *101*(D8), 12847-12854. Retrieved from https://agupubs.onlinelibrary.wiley.com/doi/abs/10.1029/96JD00575 doi: 10.1029/96JD00575

Burrell, A., Goel, A., Ridley, A., & Bernstein, D. (2015). Correction of the photoelectron heating efficiency within the global ionosphereâĂŘthermosphere model using retrospective cost model refinement. *Journal of Atmospheric and Solar-Terrestrial Physics*, *124*, 30-38. Retrieved from https://www.sciencedirect.com/science/article/pii/S1364682615000061 doi: https://doi.org/10.1016/j.jastp.2015.01.004

Cageao, R., & Kerr, R. (1984). Global distribution of helium in the upper atmosphere during solar minimum. *Planetary and Space Science*, *32*(12), 1523 - 1529. Retrieved from http://www.sciencedirect.com/science/article/pii/0032063384900199 doi: https://doi.org/10.1016/0032-0633(84)90019-9

Camporeale, E. (2019). The challenge of machine learning in space weather: Nowcasting and forecasting. *Space Weather*, *17*(8), 1166-1207. Retrieved from https://agupubs.onlinelibrary.wiley.com/doi/abs/10.1029/2018SW002061 doi: https://doi.org/10.1029/2018SW002061

Chamberlin, P. C., Woods, T. N., & Eparvier, F. G. (2007). Flare irradiance spectral model (fism): Daily component algorithms and results. *Space Weather*, *5*(7). Retrieved from https://agupubs.onlinelibrary.wiley.com/doi/abs/10.1029/2007SW000316 doi: https://doi.org/10.1029/2007SW000316

Chamberlin, P. C., Woods, T. N., & Eparvier, F. G. (2008). Flare irradiance spectral model (FISM): Flare component algorithms and results. *Space Weather*, *6*(5). Retrieved from https://agupubs.onlinelibrary.wiley.com/doi/abs/10.1029/2007SW000372 doi: 10.1029/2007SW000372

Che, Z., Purushotham, S., Cho, K., Sontag, D., & Liu, Y. (2018). Recurrent Neural Networks for Multivariate Time Series with Missing Values. *Scientific Reports*, *8*.

Chiu, Y. (1975). An improved phenomenological model of ionospheric density. *Journal of Atmospheric and Terrestrial Physics*, *37*(12), 1563-1570. Retrieved from https://www.sciencedirect.com/science/article/pii/0021916975900355 doi: https://doi.org/10.1016/0021-9169(75)90035-5

Cho, K., van Merriënboer, B., Gulcehre, C., Bahdanau, D., Bougares, F., Schwenk, H., & Bengio, Y. (2014, October). Learning phrase representations using RNN

encoder–decoder for statistical machine translation. In *Proceedings of the 2014 conference on empirical methods in natural language processing (EMNLP)* (pp. 1724–1734). Doha, Qatar: Association for Computational Linguistics. Retrieved from https://www.aclweb.org/anthology/D14-1179 doi: 10.3115/v1/D14-1179

Christensen, A. B., Paxton, L. J., Avery, S., Craven, J., Crowley, G., Humm, D. C., ... Zhang, Y. (2003). Initial observations with the Global Ultraviolet Imager (GUVI) in the NASA TIMED satellite mission. *Journal of Geophysical Research: Space Physics*, *108*(A12). Retrieved from https://agupubs.onlinelibrary.wiley.com/doi/abs/10.1029/2003JA009918 doi: 10.1029/2003JA009918

Christensen, A. B., Walterscheid, R. L., Ross, M. N., Meng, C.-I., Paxton, L. J., Jr., D. E. A., ... Strickland, D. J. (1994). Global Ultraviolet Imager (GUVI) for the NASA Thermosphere-Ionsphere-Mesosphere Energetics and Dynamics (TIMED) mission. In J. Wang & P. B. Hays (Eds.), *Optical spectroscopic techniques and instrumentation for atmospheric and space research* (Vol. 2266, pp. 451 – 466). SPIE. Retrieved from https://doi.org/10.1117/12.187583 doi: 10.1117/12.187583

Clark, T. L., Hauf, T., & Kuettner, J. P. (1986). Convectively forced internal gravity waves: Results from two-dimensional numerical experiments. *Quarterly Journal of the Royal Meteorological Society*, *112*(474), 899-925. Retrieved from https://rmets.onlinelibrary.wiley.com/doi/abs/10.1002/qj.49711247402 doi: https://doi.org/10.1002/qj.49711247402

Colegrove, F. D., Johnson, F. S., & Hanson, W. B. (1966). Atmospheric composition in the lower thermosphere. *Journal of Geophysical Research (1896-1977)*, *71*(9), 2227-2236. Retrieved from https://agupubs.onlinelibrary.wiley.com/doi/abs/10.1029/JZ071i009p02227 doi: 10.1029/JZ071i009p02227

Cook, G. (1967). The large semi-annual variation in exospheric density: A possible explanation. *Planetary and Space Science*, *15*(4), 627 - 632. Retrieved from http://www.sciencedirect.com/science/article/pii/0032063367900360 doi: https://doi.org/10.1016/0032-0633(67)90036-0

Cook, G., & Scott, D. W. (1966). Exospheric densities near solar minimum derived from the orbit of echo 2. *Planetary and Space Science*, *14*(11), 1149 - 1165. Retrieved from http://www.sciencedirect.com/science/article/pii/0032063366900298 doi: https://doi.org/10.1016/0032-0633(66)90029-8

Cook, G. E. (1969a). Semi-annual variation in density at a height of 90 km. *Nature*, *222*, 969-971. Retrieved from https://doi.org/10.1038/222969a0 doi: 10.1038/222969a0

Cook, G. E. (1969b, January). The semi-annual variation in the upper atmosphere: A review. *Annales de Geophysique*, *25*, 451-469.

Danilov, A., & Kalgin, Y. (1996). Eddy diffusion studies in the lower thermosphere. *Advances in Space Research*, *17*(11), 17-24. Retrieved from https://www.sciencedirect.com/science/article/pii/027311779500726U doi: https://doi.org/10.1016/0273-1177(95)00726-U

de Lima, G. R. T., Stephany, S., de Paula, E. R., Batista, I. S., & Abdu, M. A. (2015). Prediction of the level of ionospheric scintillation at equatorial latitudes in brazil using a neural network. *Space Weather*, *13*.

Demaeyer, J., & Vannitsem, S. (2018). Stochastic parameterization of subgrid-scale processes: A review of recent physically based approaches. In A. A. Tsonis (Ed.), *Advances in nonlinear geosciences* (pp. 55–85). Cham: Springer International Publishing. Retrieved from https://doi.org/10.1007/978-3-319-58895-7_3 doi: 10.1007/978-3-319-58895-7_3

Deng, Y., Richmond, A. D., Ridley, A. J., & Liu, H.-L. (2008). Assessment of the non-hydrostatic effect on the upper atmosphere using a general circulation model (GCM). *Geophysical Research Letters*, *35*(1). Retrieved from https://agupubs.onlinelibrary.wiley.com/doi/abs/10.1029/2007GL032182 doi: 10.1029/2007GL032182

Dickinson, R. E., Ridley, E. C., & Roble, R. G. (1981). A three-dimensional general circulation model of the thermosphere. *Journal of Geophysical Research: Space Physics*, *86*(A3), 1499-1512. Retrieved from https://agupubs.onlinelibrary.wiley.com/doi/abs/10.1029/JA086iA03p01499 doi: https://doi.org/10.1029/JA086iA03p01499

Dickinson, R. E., Ridley, E. C., & Roble, R. G. (1984). Thermospheric general circulation with coupled dynamics and composition. *Journal of Atmospheric Sciences*, *41*(2), 205 - 219. Retrieved from https://journals.ametsoc.org/view/journals/atsc/41/2/1520-0469_1984_041_0205_tgcwcd_2_0_co_2.xml doi: 10.1175/1520-0469(1984)041<0205:TGCWCD>2.0.CO;2

Dieminger, W., Hartmann, G. K., & Leitinger, R. (1996). *The upper atmosphere. Data analysis and interpretation.*

Drob, D. P., Emmert, J. T., Meriwether, J. W., Makela, J. J., Doornbos, E., Conde, M., ... Klenzing, J. H. (2015). An update to the horizontal wind model (hwm): The quiet time thermosphere. *Earth and Space Science*, *2*(7), 301-319. Retrieved from https://agupubs.onlinelibrary.wiley.com/doi/abs/10.1002/2014EA000089 doi: https://doi.org/10.1002/2014EA000089

Dunker, T., Hoppe, U.-P., Feng, W., Plane, J. M., & Marsh, D. R. (2015). Mesospheric temperatures and sodium properties measured with the alomar na lidar compared with waccm. *Journal of Atmospheric and Solar-Terrestrial Physics*, *127*, 111 - 119. Retrieved from http://www.sciencedirect.com/science/article/pii/S136468261500005X (Layered Phenomena in the Mesopause Region) doi: https://doi.org/10.1016/j.jastp.2015.01.003

Eckermann, S. D., Hoppel, K. W., Coy, L., McCormack, J. P., Siskind, D. E., Nielsen, K., ... Hervig, M. (2009). High-altitude data assimilation system experiments for the northern summer mesosphere season of 2007. *Journal of Atmospheric and Solar-Terrestrial Physics*, *71*(3), 531-551. Retrieved from https://www.sciencedirect.com/science/article/pii/S1364682608002575 (Global Perspectives on the Aeronomy of the Summer Mesopause Region) doi: https://doi.org/10.1016/j.jastp.2008.09.036

Editors: Russell, C. T., & Kivelson, M. G. (2005). Introduction to space physics. *Cambridge Univ. Press*.

Emmert, J. (2015). Thermospheric mass density: A review. *Advances in Space Research*, *56*(5), 773 - 824. Retrieved from http://www.sciencedirect.com/science/article/pii/S0273117715003944 doi: https://doi.org/10.1016/j.asr.2015.05.038

Emmert, J. T. (2009). A long-term data set of globally averaged thermospheric total mass density. *Journal of Geophysical Research: Space Physics*, *114*(A6). Retrieved from https://agupubs.onlinelibrary.wiley.com/doi/abs/10.1029/2009JA014102 doi: https://doi.org/10.1029/2009JA014102

Emmert, J. T. (2015). Altitude and solar activity dependence of 1967?2005 thermospheric density trends derived from orbital drag. *Journal of Geophysical Research: Space Physics*, *120*(4), 2940-2950. Retrieved from https://agupubs.onlinelibrary.wiley.com/doi/abs/10.1002/2015JA021047 doi: https://doi.org/10.1002/2015JA021047

Emmert, J. T., Drob, D. P., Picone, J. M., Siskind, D. E., Jones Jr, M., Mlynczak, M. G., ... Yuan, T. (2020). Nrlmsis 2.0: A whole-atmosphere empirical model of temperature and neutral species densities. *Earth and Space Science*, e2020EA001321. Retrieved from https://agupubs.onlinelibrary.wiley.com/doi/abs/10.1029/2020EA001321 (e2020EA001321 2020EA001321) doi: 10.1029/2020EA001321

Emmert, J. T., McDonald, S. E., Drob, D. P., Meier, R. R., Lean, J. L., & Picone, J. M. (2014). Attribution of interminima changes in the global thermosphere and ionosphere. *Journal of Geophysical Research: Space Physics*, *119*(8), 6657-6688. Retrieved from https://agupubs.onlinelibrary.wiley.com/doi/abs/10.1002/2013JA019484 doi: https://doi.org/10.1002/2013JA019484

Emmert, J. T., Picone, J. M., & Meier, R. R. (2008). Thermospheric global average density trends, 1967?2007, derived from orbits of 5000 near-earth objects. *Geophysical Research Letters*, *35*(5). Retrieved from https://agupubs.onlinelibrary.wiley.com/doi/abs/10.1029/2007GL032809 doi: 10.1029/2007GL032809

Emmert, J. T., Stevens, M. H., Bernath, P. F., Drob, D. P., & Boone, C. D. (2012). Observations of increasing carbon dioxide concentration in earth?s thermosphere.

Nature Geoscience, *5*(12), 868–871. Retrieved from https://doi.org/10.1038/ngeo1626 doi: 10.1038/ngeo1626

Ern, M., Preusse, P., Alexander, M. J., & Warner, C. D. (2004). Absolute values of gravity wave momentum flux derived from satellite data. *Journal of Geophysical Research: Atmospheres*, *109*(D20). Retrieved from https://agupubs.onlinelibrary.wiley.com/doi/abs/10.1029/2004JD004752 doi: https://doi.org/10.1029/2004JD004752

Ern, M., Preusse, P., Gille, J. C., Hepplewhite, C. L., Mlynczak, M. G., Russell III, J. M., & Riese, M. (2011). Implications for atmospheric dynamics derived from global observations of gravity wave momentum flux in stratosphere and mesosphere. *Journal of Geophysical Research: Atmospheres*, *116*(D19). Retrieved from https://agupubs.onlinelibrary.wiley.com/doi/abs/10.1029/2011JD015821 doi: https://doi.org/10.1029/2011JD015821

Ern, M., Preusse, P., Kalisch, S., Kaufmann, M., & Riese, M. (2013). Role of gravity waves in the forcing of quasi two-day waves in the mesosphere: An observational study. *Journal of Geophysical Research: Atmospheres*, *118*(9), 3467-3485. Retrieved from https://agupubs.onlinelibrary.wiley.com/doi/abs/10.1029/2012JD018208 doi: https://doi.org/10.1029/2012JD018208

Fetzer, E. J., & Gille, J. C. (1994). Gravity wave variance in lims temperatures. part i: Variability and comparison with background winds. *Journal of Atmospheric Sciences*, *51*(17), 2461 - 2483. Retrieved from https://journals.ametsoc.org/view/journals/atsc/51/17/1520-0469_1994_051_2461_gwvilt_2_0_co_2.xml doi: 10.1175/1520-0469(1994)051<2461:GWVILT>2.0.CO;2

Forbes, J. M. (1996). Planetary waves in the thermosphere-ionosphere system. *Journal of geomagnetism and geoelectricity*, *48*(1), 91-98. doi: 10.5636/jgg.48.91

Forbes, J. M., Bruinsma, S. L., Zhang, X., & Oberheide, J. (2009). Surface-exosphere coupling due to thermal tides. *Geophysical Research Letters*, *36*(15). Retrieved from https://agupubs.onlinelibrary.wiley.com/doi/abs/10.1029/2009GL038748 doi: 10.1029/2009GL038748

Fozzard, R., Bradshaw, G., & Ceci, L. (1988). A connectionist expert system that actually works. In *Proceedings of the 1st international conference on neural information processing systems* (p. 248?255).

Fritts, D. C., & Alexander, M. J. (2003). Gravity wave dynamics and effects in the middle atmosphere. *Reviews of Geophysics*, *41*(1). Retrieved from https://agupubs.onlinelibrary.wiley.com/doi/abs/10.1029/2001RG000106 doi: https://doi.org/10.1029/2001RG000106

Fritts, D. C., & Dunkerton, T. J. (1985). Fluxes of heat and constituents due to convectively unstable gravity waves. *Journal of Atmospheric Sciences*, *42*(6),

549 - 556. Retrieved from https://journals.ametsoc.org/view/journals/atsc/42/6/1520-0469_1985_042_0549_fohacd_2_0_co_2.xml doi: 10.1175/1520-0469(1985)042<0549:FOHACD>2.0.CO;2

Fritts, D. C., & Nastrom, G. D. (1992). Sources of mesoscale variability of gravity waves. part ii: Frontal, convective, and jet stream excitation. *Journal of Atmospheric Sciences*, *49*(2), 111 - 127. Retrieved from https://journals.ametsoc.org/view/journals/atsc/49/2/1520-0469_1992_049_0111_somvog_2_0_co_2.xml doi: 10.1175/1520-0469(1992)049<0111:SOMVOG>2.0.CO;2

Fritts, D. C., & Rastogi, P. K. (1985). Convective and dynamical instabilities due to gravity wave motions in the lower and middle atmosphere: Theory and observations. *Radio Science*, *20*(6), 1247-1277. Retrieved from https://agupubs.onlinelibrary.wiley.com/doi/abs/10.1029/RS020i006p01247 doi: https://doi.org/10.1029/RS020i006p01247

Fritts, D. C., Vadas, S. L., Riggin, D. M., Abdu, M. A., Batista, I. S., Takahashi, H., ... Taylor, M. J. (2008). Gravity wave and tidal influences on equatorial spread f based on observations during the spread f experiment (spreadfex). *Annales Geophysicae*, *26*(11), 3235–3252. Retrieved from https://angeo.copernicus.org/articles/26/3235/2008/ doi: 10.5194/angeo-26-3235-2008

Frohlich, K., Schmidt, T., Ern, M., Preusse, P., de la Torre, A., Wickert, J., & Jacobi, C. (2007). The global distribution of gravity wave energy in the lower stratosphere derived from gps data and gravity wave modelling: Attempt and challenges. *Journal of Atmospheric and Solar-Terrestrial Physics*, *69*(17), 2238-2248. Retrieved from https://www.sciencedirect.com/science/article/pii/S1364682607002131 (Vertical Coupling in the Atmosphere/Ionosphere System) doi: https://doi.org/10.1016/j.jastp.2007.07.005

Fujiwara, H., & Miyoshi, Y. (2010). Morphological features and variations of temperature in the upper thermosphere simulated by a whole atmosphere gcm. *Annales Geophysicae*, *28*(2), 427–437. Retrieved from https://angeo.copernicus.org/articles/28/427/2010/ doi: 10.5194/angeo-28-427-2010

Fukao, S., Yamanaka, M. D., Ao, N., Hocking, W. K., Sato, T., Yamamoto, M., ... Kato, S. (1994). Seasonal variability of vertical eddy diffusivity in the middle atmosphere: 1. three year observations by the middle and upper atmosphere radar. *Journal of Geophysical Research: Atmospheres*, *99*(D9), 18973-18987. Retrieved from https://agupubs.onlinelibrary.wiley.com/doi/abs/10.1029/94JD00911 doi: 10.1029/94JD00911

Fukata, M., Taguchi, S., Okuzawa, T., & Obara, T. (2002). Neural network prediction of relativistic electrons at geosynchronous orbit during the storm recovery phase: effects of recurring substorms. *Annales Geophysicae*, *20*(7), 947–951. Retrieved from https://angeo.copernicus.org/articles/20/947/2002/ doi: 10.5194/angeo-20-947-2002

Fuller-Rowell, T., & Rees, D. (1983). Derivation of a conservation equation for mean molecular weight for a two-constituent gas within a three-dimensional, time-dependent model of the thermosphere. *Planetary and Space Science*, *31*(10), 1209-1222. Retrieved from https://www.sciencedirect.com/science/article/pii/0032063383901125 doi: https://doi.org/10.1016/0032-0633(83)90112-5

Fuller-Rowell, T., Rees, D., Quegan, S., Moffett, R., Codrescu, M., & Millward, G. (1996). A coupled thermosphere-ionosphere model (ctim). *STEP Report*, *239*.

Fuller-Rowell, T. J. (1998). The thermospheric spoon: A mechanism for the semiannual density variation. *Journal of Geophysical Research: Space Physics*, *103*(A3), 3951-3956. Retrieved from https://agupubs.onlinelibrary.wiley.com/doi/abs/10.1029/97JA03335 doi: 10.1029/97JA03335

Fuller-Rowell, T. J., Akmaev, R. A., Wu, F., Anghel, A., Maruyama, N., Anderson, D. N., ... Millward, G. (2008). Impact of terrestrial weather on the upper atmosphere. *Geophysical Research Letters*, *35*(9). Retrieved from https://agupubs.onlinelibrary.wiley.com/doi/abs/10.1029/2007GL032911 doi: 10.1029/2007GL032911

Fuller-Rowell, T. J., & Evans, D. S. (1987). Height-integrated Pedersen and Hall conductivity patterns inferred from the TIROS-NOAA satellite data. *Journal of Geophysical Research: Space Physics*, *92*(A7), 7606-7618. Retrieved from https://agupubs.onlinelibrary.wiley.com/doi/abs/10.1029/JA092iA07p07606 doi: 10.1029/JA092iA07p07606

Fuller-Rowell, T. J., & Rees, D. (1980). A three-dimensional time-dependent global model of the thermosphere. *Journal of Atmospheric Sciences*, *37*(11), 2545 - 2567. Retrieved from https://journals.ametsoc.org/view/journals/atsc/37/11/1520-0469_1980_037_2545_atdtdg_2_0_co_2.xml doi: 10.1175/1520-0469(1980)037<2545:ATDTDG>2.0.CO;2

Gagne II, D. J., Christensen, H. M., Subramanian, A. C., & Monahan, A. H. (2020). Machine learning for stochastic parameterization: Generative adversarial networks in the lorenz '96 model. *Journal of Advances in Modeling Earth Systems*, *12*(3), e2019MS001896. Retrieved from https://agupubs.onlinelibrary.wiley.com/doi/abs/10.1029/2019MS001896 (e2019MS001896 10.1029/2019MS001896) doi: https://doi.org/10.1029/2019MS001896

Garcia, R. F., Bruinsma, S., Massarweh, L., & Doornbos, E. (2016). Medium-scale gravity wave activity in the thermosphere inferred from goce data. *Journal of Geophysical Research: Space Physics*, *121*(8), 8089-8102. Retrieved from https://agupubs.onlinelibrary.wiley.com/doi/abs/10.1002/2016JA022797 doi: https://doi.org/10.1002/2016JA022797

Garcia, R. R., Dunkerton, T. J., Lieberman, R. S., & Vincent, R. A. (1997). Climatology of the semiannual oscillation of the tropical middle atmosphere. *Journal of Geophysical Research: Atmospheres*, *102*(D22), 26019-26032. Retrieved from https://

agupubs.onlinelibrary.wiley.com/doi/abs/10.1029/97JD00207 doi: 10.1029/97JD00207

Garcia, R. R., López-Puertas, M., Funke, B., Marsh, D. R., Kinnison, D. E., Smith, A. K., & González-Galindo, F. (2014). On the distribution of co2 and co in the mesosphere and lower thermosphere. *Journal of Geophysical Research: Atmospheres*, *119*(9), 5700-5718. Retrieved from https://agupubs.onlinelibrary.wiley.com/doi/abs/10.1002/2013JD021208 doi: https://doi.org/10.1002/2013JD021208

Garcia, R. R., Marsh, D. R., Kinnison, D. E., Boville, B. A., & Sassi, F. (2007). Simulation of secular trends in the middle atmosphere, 1950 - 2003. *Journal of Geophysical Research: Atmospheres*, *112*(D9). Retrieved from https://agupubs.onlinelibrary.wiley.com/doi/abs/10.1029/2006JD007485 doi: 10.1029/2006JD007485

Garcia, R. R., & Solomon, S. (1985). The effect of breaking gravity waves on the dynamics and chemical composition of the mesosphere and lower thermosphere. *Journal of Geophysical Research: Atmospheres*, *90*(D2), 3850-3868. Retrieved from https://agupubs.onlinelibrary.wiley.com/doi/abs/10.1029/JD090iD02p03850 doi: 10.1029/JD090iD02p03850

George, D., & Huerta, E. (2018). Deep learning for real-time gravitational wave detection and parameter estimation: Results with advanced ligo data. *Physics Letters B*, *778*, 64-70. Retrieved from https://www.sciencedirect.com/science/article/pii/S0370269317310390 doi: https://doi.org/10.1016/j.physletb.2017.12.053

Gombosi, T. I. (1998). *Physics of the space environment.* Cambridge University Press. doi: 10.1017/CBO9780511529474

Goncharenko, L. P., Chau, J. L., Liu, H.-L., & Coster, A. J. (2010). Unexpected connections between the stratosphere and ionosphere. *Geophysical Research Letters*, *37*(10). Retrieved from https://agupubs.onlinelibrary.wiley.com/doi/abs/10.1029/2010GL043125 doi: https://doi.org/10.1029/2010GL043125

Goncharenko, L. P., Coster, A. J., Chau, J. L., & Valladares, C. E. (2010). Impact of sudden stratospheric warmings on equatorial ionization anomaly. *Journal of Geophysical Research: Space Physics*, *115*(A10). Retrieved from https://agupubs.onlinelibrary.wiley.com/doi/abs/10.1029/2010JA015400 doi: https://doi.org/10.1029/2010JA015400

Gossard, E. E., & Hooke, W. H. (1975, January). Waves in the atmosphere: Atmospheric infrasound and gravity waves - Their generation and propagation. *Atmospheric Science*, *2*.

Grossmann, K., & Offermann, D. (1978). Atomic oxygen emission at 63 μm as a cooling mechanism in the thermosphere and ionosphere. *Nature*, *276*, 594-595. doi: 10.1038/276594a0

Grossmann, K. U., Kaufmann, M., & Gerstner, E. (2000). A global measurement of lower thermosphere atomic oxygen densities. *Geophysical Research Letters*, *27*(9), 1387-1390. Retrieved from https://agupubs.onlinelibrary.wiley.com/doi/abs/10.1029/2000GL003761 doi: 10.1029/2000GL003761

Groves, G. (1972). Annual and semi-annual zonal wind components and corresponding temperature and density variations, 60âĂŞ130 km. *Planetary and Space Science*, *20*(12), 2099 - 2112. Retrieved from http://www.sciencedirect.com/science/article/pii/0032063372900669 doi: https://doi.org/10.1016/0032-0633(72)90066-9

Gumbel, J. (1997). *Rocket-borne optical measurements of minor constituents in the middle atmosphere* (Unpublished doctoral dissertation). Stockholm University, Department of Meteorology. (S. 1-44: sammanfattning, s. 45-271: 6 uppsatser)

Hagan, M. E., & Forbes, J. M. (2002). Migrating and nonmigrating diurnal tides in the middle and upper atmosphere excited by tropospheric latent heat release. *Journal of Geophysical Research: Atmospheres*, *107*(D24), ACL 6-1-ACL 6-15. Retrieved from https://agupubs.onlinelibrary.wiley.com/doi/abs/10.1029/2001JD001236 doi: 10.1029/2001JD001236

Hagan, M. E., Maute, A., & Roble, R. G. (2009). Tropospheric tidal effects on the middle and upper atmosphere. *Journal of Geophysical Research: Space Physics*, *114*(A1). Retrieved from https://agupubs.onlinelibrary.wiley.com/doi/abs/10.1029/2008JA013637 doi: 10.1029/2008JA013637

Hardy, D. A., Gussenhoven, M. S., Raistrick, R., & McNeil, W. J. (1987). Statistical and functional representations of the pattern of auroral energy flux, number flux, and conductivity. *Journal of Geophysical Research: Space Physics*, *92*(A11), 12275-12294. Retrieved from https://agupubs.onlinelibrary.wiley.com/doi/abs/10.1029/JA092iA11p12275 doi: https://doi.org/10.1029/JA092iA11p12275

Harris, M. J., Arnold, N. F., & Aylward, A. D. (2002). A study into the effect of the diurnal tide on the structure of the background mesosphere and thermosphere using the new coupled middle atmosphere and thermosphere (CMAT) general circulation model. *Annales Geophysicae*, *20*(2), 225–235. Retrieved from https://angeo.copernicus.org/articles/20/225/2002/ doi: 10.5194/angeo-20-225-2002

Hays, P., Jones, R., & Rees, M. (1973). Auroral heating and the composition of the neutral atmosphere. *Planetary and Space Science*, *21*(4), 559 - 573. Retrieved from http://www.sciencedirect.com/science/article/pii/0032063373900706 doi: https://doi.org/10.1016/0032-0633(73)90070-6

Hedin, A. E. (1983). A revised thermospheric model based on mass spectrometer and incoherent scatter data: Msis-83. *Journal of Geophysical Research: Space Physics*, *88*(A12), 10170-10188. Retrieved from https://agupubs.onlinelibrary.wiley.com/doi/abs/10.1029/JA088iA12p10170 doi: 10.1029/JA088iA12p10170

Hedin, A. E. (1987). Msis-86 thermospheric model. *Journal of Geophysical Research: Space Physics*, *92*(A5), 4649-4662. Retrieved from https://agupubs.onlinelibrary.wiley.com/doi/abs/10.1029/JA092iA05p04649 doi: 10.1029/JA092iA05p04649

Hedin, A. E. (1991). Extension of the msis thermosphere model into the middle and lower atmosphere. *Journal of Geophysical Research: Space Physics*, *96*(A2), 1159-1172. Retrieved from https://agupubs.onlinelibrary.wiley.com/doi/abs/10.1029/90JA02125 doi: 10.1029/90JA02125

Hedin, A. E., Salah, J. E., Evans, J. V., Reber, C. A., Newton, G. P., Spencer, N. W., ... McClure, J. P. (1977). A global thermospheric model based on mass spectrometer and incoherent scatter data msis, 1. n2 density and temperature. *Journal of Geophysical Research (1896-1977)*, *82*(16), 2139-2147. Retrieved from https://agupubs.onlinelibrary.wiley.com/doi/abs/10.1029/JA082i016p02139 doi: https://doi.org/10.1029/JA082i016p02139

Heelis, R. A., Lowell, J. K., & Spiro, R. W. (1982). A model of the high-latitude ionospheric convection pattern. *Journal of Geophysical Research: Space Physics*, *87*(A8), 6339-6345. Retrieved from https://agupubs.onlinelibrary.wiley.com/doi/abs/10.1029/JA087iA08p06339 doi: https://doi.org/10.1029/JA087iA08p06339

Hines, C. O. (1997). Doppler-spread parameterization of gravity-wave momentum deposition in the middle atmosphere. part 1: Basic formulation. *Journal of Atmospheric and Solar-Terrestrial Physics*, *59*(4), 371-386. Retrieved from https://www.sciencedirect.com/science/article/pii/S136468269600079X doi: https://doi.org/10.1016/S1364-6826(96)00079-X

Hinton, G., Deng, L., Yu, D., Dahl, G. E., Mohamed, A., Jaitly, N., ... Kingsbury, B. (2012). Deep neural networks for acoustic modeling in speech recognition: The shared views of four research groups. *IEEE Signal Processing Magazine*, *29*(6), 82-97. doi: 10.1109/MSP.2012.2205597

Hocke, K., & Schlegel, K. (1996, September). A review of atmospheric gravity waves and travelling ionospheric disturbances: 1982-1995. *Annales Geophysicae*, *14*(9), 917-940. doi: 10.1007/s00585-996-0917-6

Hocking, W. (1990). Turbulence in the region 80-120 km. *Advances in Space Research*, *10*(12), 153-161. Retrieved from https://www.sciencedirect.com/science/article/pii/027311779090394F doi: https://doi.org/10.1016/0273-1177(90)90394-F

Hodges, R. R. (1969). Eddy diffusion coefficients due to instabilities in internal gravity waves. *Journal of Geophysical Research*, *74*(16), 4087-4090. Retrieved from https://agupubs.onlinelibrary.wiley.com/doi/abs/10.1029/JA074i016p04087 doi: 10.1029/JA074i016p04087

Hodges Jr., R. R. (1967). Generation of turbulence in the upper atmosphere by internal gravity waves. *Journal of Geophysical Research (1896-1977)*, *72*(13), 3455-3458. Retrieved from https://agupubs.onlinelibrary.wiley.com/doi/abs/10.1029/JZ072i013p03455 doi: https://doi.org/10.1029/JZ072i013p03455

Holton, J. R. (1983, 10). The Influence of Gravity Wave Breaking on the General Circulation of the Middle Atmosphere. *Journal of the Atmospheric Sciences*, *40*(10), 2497-2507. Retrieved from https://doi.org/10.1175/1520-0469(1983)040<2497:TIOGWB>2.0.CO;2 doi: 10.1175/1520-0469(1983)040<2497:TIOGWB>2.0.CO;2

Hoppel, K. W., Baker, N. L., Coy, L., Eckermann, S. D., McCormack, J. P., Nedoluha, G. E., & Siskind, D. E. (2008). Assimilation of stratospheric and mesospheric temperatures from mls and saber into a global nwp model. *Atmospheric Chemistry and Physics*, *8*(20), 6103–6116. Retrieved from https://acp.copernicus.org/articles/8/6103/2008/ doi: 10.5194/acp-8-6103-2008

Huba, J. D., Joyce, G., & Fedder, J. A. (2000). Sami2 is another model of the ionosphere (sami2): A new low-latitude ionosphere model. *Journal of Geophysical Research: Space Physics*, *105*(A10), 23035-23053. Retrieved from https://agupubs.onlinelibrary.wiley.com/doi/abs/10.1029/2000JA000035 doi: https://doi.org/10.1029/2000JA000035

Huba, J. D., & Liu, H.-L. (2020). Global modeling of equatorial spread f with sami3/waccm-x. *Geophysical Research Letters*, *47*(14), e2020GL088258. Retrieved from https://agupubs.onlinelibrary.wiley.com/doi/abs/10.1029/2020GL088258 (e2020GL088258 10.1029/2020GL088258) doi: https://doi.org/10.1029/2020GL088258

Huba, J. D., Maute, A., & Crowley, G. (2017). SAMI3_ICON: Model of the Ionosphere/Plasmasphere System. *Space Sci Rev.*, *212*(1-2), 731-742. doi: 10.1007/s11214-017-0415-z

Humm, D. C., Ogorzalek, B. S., Elko, M. J., Morrison, D., & Paxton, L. J. (1999). Optical calibration of the Global Ultraviolet Imager (GUVI). *Proc.SPIE*, *3818*, 3818 - 3818 - 12. Retrieved from https://doi.org/10.1117/12.364144 doi: 10.1117/12.364144

Humm, D. C., Paxton, L. J., Christensen, A. B., Ogorzalek, B. S., Pardoe, C. T., Meng, C.-I., ... Ercol, C. J. (1998). Design and performance of the Global Ultraviolet Imager (GUVI). *Proc.SPIE*, *3445*, 3445 - 3445 - 11. Retrieved from https://doi.org/10.1117/12.330325 doi: 10.1117/12.330325

Hysell, D. L., Kelley, M. C., Swartz, W. E., & Woodman, R. F. (1990). Seeding and layering of equatorial spread F by gravity waves. *Journal of Geophysical Research: Space Physics*, *95*(A10), 17253-17260. Retrieved from https://agupubs.onlinelibrary.wiley.com/doi/abs/10.1029/JA095iA10p17253 doi: 10.1029/JA095iA10p17253

Hyvarinen, O. (2014). A probabilistic derivation of heidke skill score. *Weather and Forecasting*, *29*.

Immel, T. J., Sagawa, E., England, S. L., Henderson, S. B., Hagan, M. E., Mende, S. B., ... Paxton, L. J. (2006). Control of equatorial ionospheric morphology by atmospheric tides. *Geophysical Research Letters*, *33*(15). Retrieved from https://agupubs.onlinelibrary.wiley.com/doi/abs/10.1029/2006GL026161 doi: 10.1029/2006GL026161

Jacchia, L. G. (1965, January). Static Diffusion Models of the Upper Atmosphere with Empirical Temperature Profiles. *Smithsonian Contributions to Astrophysics*, *8*, 215.

Jacchia, L. G. (1970, May). New Static Models of the Thermosphere and Exosphere with Empirical Temperature Profiles. *SAO Special Report*, *313*.

Jacchia, L. G. (1971, May). Revised Static Models of the Thermosphere and Exosphere with Empirical Temperature Profiles. *SAO Special Report*, *332*.

Jacchia, L. G. (1977, March). Thermospheric Temperature, Density, and Composition: New Models. *SAO Special Report*, *375*.

Jacchia, L. G., Slowey, J. H., & Campbell, I. (1969). A study of the semi-annual density variation in the upper atmosphere from 1958 to 1966, based on satellite drag analysis. *Planetary and Space Science*, *17*(1), 49 - 60. Retrieved from http://www.sciencedirect.com/science/article/pii/0032063369901226 doi: https://doi.org/10.1016/0032-0633(69)90122-6

Jackson, D. R., Fuller-Rowell, T. J., Griffin, D. J., Griffith, M. J., Kelly, C. W., Marsh, D. R., & Walach, M.-T. (2019). Future directions for whole atmosphere modeling: Developments in the context of space weather. *Space Weather*, *17*(9), 1342-1350. Retrieved from https://agupubs.onlinelibrary.wiley.com/doi/abs/10.1029/2019SW002267 doi: https://doi.org/10.1029/2019SW002267

Jiao, Y., Morton, Y. T., Taylor, S., & Pelgrum, W. (2013). Characterization of high-latitude ionospheric scintillation of gps signals. *Radio Science*, *48*.

Jin, H., Miyoshi, Y., Fujiwara, H., Shinagawa, H., Terada, K., Terada, N., ... Saito, A. (2011). Vertical connection from the tropospheric activities to the ionospheric longitudinal structure simulated by a new earth's whole atmosphere ionosphere coupled model. *Journal of Geophysical Research: Space Physics*, *116*(A1). Retrieved from https://agupubs.onlinelibrary.wiley.com/doi/abs/10.1029/2010JA015925 doi: 10.1029/2010JA015925

Jin, H., Miyoshi, Y., Pancheva, D., Mukhtarov, P., Fujiwara, H., & Shinagawa, H. (2012). Response of migrating tides to the stratospheric sudden warming in 2009 and their effects on the ionosphere studied by a whole atmosphere-ionosphere model gaia with cosmic and timed/saber observations. *Journal of Geophysical Research: Space Physics*, *117*(A10). Retrieved from https://agupubs

.onlinelibrary.wiley.com/doi/abs/10.1029/2012JA017650 doi: https://doi.org/10.1029/2012JA017650

John, S., & Kumar, K. (2012). Timed/saber observations of global gravity wave climatology and their interannual variability from stratosphere to mesosphere lower thermosphere. *Clim Dyn*, *39*, 1489–1505. Retrieved from https://doi.org/10.1007/s00382-012-1329-9

Johnson, F. S. (1964). Composition changes in the upper atmosphere. *Electron Density Distribution in Ionosphere and ExosphereE. Thrane, 81, NorthâĂŽÃĎÃłHolland, Amsterdam*.

Johnson, F. S. (1973). Horizontal variations in thermospheric composition. *Reviews of Geophysics*, *11*(3), 741-754. Retrieved from https://agupubs.onlinelibrary.wiley.com/doi/abs/10.1029/RG011i003p00741 doi: 10.1029/RG011i003p00741

Johnson, F. S., & Gottlieb, B. (1970). Eddy mixing and circulation at ionospheric levels. *Planetary and Space Science*, *18*(12), 1707 - 1718. Retrieved from http://www.sciencedirect.com/science/article/pii/0032063370900048 doi: https://doi.org/10.1016/0032-0633(70)90004-8

Johnson, F. S., & Gottlieb, B. (1973). Atomic oxygen transport in the thermosphere. *Planetary and Space Science*, *21*(6), 1001 - 1009. Retrieved from http://www.sciencedirect.com/science/article/pii/0032063373901463 doi: https://doi.org/10.1016/0032-0633(73)90146-3

Johnson, F. S., & Wilkins, E. M. (1965). Thermal upper limit on eddy diffusion in the mesosphere and lower thermosphere. *Journal of Geophysical Research (1896-1977)*, *70*(6), 1281-1284. Retrieved from https://agupubs.onlinelibrary.wiley.com/doi/abs/10.1029/JZ070i006p01281 doi: https://doi.org/10.1029/JZ070i006p01281

Jones Jr., M., Drob, D. P., Siskind, D. E., McCormack, J. P., Maute, A., McDonald, S. E., & Dymond, K. F. (2018). Evaluating different techniques for constraining lower atmospheric variability in an upper atmosphere general circulation model: A case study during the 2010 sudden stratospheric warming. *Journal of Advances in Modeling Earth Systems*, *10*(12), 3076-3102. Retrieved from https://agupubs.onlinelibrary.wiley.com/doi/abs/10.1029/2018MS001440 doi: https://doi.org/10.1029/2018MS001440

Jones Jr., M., Emmert, J. T., Drob, D. P., Picone, J. M., & Meier, R. R. (2018). Origins of the thermosphere-ionosphere semiannual oscillation: Reformulating the thermospheric spoon mechanism. *Journal of Geophysical Research: Space Physics*, *123*(1), 931-954. Retrieved from https://agupubs.onlinelibrary.wiley.com/doi/abs/10.1002/2017JA024861 doi: 10.1002/2017JA024861

Jones Jr., M., Emmert, J. T., Drob, D. P., & Siskind, D. E. (2017). Middle atmosphere dynamical sources of the semiannual oscillation in the thermosphere and ionosphere. *Geophysical Research Letters*, *44*(1), 12-21. Retrieved from https://agupubs.onlinelibrary.wiley.com/doi/abs/10.1002/2016GL071741 doi: 10.1002/2016GL071741

Jones Jr., M., Forbes, J. M., & Hagan, M. E. (2014). Tidal-induced net transport effects on the oxygen distribution in the thermosphere. *Geophysical Research Letters*, *41*(14), 5272-5279. Retrieved from https://agupubs.onlinelibrary.wiley.com/doi/abs/10.1002/2014GL060698 doi: https://doi.org/10.1002/2014GL060698

Jones Jr., M., Sutton, E. K., Emmert, J. T., Siskind, D. E., & Drob, D. P. (2021). On the effects of mesospheric and lower thermospheric oxygen chemistry on the thermosphere and ionosphere semiannual oscillation. *Journal of Geophysical Research: Space Physics*, e2020JA028647. Retrieved from https://agupubs.onlinelibrary.wiley.com/doi/abs/10.1029/2020JA028647 (e2020JA028647 2020JA028647) doi: https://doi.org/10.1029/2020JA028647

Justus, C. G. (1967). The eddy diffusivities, energy balance parameters, and heating rate of upper atmospheric turbulence. *Journal of Geophysical Research (1896-1977)*, *72*(3), 1035-1039. Retrieved from https://agupubs.onlinelibrary.wiley.com/doi/abs/10.1029/JZ072i003p01035 doi: https://doi.org/10.1029/JZ072i003p01035

Keating, G. M., & Prior, E. J. (1968). The winter He bulge. *Space Res., 8, 982*.

Keating, G. M., Tolson, R. H., & Bradford, M. S. (2000). Evidence of long term global decline in the earth's thermospheric densities apparently related to anthropogenic effects. *Geophysical Research Letters*, *27*(10), 1523-1526. Retrieved from https://agupubs.onlinelibrary.wiley.com/doi/abs/10.1029/2000GL003771 doi: https://doi.org/10.1029/2000GL003771

Kelley, M. C. (2009). Introductory and background material. In M. C. Kelley (Ed.), *The earth's ionosphere* (Vol. 96, p. 1-26). Academic Press. Retrieved from https://www.sciencedirect.com/science/article/pii/S0074614209602187 doi: https://doi.org/10.1016/S0074-6142(09)60218-7

Kelly, M. A., Comberiate, J. M., Miller, E. S., & Paxton, L. J. (2014). Progress toward forecasting of space weather effects on uhf satcom after operation anaconda. *Space Weather*, *12*(10), 601-611. Retrieved from https://agupubs.onlinelibrary.wiley.com/doi/abs/10.1002/2014SW001081 doi: 10.1002/2014SW001081

Kielty, C. L., Bialek, S., Fabbro, S., Venn, K. A., O'Briain, T., Jahandar, F., & Monty, S. (2018). StarNet: a deep learning analysis of infrared stellar spectra. In J. C. Guzman & J. Ibsen (Eds.), *Software and cyberinfrastructure for astronomy v* (Vol. 10707, pp. 814 – 824). SPIE. Retrieved from https://doi.org/10.1117/12.2313544 doi: 10.1117/12.2313544

King, G. A. M. (1964). The dissociation of oxygen and high level circulation in the atmosphere. *Journal of the Atmospheric Sciences*, *21*(3), 231-237. doi: 10.1175/1520-0469(1964)0210231:TDOOAH2.0.CO;2

King-Hele, D. G. (1966). Semi-annual Variation in Upper-atmosphere Density. *Nature*, *210*(5040), 1032. Retrieved from https://doi.org/10.1038/2101032a0 doi: 10.1038/2101032a0

King-Hele, D. G. (1967, December). Upper Atmosphere Density in 1966-67 : the Dominance of a Semi-annual Variation at Heights near 200 km. *Nature*, *216*(5118), 880. doi: 10.1038/216880a0

King-Hele, D., & Kingston, J. (1968). Air density at heights near 190 km in 1966?67, from the orbit of secor 6. *Planetary and Space Science*, *16*(5), 675 - 691. Retrieved from http://www.sciencedirect.com/science/article/pii/0032063368901062 doi: https://doi.org/10.1016/0032-0633(68)90106-2

King-Hele, D., & Walker, D. M. (1969). Revised profiles of air density at heights of 130?180 km, from the orbits of 1968-59a and b. *Planetary and Space Science*, *17*(12), 2027 - 2029. Retrieved from http://www.sciencedirect.com/science/article/pii/003206336990141X doi: https://doi.org/10.1016/0032-0633(69)90141-X

Kintner, P. M., Ledvina, B. M., & de Paula, E. R. (2007). Gps and ionospheric scintillations. *Space Weather*, *5*. doi: 10.1029/2006SW000260

Kirchhoff, V. W. J. H., & Clemesha, B. R. (1983a). The atmospheric neutral sodium layer: 2. diurnal variations. *Journal of Geophysical Research: Space Physics*, *88*(A1), 442-450. Retrieved from https://agupubs.onlinelibrary.wiley.com/doi/abs/10.1029/JA088iA01p00442 doi: 10.1029/JA088iA01p00442

Kirchhoff, V. W. J. H., & Clemesha, B. R. (1983b). Eddy diffusion coefficients in the lower thermosphere. *Journal of Geophysical Research: Space Physics*, *88*(A7), 5765-5768. Retrieved from https://agupubs.onlinelibrary.wiley.com/doi/abs/10.1029/JA088iA07p05765 doi: https://doi.org/10.1029/JA088iA07p05765

Krizhevsky, A., Sutskever, I., & Hinton, G. E. (2017, May). Imagenet classification with deep convolutional neural networks. *Commun. ACM*, *60*(6), 84?90. Retrieved from https://doi.org/10.1145/3065386 doi: 10.1145/3065386

Kurosaki, S., Yamanaka, M., Hashiguchi, H., Sato, T., & Fukao, S. (1996). Vertical eddy diffusivity in the lower and middle atmosphere: A climatology based on the mu radar observations during 1986âĂŞ1992. *Journal of Atmospheric and Terrestrial Physics*, *58*(6), 727-734. Retrieved from https://www.sciencedirect.com/science/article/pii/0021916995000704 (Ionosphere-Middle and Lower Atmosphere Interactions) doi: https://doi.org/10.1016/0021-9169(95)00070-4

Lamb, K., Malhotra, G., Vlontzos, A., Wagstaff, E., Baydin, A. G., Bhiwandiwalla, A., ... Bhatt, A. (2019). *Prediction of gnss phase scintillations: A machine learning approach.*

Lehmacher, G., & Lübken, F.-J. (1995). Simultaneous observation of convective adjustment and turbulence generation in the mesosphere. *Geophysical Research Letters*, *22*(18), 2477-2480. Retrieved from https://agupubs.onlinelibrary.wiley.com/doi/abs/10.1029/95GL02351 doi: https://doi.org/10.1029/95GL02351

Lehmacher, G. A., Croskey, C. L., Mitchell, J. D., Friedrich, M., Lübken, F.-J., Rapp, M., ... Fritts, D. C. (2006). Intense turbulence observed above a mesospheric temperature inversion at equatorial latitude. *Geophysical Research Letters*, *33*(8). Retrieved from https://agupubs.onlinelibrary.wiley.com/doi/abs/10.1029/2005GL024345 doi: https://doi.org/10.1029/2005GL024345

Lehmacher, G. A., Scott, T. D., Larsen, M. F., Bilén, S. G., Croskey, C. L., Mitchell, J. D., ... Collins, R. L. (2011). The turbopause experiment: atmospheric stability and turbulent structure spanning the turbopause altitude. *Annales Geophysicae*, *29*(12), 2327–2339. Retrieved from https://angeo.copernicus.org/articles/29/2327/2011/ doi: 10.5194/angeo-29-2327-2011

Lei, J., Matsuo, T., Dou, X., Sutton, E., & Luan, X. (2012). Annual and semiannual variations of thermospheric density: Eof analysis of champ and grace data. *Journal of Geophysical Research: Space Physics*, *117*(A1). Retrieved from https://agupubs.onlinelibrary.wiley.com/doi/abs/10.1029/2011JA017324 doi: https://doi.org/10.1029/2011JA017324

Lethy, A., El-Eraki, M. A., Samy, A., & Deebes, H. A. (2018). Prediction of the dst index and analysis of its dependence on solar wind parameters using neural network. *Space Weather*, *16*(9), 1277-1290. Retrieved from https://agupubs.onlinelibrary.wiley.com/doi/abs/10.1029/2018SW001863 doi: https://doi.org/10.1029/2018SW001863

Lieberman, R. S., Akmaev, R. A., Fuller-Rowell, T. J., & Doornbos, E. (2013). Thermospheric zonal mean winds and tides revealed by champ. *Geophysical Research Letters*, *40*(10), 2439-2443. Retrieved from https://agupubs.onlinelibrary.wiley.com/doi/abs/10.1002/grl.50481 doi: https://doi.org/10.1002/grl.50481

Lin, F. J., Chance, K. V., & Traub, W. A. (1987). Atomic oxygen in the lower thermosphere. *Journal of Geophysical Research: Atmospheres*, *92*(D4), 4325-4336. Retrieved from https://agupubs.onlinelibrary.wiley.com/doi/abs/10.1029/JD092iD04p04325 doi: 10.1029/JD092iD04p04325

Lin, S.-J. (2004). A "vertically lagrangian" finite-volume dynamical core for global models. *Monthly Weather Review*, *132*(10), 2293-2307. Retrieved from https://doi.org/10.1175/1520-0493(2004)132<2293:AVLFDC>2.0.CO;2 doi: 10.1175/1520-0493(2004)132<2293:AVLFDC>2.0.CO;2

Lindzen, R. S. (1981). Turbulence and stress owing to gravity wave and tidal breakdown. *Journal of Geophysical Research: Oceans*, *86*(C10), 9707-9714. Retrieved from https://agupubs.onlinelibrary.wiley.com/doi/abs/10.1029/JC086iC10p09707 doi: 10.1029/JC086iC10p09707

Liu, A. Z. (2009). Estimate eddy diffusion coefficients from gravity wave vertical momentum and heat fluxes. *Geophysical Research Letters*, *36*(8). Retrieved from https://agupubs.onlinelibrary.wiley.com/doi/abs/10.1029/2009GL037495 doi: https://doi.org/10.1029/2009GL037495

Liu, H., Foster, B. T., Hagan, M. E., McInerney, J. M., Maute, A., Qian, L., ... Oberheide, J. (2010). Thermosphere extension of the Whole Atmosphere Community Climate Model. *Journal of Geophysical Research: Space Physics*, *115*(A12). Retrieved from https://agupubs.onlinelibrary.wiley.com/doi/abs/10.1029/2010JA015586 doi: 10.1029/2010JA015586

Liu, H., Pedatella, N., & Hocke, K. (2017). Medium-scale gravity wave activity in the bottomside f region in tropical regions. *Geophysical Research Letters*, *44*(14), 7099-7105. Retrieved from https://agupubs.onlinelibrary.wiley.com/doi/abs/10.1002/2017GL073855 doi: https://doi.org/10.1002/2017GL073855

Liu, H.-L. (2007). On the large wind shear and fast meridional transport above the mesopause. *Geophysical Research Letters*, *34*(8). Retrieved from https://agupubs.onlinelibrary.wiley.com/doi/abs/10.1029/2006GL028789 doi: 10.1029/2006GL028789

Liu, H.-L. (2021). Effective vertical diffusion by atmospheric gravity waves. *Geophysical Research Letters*, *48*(1), e2020GL091474. Retrieved from https://agupubs.onlinelibrary.wiley.com/doi/abs/10.1029/2020GL091474 (e2020GL091474 2020GL091474) doi: https://doi.org/10.1029/2020GL091474

Liu, H.-L., Bardeen, C. G., Foster, B. T., Lauritzen, P., Liu, J., Lu, G., ... Wang, W. (2018). Development and validation of the Whole Atmosphere Community Climate Model With Thermosphere and Ionosphere Extension (WACCM-X 2.0). *Journal of Advances in Modeling Earth Systems*, *10*(2), 381-402. Retrieved from https://agupubs.onlinelibrary.wiley.com/doi/abs/10.1002/2017MS001232 doi: 10.1002/2017MS001232

Liu, H. L., Hays, P. B., & Roble, R. G. (1999). A numerical study of gravity wave breaking and impacts on turbulence and mean state. *Journal of the Atmospheric Sciences*, *56*(13), 2152 - 2177. Retrieved from https://journals.ametsoc.org/view/journals/atsc/56/13/1520-0469_1999_056_2152_ansogw_2.0.co_2.xml doi: 10.1175/1520-0469(1999)056<2152:ANSOGW>2.0.CO;2

Liu, H.-L., McInerney, J. M., Santos, S., Lauritzen, P. H., Taylor, M. A., & Pedatella, N. M. (2014). Gravity waves simulated by high-resolution whole atmo-

sphere community climate model. *Geophysical Research Letters*, *41*(24), 9106-9112. Retrieved from https://agupubs.onlinelibrary.wiley.com/doi/abs/10.1002/2014GL062468 doi: https://doi.org/10.1002/2014GL062468

Liu, H.-L., & Roble, R. G. (2002). A study of a self-generated stratospheric sudden warming and its mesospheric?lower thermospheric impacts using the coupled time-gcm/ccm3. *Journal of Geophysical Research: Atmospheres*, *107*(D23), ACL 15-1-ACL 15-18. Retrieved from https://agupubs.onlinelibrary.wiley.com/doi/abs/10.1029/2001JD001533 doi: https://doi.org/10.1029/2001JD001533

Liu, J., Liu, H., Wang, W., Burns, A. G., Wu, Q., Gan, Q., ... Schreiner, W. S. (2018). First results from the ionospheric extension of waccm-x during the deep solar minimum year of 2008. *Journal of Geophysical Research: Space Physics*, *123*(2), 1534-1553. Retrieved from https://agupubs.onlinelibrary.wiley.com/doi/abs/10.1002/2017JA025010 doi: https://doi.org/10.1002/2017JA025010

Liu, X. (2013). The effects of composition on thermosphere mass density response to geomagnetic activity. *ProQuest Dissertations and Theses*, 183. Retrieved from https://proxy.lib.umich.edu/login?url=https://www.proquest.com/dissertations-theses/effects-composition-on-thermosphere-mass-density/docview/1493002690/se-2?accountid=14667 (Copyright - Database copyright ProQuest LLC; ProQuest does not claim copyright in the individual underlying works; Last updated - 2020-11-25)

Liu, X., & Ridley, A. (2015). A simulation study of the thermosphere mass density response to substorms using gitm. *Journal of Geophysical Research: Space Physics*, *120*(9), 7987-8001. Retrieved from https://agupubs.onlinelibrary.wiley.com/doi/abs/10.1002/2014JA020962 doi: https://doi.org/10.1002/2014JA020962

Liu, X., Wang, W., Thayer, J. P., Burns, A., Sutton, E., Solomon, S. C., ... Lucas, G. (2014). The winter helium bulge revisited. *Geophysical Research Letters*, *41*(19), 6603-6609. Retrieved from https://agupubs.onlinelibrary.wiley.com/doi/abs/10.1002/2014GL061471 doi: 10.1002/2014GL061471

Liu, X., Yue, J., Xu, J., Garcia, R. R., Russell III, J. M., Mlynczak, M., ... Nakamura, T. (2017). Variations of global gravity waves derived from 14 years of saber temperature observations. *Journal of Geophysical Research: Atmospheres*, *122*(12), 6231-6249. Retrieved from https://agupubs.onlinelibrary.wiley.com/doi/abs/10.1002/2017JD026604 doi: https://doi.org/10.1002/2017JD026604

Lubken, F.-J. (1997). Seasonal variation of turbulent energy dissipation rates at high latitudes as determined by in situ measurements of neutral density fluctuations. *Journal of Geophysical Research: Atmospheres*, *102*(D12), 13441-13456. Retrieved from https://agupubs.onlinelibrary.wiley.com/doi/abs/10.1029/97JD00853 doi: https://doi.org/10.1029/97JD00853

Lühr, H., Rother, M., Köhler, W., Ritter, P., & Grunwaldt, L. (2004). Thermospheric upwelling in the cusp region: Evidence from champ observations. *Geophysical Research Letters*, *31*(6). Retrieved from https://agupubs.onlinelibrary.wiley.com/doi/abs/10.1029/2003GL019314 doi: https://doi.org/10.1029/2003GL019314

Malhotra, G., & Ridley, A. (2020). Data for Global Ionosphere Thermosphere Model Simulations with MSIS and WACCM-X boundary conditions [Data set. *University of Michigan - Deep Blue*. Retrieved from https://doi.org/10.7302/yagm-xv95

Malhotra, G., & Ridley, A. (2021). Impacts of Lower Thermospheric Atomic Oxygen and Dynamics on Thermospheric Semiannual Oscillation, using GITM and WACCM-X [Data set]. *University of Michigan - Deep Blue*. Retrieved from https://doi.org/10.7302/9gp8-kx76

Malhotra, G., Ridley, A. J., Marsh, D. R., Wu, C., Paxton, L. J., & Mlynczak, M. G. (2020). Impacts of lower thermospheric atomic oxygen on thermospheric dynamics and composition using the global ionosphere thermosphere model. *Journal of Geophysical Research: Space Physics*, *125*(9), e2020JA027877. Retrieved from https://agupubs.onlinelibrary.wiley.com/doi/abs/10.1029/2020JA027877 (e2020JA027877 10.1029/2020JA027877) doi: 10.1029/2020JA027877

Malhotra, G., Ruohoniemi, J. M., Baker, J. B. H., Hibbins, R. E., & McWilliams, K. A. (2016). Hf radar observations of a quasi-biennial oscillation in midlatitude mesospheric winds. *Journal of Geophysical Research: Atmospheres*, *121*(21), 12,677-12,689. Retrieved from https://agupubs.onlinelibrary.wiley.com/doi/abs/10.1002/2016JD024935 doi: 10.1002/2016JD024935

Marsh, D. R., Mills, M. J., Kinnison, D. E., Lamarque, J.-F., Calvo, N., & Polvani, L. M. (2013). Climate change from 1850 to 2005 simulated in cesm1(waccm). *Journal of Climate*, *26*(19), 7372-7391. Retrieved from https://doi.org/10.1175/JCLI-D-12-00558.1 doi: 10.1175/JCLI-D-12-00558.1

Maruyama, N., Sun, Y.-Y., Richards, P. G., Middlecoff, J., Fang, T.-W., Fuller-Rowell, T. J., ... Valladares, C. E. (2016). A new source of the midlatitude ionospheric peak density structure revealed by a new ionosphere-plasmasphere model. *Geophysical Research Letters*, *43*(6), 2429-2435. Retrieved from https://agupubs.onlinelibrary.wiley.com/doi/abs/10.1002/2015GL067312 doi: https://doi.org/10.1002/2015GL067312

Matsuno, T. (1982). A quasi one-dimensional model of the middle atmosphere circulation interacting with internal gravity waves. *Journal of the Meteorological Society of Japan. Ser. II*, *60*(1), 215-226. doi: 10.2151/jmsj1965.60.1_215

Maute, A. (2017). Thermosphere-ionosphere-electrodynamics general circulation model for the ionospheric connection explorer: Tiegcm-icon. *Space Science Reviews*,

212(1), 523–551. Retrieved from https://doi.org/10.1007/s11214-017-0330-3 doi: 10.1007/s11214-017-0330-3

Maute, A., Hagan, M. E., Yudin, V., Liu, H.-L., & Yizengaw, E. (2015). Causes of the longitudinal differences in the equatorial vertical e Œ b drift during the 2013 ssw period as simulated by the time-gcm. *Journal of Geophysical Research: Space Physics*, *120*(6), 5117-5136. Retrieved from https://agupubs.onlinelibrary.wiley.com/doi/abs/10.1002/2015JA021126 doi: https://doi.org/10.1002/2015JA021126

Mayr, H. G., Harris, I., & Spencer, N. W. (1978). Some properties of upper atmosphere dynamics. *Reviews of Geophysics*, *16*(4), 539-565. Retrieved from https://agupubs.onlinelibrary.wiley.com/doi/abs/10.1029/RG016i004p00539 doi: 10.1029/RG016i004p00539

Mayr, H. G., & Volland, H. (1972). Theoretical model for the latitude dependence of the thermospheric annual and semiannual variations. *Journal of Geophysical Research (1896-1977)*, *77*(34), 6774-6790. Retrieved from https://agupubs.onlinelibrary.wiley.com/doi/abs/10.1029/JA077i034p06774 doi: https://doi.org/10.1029/JA077i034p06774

McDonald, S. E., Sassi, F., & Mannucci, A. J. (2015). Sami3/sd-waccm-x simulations of ionospheric variability during northern winter 2009. *Space Weather*, *13*(9), 568-584. Retrieved from https://agupubs.onlinelibrary.wiley.com/doi/abs/10.1002/2015SW001223 doi: https://doi.org/10.1002/2015SW001223

McGranaghan, R. M., Mannucci, A. J., Wilson, B., Mattmann, C. A., & Chadwick, R. (2018). New capabilities for prediction of high-latitude ionospheric scintillation: A novel approach with machine learning. *Space Weather*, *16*.

McIntyre, M. E. (1989). On dynamics and transport near the polar mesopause in summer. *Journal of Geophysical Research: Atmospheres*, *94*(D12), 14617-14628. Retrieved from https://agupubs.onlinelibrary.wiley.com/doi/abs/10.1029/JD094iD12p14617 doi: https://doi.org/10.1029/JD094iD12p14617

McLandress, C., Shepherd, G. G., Solheim, B. H., Burrage, M. D., Hays, P. B., & Skinner, W. R. (1996). Combined mesosphere/thermosphere winds using windii and hrdi data from the upper atmosphere research satellite. *Journal of Geophysical Research: Atmospheres*, *101*(D6), 10441-10453. Retrieved from https://agupubs.onlinelibrary.wiley.com/doi/abs/10.1029/95JD01706 doi: 10.1029/95JD01706

Medvedev, A. S., & Klaassen, G. P. (1995). Vertical evolution of gravity wave spectra and the parameterization of associated wave drag. *Journal of Geophysical Research: Atmospheres*, *100*(D12), 25841-25853. Retrieved from https://agupubs.onlinelibrary.wiley.com/doi/abs/10.1029/95JD02533 doi: https://doi.org/10.1029/95JD02533

Meier, R. R., Picone, J. M., Drob, D., Bishop, J., Emmert, J. T., Lean, J. L., ... Gibson, S. T. (2014). Remote sensing of earth's limb by timed/guvi: Retrieval of thermospheric composition and temperature. *Earth and Space Science*, *2*(1), 1-37. Retrieved from https://agupubs.onlinelibrary.wiley.com/doi/abs/10.1002/2014EA000035 doi: 10.1002/2014EA000035

Millward, G. H., Müller-Wodarg, I. C. F., Aylward, A. D., Fuller-Rowell, T. J., Richmond, A. D., & Moffett, R. J. (2001). An investigation into the influence of tidal forcing on f region equatorial vertical ion drift using a global ionosphere-thermosphere model with coupled electrodynamics. *Journal of Geophysical Research: Space Physics*, *106*(A11), 24733-24744. Retrieved from https://agupubs.onlinelibrary.wiley.com/doi/abs/10.1029/2000JA000342 doi: https://doi.org/10.1029/2000JA000342

Mitchell, E. J., Newell, P. T., Gjerloev, J. W., & Liou, K. (2013). Ovation-sm: A model of auroral precipitation based on supermag generalized auroral electrojet and substorm onset times. *Journal of Geophysical Research: Space Physics*, *118*(6), 3747-3759. Retrieved from https://agupubs.onlinelibrary.wiley.com/doi/abs/10.1002/jgra.50343 doi: https://doi.org/10.1002/jgra.50343

Miyahara, S., Yoshida, Y., & Miyoshi, Y. (1993). Dynamic coupling between the lower and upper atmosphere by tides and gravity waves. *Journal of Atmospheric and Terrestrial Physics*, *55*(7), 1039-1053. Retrieved from https://www.sciencedirect.com/science/article/pii/002191699390096H (The First Pacific Regional Step Conference) doi: https://doi.org/10.1016/0021-9169(93)90096-H

Miyoshi, Y., & Fujiwara, H. (2003). Day-to-day variations of migrating diurnal tide simulated by a gcm from the ground surface to the exobase. *Geophysical Research Letters*, *30*(15). Retrieved from https://agupubs.onlinelibrary.wiley.com/doi/abs/10.1029/2003GL017695 doi: https://doi.org/10.1029/2003GL017695

Miyoshi, Y., Fujiwara, H., Jin, H., & Shinagawa, H. (2014). A global view of gravity waves in the thermosphere simulated by a general circulation model. *Journal of Geophysical Research: Space Physics*, *119*(7), 5807-5820. Retrieved from https://agupubs.onlinelibrary.wiley.com/doi/abs/10.1002/2014JA019848 doi: 10.1002/2014JA019848

Miyoshi, Y., Jin, H., Fujiwara, H., & Shinagawa, H. (2018). Numerical study of traveling ionospheric disturbances generated by an upward propagating gravity wave. *Journal of Geophysical Research: Space Physics*, *123*(3), 2141-2155. Retrieved from https://agupubs.onlinelibrary.wiley.com/doi/abs/10.1002/2017JA025110 doi: https://doi.org/10.1002/2017JA025110

Mlynczak, M. G. (1996). Energetics of the middle atmosphere: Theory and observation requirements. *Advances in Space Research*, *17*(11), 117 - 126. Retrieved from http://www.sciencedirect.com/science/article/pii/0273117795007392 doi: https://doi.org/10.1016/0273-1177(95)00739-2

Mlynczak, M. G. (1997). Energetics of the mesosphere and lower thermosphere and the SABER experiment. *Advances in Space Research*, *20*(6), 1177 - 1183. Retrieved from http://www.sciencedirect.com/science/article/pii/S0273117797007692 (Coupling and Energetics in the Stratosphere-Mesosphere-Thermosphere- Ionosphere System) doi: https://doi.org/10.1016/S0273-1177(97)00769-2

Mlynczak, M. G., Hunt, L. A., Mast, J. C., Thomas Marshall, B., Russell III, J. M., Smith, A. K., ... Gordley, L. L. (2013). Atomic oxygen in the mesosphere and lower thermosphere derived from SABER: Algorithm theoretical basis and measurement uncertainty. *Journal of Geophysical Research: Atmospheres*, *118*(11), 5724-5735. Retrieved from https://agupubs.onlinelibrary.wiley.com/doi/abs/10.1002/jgrd.50401 doi: 10.1002/jgrd.50401

Mlynczak, M. G., Hunt, L. A., Russell III, J. M., & Marshall, B. T. (2018). Updated SABER Night Atomic Oxygen and implications for SABER Ozone and Atomic Hydrogen. *Geophysical Research Letters*, *45*(11), 5735-5741. Retrieved from https://agupubs.onlinelibrary.wiley.com/doi/abs/10.1029/2018GL077377 doi: 10.1029/2018GL077377

Mlynczak, M. G., Hunt, L. A., Thomas Marshall, B., Martin-Torres, F. J., Mertens, C. J., Russell III, J. M., ... Gordley, L. L. (2010). Observations of infrared radiative cooling in the thermosphere on daily to multiyear timescales from the timed/saber instrument. *Journal of Geophysical Research: Space Physics*, *115*(A3). Retrieved from https://agupubs.onlinelibrary.wiley.com/doi/abs/10.1029/2009JA014713 doi: https://doi.org/10.1029/2009JA014713

Mlynczak, M. G., Martin-Torres, F. J., Johnson, D. G., Kratz, D. P., Traub, W. A., & Jucks, K. (2004). Observations of the O(3P) fine structure line at 63μm in the upper mesosphere and lower thermosphere. *Journal of Geophysical Research: Space Physics*, *109*(A12). Retrieved from https://agupubs.onlinelibrary.wiley.com/doi/abs/10.1029/2004JA010595 doi: 10.1029/2004JA010595

Nastrom, G. D., & Fritts, D. C. (1992). Sources of mesoscale variability of gravity waves. part i: Topographic excitation. *Journal of Atmospheric Sciences*, *49*(2), 101 - 110. Retrieved from https://journals.ametsoc.org/view/journals/atsc/49/2/1520-0469_1992_049_0101_somvog_2_0_co_2.xml doi: 10.1175/1520-0469(1992)049<0101:SOMVOG>2.0.CO;2

Nastrom, G. D., Fritts, D. C., & Gage, K. S. (1987). An investigation of terrain effects on the mesoscale spectrum of atmospheric motions. *Journal of Atmospheric Sciences*, *44*(20), 3087 - 3096. Retrieved from https://journals.ametsoc.org/view/journals/atsc/44/20/1520-0469_1987_044_3087_aioteo_2_0_co_2.xml doi: 10.1175/1520-0469(1987)044<3087:AIOTEO>2.0.CO;2

Newell, P. T., Sotirelis, T., & Wing, S. (2009). Diffuse, monoenergetic, and broadband aurora: The global precipitation budget. *Journal of Geophysical Research: Space Physics*, *114*(A9). Retrieved from https://agupubs.onlinelibrary.wiley.com/doi/abs/10.1029/2009JA014326 doi: https://doi.org/10.1029/2009JA014326

Newell, R. E. (1966). Thermospheric energetics and a possible explanation of some observations of geomagnetic disturbances and radio aurorae. *Nature*, *211*, 700-703. Retrieved from https://doi.org/10.1038/211700a0 doi: 10.1038/211700a0

Nicolis, C., & Nicolis, G. (1981). Stochastic aspects of climatic transitions?-additive fluctuations. *Tellus*, *33*(3), 225-234. Retrieved from https://onlinelibrary.wiley.com/doi/abs/10.1111/j.2153-3490.1981.tb01746.x doi: https://doi.org/10.1111/j.2153-3490.1981.tb01746.x

Oberheide, J., Forbes, J. M., Zhang, X., & Bruinsma, S. L. (2011). Wave-driven variability in the ionosphere-thermosphere-mesosphere system from timed observations: What contributes to the ?wave 4?? *Journal of Geophysical Research: Space Physics*, *116*(A1). Retrieved from https://agupubs.onlinelibrary.wiley.com/doi/abs/10.1029/2010JA015911 doi: https://doi.org/10.1029/2010JA015911

O'Connor, A. C., Gallaher, M. P., Clark-Sutton, K., Lapidus, D., & Oliver, Z. T. (2019). Economic benefits of the global positioning system (gps). *National Institute of Standards and Technology Report*.

Offermann, D. (1974). Composition variations in the lower thermosphere. *Journal of Geophysical Research (1896-1977)*, *79*(28), 4281-4293. Retrieved from https://agupubs.onlinelibrary.wiley.com/doi/abs/10.1029/JA079i028p04281 doi: 10.1029/JA079i028p04281

Ortland, D. A. (2017). Daily estimates of the migrating tide and zonal mean temperature in the mesosphere and lower thermosphere derived from saber data. *Journal of Geophysical Research: Atmospheres*, *122*(7), 3754-3785. Retrieved from https://agupubs.onlinelibrary.wiley.com/doi/abs/10.1002/2016JD025573 doi: https://doi.org/10.1002/2016JD025573

Paetzold, H. K., & Zschörner, H. (1961). An annual and a semiannual variation of the upper air density. *Geofisica Pura e Applicata*, *48*, 85–92. Retrieved from https://doi.org/10.1007/BF01992371

Panka, P. A., Kutepov, A. A., Rezac, L., Kalogerakis, K. S., Feofilov, A. G., Marsh, D., ... Yi?it, E. (2018). Atomic oxygen retrieved from the saber 2.0- and 1.6-?m radiances using new first-principles nighttime oh(v) model. *Geophysical Research Letters*, *45*(11), 5798-5803. Retrieved from https://agupubs.onlinelibrary.wiley.com/doi/abs/10.1029/2018GL077677 doi: https://doi.org/10.1029/2018GL077677

Park, J., Luhr, H., Lee, C., Kim, Y. H., Jee, G., & Kim, J.-H. (2014). A climatology of medium-scale gravity wave activity in the midlatitude/low-latitude daytime upper thermosphere as observed by champ. *Journal of Geophysical Research: Space Physics*, *119*(3), 2187-2196. Retrieved from https://agupubs.onlinelibrary.wiley.com/doi/abs/10.1002/2013JA019705 doi: https://doi.org/10.1002/2013JA019705

Pawlowski, D. J., & Ridley, A. J. (2009). Quantifying the effect of thermospheric parameterization in a global model. *Journal of Atmospheric and Solar-Terrestrial Physics*, *71*(17), 2017-2026. Retrieved from https://www.sciencedirect.com/science/article/pii/S1364682609002375 doi: https://doi.org/10.1016/j.jastp.2009.09.007

Paxton, L. J., Christensen, A. B., Humm, D. C., Ogorzalek, B. S., Pardoe, C. T., Morrison, D., ... Meng, C.-I. (1999). Global Ultraviolet Imager (GUVI): measuring composition and energy inputs for the NASA Thermosphere Ionosphere Mesosphere Energetics and Dynamics (TIMED) mission. In A. M. Larar (Ed.), *Optical spectroscopic techniques and instrumentation for atmospheric and space research iii* (Vol. 3756, pp. 265 – 276). SPIE. Retrieved from https://doi.org/10.1117/12.366380 doi: 10.1117/12.366380

Paxton, L. J., Christensen, A. B., Morrison, D., Wolven, B., Kil, H., Zhang, Y., ... Meng, C.-I. (2004). GUVI: a hyperspectral imager for geospace. In C. A. Nardell, P. G. Lucey, J.-H. Yee, & J. B. Garvin (Eds.), *Instruments, science, and methods for geospace and planetary remote sensing* (Vol. 5660, pp. 228 – 240). SPIE. Retrieved from https://doi.org/10.1117/12.579171 doi: 10.1117/12.579171

Perlongo, N. J., Ridley, A. J., Cnossen, I., & Wu, C. (2018). A year-long comparison of gps tec and global ionosphere-thermosphere models. *Journal of Geophysical Research: Space Physics*, *123*(2), 1410-1428. Retrieved from https://agupubs.onlinelibrary.wiley.com/doi/abs/10.1002/2017JA024411 doi: 10.1002/2017JA024411

Picone, J. M., Hedin, A. E., Drob, D. P., & Aikin, A. C. (2002). Nrlmsise-00 empirical model of the atmosphere: Statistical comparisons and scientific issues. *Journal of Geophysical Research: Space Physics*, *107*(A12), SIA 15-1-SIA 15-16. Retrieved from https://agupubs.onlinelibrary.wiley.com/doi/abs/10.1029/2002JA009430 doi: 10.1029/2002JA009430

Picone, J. M., Meier, R. R., & Emmert, J. T. (2013). Theoretical tools for studies of low-frequency thermospheric variability. *Journal of Geophysical Research: Space Physics*, *118*(9), 5853-5873. Retrieved from https://agupubs.onlinelibrary.wiley.com/doi/abs/10.1002/jgra.50472 doi: 10.1002/jgra.50472

Pilinski, M. D., & Crowley, G. (2015). Seasonal variability in global eddy diffusion and the effect on neutral density. *Journal of Geophysical Research: Space Physics*, *120*(4), 3097-3117. Retrieved from https://agupubs.onlinelibrary.wiley.com/doi/abs/10.1002/2015JA021084 doi: 10.1002/2015JA021084

Prakash, S. (1999). Production of electric field perturbations by gravity wave winds in the e region suitable for initiating equatorial spread f. *Journal of Geophysical Research: Space Physics*, *104*(A5), 10051-10069. Retrieved from https://agupubs.onlinelibrary.wiley.com/doi/abs/10.1029/1999JA900028 doi: 10.1029/1999JA900028

Preusse, P., Eckermann, S. D., & Ern, M. (2008). Transparency of the atmosphere to short horizontal wavelength gravity waves. *Journal of Geophysical Research: Atmospheres*, *113*(D24). Retrieved from https://agupubs.onlinelibrary.wiley.com/doi/abs/10.1029/2007JD009682 doi: https://doi.org/10.1029/2007JD009682

Preusse, P., Eckermann, S. D., Ern, M., Oberheide, J., Picard, R. H., Roble, R. G., ... Mlynczak, M. G. (2009). Global ray tracing simulations of the saber gravity wave climatology. *Journal of Geophysical Research: Atmospheres*, *114*(D8). Retrieved from https://agupubs.onlinelibrary.wiley.com/doi/abs/10.1029/2008JD011214 doi: https://doi.org/10.1029/2008JD011214

Priyadarshi, S. (2015). A review of ionospheric scintillation models. *Surveys in Geophysics*, *36*.

Qian, L., Burns, A., & Yue, J. (2017). Evidence of the Lower Thermospheric Winter-to-Summer circulation from SABER CO2 observations. *Geophysical Research Letters*, *44*(20), 10,100-10,107. Retrieved from https://agupubs.onlinelibrary.wiley.com/doi/abs/10.1002/2017GL075643 doi: 10.1002/2017GL075643

Qian, L., Burns, A. G., Emery, B. A., Foster, B., Lu, G., Maute, A., ... Wang, W. (2014). The ncar tie-gcm. In *Modeling the ionosphere thermosphere system* (p. 73-83). American Geophysical Union (AGU). Retrieved from https://agupubs.onlinelibrary.wiley.com/doi/abs/10.1002/9781118704417.ch7 doi: 10.1002/9781118704417.ch7

Qian, L., Burns, A. G., Solomon, S. C., & Wang, W. (2013). Annual/semiannual variation of the ionosphere. *Geophysical Research Letters*, *40*(10), 1928-1933. Retrieved from https://agupubs.onlinelibrary.wiley.com/doi/abs/10.1002/grl.50448 doi: 10.1002/grl.50448

Qian, L., Burns, A. G., Solomon, S. S., Smith, A. K., McInerney, J. M., Hunt, L. A., ... Vitt, F. M. (2018). Temporal Variability of Atomic Hydrogen From the Mesopause to the Upper Thermosphere. *Journal of Geophysical Research: Space Physics*, *123*(1), 1006-1017. Retrieved from https://agupubs.onlinelibrary.wiley.com/doi/abs/10.1002/2017JA024998 doi: 10.1002/2017JA024998

Qian, L., Solomon, S. C., & Kane, T. J. (2009). Seasonal variation of thermospheric density and composition. *Journal of Geophysical Research: Space Physics*, *114*(A1). Retrieved from https://agupubs.onlinelibrary.wiley.com/doi/abs/10.1029/2008JA013643 doi: 10.1029/2008JA013643

Qian, L., & Yue, J. (2017). Impact of the lower thermospheric winter-to-summer residual circulation on thermospheric composition. *Geophysical Research Letters*, *44*(9), 3971-3979. Retrieved from https://agupubs.onlinelibrary.wiley.com/doi/abs/10.1002/2017GL073361 doi: 10.1002/2017GL073361

Quegan, S., Bailey, G., Moffett, R., Heelis, R., Fuller-Rowell, T., Rees, D., & Spiro, R. (1982). A theoretical study of the distribution of ionization in the high-latitude ionosphere and the plasmasphere: first results on the mid-latitude trough and the light-ion trough. *Journal of Atmospheric and Terrestrial Physics*, *44*(7), 619-640. Retrieved from https://www.sciencedirect.com/science/article/pii/0021916982900733 doi: https://doi.org/10.1016/0021-9169(82)90073-3

Reber, C. A., Cooley, J. E., & Harpold, D. N. (1968). Upper atmosphere hydrogen and helium measurements from the explorer 32 satellite. *Space Res., 8, 993*.

Reber, C. A., & Hays, P. B. (1973). Thermospheric wind effects on the distribution of helium and argon in the earth's upper atmosphere. *Journal of Geophysical Research (1896-1977)*, *78*(16), 2977-2991. Retrieved from https://agupubs.onlinelibrary.wiley.com/doi/abs/10.1029/JA078i016p02977 doi: 10.1029/JA078i016p02977

Rees, D., & Fuller-Rowell, T. (1988). Understanding the transport of atomic oxygen within the thermosphere, using a numerical global thermospheric model. *Planetary and Space Science*, *36*(9), 935-948. Retrieved from https://www.sciencedirect.com/science/article/pii/0032063388901018 (Special Issue: Atomic Oxygen Abundance in Thermosphere) doi: https://doi.org/10.1016/0032-0633(88)90101-8

Rees, D., & Fuller-Rowell, T. (1990). Numerical simulations of the seasonal/latitudinal variations of atomic oxygen and nitric oxide in the lower thermosphere and mesosphere. *Advances in Space Research*, *10*(6), 83-102. Retrieved from https://www.sciencedirect.com/science/article/pii/027311779090240Z doi: https://doi.org/10.1016/0273-1177(90)90240-Z

Rees, D., & Fuller-Rowell, T. (2011). Impact of cir storms on thermosphere density variability during the solar minimum of 2008. *Solar Physics*, *274*(1), 427–437. Retrieved from https://doi.org/10.1007/s11207-010-9563-y doi: 10.1007/s11207-010-9563-y

Reigber, C., Lühr, H., & Schwintzer, P. (2002). Champ mission status. *Advances in Space Research*, *30*(2), 129-134. Retrieved from https://www.sciencedirect.com/science/article/pii/S0273117702002764 doi: https://doi.org/10.1016/S0273-1177(02)00276-4

Rezac, L., Jian, Y., Yue, J., Russell III, J. M., Kutepov, A., Garcia, R., ... Bernath, P. (2015). Validation of the global distribution of CO2 volume mixing ratio in the mesosphere and lower thermosphere from SABER. *Journal of Geophysical Research: Atmospheres*, *120*(23), 12,067-12,081. Retrieved from https://

agupubs.onlinelibrary.wiley.com/doi/abs/10.1002/2015JD023955 doi: 10.1002/2015JD023955

Richmond, A. D. (1983). Thermospheric dynamics and electrodynamics. In R. L. Carovillano & J. M. Forbes (Eds.), *Solar-terrestrial physics* (pp. 523–607). Dordrecht: Springer Netherlands.

Richmond, A. D. (1995). Ionospheric electrodynamics using magnetic apex coordinates. *Journal of geomagnetism and geoelectricity*, *47*(2), 191-212. doi: 10.5636/jgg.47.191

Richmond, A. D., & Kamide, Y. (1988). Mapping electrodynamic features of the high-latitude ionosphere from localized observations: Technique. *Journal of Geophysical Research: Space Physics*, *93*(A6), 5741-5759. Retrieved from https://agupubs.onlinelibrary.wiley.com/doi/abs/10.1029/JA093iA06p05741 doi: https://doi.org/10.1029/JA093iA06p05741

Richmond, A. D., Ridley, E. C., & Roble, R. G. (1992). A thermosphere/ionosphere general circulation model with coupled electrodynamics. *Geophysical Research Letters*, *19*(6), 601-604. Retrieved from https://agupubs.onlinelibrary.wiley.com/doi/abs/10.1029/92GL00401 doi: 10.1029/92GL00401

Ridley, A., Deng, Y., & Toth, G. (2006). The global ionosphere thermosphere model. *Journal of Atmospheric and Solar-Terrestrial Physics*, *68*(8), 839 - 864. Retrieved from http://www.sciencedirect.com/science/article/pii/S1364682606000071 doi: https://doi.org/10.1016/j.jastp.2006.01.008

Ridley, A. J., Crowley, G., & Freitas, C. (2000). An empirical model of the ionospheric electric potential. *Geophysical Research Letters*, *27*(22), 3675-3678. Retrieved from https://agupubs.onlinelibrary.wiley.com/doi/abs/10.1029/1999GL011161 doi: https://doi.org/10.1029/1999GL011161

Rienecker, M. M., Suarez, M. J., Gelaro, R., Todling, R., Bacmeister, J., Liu, E., ... Woollen, J. (2011). MERRA: NASA's modern-era retrospective analysis for research and applications. *Journal of Climate*, *24*(14), 3624-3648. Retrieved from https://doi.org/10.1175/JCLI-D-11-00015.1 doi: 10.1175/JCLI-D-11-00015.1

Rishbeth, H. (1998). How the thermospheric circulation affects the ionospheric f2-layer. *Journal of Atmospheric and Solar-Terrestrial Physics*, *60*(14), 1385 - 1402. Retrieved from http://www.sciencedirect.com/science/article/pii/S1364682698000625 doi: https://doi.org/10.1016/S1364-6826(98)00062-5

Rishbeth, H. (2007). Thermospheric targets. *Eos, Transactions American Geophysical Union*, *88*(17), 189-193. Retrieved from https://agupubs.onlinelibrary.wiley.com/doi/abs/10.1029/2007EO170002 doi: 10.1029/2007EO170002

Rishbeth, H., & Mendillo, M. (2001). Patterns of f2-layer variability. *Journal of Atmospheric and Solar-Terrestrial Physics*, *63*(15), 1661 - 1680. Retrieved from http://www.sciencedirect.com/science/article/pii/S1364682601000360 doi: https://doi.org/10.1016/S1364-6826(01)00036-0

Rishbeth, H., & Müller-Wodarg, I. C. F. (1999). Vertical circulation and thermospheric composition: a modelling study. *Annales Geophysicae*, *17*(6), 794–805. Retrieved from https://angeo.copernicus.org/articles/17/794/1999/ doi: 10.1007/s00585-999-0794-x

Rishbeth, H., & Roble, R. (1992). Cooling of the upper atmosphere by enhanced greenhouse gases âĂŤ modelling of thermospheric and ionospheric effects. *Planetary and Space Science*, *40*(7), 1011-1026. Retrieved from https://www.sciencedirect.com/science/article/pii/003206339290141A doi: https://doi.org/10.1016/0032-0633(92)90141-A

Rishbeth, H., Sedgemore-Schulthess, K. J. F., & Ulich, T. (2000). Semiannual and annual variations in the height of the ionospheric f2-peak. *Annales Geophysicae*, *18*(3), 285–299. Retrieved from https://angeo.copernicus.org/articles/18/285/2000/ doi: 10.1007/s00585-000-0285-6

Roble, R. (2013). On the feasibility of developing a global atmospheric model extending from the ground to the exosphere. In *Atmospheric science across the stratopause* (p. 53-67). American Geophysical Union (AGU). Retrieved from https://agupubs.onlinelibrary.wiley.com/doi/abs/10.1029/GM123p0053 doi: 10.1029/GM123p0053

Roble, R. G. (1995). Energetics of the mesosphere and thermosphere. In *The upper mesosphere and lower thermosphere: A review of experiment and theory* (p. 1-21). American Geophysical Union (AGU). Retrieved from https://agupubs.onlinelibrary.wiley.com/doi/abs/10.1029/GM087p0001 doi: https://doi.org/10.1029/GM087p0001

Roble, R. G., & Dickinson, R. E. (1989). How will changes in carbon dioxide and methane modify the mean structure of the mesosphere and thermosphere? *Geophysical Research Letters*, *16*(12), 1441-1444. Retrieved from https://agupubs.onlinelibrary.wiley.com/doi/abs/10.1029/GL016i012p01441 doi: https://doi.org/10.1029/GL016i012p01441

Roble, R. G., & Ridley, E. C. (1987, December). An auroral model for the NCAR thermospheric general circulation model (TGCM). *Annales Geophysicae*, *5*, 369-382.

Roble, R. G., & Ridley, E. C. (1994). A thermosphere-ionosphere-mesosphere-electrodynamics general circulation model (time-gcm): Equinox solar cycle minimum simulations (30?500 km). *Geophysical Research Letters*, *21*(6), 417-420. Retrieved from https://agupubs.onlinelibrary.wiley.com/doi/abs/10.1029/93GL03391 doi: https://doi.org/10.1029/93GL03391

Roble, R. G., Ridley, E. C., Richmond, A. D., & Dickinson, R. E. (1988). A coupled thermosphere/ionosphere general circulation model. *Geophysical Research Letters*, *15*(12), 1325-1328. Retrieved from https://agupubs.onlinelibrary.wiley.com/doi/abs/10.1029/GL015i012p01325 doi: https://doi.org/10.1029/GL015i012p01325

Rottger, J. (1973). Wave-like structures of large-scale equatorial spread-f irregularities. *Journal of Atmospheric and Terrestrial Physics*, *35*(6), 1195 - 1206. Retrieved from http://www.sciencedirect.com/science/article/pii/0021916973900160 doi: https://doi.org/10.1016/0021-9169(73)90016-0

Russell, C. T., & McPherron, R. L. (1973). Semiannual variation of geomagnetic activity. *Journal of Geophysical Research (1896-1977)*, *78*(1), 92-108. Retrieved from https://agupubs.onlinelibrary.wiley.com/doi/abs/10.1029/JA078i001p00092 doi: 10.1029/JA078i001p00092

Russell, J. P., Lowe, R., & Ward, W. (2004). Atomic oxygen annual and semi-annual variations in the mesopause region for mid and equatorial latitudes. *Journal of Atmospheric and Solar-Terrestrial Physics*, *66*(6), 451 - 461. Retrieved from http://www.sciencedirect.com/science/article/pii/S1364682604000124 (Dynamics and Chemistry of the MLT Region - PSMOS 2002 International Symposium) doi: https://doi.org/10.1016/j.jastp.2004.01.004

Russell III, J., Mlynczak, M., Gordley, L., Tansock, J., & Esplin, R. (1999, 10). Overview of the SABER experiment and preliminary calibration results. *Proceedings of SPIE - The International Society for Optical Engineering*, *3756*.

Salinas, C. C. J. H., Chang, L. C., Liang, M.-C., Yue, J., Russell, J., & Mlynczak, M. (2016). Impacts of SABER CO2-based eddy diffusion coefficients in the lower thermosphere on the ionosphere/thermosphere. *Journal of Geophysical Research: Space Physics*, *121*(12), 12,080-12,092. Retrieved from https://agupubs.onlinelibrary.wiley.com/doi/abs/10.1002/2016JA023161 doi: 10.1002/2016JA023161

Sasi, M. N., & Vijayan, L. (2001). Turbulence characteristics in the tropical mesosphere as obtained by mst radar at gadanki (13.5Âř n, 79.2Âř e). *Annales Geophysicae*, *19*(8), 1019–1025. Retrieved from https://angeo.copernicus.org/articles/19/1019/2001/ doi: 10.5194/angeo-19-1019-2001

Sassi, F., Liu, H.-L., & Emmert, J. T. (2016). Traveling planetary-scale waves in the lower thermosphere: Effects on neutral density and composition during solar minimum conditions. *Journal of Geophysical Research: Space Physics*, *121*(2), 1780-1801. Retrieved from https://agupubs.onlinelibrary.wiley.com/doi/abs/10.1002/2015JA022082 doi: 10.1002/2015JA022082

Schunk, R., & Nagy, A. (2009). *Ionospheres: Physics, plasma physics, and chemistry* (2nd ed.). Cambridge University Press. doi: 10.1017/CBO9780511635342

Sela, J. G. (1980). Spectral modeling at the national meteorological center. *Monthly Weather Review*, *108*(9), 1279 - 1292. Retrieved from https://journals.ametsoc.org/view/journals/mwre/108/9/1520-0493_1980_108_1279_smatnm_2_0_co_2.xml doi: 10.1175/1520-0493(1980)108<1279:SMATNM>2.0.CO;2

Sheese, P. E., McDade, I. C., Gattinger, R. L., & Llewellyn, E. J. (2011). Atomic oxygen densities retrieved from Optical Spectrograph and Infrared Imaging System observations of O2 A-band airglow emission in the mesosphere and lower thermosphere. *Journal of Geophysical Research: Atmospheres*, *116*(D1). Retrieved from https://agupubs.onlinelibrary.wiley.com/doi/abs/10.1029/2010JD014640 doi: 10.1029/2010JD014640

Shimazaki, T. (1965). On the continuity equation for electron density in the ionosphere. *Journal of Atmospheric and Terrestrial Physics*, *27*(5), 593 - 604. Retrieved from http://www.sciencedirect.com/science/article/pii/0021916965901273 doi: https://doi.org/10.1016/0021-9169(65)90127-3

Shimazaki, T. (1966). Nighttime variations of fâĂŽÃĎÃłregion electron density profiles at puerto rico: 2. an attempt to separate the effects of temperature variation and drift velocity. *Journal of Geophysical Research*, *71*(13), 3177-3190. Retrieved from https://agupubs.onlinelibrary.wiley.com/doi/abs/10.1029/JZ071i013p03177 doi: 10.1029/JZ071i013p03177

Shimazaki, T. (1967). Dynamic effects on atomic and molecular oxygen density distributions in the upper atmosphere: a numerical solution to equations of motion and continuity. *Journal of Atmospheric and Terrestrial Physics*, *29*(6), 723 - 747. Retrieved from http://www.sciencedirect.com/science/article/pii/0021916967902164 doi: https://doi.org/10.1016/0021-9169(67)90216-4

Shimazaki, T. (1968). Dynamic effects on height distributions of neutral constituents in the Earth's upper atmosphere: a calculation of atmospheric model between 70 km and 500 km. *Journal of Atmospheric and Terrestrial Physics*, *30*(7), 1279 - 1292. Retrieved from http://www.sciencedirect.com/science/article/pii/S0021916968911070 doi: https://doi.org/10.1016/S0021-9169(68)91107-0

Siskind, D. E., & Drob, D. P. (2014). Use of nogaps-alpha as a bottom boundary for the ncar/tiegcm. In *Modeling the ionosphere?thermosphere system* (p. 171-180). American Geophysical Union (AGU). Retrieved from https://agupubs.onlinelibrary.wiley.com/doi/abs/10.1002/9781118704417.ch15 doi: https://doi.org/10.1002/9781118704417.ch15

Siskind, D. E., Drob, D. P., Dymond, K. F., & McCormack, J. P. (2014). Simulations of the effects of vertical transport on the thermosphere and ionosphere using two coupled models. *Journal of Geophysical Research: Space Physics*, *119*(2), 1172-1185. Retrieved from https://agupubs.onlinelibrary.wiley.com/doi/abs/10.1002/2013JA019116 doi: 10.1002/2013JA019116

Smith, A. K., Garcia, R. R., Marsh, D. R., & Richter, J. H. (2011). WACCM simulations of the mean circulation and trace species transport in the winter mesosphere. *Journal of Geophysical Research: Atmospheres*, *116*(D20). Retrieved from https://agupubs.onlinelibrary.wiley.com/doi/abs/10.1029/2011JD016083 doi: 10.1029/2011JD016083

Smith, A. K., Harvey, V. L., Mlynczak, M. G., Funke, B., GarciaĽăa-Comas, M., Hervig, M., ... Walker, K. A. (2013). Satellite observations of ozone in the upper mesosphere. *Journal of Geophysical Research: Atmospheres*, *118*(11), 5803-5821. Retrieved from https://agupubs.onlinelibrary.wiley.com/doi/abs/10.1002/jgrd.50445 doi: 10.1002/jgrd.50445

Smith, A. K., Marsh, D. R., Mlynczak, M. G., & Mast, J. C. (2010). Temporal variations of atomic oxygen in the upper mesosphere from SABER. *Journal of Geophysical Research: Atmospheres*, *115*(D18). Retrieved from https://agupubs.onlinelibrary.wiley.com/doi/abs/10.1029/2009JD013434 doi: 10.1029/2009JD013434

Solomon, S., & Roble, R. (2015). Thermosphere. In G. R. North, J. Pyle, & F. Zhang (Eds.), *Encyclopedia of atmospheric sciences (second edition)* (Second Edition ed., p. 402-408). Oxford: Academic Press. Retrieved from https://www.sciencedirect.com/science/article/pii/B9780123822253004084 doi: https://doi.org/10.1016/B978-0-12-382225-3.00408-4

Strickland, D. J., Evans, J. S., & Paxton, L. J. (1995). Satellite remote sensing of thermospheric o/n2 and solar euv: 1. theory. *Journal of Geophysical Research: Space Physics*, *100*(A7), 12217-12226. Retrieved from https://agupubs.onlinelibrary.wiley.com/doi/abs/10.1029/95JA00574 doi: https://doi.org/10.1029/95JA00574

Strobel, D. F., Apruzese, J. P., & Schoeberl, M. R. (1985). Energy balance constraints on gravity wave induced eddy diffusion in the mesosphere and lower thermosphere. *Journal of Geophysical Research: Atmospheres*, *90*(D7), 13067-13072. Retrieved from https://agupubs.onlinelibrary.wiley.com/doi/abs/10.1029/JD090iD07p13067 doi: https://doi.org/10.1029/JD090iD07p13067

Sutton, E. K. (2011). Accelerometer-derived atmospheric density from the CHAMP and GRACE satellites. *Tech. Memo., DTIC ADA537198, Air Force Res. Lab., Kirtland AFB, N. M.*. Retrieved from https://apps.dtic.mil/sti/pdfs/ADA537198.pdf

Sutton, E. K. (2016). Interhemispheric transport of light neutral species in the thermosphere. *Geophysical Research Letters*, *43*(24), 12,325-12,332. Retrieved from https://agupubs.onlinelibrary.wiley.com/doi/abs/10.1002/2016GL071679 doi: 10.1002/2016GL071679

Swenson, G., Yee, Y., Vargas, F., & Liu, A. (2018). Vertical diffusion transport of atomic oxygen in the mesopause region consistent with chemical losses and continuity: Global mean and inter-annual variability. *Journal of Atmospheric and Solar-Terrestrial Physics*, *178*, 47 - 57. Retrieved from http://www.sciencedirect.com/science/article/pii/S1364682617305552 doi: https://doi.org/10.1016/j.jastp.2018.05.014

Swenson, G. R., Salinas, C. C. J. H., Vargas, F., Zhu, Y., Kaufmann, M., Jones Jr., M., ... Yee, J. H. (2019). Determination of global mean eddy diffusive transport in the mesosphere and lower thermosphere from atomic oxygen and carbon dioxide climatologies. *Journal of Geophysical Research: Atmospheres*, *124*(23), 13519-13533. Retrieved from https://agupubs.onlinelibrary.wiley.com/doi/abs/10.1029/2019JD031329 doi: https://doi.org/10.1029/2019JD031329

Szewczyk, A., Strelnikov, B., Rapp, M., Strelnikova, I., Baumgarten, G., Kaifler, N., ... Hoppe, U.-P. (2013). Simultaneous observations of a mesospheric inversion layer and turbulence during the ecoma-2010 rocket campaign. *Annales Geophysicae*, *31*(5), 775–785. Retrieved from https://angeo.copernicus.org/articles/31/775/2013/ doi: 10.5194/angeo-31-775-2013

Tapley, B. D., Bettadpur, S., Watkins, M., & Reigber, C. (2004). The gravity recovery and climate experiment: Mission overview and early results. *Geophysical Research Letters*, *31*(9). Retrieved from https://agupubs.onlinelibrary.wiley.com/doi/abs/10.1029/2004GL019920 doi: https://doi.org/10.1029/2004GL019920

Trinh, Q. T., Ern, M., Doornbos, E., Preusse, P., & Riese, M. (2018). Satellite observations of middle atmosphere–thermosphere vertical coupling by gravity waves. *Annales Geophysicae*, *36*(2), 425–444. Retrieved from https://angeo.copernicus.org/articles/36/425/2018/ doi: 10.5194/angeo-36-425-2018

Triplett, C. C., Li, J., Collins, R. L., Lehmacher, G. A., Barjatya, A., Fritts, D. C., ... Varney, R. H. (2018). Observations of Reduced Turbulence and Wave Activity in the Arctic Middle Atmosphere Following the January 2015 Sudden Stratospheric Warming. *Journal of geophysical research. Atmospheres : JGR*, *123*(23), 13259–13276. Retrieved from https://pubmed.ncbi.nlm.nih.gov/31187016 doi: 10.1029/2018JD028788

Tsuda, T. (2014, January). Characteristics of atmospheric gravity waves observed using the MU (Middle and Upper atmosphere) radar and GPS (Global Positioning System) radio occultation. *Proceeding of the Japan Academy, Series B, Physical and biological sciences*, *90*(1), 12-27. Retrieved from https://doi.org/10.2183/pjab.90.12 doi: 10.2183/pjab.90.12

Tsuda, T., Kato, S., Yokoi, T., Inoue, T., Yamamoto, M., VanZandt, T. E., ... Sato, T. (1990). Gravity waves in the mesosphere observed with the middle and upper atmosphere radar. *Radio Science*, *25*(5), 1005-1018. Retrieved from https://agupubs.onlinelibrary.wiley.com/doi/abs/10.1029/RS025i005p01005 doi: https://doi.org/10.1029/RS025i005p01005

Tóth, G., Sokolov, I. V., Gombosi, T. I., Chesney, D. R., Clauer, C. R., De Zeeuw, D. L., ... Kóta, J. (2005). Space weather modeling framework: A new tool for the space science community. *Journal of Geophysical Research: Space Physics*, *110*(A12). Retrieved from https://agupubs.onlinelibrary.wiley.com/doi/abs/10.1029/2005JA011126 doi: https://doi.org/10.1029/2005JA011126

Vadas, S. L. (2007). Horizontal and vertical propagation and dissipation of gravity waves in the thermosphere from lower atmospheric and thermospheric sources. *Journal of Geophysical Research: Space Physics*, *112*(A6). Retrieved from https://agupubs.onlinelibrary.wiley.com/doi/abs/10.1029/2006JA011845 doi: https://doi.org/10.1029/2006JA011845

van der Meeren, C., Oksavik, K., Lorentzen, D. A., Rietveld, M. T., & Clausen, L. B. N. (2015). Severe and localized gnss scintillation at the poleward edge of the nightside auroral oval during intense substorm aurora. *Journal of Geophysical Research: Space Physics*, *120*.

Vierinen, J., Coster, A. J., Rideout, W. C., Erickson, P. J., & Norberg, J. (2016). Statistical framework for estimating gnss bias. *Atmospheric Measurement Techniques*, *9*(3), 1303–1312. Retrieved from https://amt.copernicus.org/articles/9/1303/2016/ doi: 10.5194/amt-9-1303-2016

Vlasov, M. N., & Kelley, M. C. (2014). Specific features of eddy turbulence in the turbopause region. *Annales Geophysicae*, *32*(4), 431–442. Retrieved from https://angeo.copernicus.org/articles/32/431/2014/ doi: 10.5194/angeo-32-431-2014

Vlasov, M. N., & Kelley, M. C. (2015). Eddy diffusion coefficients and their upper limits based on application of the similarity theory. *Annales Geophysicae*, *33*(7), 857–864. Retrieved from https://angeo.copernicus.org/articles/33/857/2015/ doi: 10.5194/angeo-33-857-2015

Volland, H., Wulf-Mathies, C., & Priester, W. (1972). On the annual and semiannual variations of the thermospheric density. *Journal of Atmospheric and Terrestrial Physics*, *34*(6), 1053 - 1063. Retrieved from http://www.sciencedirect.com/science/article/pii/0021916972900943 doi: https://doi.org/10.1016/0021-9169(72)90094-3

von Zahn, U. (1967). Mass spectrometric measurements of atomic oxygen in the upper atmosphere: A critical review. *Journal of Geophysical Research (1896-1977)*, *72*(23), 5933-5937. Retrieved from https://agupubs.onlinelibrary.wiley.com/doi/abs/10.1029/JZ072i023p05933 doi: 10.1029/JZ072i023p05933

Walker, J. C. G. (1965). Analytic representation of upper atmosphere densities based on Jacchia's Static Diffusion Models. *Journal of the Atmospheric Sciences*, *22*(4), 462-463. Retrieved from https://doi.org/10.1175/1520-0469(1965)022<0462:AROUAD>2.0.CO;2 doi: 10.1175/1520-0469(1965)022<0462:AROUAD>2.0.CO;2

Walterscheid, R. L. (1982). The semiannual oscillation in the thermosphere as a conduction mode. *Journal of Geophysical Research: Space Physics*, *87*(A12), 10527-10535. Retrieved from https://agupubs.onlinelibrary.wiley.com/doi/abs/10.1029/JA087iA12p10527 doi: 10.1029/JA087iA12p10527

Walterscheid, R. L., & Christensen, A. B. (2016). Low-latitude gravity wave variances in the mesosphere and lower thermosphere derived from saber temperature observation and compared with model simulation of waves generated by deep tropical convection. *Journal of Geophysical Research: Atmospheres*, *121*(20), 11,900-11,912. Retrieved from https://agupubs.onlinelibrary.wiley.com/doi/abs/10.1002/2016JD024843 doi: https://doi.org/10.1002/2016JD024843

Wang, H., Akmaev, R. A., Fang, T.-W., Fuller-Rowell, T. J., Wu, F., Maruyama, N., & Iredell, M. D. (2014). First forecast of a sudden stratospheric warming with a coupled whole-atmosphere/ionosphere model idea. *Journal of Geophysical Research: Space Physics*, *119*(3), 2079-2089. Retrieved from https://agupubs.onlinelibrary.wiley.com/doi/abs/10.1002/2013JA019481 doi: https://doi.org/10.1002/2013JA019481

Wang, H., Cui, Y. M., Li, R., Zhang, L. Y., & Han, H. (2008). Solar flare forecasting model supported with artificial neural network techniques. *Advances in Space Research*, *42*(9), 1464-1468. Retrieved from https://www.sciencedirect.com/science/article/pii/S0273117707007405 doi: https://doi.org/10.1016/j.asr.2007.06.070

Wang, J. C., Chang, L. C., Yue, J., Wang, W., & Siskind, D. E. (2017). The quasi 2 day wave response in time-gcm nudged with nogaps-alpha. *Journal of Geophysical Research: Space Physics*, *122*(5), 5709-5732. Retrieved from https://agupubs.onlinelibrary.wiley.com/doi/abs/10.1002/2016JA023745 doi: https://doi.org/10.1002/2016JA023745

Wang, W., Killeen, T., Burns, A., & Roble, R. (1999). A high-resolution, three-dimensional, time dependent, nested grid model of the coupled thermosphereâĂŞionosphere. *Journal of Atmospheric and Solar-Terrestrial Physics*, *61*(5), 385-397. Retrieved from https://www.sciencedirect.com/science/article/pii/S1364682698000790 doi: https://doi.org/10.1016/S1364-6826(98)00079-0

Wang, W., Killeen, T. L., Burns, A. G., & Reinisch, B. W. (2001). A real-time model-observation comparison of f 2 peak electron densities during the upper atmospheric research collaboratory campaign of october 1997. *Journal of Geophysical Research: Space Physics*, *106*(A10), 21077-21082. Retrieved from https://agupubs.onlinelibrary.wiley.com/doi/abs/10.1029/2000JA000211 doi: https://doi.org/10.1029/2000JA000211

Wei, L., Zhong, Q., Lin, R., Wang, J., Liu, S., & Cao, Y. (2018). Quantitative prediction of high-energy electron integral flux at geostationary orbit based on

deep learning. *Space Weather*, *16*(7), 903-916. Retrieved from https://agupubs.onlinelibrary.wiley.com/doi/abs/10.1029/2018SW001829 doi: https://doi.org/10.1029/2018SW001829

Weimer, D. R. (2005). Improved ionospheric electrodynamic models and application to calculating joule heating rates. *Journal of Geophysical Research: Space Physics*, *110*(A5). Retrieved from https://agupubs.onlinelibrary.wiley.com/doi/abs/10.1029/2004JA010884 doi: 10.1029/2004JA010884

Weimer, D. R., Mlynczak, M. G., Emmert, J. T., Doornbos, E., Sutton, E. K., & Hunt, L. A. (2018). Correlations between the Thermosphere's Semiannual Density Variations and Infrared Emissions Measured With the SABER Instrument. *Journal of Geophysical Research: Space Physics*, *123*(10), 8850-8864. Retrieved from https://agupubs.onlinelibrary.wiley.com/doi/abs/10.1029/2018JA025668 doi: 10.1029/2018JA025668

Wintoft, P., Wik, Magnus, Matzka, Jürgen, & Shprits, Yuri. (2017). Forecasting kp from solar wind data: input parameter study using 3-hour averages and 3-hour range values. *J. Space Weather Space Clim.*, *7*, A29. Retrieved from https://doi.org/10.1051/swsc/2017027 doi: 10.1051/swsc/2017027

Wu, D. L., Yee, J.-H., Schlecht, E., Mehdi, I., Siles, J., & Drouin, B. J. (2016). Thz limb sounder (tls) for lower thermospheric wind, oxygen density, and temperature. *Journal of Geophysical Research: Space Physics*, *121*(7), 7301-7315. Retrieved from https://agupubs.onlinelibrary.wiley.com/doi/abs/10.1002/2015JA022314 doi: 10.1002/2015JA022314

Wu, Q., Ortland, D., Foster, B., & Roble, R. (2012). Simulation of nonmigrating tide influences on the thermosphere and ionosphere with a timed data driven tiegcm. *Journal of Atmospheric and Solar-Terrestrial Physics*, *90-91*, 61-67. Retrieved from https://www.sciencedirect.com/science/article/pii/S1364682612000429 (Recent Progress in the Vertical Coupling in the Atmosphere-Ionosphere System) doi: https://doi.org/10.1016/j.jastp.2012.02.009

Wu, Q., Schreiner, W. S., Ho, S.-P., Liu, H.-L., & Qian, L. (2017). Observations and simulations of eddy diffusion and tidal effects on the semiannual oscillation in the ionosphere. *Journal of Geophysical Research: Space Physics*, *122*(10), 10,502-10,510. Retrieved from https://agupubs.onlinelibrary.wiley.com/doi/abs/10.1002/2017JA024341 doi: 10.1002/2017JA024341

Yamazaki, Y., & Richmond, A. D. (2013). A theory of ionospheric response to upward-propagating tides: Electrodynamic effects and tidal mixing effects. *Journal of Geophysical Research: Space Physics*, *118*(9), 5891-5905. Retrieved from https://agupubs.onlinelibrary.wiley.com/doi/abs/10.1002/jgra.50487 doi: 10.1002/jgra.50487

Yee, J. H. (2003). TIMED mission science overview. *John Hopkins APL Technical Digest*, *24*(2), 136-141 Apr-Jun.

Yigit, E., Aylward, A. D., & Medvedev, A. S. (2008). Parameterization of the effects of vertically propagating gravity waves for thermosphere general circulation models: Sensitivity study. *Journal of Geophysical Research: Atmospheres*, *113*(D19). Retrieved from https://agupubs.onlinelibrary.wiley.com/doi/abs/10.1029/2008JD010135 doi: https://doi.org/10.1029/2008JD010135

Yigit, E., & Medvedev, A. S. (2009). Heating and cooling of the thermosphere by internal gravity waves. *Geophysical Research Letters*, *36*(14). Retrieved from https://agupubs.onlinelibrary.wiley.com/doi/abs/10.1029/2009GL038507 doi: https://doi.org/10.1029/2009GL038507

Yigit, E., & Medvedev, A. S. (2017). Influence of parameterized small-scale gravity waves on the migrating diurnal tide in earth's thermosphere. *Journal of Geophysical Research: Space Physics*, *122*(4), 4846-4864. Retrieved from https://agupubs.onlinelibrary.wiley.com/doi/abs/10.1002/2017JA024089 doi: https://doi.org/10.1002/2017JA024089

Yu, T., Ren, Z., Yu, Y., Yue, X., Zhou, X., & Wan, W. (2020). Comparison of reference heights of o/n2 and ?o/n2 based on guvi dayside limb measurement. *Space Weather*, *18*(1), e2019SW002391. Retrieved from https://agupubs.onlinelibrary.wiley.com/doi/abs/10.1029/2019SW002391 (e2019SW002391 2019SW002391) doi: https://doi.org/10.1029/2019SW002391

Yue, J., Jian, Y., Wang, W., Meier, R., Burns, A., Qian, L., ... Mlynczak, M. (2019). Annual and Semiannual Oscillations of Thermospheric Composition in TIMED/GUVI Limb measurements. *Journal of Geophysical Research: Space Physics*, *124*(4), 3067-3082. Retrieved from https://agupubs.onlinelibrary.wiley.com/doi/abs/10.1029/2019JA026544 doi: 10.1029/2019JA026544

Zhang, S. P., McLandress, C., & Shepherd, G. G. (2007). Satellite observations of mean winds and tides in the lower thermosphere: 2. wind imaging interferometer monthly winds for 1992 and 1993. *Journal of Geophysical Research: Atmospheres*, *112*(D21). Retrieved from https://agupubs.onlinelibrary.wiley.com/doi/abs/10.1029/2007JD008457 doi: 10.1029/2007JD008457

Zhang, X., Forbes, J. M., & Hagan, M. E. (2010a). Longitudinal variation of tides in the mlt region: 1. tides driven by tropospheric net radiative heating. *Journal of Geophysical Research: Space Physics*, *115*(A6). Retrieved from https://agupubs.onlinelibrary.wiley.com/doi/abs/10.1029/2009JA014897 doi: 10.1029/2009JA014897

Zhang, X., Forbes, J. M., & Hagan, M. E. (2010b). Longitudinal variation of tides in the MLT region: 2. relative effects of solar radiative and latent heating. *Journal of Geophysical Research: Space Physics*, *115*(A6). Retrieved from https://agupubs.onlinelibrary.wiley.com/doi/abs/10.1029/2009JA014898 doi: 10.1029/2009JA014898

Zhang, Y., & Paxton, L. (2008). An empirical kp-dependent global auroral model based on timed/guvi fuv data. *Journal of Atmospheric and Solar-Terrestrial Physics*, *70*(8), 1231-1242. Retrieved from https://www.sciencedirect.com/science/article/pii/S1364682608000758 doi: https://doi.org/10.1016/j.jastp.2008.03.008

Zhang, Y., Paxton, L., Morrison, D., Marsh, D., & Kil, H. (2014). Storm-time behaviors of O/N_2 and NO variations. *Journal of Atmospheric and Solar-Terrestrial Physics*, *114*, 42 - 49. Retrieved from http://www.sciencedirect.com/science/article/pii/S136468261400087X doi: https://doi.org/10.1016/j.jastp.2014.04.003

Zhang, Y., Paxton, L. J., Morrison, D., Wolven, B., Kil, H., Meng, C.-I., ... Immel, T. J. (2004). O/N_2 changes during 1–4 october 2002 storms: IMAGE SI –13 and TIMED/GUVI observations. *Journal of Geophysical Research: Space Physics*, *109*(A10). Retrieved from https://agupubs.onlinelibrary.wiley.com/doi/abs/10.1029/2004JA010441 doi: 10.1029/2004JA010441

Zhu, J., & Ridley, A. J. (2016). Investigating the performance of simplified neutral-ion collisional heating rate in a global it model. *Journal of Geophysical Research: Space Physics*, *121*(1), 578-588. Retrieved from https://agupubs.onlinelibrary.wiley.com/doi/abs/10.1002/2015JA021637 doi: https://doi.org/10.1002/2015JA021637

Zimmerman, S. P., & Murphy, E. A. (1977). Stratospheric and mesospheric turbulence. In B. Grandal & J. A. Holtet (Eds.), *Dynamical and chemical coupling between the neutral and ionized atmosphere* (pp. 35–47). Dordrecht: Springer Netherlands.